

ANNUAL REPORT 2010



COLUMBIA UNIVERSITY

*College of Physicians
and Surgeons*



ANNUAL REPORT 2010



David J. Brenner
Director

Howard B. Lieberman
Editor

Margaret L. Zhu
Assistant Editor



COLUMBIA UNIVERSITY

*College of Physicians
and Surgeons*



Table of Contents

CONTENTS.....	1
COLLABORATING DEPARTMENTS AND INSTITUTIONS.....	4
ACKNOWLEDGEMENT OF SUPPORT.....	5
RELATED WEB SITES.....	5
INTRODUCTION.....	6
STAFF NEWS.....	7
COLUMBIA COLLOQUIUM AND LABORATORY SEMINARS.....	8
STAFF LISTING.....	9
STAFF PHOTO.....	10
RESEARCH REPORTS	
<u>MICROBEAM DEVELOPMENT AND EXPERIMENTAL STUDIES</u>	
Optoelectronic Tweezer Integration on the Columbia University Microbeam	
Michael Grad, Alan W. Bigelow, Guy Y. Garty, David J. Brenner and Daniel Attinger.....	11
DNA Base Damage Induced by the UV Microspot at RARAF	
Alan W. Bigelow, Helen C. Turner, Gerhard Randers-Pehrson, Andrew Durocher, Charles R. Geard, David J. Brenner and Aroumougame Asaithambya.....	13
Enhanced Imaging for the Microbeam Irradiator	
Andrew D. Harken, Gerhard Randers-Pehrson and David J. Brenner.....	15
Proton Induced Soft X-ray Microbeam at RARAF	
Andrew D. Harken, Gerhard Randers-Pehrson, Gary W. Johnson and David J. Brenner.....	16
Simultaneous Immersion Mirau Interferometry	
Oleksandra V. Lyulko, Gerhard Randers-Pehrson and David J. Brenner.....	17
Neutron Microbeam	
Yanping Xu.....	19
<u>BYSTANDER STUDIES</u>	
A Protective Role of Heme Oxygenase-1 (HO-1) Against Oxidative Stress-induced Cell Death Could be Quantitatively Different in Normal and Cancer Cells	
Vladimir N. Ivanov and Tom K. Hei.....	21
Mitochondrial Alteration in Cytoplasmic Irradiation	
Hongning Zhou, Sarah Huang, Alan W. Bigelow and Tom K. Hei.....	27
The Role of Rad9 in Genomic Instability in Directly Irradiated and Bystander Cells	
Brian Ponnaiya, Kevin M. Hopkins and Howard B. Lieberman.....	28
Induction of Genomic Instability in Bystander Cells Via Media Transfer Following Si490 Irradiation	
Brian Ponnaiya, Masao Suzukia, Chirzuru Tsuruokaa, Yukio Uchihoria and Tom K. Hei.....	30
Cox2 Expression in Irradiated and Bystander Mouse Mammary Tissues	
Brian Ponnaiya, Yunfei Chai, Charles R. Geard and Tom K. Hei.....	34
TGFBI Potentiates in Vitro Invasion Ability in Mesothelioma Cells	
Gengyun Wen, Wupeng Liao, Vina Pulido and Tom K. Hei.....	36

Epigenetic Inactivation of the TGFBI in Human Leukemia	
Hongbo Fang, Tom K. Hei and Yongliang Zhao.....	39
Differential Gene Expression in Nuclear and Cytoplasmic Microbeam Irradiated Normal Human Fibroblasts	
Shanaz A. Ghandhi and Sally A. Amundson.....	41
Heavy Ion radiation Induced Non-targeted Effects in Breast Tissue	
Tony JC.Wang, Yunfei Chai and Tom K. Hei.....	43
<u>MOLECULAR STUDIES</u>	
Rad9 Contributes to Prostate Cancer Cell Growth and Metastasis	
Constantinos G. Broustas and Howard B. Lieberman	48
<i>Mrad9^{-/-}</i> but Not <i>Mrad9b^{-/-}</i> Mouse Embryonic Stem Cells Are Sensitive to PARP-1 Inhibition	
Relative to Wild Type Controls	
Corinne Leloup, Adayabalam Balajee, Kevin M. Hopkins and Howard B. Lieberman	51
DNMT3B Knockdown in Prostate Cancer Cells Reduces Tumor Formation in Nude Mice	
Corinne Leloup, Aiping Zhu, Xiangyuan Wang and Howard B. Lieberman	54
Mrad9 Plays an Important Role In Spermatogenesis	
Ana Vasileva, Kevin Hopkins,XiangYuan Wang, Melissa Weissbach, Aiping Zhu, Debra Wolgemuth and Howard Lieberman.....	57
Human Rad9 Subcellular Localization as Induced by Microirradiation	
Joshua D. Bernstock, Kevin M. Hopkins, Aiping Zhu, Constantinos G. Broustas and Howard B. Lieberman.....	60
Genetic Control of the Trigger for the G2/M Checkpoint	
Erik F. Young, Lubomir B. Smilenov and Eric J. Hall.....	62
Generation of a Low Cost Live Cell Imaging Capability	
Erik F. Young	63
<u>CELLULAR STUDIES</u>	
Effects of Ionizing Radiation on DNA Repair Dynamics in 3-Dimensional Human Vessel Models:	
Differential Effects According to Radiation Quality	
Peter W. Grabham, Burong Hu, Alan W. Bigelow and Charles R. Geard.....	66
Development of Human 3-Dimensional Brain Tissue Culture Model for the Study of Space	
Radiation Effects on the Degeneration of the Central Nervous System	
Preety Sharma and Peter W. Grabham	69
Effect of Ionizing Radiation on Endothelial Monolayer Permeability and Barrier Function	
Preety Sharma and Peter W. Grabham	71
Ultraviolet light Exposure Influences Skin Cancer in Association with Latitude	
Miguel Rivas, María C. Araya, Fresia Caba, Elisa Rojas and Gloria M. Calaf	75
<u>POPULATION-BASED RADIOLOGY OR RADIOTHERAPY ORIENTED STUDIES</u>	
The Balance between Initiation and Promotion in Radiation-induced Murine Carcinogenesis	
Igor Shuryak, Robert L. Ullrich, Rainer K. Sachs and David J. Brenner	80
Effects of Radiation Quality on Interactions between Oxidative Stress, Protein and DNA Damage in	
Deinococcus Radiodurans	
Igor Shuryak and David J. Brenner	82

Identify Urinary Biomarkers in Response to Radiation using NMR Spectroscopy	
Congju Chen, Truman R. Browna and David J. Brenner	84
Progress in Adapting the X-ray Machine to Low Dose Rate Studies	
Carl D. Elliston, Sally A. Amundson, Sunirmal Paul, Gary W. Johnson, Lubomir B. Smilenov and David J. Brenner.....	87
Predicting the Risk of Secondary Lung Malignancy Associated with Breast Radiation Therapy	
John Ng, Igor Shuryak, Yanguang Xu, KS Clifford Chao, Ryan J. Burri, Tom K. Hei and David J. Brenner	89
<u>CENTER FOR HIGH-THROUGHPUT MINIMALLY-INVASIVE RADIATION BIODOSIMETRY (U19)</u>	
New Directions for the Center for High Throughput Minimally Invasive Radiation Biodosimetry	
Guy Y. Garty, Sally A. Amundson, Albert J. Fornace and David J. Brenner.....	94
Advances in the Lymphocyte Harvesting Module on the RABiT	
Guy Y. Garty, Youhua Chen, Jian Zhang, Hongliang Wang, Nabil Simaan, Y. Lawrence Yao and David J. Brenner	95
Effects of <i>Ex Vivo</i> Culture on Gene Expression in Human Peripheral Blood Cells	
Sunirmal Paul and Sally A. Amundson	97
Post-irradiation Kinetics of γ-H2AX in Peripheral Lymphocytes after Radiotherapy Treatment	
Helen C. Turner, Guy Y. Garty, Maria Taveras, Antonella Bertucci, Israel Deutsch and David J. Brenner	99
γ-H2AX Signal Preservation in Blood Samples Shipped for Biodosimetry Analysis	
Maria Taveras, Guy Y. Garty, David J. Brenner and Helen C. Turner.....	101
Automated Image Analysis for Micronucleus Assay in RABiT	
Oleksandra V. Lyulko, Guy Y. Garty, Helen C. Turner, Gerhard Randers-Pehrson and David J. Brenner	105
Gene Expression Responses to Low-dose Radiation Exposure in Human Peripheral Blood	
Sally A. Amundson and Sunirmal Paul	108
Whole Mouse Blood MicroRNAs as Biomarkers for Exposure to γ-rays and ^{56}Fe Ions	
Thomas Templin, Sally A. Amundson, David J. Brenner, and Lubomir B. Smilenov	110
Radiation-induced MicroRNA Expression Changes in Peripheral Blood Cells of Radiotherapy Patients	
Thomas Templin, Sunirmal Paul, Sally A. Amundson, Erik F. Young, Christopher A. Barker, Suzanne L. Woldena and Lubomir B. Smilenov	112
Validation of the Micronucleus Assay as A Biodosimeter in the C57Bl Mouse Model	
Brian Ponnaiya, Antonella Bertucci, Helen C. Turner and David J. Brenner.....	115
THE RADIOLOGICAL RESEARCH ACCELERATOR FACILITY – an NIH-Supported Resource Center	
<i>Dir., David J. Brenner, PhD, DSc; Assoc. Dir. Gerhard Randers-Pehrson, PhD; Mnger., Stephen A. Marino, MS</i>	
Table of Contents.....	117
RARAF Professional Staff and Picture	117
Research using RARAF	118
Development of Facilities	121
Singletron Utilization and Operation.....	125
Training.....	126
Dissemination.....	126
Personnel	126
Recent Publications of Work Performed at RARAF.....	127
PUBLICATIONS	128

Collaborating Institutions

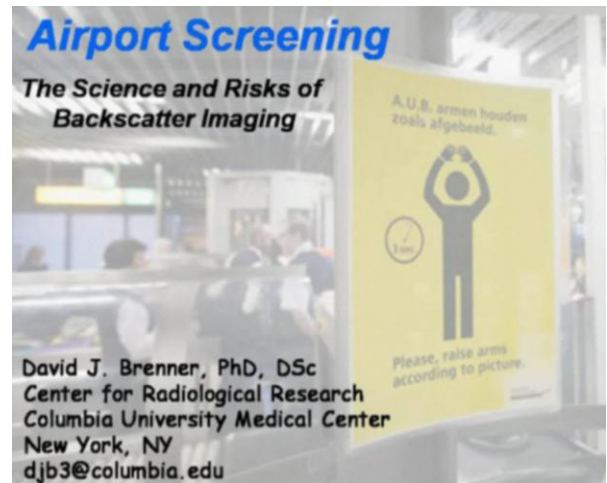
Individuals from the following institutions collaborated with the Center's faculty and staff in the research reports included in this year's publication (for individual attributions see specific reports):

Collaborating Columbia University Departments:

- ARMA -Advanced Robotics & Mechanism Applications lab in the Department of Mechanical Engineering
- Department of Biochemistry and Molecular Biophysics, Howard Hughes Medical Institute
- Department of Biostatistics, Mailman School of Public Health
- Department of Genetics and Development
- Department of Mechanical Engineering
- Department of Medicine
- Department of Neurology
- Department of Radiology
- Department of Radiation Oncology
- Institute for Cancer Genetics

Collaborating Institutions:

- Departments of Mathematics and Physics, University of California, Berkeley, CA
- Instituto de Alta Investigación, Universidad de Tarapacá, Arica, Chile
- Instituto de Nutrición y Tecnología de Alimentos, Universidad de Chile, Santiago, Chile.
- National Heart Lung and Blood Institute, NIH
- National Institute of Radiological Sciences, Chiba, Japan
- Physics Department, New York University, New York, NY
- Toshiba American Medical Systems
- Lombardi Comprehensive Cancer Center, Georgetown University
- Center for Countermeasures Against Radiation, Lovelace Respiratory Research Institute, NM
- Translational Genomics Research Institute (TGen), AZ
- New York University School of Medicine
- Institut für Klinische Pharmakologie (IKPVF), University of Bern, Switzerland
- Department of Radiation Oncology, University of Medicine and Dentistry New Jersey
- Memorial Sloan-Kettering Cancer Center
- Laboratoire des Lésions des Acides Nucléiques, Institut for Nanoscience and Cryogenics, France
- Radiation Biophysics Laboratory, NASA Johnson Space Center
- Monash Institute for Medical Research, Monash University, Australia
- Washington University School of Medicine ■



Dr. David Brenner speaks about Airport Screening on Capitol Hill "Congressional Biomedical Research Caucus Presentation", March 17, 2010.

Acknowledgment of Support

In 2010, the Center for Radiological Research was supported by competitively awarded grants from the following agencies:

- Department of Defense
 - Defense Threat Reduction Agency
- Department of Energy
 - Office of Science, Office of Biological and Environmental Research [Low Dose Radiation Research Program]
- Department of Health and Human Services
 - National Institutes of Health:
 - National Cancer Institute [Program Project (PO1) & Individual Research Grants (RO1s)]
- National Institute of Biomedical Imaging and Bioengineering (P41)
- National Institute of Allergy and Infectious Disease (U19)
- National Institute of Environmental Health and Safety (RO1s & R21)
- National Institute of General Medical Sciences (RO1)
- National Aeronautics and Space Administration ■

Web Sites

- Center for Radiological Research <http://crr-cu.org>
 - Radiological Research Accelerator Facility <http://www.raraf.org>
 - Center for High-Throughput Minimally-Invasive Radiation Biodosimetry <http://www.cmcrcolumbia.edu>
 - Mechanism of Bystander Effects <http://www.radiation-bystander.columbia.edu>
 - Web-Rad-Train <http://www.web-rad-train.org>
 - Department of Radiation Oncology <http://cpmcnet.columbia.edu/dept/radoncology>
 - Radiation Safety Office <http://rso.cumc.columbia.edu>
- CRR Annual Reports (1998–present) <http://crr-cu.org/reports.htm>



Center for Radiological Research 2010 Picnic (L-r): Dr. Sally Amundson, Dr. Charles Geard and Dr. Hongning Zhou.

Introduction

2010 was a stimulating and rewarding year for our Center. Our three major research programs, the Center for High Throughput Minimally Invasive Biodosimetry (www.cmcr.columbia.edu), the Radiation-induced Bystander effects: Mechanisms (www.radiation-bystander.columbia.edu), and Radiological Research Accelerator Facility (www.raraf.org) are all in the midst of their five-year funding cycles, which has allowed us to buckle down and do science, with only half an eye on grant renewing! For example, in our biodosimetry studies, we focused this year on the effect on our biodosimetry assays of protracting exposures. At our RARAF accelerator, we have come up with a design for an “ultra microbeam” where we hope to break the 100 nm beam size barrier. Our bystander response research has made a major move from *in-vitro* to *in-vivo* models, which is technically challenging but mechanistically much more relevant.

We have also diversified somewhat, starting our first studies for many years on the biological effects of UV irradiation, initiating an innovative project to sterilize wounds in an operating room setting without damaging normal human tissue. This project has opened up new collaborations with the Department of Surgery.

We continue to collaborate extensively with scientists from other Columbia departments, such as the Departments of Environmental Sciences and Biostatistics (at the Mailman School of Public Health), Radiology, Biochemistry, Genetics and Development, Electrical Engineering, and Mechanical Engineering. This is of course in addition to the increasing collaborations with the physicians and physicists at our own Department of Radiation Oncology. Outside Columbia, we have a worldwide network of collaborators in Japan, Russia, and Europe, as well as in the U.S. at NYU, Memorial Sloan Kettering Cancer Center, New Jersey Medical School, University of Texas Medical Branch, Duke, Georgetown, UC Berkeley, UC San Francisco, University of Arizona, Arizona State University, the NCI, and Northrop Grumman Corporation.

We continue to be called upon extensively to inform Congress and the general public about issues associated with radiation exposure. Dr David Brenner, is shown here with U.S. Representative Rush Holt, briefing staffers at the House



of Representatives Congressional Biomedical Caucus. Of course the Fukushima disaster occurred early in 2011, so much more about that in the 2011 Annual Report, but suffice to say that members at the Center played a leading role in interpreting the events there to a world wide audience, both in print, on the TV and the radio.

Finally, it is with much sadness that we note the untimely passing in 2010 of Dr Elaine Ron, Senior Epidemiologist at the National Cancer Institute. Elaine was for many years an Adjunct Professor at our Center for Radiological Research. Many of the research projects that are currently thriving at our Center owe much to Elaine’s advice and support, such as the studies of CT risks, and of radiotherapy-induced second cancers. She is sorely missed. ■



Staff News

Dr. David Brenner's research on CT imaging was featured in a news article in Science Magazine. He played a prominent role in interpreting the events at Fukushima for the general public, both on TV, radio, and in print. He was featured in the "Scientist at Work" series in the New York Times, and wrote an Editorial in the Wall Street Journal. Dr. Brenner testified to the Congressional House Oversight and Government Reform Subcommittee on National Security, on the issue of x-ray scanners in airports. He was elected as Physics Councilor for the International Association of Radiation Research and remains an Associate Editor of *Radiation and Environmental Biophysics*.

Dr. Tom Hei was elected Vice-President Elect of the Radiation Research Society, and will assume office at the 2012 meeting of the Society in Puerto Rico. Dr. Hei is the fourth member of the Center to be elected to this office in the largest radiation research society in the world, a record not equaled by any other laboratory.

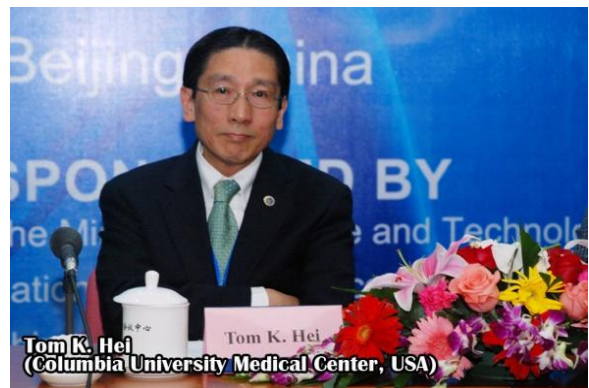
Dr. Howard Lieberman was appointed to permanent membership on the NIH Radiation Therapeutics and Biology Study Section. He continues to serve on the Scientific Advisory Board for the Israel Cancer Research Fund. He also remains an Associate Editor of the journals *Radiation Research* and *Journal of Cellular Physiology*.

Dr. Sally Amundson was re-elected to the National Council for Radiation Protection and Measurements (NCRP) and continues to serve on the Scientific Council of the joint US-Japan Radiation Effects Research Foundation (RERF). She also returned as a study section member for the National Institute of Biomedical Imaging and Bioengineering panel "Biomedical Research on the International Space Station," and continued service as an Associate Editor of the journal *Radiation Research*.

We will miss several staff members who left the Center during the past year, and we wish them well in their new ventures. Dr. Stephane Lucas returned to Belgium after a period as visiting research scientist at RARAF. Drs Barbara Szolc and Alexandre Mezentsev, and Jingshuang Lu left for new positions elsewhere. Xuelian (Sarah) Huang left to take up a post-doctoral position at Mt Sinai Medical School, and Abel Bencosme left us to train as a nurse practitioner.

Three new post-doctoral fellows joined us this year: Dr Preeti Sharma in the groups of Drs. Grabham and Brenner, Dr Hongbo Fang in Dr. Zhao's group, and Dr. Erik Young in Lubomir Smilenov's group. Dr. Constantinos Broustas and Dr. Ana Vasileva both joined Dr. Lieberman's group as Associate Research Scientists. Maria Taveras joined Dr. Brenner's group as a research nurse.

We were delighted that several CRR members were promoted during the year. Drs. Igor Shuryak, Gengyun Wen and Congju (Maggie) Chen were all promoted to Associate Research Scientist, and Angela Lugo was promoted to Administrative Coordinator. ■



Columbia Colloquium and Laboratory Seminars

At regular intervals during the year the Center for Radiological Research is pleased to welcome accomplished specialists from around the world to present formal seminars and/or spend time discussing ongoing research.

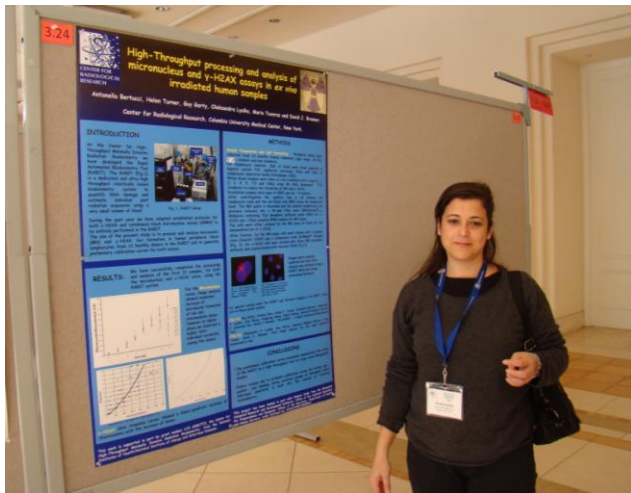
The seminars are attended by Center and RARAF professional staff, senior technical staff and graduate students, as well as doctors and scientists from other departments of the College of Physicians & Surgeons interested in collaborative research. Attention has focused on recent findings and future plans, with special emphasis on the interdisciplinary nature of our research effort.

The 2010 sessions included the following guest speakers (listed alphabetically):

- Dr. Mary Helen Barcellos-Hoff, Ph.D., Departments of Radiation Oncology and Cell Biology, New York University: “Routes and Roadblocks in Radiation Carcinogenesis and Therapy.”
- Dr. Xinbin Chen, Ph.D., Department of Surgical and Radiological Sciences, School of Veterinary Medicine, University of California-Davis: “P53-RNPC1, A Novel Feedback Regulatory Loop of the P53 Family.”
- Dr. Chandan Guha, Ph.D., Department of Radiation Oncology, Albert Einstein College of Medicine: “Stem cell-based therapies for acute radiation syndromes.”
- Dr. Marcus Hafner, Ph.D., Laboratory of RNA Molecular Biology, Howard Hughes Medical Institute, Rockefeller University: “Transcriptome-wide experimental miRNA target identification by PAR-CLIP.”
- Dr. Haiying Hang, Ph.D., Institute of Biophysics, Chinese Academy of Sciences, Beijing, China: “The role of Rad9 methylation in DNA damage repair and cell cycle checkpoint.”
- Dr. Jan Kitajewski, Ph.D., Institute for Cancer Genetics, Columbia University: “Notch regulates angiogenesis by diverse mechanisms.”
- Dr. Stephan Lucas, Ph.D., Research Center in Physics of Matter and Radiation, University of Namur, Belgium: “Radioimmunotherapy with radioactive nanoparticles: a short description of the on-going project ‘TARGAN’.”
- Dr. Frank Slack, Ph.D., Department of Molecular, Cellular and Development Biology, Yale University: “A Roundtable discussion on MicroRNA and cancer.”

Seminars were also conducted by professionals from our own Center staff:

- Dr. Constantinos Broustas: “BLID, a BH3-like containing pro-apoptotic protein, is down-regulated in breast cancer and its decline correlates with poor patient survival.”
- Dr. Igor Shuryak: “The balance between initiation and promotion in radiation-induced murine carcinogenesis.”
- Dr. Thomas Templin: miRNA as Biomarker for Radiation Exposure.”
- Dr. Erik Young: “Impedance based surveillance of biological systems.”
- Dr. Yongliang Zhao: “Molecular events related to malignant conversion of normal human mammary epithelial cells.” ■



Dr. Antonella Bertucci and her poster at the 2010 Annual Radiation Research Society Meeting, Maui, Hawaii.



(L-r): Dr. Helen Turner, Dr. Antonella Bertucci and Dr. Jarah Meador at the 2010 Annual Radiation Research Society Meeting, Maui, Hawaii.

Faculty and Staff

Faculty:

DAVID J. BRENNER, Ph.D., D.Sc.
 — *Director*
 — *RARAF Director*
 Higgins Professor of Radiation Biophysics
 Professor of Radiation Oncology
 Professor of Environmental Health Science
 Chairman, Joint Radiation Safety Committee
 Chairman, Radioactive Drug Research Committee

TOM K. HEI, Ph.D.
 — *Vice-Chairman, Dept. of Radiation Oncology*
 — *Associate Director*
 Professor of Radiation Oncology
 Professor of Environmental Health Sciences

ERIC J. HALL, D.Phil., D.Sc., FACR, FRCR, FASTRO
 Higgins Professor Emeritus,
 Special Lecturer in Radiation Oncology,
 Special Research Scientist

CHARLES R. GEARD, Ph.D.
 Professor of Clinical Radiation Oncology

HOWARD B. LIEBERMAN, Ph.D.
 Professor of Radiation Oncology
 Professor of Environmental Health Sciences

SALLY A. AMUNDSON, Sc.D.
 Associate Professor of Radiation Oncology

LUBOMIR SMILENOV, Ph.D.
 Assistant Professor of Radiation Oncology

YONGLIANG ZHAO, Ph.D.
 Assistant Professor of Radiation Oncology

Research Staff:

GERHARD RANDERS-PEHRSON, Ph.D.
 Senior Research Scientist

ADAYABALAM BALAJEE, Ph.D.
 Research Scientist

GUY GARTY, Ph.D.
 Research Scientist

VLADIMIR IVANOV, Ph.D.
 Research Scientist

HONGNING ZHOU, M.D.
 Research Scientist

ALAN BIGELOW, Ph.D.
 Associate Research Scientist

CONSTANTINOS BROUSTAS, Ph.D.
 Associate Research Scientist

GLORIA CALAF, Ph.D.
 Adj. Associate Research Scientist

SHANAZ GHANDHI, Ph.D.
 Associate Research Scientist

PETER GRABHAM, Ph.D.
 Associate Research Scientist

CORINNE LELOUP, Ph.D.
 Associate Research Scientist

JARAH MEADOR, PH.D.
 Associate Research Scientist

ALEXANDRE MEZENTSEV, Ph.D.
 Associate Research Scientist

SUNIRMAL PAUL, Ph.D.
 Associate Research Scientist

BRIAN PONNAIYA, Ph.D.
 Associate Research Scientist

IGOR SHURYAK, M.D., Ph.D.
 Associate Research Scientist

HELEN TURNER, Ph.D.
 Associate Research Scientist

ANA VASILEVA, Ph.D.
 Associate Research Scientist

CARL ELLISTON, M.S.
 Senior Staff Associate

KEVIN M. HOPKINS, M.S.
 Senior Staff Associate

STEPHEN A. MARINO, M.S.
 Senior Staff Associate

AIPING ZHU, M.D.
 Senior Staff Associate

JINSHUANG LU, M.S.
 Junior Programmer

MARIA TEVERAS, R.N.
 Research Nurse

Post-Doctoral Research Scientists:

ANTONELLA BERTUCCI, Ph.D.
YUNFEI CHAI, Ph.D.
HONGBO FANG, Ph.D.
ANDREW HARKEN, Ph.D.
SARAH HUANG, Ph.D.
PING LU, Ph.D.
BARBARA SZOLC, Ph.D.
PREETY SHARMA, Ph.D.
THOMAS TEMPLIN, Ph.D.
GENYUN WEN, Ph.D.
YANPING XU, Ph.D.
ERIC YOUNG, Ph.D.

Design & Instrument Shop:

GARY W. JOHNSON, A.A.S., Senior Staff Associate
 — *Design & Instrument Shop Director*
DAVID CUNIBERTI, B.A., Instrument Maker
DENNIS KEAVENEY, Instrument Maker
ROBERT C. MORTON, Instrument Maker

Technical Staff:

JOSHUA BERNSTOCK, M.S., Research Worker
LIHUA MING, M.S., Technician B
CUI-XIA KUAN, Technical Assistant

Administrative & Secretarial Staff:

MONIQUE REY, B.A., Center Administrator
LILIAN OLING, M.A., Project Manager
MARGARET LIN ZHU, M.A., Business Manager
YVETTE ACEVEDO, Administrative Assistant
ANGELA LUGO, Administrative Coordinator
ANNERYS RODRIGUEZ, Bookkeeper

Faculty and Staff



Front row (l-r): Dr. Sally Amundson, Dr. Charles Geard, Dr. Tom Hei, Dr. David Brenner, Dr. Howard Lieberman, Dr. Gerhard Randers-Pehrson.

2nd row: Ms. Annerys Rodriguez, Dr. Shanaz Ghandhi, Dr. Helen Turner, Ms. Angela Lugo, Dr. Corinne Leloup, Ms. Lilian Oling, Dr. Congju Chen, Ms. Margaret Zhu, Ms. Sasha Lyulko, Ms. Yvette Acevedo, Mr. Hamin Jeon, Dr. Gengyun Wen, Dr. Vladmir Ivanov.

3rd row: Mr. Gary Johnson, Dr. Winston Liao, Dr. Alan Bigelow, Dr. Guy Garty, Mr. Vatche Zohrabian, Dr. Constantinos Broustas, Dr. Peter Grabham, Mr. Joshua Bernstock, Dr. Hongning Zhou.

Back row: Mr. Dennis Keaveney, Mr. Roy Lam, Dr. Hongbo Fang, Dr. Lubomir Smilenov, Mr. Stephen Marino, Dr. Andrew Harken, Dr. Igor Shuryak, Mr. Kevin Hopkins, Dr. Erik Young, Mr. David Cuniberti.

Not pictured: Dr. Eric Hall, Ms. Monique Rey, Dr. Gloria Calaf, Dr. Antonella Bertucci, Dr. Jarah Meador, Ms. Maria Taveras, Mrs. Cui-Xia Kuan, Dr. Preeti Sharma, Dr. Yanping Xu, Mr. Lihua Ming, Dr. Yongliang Zhao, Dr. Sunirmal Paul, Dr. Adayabalam Balajee, Dr. Thomas Templin, Dr. Brian Ponnaiya, Mr. Robert Morton.

Optoelectronic Tweezer Integration on the Columbia University Microbeam

Michael Grad^a, Alan W. Bigelow, Guy Y. Garty, David J. Brenner and Daniel Attinger^a

In order to allow irradiation of non-adherent cells (e.g. lymphocytes) a novel cellular manipulation technique is being adapted for the microbeam endstation at RARAF. We are currently developing an Optoelectronic Tweezer (OET) system, initially developed by our collaborators at Berkeley [1], to handle these cells. To date, we have created a set of OET electrodes using the equipment provided in the cleanroom at Columbia University. As a preliminary test, we manufactured the devices on 1 mm thick glass slides. Future work will focus on reducing the thickness of the bottom substrate to allow charged particles to easily pass through. Here we describe the fabrication and testing of the 1 mm substrates.

The OET consists of two parallel plate Indium Tin Oxide (ITO) electrodes. The top electrode is covered with a 1 μm thick layer of hydrogenated amorphous silicon (a-Si:H), a thin film semiconductor that acts as a photoconductive layer. Figure 1 shows the cross section of an OET device.

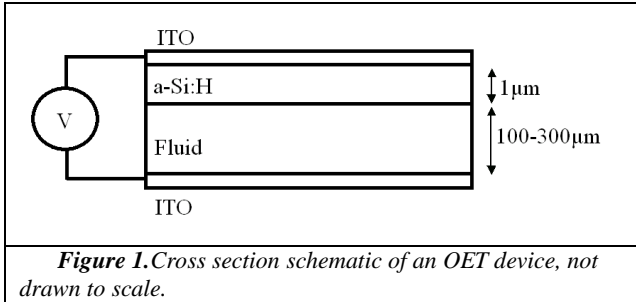


Figure 1. Cross section schematic of an OET device, not drawn to scale.

When light is focused on the surface of the a-Si:H, its conductivity increases by several orders of magnitude [2]. By patterning a dynamic image, using a computer and a projector, a reconfigurable virtual electrode is created. When the virtual electrode and its opposing plate electrode are biased with an AC voltage (~5-10 V), a non-uniform AC field is created between the electrodes.

In the presence of a non-uniform electric field, a dielectric particle will feel a force caused by dielectric polarization (Dielectrophoresis, DEP), given by [3]:

$$F_{DEP} = 2\pi r^3 \epsilon_m \text{Re}[f_{cm}(\omega)] \nabla(E^2) \quad (\text{eq 1})$$

Where r is the particle radius [m], ϵ_m is the permittivity of the medium [C/V/m], $\nabla(E^2)$ is the gradient of the square of the electric field [V²/m³]. $\text{Re}[f_{cm}(\omega)]$ is the real part of the Clausius-Mossotti factor, given by [3]:

$$\text{Re}[f_{cm}(\omega)] = \frac{\epsilon_p^* - \epsilon_m^*}{\epsilon_p^* + 2\epsilon_m^*}, \text{ and } \epsilon_i^* = \epsilon_i - j \frac{\sigma_i}{\omega} \quad (\text{eq 2})$$

Where σ is the conductivity of the particle or medium [S/m], and ω is the angular frequency of the electric field [rad/s].

In order to prevent evaporation of the fluid and to easily control the spacing between the parallel plates, a rubber gasket was placed between the electrodes, and a plastic clamp was used to hold the two plates together. The following images in Figure 2 show the clamp and gasket setup.

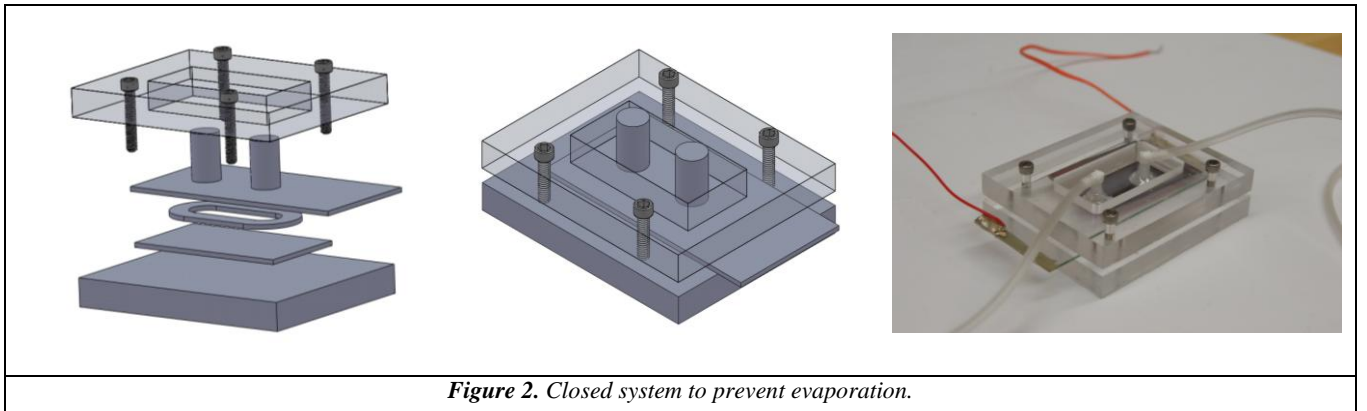


Figure 2. Closed system to prevent evaporation.

^a Department of Mechanical Engineering, Columbia University, New York, NY

A custom MATLAB program was designed to project a red square along the incident light path of a microscope and onto the a-Si:H substrate. The user can easily control the translation, dilation, rotation, speed and linewidth of the shape using simple keyboard commands. Using this projected image, the optoelectronic tweezers were tested

using 20 μm latex beads. Figure 3 shows the projected image (left) and a trapped bead resulting from the light induced dielectrophoresis. The bead is not fluorescent, but still visible from the scattered light. A red arrow pointing to the bead is included to guide the reader.

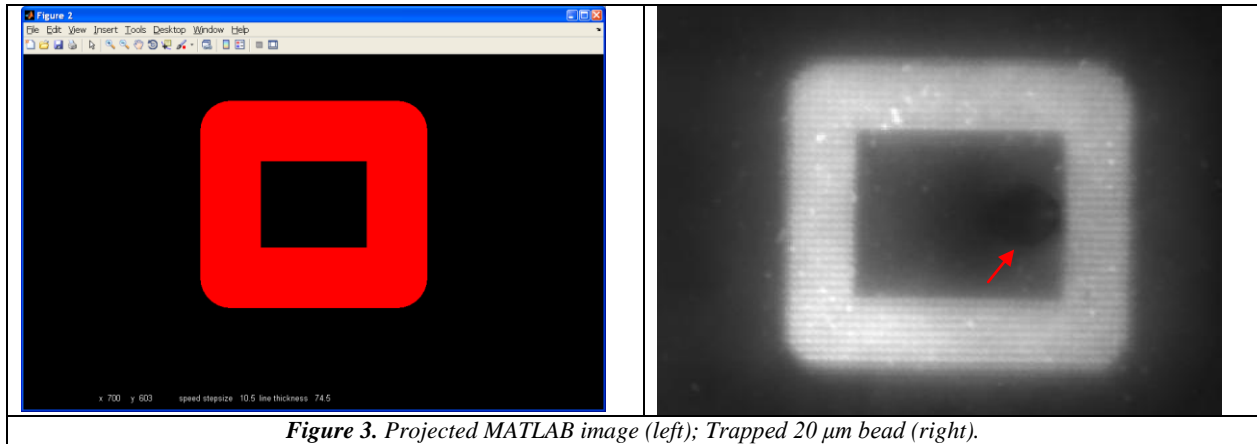


Figure 3. Projected MATLAB image (left); Trapped 20 μm bead (right).

The conductivity of the fluid in the chamber must be carefully controlled as it will strongly affect the electric field in the fluid layer of the OET sandwich. If the fluidic resistance is greater than the a-Si:H resistance, the voltage drop is highest in the fluid layer. If the resistance of the fluid layer is less than that of the a-Si:H, then the voltage drop will occur in the a-Si:H layer, and dielectrophoresis

effect will be reduced in the liquid. Additionally, the force experience by the particle is determined by the conductivity of the fluid, via the real part of the Clausius-Mossotti factor (equation 2). The left side of Figure 4 shows a plot of these two parameters as a function of fluid conductivity.

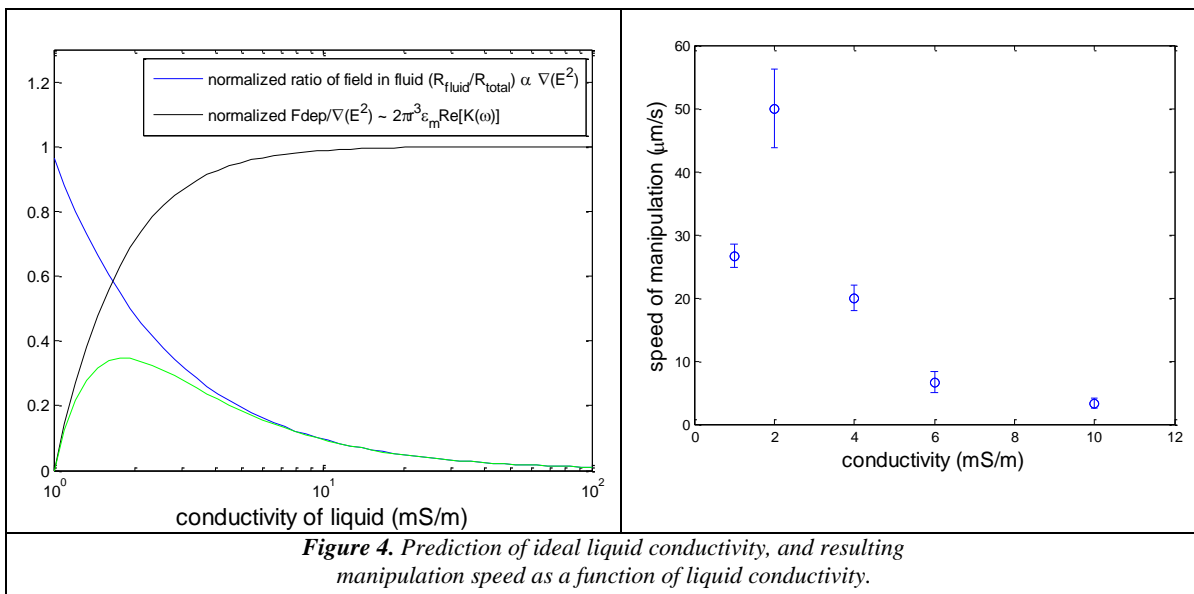


Figure 4. Prediction of ideal liquid conductivity, and resulting manipulation speed as a function of liquid conductivity.

In the left side of Figure 4, the blue curve plots the ratio of the fluid resistance to the total resistance ($R_{\text{fluid}}/R_{\text{total}}$) as a function of fluid conductivity, giving an approximation of the amount of electric field that will be in the fluid layer. This plot shows that the amount of electric field in the fluid increases with decreasing fluid conductivity. The black curve plots F_{DEP} normalized by

the gradient term, and shows an increase in the dielectrophoresis force with increasing fluid conductivity. The green curve is the product of the blue and the black curves, representing F_{DEP} . There is a maximum at ~2 mS/m, suggesting that this is the ideal conductivity to use in experiments.

The right side of figure 4 shows experimental results performed with 19 μm (+/- 16%) polystyrene beads suspended in 13 mL of DI water, mixed with 0.4 mg/mL non-ionic surfactant, and 1 mL KCl (measured at 141 mS/m), and diluted with DI water to achieve different conductivities. The height of the chamber is 100 μm , and the voltage and frequency were 18 V_{p-p} , and 55k Hz. As predicted, the maximum manipulation velocity was found when fluid conductivity was ~ 2 mS/m, and measured approximately 50 $\mu\text{m/s}$.

References

1. Chiou, P.Y., A.T. Ohta, and M.C. Wu, Massively

parallel manipulation of single cells and microparticles using optical images. *Nature*, 2005. 436(7049): p. 370-372.

2. Ohta, A.T., C. Pei-Yu, T.H. Han, J.C. Liao, U. Bhardwaj, E.R.B. McCabe, Y. Fuqu, S. Ren, and M.C. Wu, Dynamic Cell and Microparticle Control via Optoelectronic Tweezers. *Microelectromechanical Systems, Journal of*, 2007. 16(3): p. 491-499.
3. Chang, H.-C. and L.Y. Yeo, *Electrokinetically Driven Microfluidics and Nanofluidics*. 2010, Cambridge: Cambridge University Press. ■

DNA Base Damage Induced by the UV Microspot at RARAF

Alan W. Bigelow, Helen C. Turner, Gerhard Randers-Pehrson, Andrew Durocher, Charles R. Geard, David J. Brenner and Aroumougame Asaithamby^a

Introduction

Following up on previous particle-induced foci formation experiments, our user Aroumougame Asaithamby was interested in extending his work at RARAF to investigate base-damage-repair dynamics. Whereas, his previous work involved fluorescent protein tagged to either single-strand-break-repair protein or double-strand-break-repair protein, this work involved fluorescent protein attached to the base-repair protein 8-oxoguanine DNA glycosylase 1 (OGG1) in HT1080 fibrosarcoma cells. In a preliminary step to investigating OGG1 foci formation using the RARAF microbeam, we took a qualitative approach to verify that UV laser induction of OGG1 foci at UT Southwestern also occurs at RARAF using the UV microspot irradiator, a novel irradiator based on a multiphoton excitation volume.

Procedure

To produce laser-induced foci in HT1080 fibrosarcoma cells with enhanced green fluorescent protein (EGFP)-tagged OGG1, the multiphoton microscope at RARAF was used in two modes: as an imaging device and as a UV microspot irradiator. For pre- and post-irradiation multiphoton microscopy imaging, 970 nm incident laser light, which acts as 485 nm during two-photon excitation, was used to excite EGFP. For UV microspot irradiation, the laser was tuned to 700 nm incident laser light, which acts as 350 nm at the microspot, to induce DNA damage in the cell nuclei.

For consistency and convenience, a 60X water-dipping lens was selected for both imaging and irradiation modes. The laser attenuator was set for about 20 mW laser power for both imaging at 970 nm and irradiating at 700 nm. A heater ring set for 37 Celsius was placed in a cell dish to approximate physiological conditions during the experiment. UV microspot irradiation energy delivery is simply laser power delivered multiplied by the irradiation time. The UV microspot volume is defined by the point spread function of the laser focus, an ellipsoid with full widths at half maximum in the axial and radial direction measuring 2.8 and 0.65 μm , respectively. Cell nuclei were irradiated along lines, where each "pass" was about 1 s. While imaging, the control software was set for a 20X zoom factor and 3X averaging. A post-processing routine in Matlab was applied to each image for optimal contrast.

Observations

We observed that when the laser energy delivered to a cell nucleus was excessive, the cell nucleus was virtually annihilated. As energy was reduced, OGG1-foci formation was observed along with EGFP migrating beyond the damaged nuclear membrane and filling the cytoplasmic area, as shown in the time-lapse images in Figure 1. When the delivered energy was reduced below the cell-killing threshold, OGG1-foci formation was observed along with an intact cell nucleus, as shown in the time-lapse images in Figure 2.

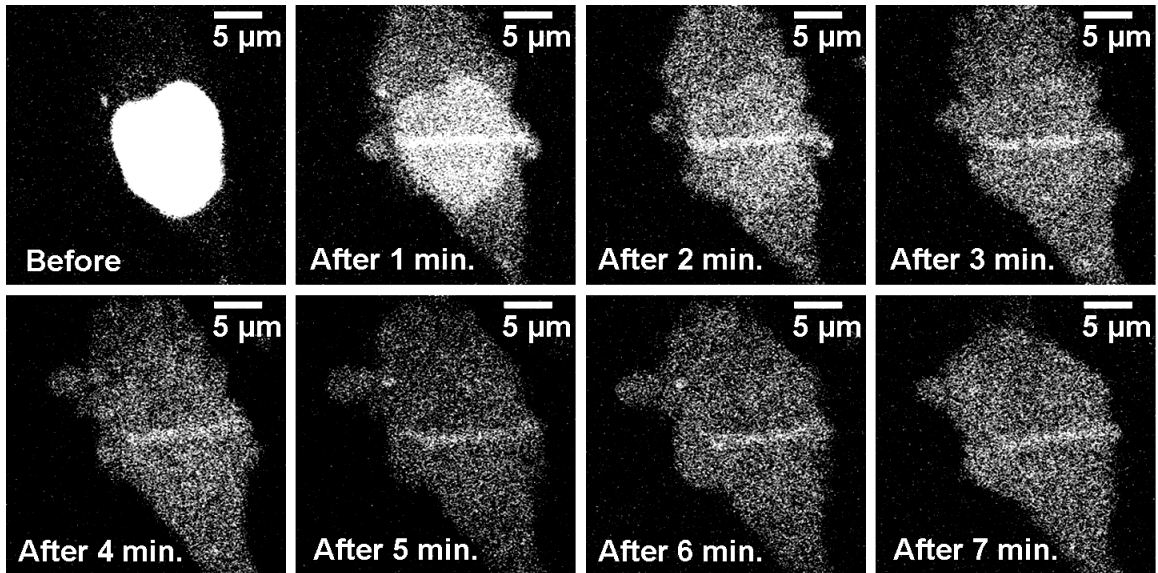


Figure 1. Time-lapse multiphoton images of an HT1080 fibrosarcoma nucleus irradiated with the UV microspot at RARAF. The irradiation pattern consisted of 30 line scans across the center of the cell nucleus. Energy delivered to the cell nucleus was approximately 300 mJ. The cell response is manifest by: 1) EGFP-tagged OGG1 foci formation along a line, and 2) EGFP spreading beyond the nuclear membrane, implying a damaged nuclear membrane and cell death.

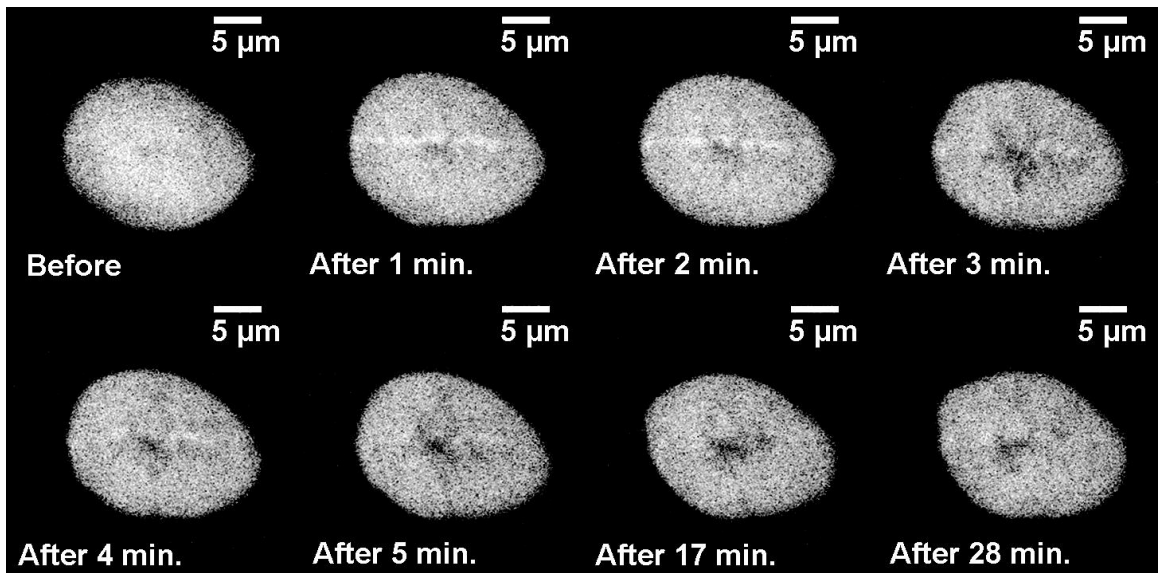


Figure 2. Time-lapse multiphoton images of an HT1080 fibrosarcoma nucleus irradiated with the UV microspot at RARAF. The irradiation pattern consisted of 5 line scans across the center of the cell nucleus. Energy delivered to the cell nucleus was approximately 50 mJ. The cell response is manifest by: 1) EGFP-tagged OGG1 foci formation along a line, and 2) an intact nuclear membrane, suggesting cell viability.

Conclusion

The UV microspot, a recently added irradiator at RARAF, was used to verify laser-induced OGG1 foci formation in single-cell nuclei. From the results shown

here, the UV microspot can induce micron-sized damage to cell nuclei. This irradiator has the capacity for high accuracy targeting and for determining energy thresholds, such as that for foci formation without cell killing. ■

^a University of Texas Southwestern Medical Center

Enhanced Imaging for the Microbeam Irradiator

Andrew D. Harken, Gerhard Randers-Pehrson and David J. Brenner

Introduction

This past year we have installed an electron multiplying CCD camera (EMCCD) (PhotonMAX512:B, Princeton Instruments, Trenton, NJ, USA) on the charged particle microbeam end station. This new EMCCD camera has allowed significant improvements in the standard imaging for microbeam irradiations and the exploration of oblique illumination imaging for non-stain cell targeting.

Enhanced Imaging

The EMCCD camera uses a Peltier cooled sensor to reduce the thermoelectrical noise present in all solid state devices. This lower electrical noise allows this camera to acquire images with significantly fewer photons than the previously used intensified CCD (ICCD) camera. The ICCD camera would require taking several images and averaging them to achieve a usable image for microbeam targeting. The EMCCD uses a single frame acquisition to achieve the same – or better – image quality. Figure 1 is a side by side comparison of an aggregate ICCD image and a single-frame EMCCD image.

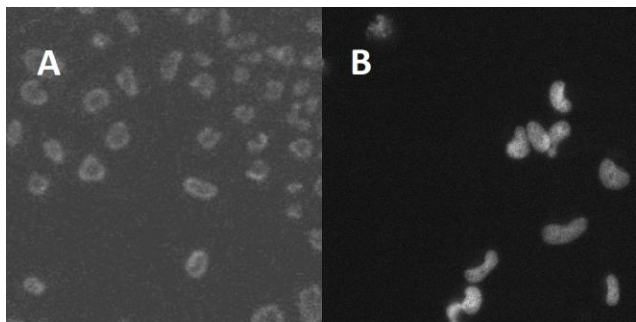


Figure 1. Comparison images from microbeam irradiations. Image A was acquired with the ICCD camera while image B was acquired with the EMCCD camera.

The ability of the EMCCD camera to acquire the needed images in a single frame has allowed the imaging step during irradiations to be performed in half the time as the ICCD camera. This reduces exposure of the samples to the laboratory environment through the reduction in require time for the sample to be on the end station stage. We look to further reduce the imaging time requirements by interfacing the EMCCD camera with the light source and control programming where the camera will control the imaging timing.

Oblique Illumination Imaging

The microbeam end station prevents on-axis sample illumination from below the samples. Axial transmission illumination is required for most types of non-stain

imaging for cells (Normarski interference, Hoffman modulation, etc.). Oblique illumination uses an off-axis epi-illumination light source that is reflected off a surface, back through the sample and into the imaging system. This allows interference imaging without the transmission illumination. Figure 2 is a sample image obtained using oblique illumination. Oblique illumination allows recognition of complete cells and some sub cellular systems.

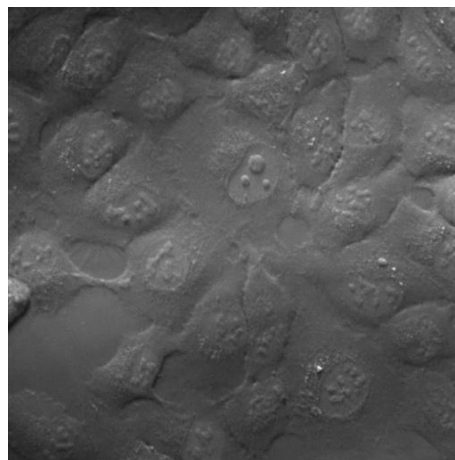


Figure 2. Image of HT1080 fibrosarcoma cells using non-stain oblique illumination on the microbeam end station.

Modification of the vacuum exit port of the microbeam irradiator is required to increase the reflectivity of the silicon nitride window to get sufficient light through the sample for image formation. A thin layer of aluminum (<75nm) will be sufficient for this imaging technique.

While the images obtained from oblique illumination imaging are easily interpreted by the human eye, automated computer recognition of the cells and sub-cellular targets is an ongoing process. Image analysis techniques have been previously designed for cellular recognition of using non-stain interference techniques, such as those listed previously, most are computationally intensive and require a significant analysis time (10's of seconds to several minutes). Our requirements for throughput of the microbeam (several 10's of images per minute) will require custom programming of our image analysis systems.

Conclusion

We are continuing the integration of the EMCCD camera into our end station to improve target. ■

Proton Induced Soft X-ray Microbeam at RARAF

Andrew D. Harken, Gerhard Randers-Pehrson, Gary W. Johnson and David J. Brenner

Introduction

The development of the proton-induced soft x-ray microbeam for low-LET ionization of single cells and sub-cellular organelles is continuing. The x-ray microbeam has seen the replacement of the proton focusing lens with a newer design and has an appreciable increase in the dose delivery rate.

End Station Design

The x-ray microbeam is installed on a horizontal beam line at RARAF. Figure 1 is a schematic representation of the microbeam end station with the proton beam coming in from the right. The protons (1.8 MeV) are focused on a titanium target ($K\alpha = 4.5$ keV) using an electrostatic quadrupole quadruplet. The titanium target is cut at a 70 degree angle to the incident proton beam which allows a portion of the generated x-rays to be emitted in the vertical direction. The x-rays are focused using a Fresnel zone plate diffractive optic (Zoneplates, Inc, London, UK) to a current spot size of 5 μm in diameter.

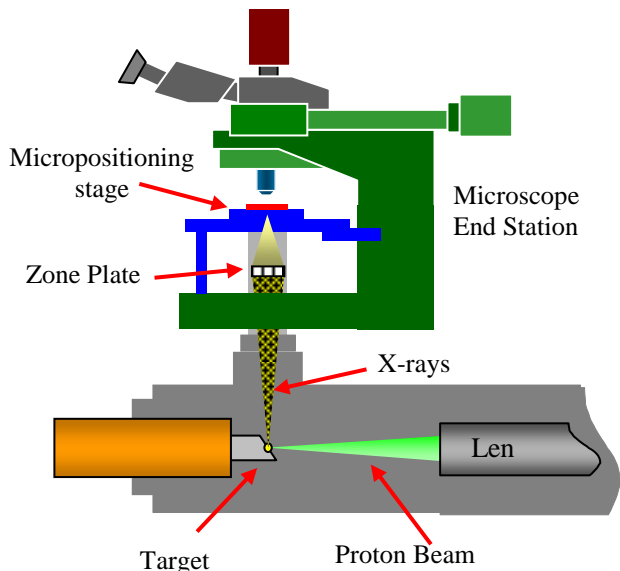


Figure 1. Schematic diagram of the x-ray microbeam endstation.

The samples are positioned using a combination micro- and nano-positioning stage (Mad City Labs, Madison, Wisconsin, USA). This design of horizontal staging allows the same biological protocols to be used on the x-ray microbeam that have been developed on the charge-particle beam system making beam type comparative studies more easily accessible.

X-ray Beam Profile

The current beam size for the x-ray beam spot size is 5 μm in diameter. Figure 2 shows the orthogonal knife-edge occlusion measurements of the x-ray spot size. The symmetric beam is generated by having the proton beam size of 120 μm vertically x 50 μm horizontally. The 70 degree angle of the face of the titanium target projects the 120 μm vertical beam diameter as a 50 μm spot as the x-ray generation object for the zone plate optic. We have determined that 5 mm beam size will be sufficient for current irradiation needs on the x-ray microbeam system. The larger proton spot also allows for larger proton currents on target without concern of localized damage to the titanium target face.

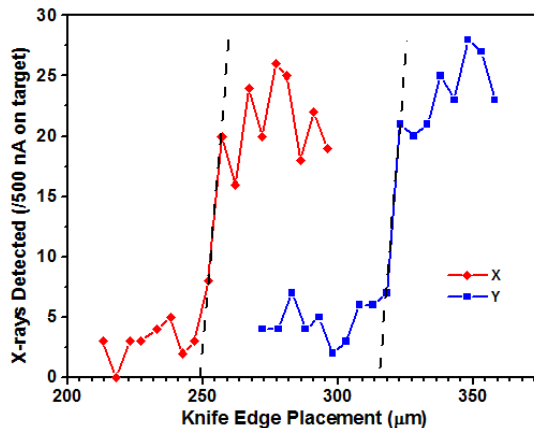


Figure 2. Knife-edge occlusion measurements for the x-ray spot size. Both directions are 5 μm in diameter.

New Lens Design

The new electrostatic quadrupole quadruplet design has had two ground planes inserted between the first and second as well as the third and fourth elements. These added ground planes make the lens more stable and could potentially allow higher focusing voltages. The new ground planes also have the central beam pass-through holes enlarged to 8 mm in diameter. The enlarged pass-through holes have enabled the proton current on the titanium target to be increased by a factor of 25. The increased proton current gives greater x-ray generation rates and will result in an increase in the ultimate x-ray dose rate being increased to >10 mGy/sec.

Conclusion

The proton induced x-ray microbeam development is continuing with further evaluation of the new lens and x-ray beam properties. We look forward to offering this new tool to RARAF users. ■

Simultaneous Immersion Mirau Interferometry

Oleksandra V. Lyulko, Gerhard Randers-Pehrson and David J. Brenner

Simultaneous Immersion Mirau Interferometry (SIMI) is an epi-illumination non-stain, no-UV imaging technique, currently being built at Columbia University Radiological Research Accelerator Facility. SIMI is a modification of Immersion Mirau Interferometry (IMI), which is aimed at targeting live cells in medium during irradiation experiments in the absence of confounding factors such as fluorescent staining or UV-illumination. IMI is based on the principles of phase-shifting interferometry (PSI) and shares its sensitivity to environmental vibrations, because it requires consecutive acquisition of several interferograms as the sample is positioned at different heights with nanometer precision. This limits its use only to workstations with vibration isolation which conflicts with the constraints of the

RARAF microbeam endstation.

SIMI will help to overcome this limitation, as it is based on simultaneous acquisition of all interferograms and eliminates the effects of vibration. The schematics of SIMI design is shown in Fig.1. A $\lambda/8$ waveplate is introduced between the beamsplitter of the interferometric attachment and the sample. The waveplate creates a 90° phase difference between the x and y components of the test beam. Therefore, the output of the interferometer contains two interferograms with a relative phase shift of 90° (Fig. 2). The interferograms are spatially separated by a polarization beam displacer and are recorded by a single CMOS sensor. The interferograms are combined with the background image to reconstruct the intensity map of the specimen.

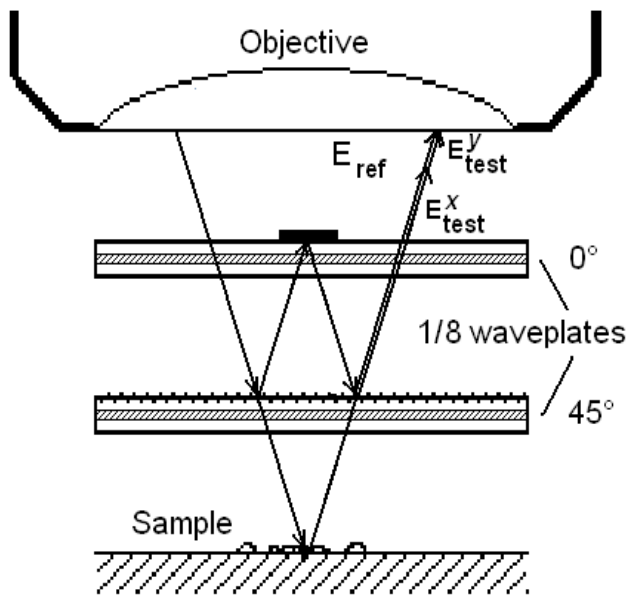


Figure 1. Schematics of the simultaneous Mirau interferometer: a) A $\lambda/8$ waveplate with its fast axis at 45° to the light polarization placed in the test arm introduces a $\pi/2$ delay between the x and y components of the test beam; b) a second waveplate oriented at 0° equalizes the test and reference path lengths.

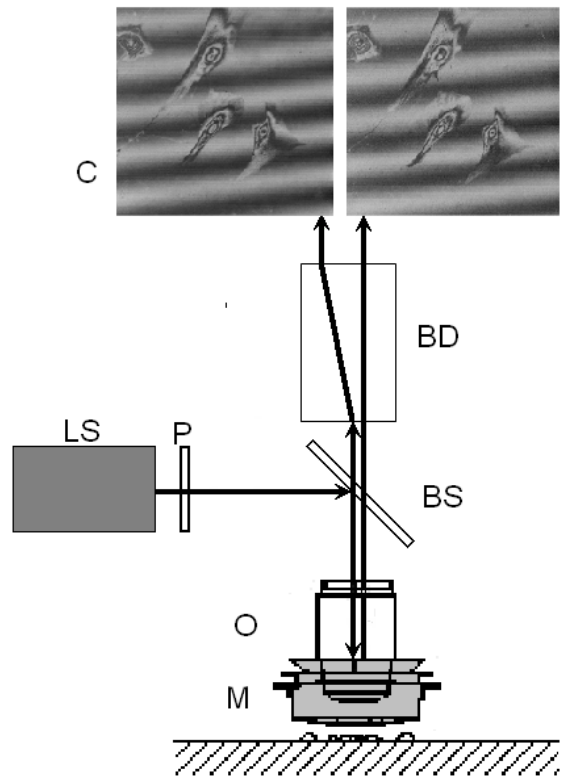


Figure 2. Layout of the Simultaneous Mirau imaging system. The light beam is separated into two parallel beams by a polarization beam displacer (BD) and can be sent onto the sensor of a single camera (C).

Note: the paired interferograms are the results of an actual experiment with fixed fibroblast cells - notice the quarter-wavelength phase shift.

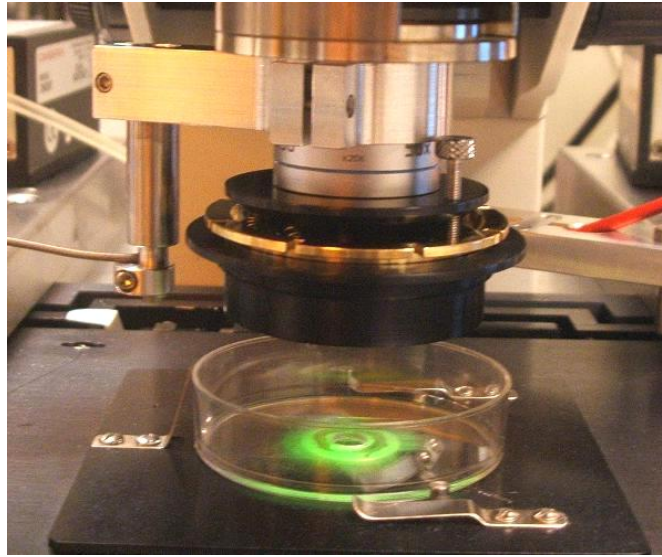


Figure 3. *Mirau interferometric attachment is positioned on a microscope objective at the microbeam endstation.*

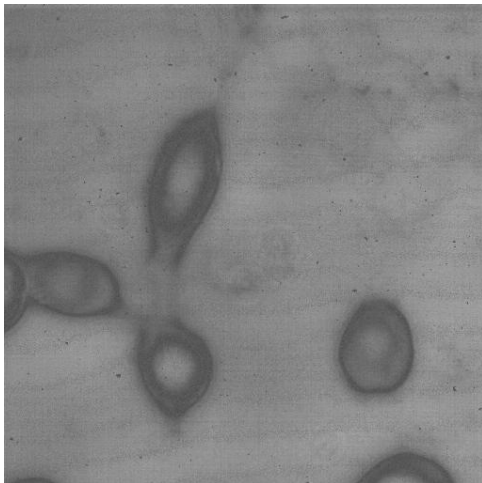


Figure 4. *Unstained live fibroblast cells submerged in Phosphate Buffered Saline imaged with IMI.*

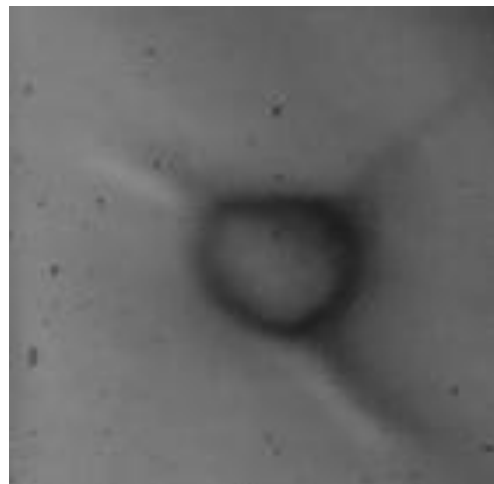


Figure 5. *Live 3T3 cell in medium imaged with SIMI.*

Recent developments have been focused on manufacturing the polarization optics that will be incorporated into the Mirau attachment and will allow simultaneous interferometry. Precision windows will be coated with fully reflective and partially reflective coatings with polarization-independent properties. The layers of glass will be laminated with polymer retarder.

Fig. 5 demonstrates a result of imaging of 3T3 cells in medium with an experimental SIMI arrangement. Our results show that this system produces images of a quality that is sufficient to perform targeted cellular irradiation experiments

Neutron Microbeam

Yangping Xu

We are developing a neutron microbeam, as far as we know the first such microbeam in the world. Protons just above the threshold of the Li(p,n) reaction (1.881 MeV) will be focused to a beam spot $\sim 10 \mu\text{m}$ in diameter on a $1 \mu\text{m}$ thick LiF target and used to produce neutrons with energies from 0 to 60 keV in a narrow forward cone. A $20 \mu\text{m}$ thick gold foil will be used to stop the protons, so cells plated on $3 \mu\text{m}$ thick polypropylene will only be irradiated by neutrons. Because of the proximity of the cells to the target ($<25 \mu\text{m}$) and the small half-angle of the cone ($\sim 15^\circ$), the neutron beam spot at the cells will be $15\text{--}20 \mu\text{m}$ in diameter.

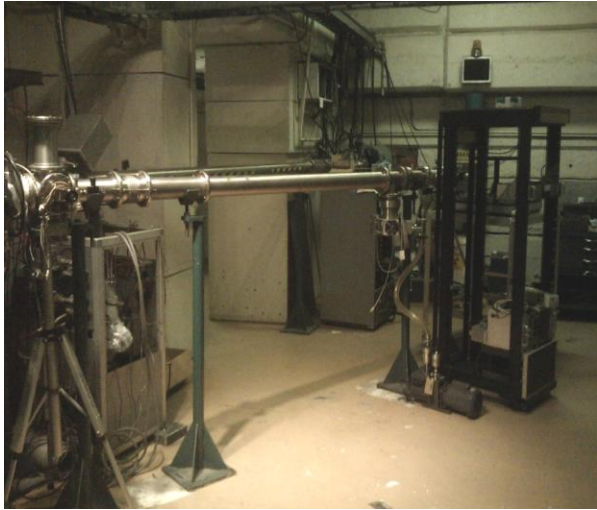


Figure 1. The neutron microbeam line.

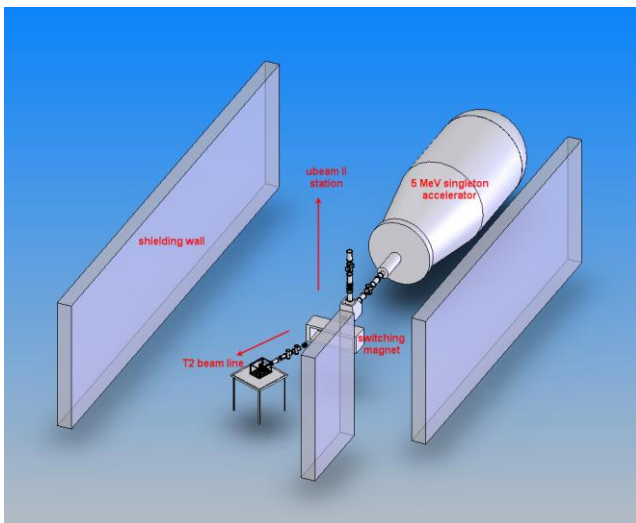


Figure 2. The designed neutron microbeam line.

Construction of the neutron microbeam^[1] has been initiated on the T2 beam line in the T area at RARAF. This is a horizontal beam line on the 30-degree port of the switching/bending magnet, whose magnetic field will be calibrated with the threshold of the Li(p,n) reaction. The purpose of building our neutron microbeam in the T area is that we want to improve beam transport to the target station, increasing the proton beam current to $>10 \text{ nA}$. The correlated neutron yield will be increased up to about 6000 neutrons per second.

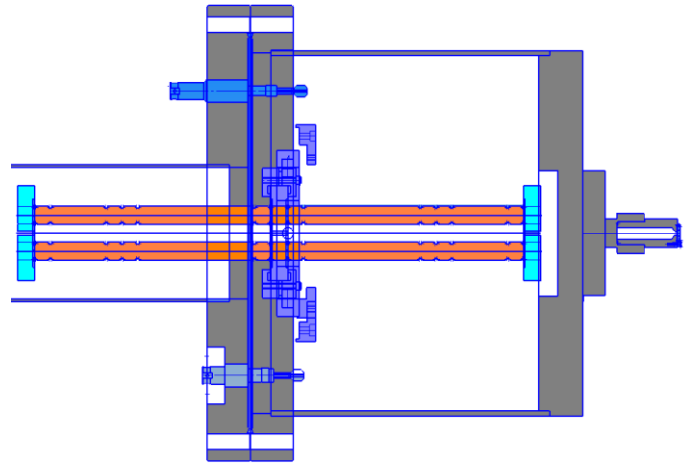


Figure 3. The redesigned lens holder system.

To make the beam line fit into the T area, the distance from the object aperture to the limiting aperture is 3.5 m. The original long-focusing-length design (using $\leq 5000 \text{ V}$ on the lens) had become difficult to setup because of the physical space limitations. The focal distance of the electrostatic quadrupole quadruplet was reduced to 0.22 m by increasing the working voltage on the lens. After re-calculating and re-adjusting the geometry of the system (Figures 1 and 2), the system is better accommodated by the T area and the system demagnification is about 22.

Since we have to use a higher-voltage configuration, the lens holder has been redesigned. One end of the lens is inserted into an 8" diameter chamber. This provides enough space on the upstream flange for four 10 kV and four 5 kV feedthroughs and in the interior to connect 10 kV high voltage cables to the lens rods. The quadruplet lens with ABBA focusing style is mounted on the downstream flange with a 2D pivot adjustment plate in the middle (Figure 3). By adjusting the pivot plate tilt angle, the lens will be aligned with the beam. The whole lens holder system will be mounted on rails on the beam end station table.

The quadruplet lens has been tested in a customized glass bell jar vacuum chamber with sixteen 10 kV feedthroughs on the back plate (Figure 4). A Bertan power supply was used to provide high voltage and a vacuum ion gauge and a residual gas analyzer were used to monitor vacuum changes. The lens was held at 10 KV without sparking or vacuum changes.

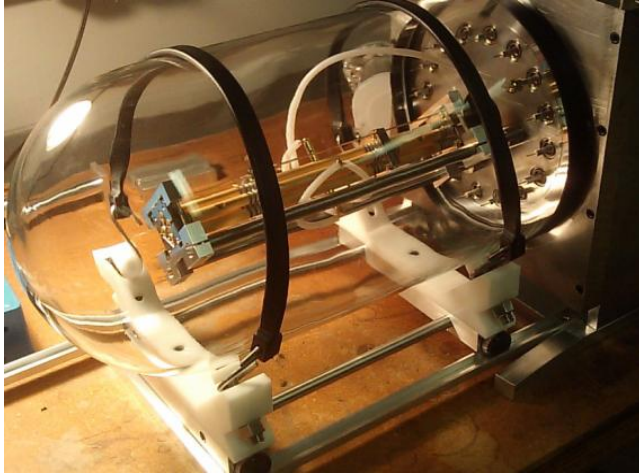


Figure 4. The lens testing chamber.

Setting up the neutron microbeam end station and the beam testing instrument is ongoing (Figure 5). A Thorlabs X-Y-Z 3D motion stage and stepping motor controller for controlling the dish movement have been tested. The automatic lens voltage control has been tested using a CyberResearch Digital to Analog Converter (DAC) card and in-house control code, which has been integrated into the beam spot resolution scan. It will be used for Simplex lens tuning. The imaging system includes a telescope-style relay lens tube and a fast Camlink CMOS camera, which has been tested. The image frame grabber is a Matrox Helio card, which was installed in the main control computer. The image processing using the MIL

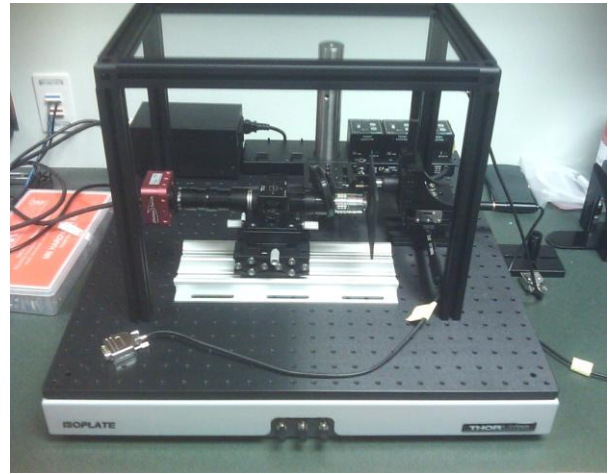
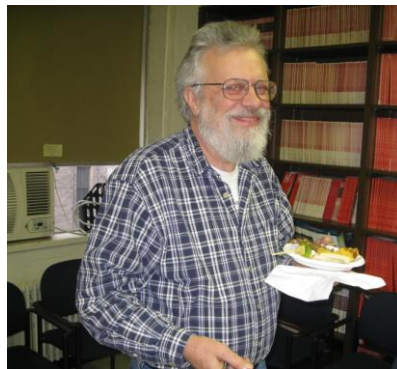


Figure 5. The neutron microbeam end station testing system.

9.0 library has been tested and automation of the imaging system is still in progress. A solid state semiconductor detector (Si detector) will be positioned behind a dish with thin knife-edge foils to detect protons during the proton resolution scan, when a thin silicon nitride window will replace the LIF target so that the proton beam will not be stopped. The data acquisition system using a Cyber research PCI version CTM05 counter card has been tested. The detector counting code has been integrated into the microbeam beam spot resolution scan program. The entire setup is on an isolation table and covered by a blackout enclosure (Figure 5).

References

1. Xu Y., Randers-Pehrson G., Marino S.A., Bigelow A.W., Akselrod M.S., Sykora J.G. and Brenner D.J. An accelerator-based neutron microbeam system for studies of radiation effects. *Radiat. Prot. Dosimetry* epub ahead of print Dec. 3 (2010). ■



Center for Radiological Research 2010 Christmas Party (L-r): Dr. Charles Geard, Dr. Adayabalam Balajee, Dr. Gerhard Randers-Pehrson and Dr. Alan Bigelow.

A Protective Role of Heme Oxygenase-1 (HO-1) Against Oxidative Stress-Induced Cell Death Could Be Quantitatively Different In Normal and Cancer Cells

Vladimir N. Ivanov and Tom K. Hei

Suppression of oxidative stress in living cells requires activation of numerous protective mechanisms, including induction of gene expression of several NF- κ B-dependent antioxidant enzymes, such as catalase, superoxide dismutase-2 (SOD-2) and heme oxygenase-1 (HO-1). HO-1 catalyzes the first rate-limiting step of heme degradation producing carbon monoxide (CO) and biliverdin, which is further converted in bilirubin with a strong anti-oxidant activity. On the other hand, CO inhibits enzymatic activities of the numerous hemoproteins resulting in a blockage of ROS production [1, 2]. Since inflammation is tightly connected with production of ROS and oxidative stress, inducible HO-1 enzymatic activity is also involved in the protective anti-inflammatory response [3]. In contrast, a possible approach for killing cancer cells could represent the specific induction of oxidative stress for these cells in conditions of blockage of anti-oxidant protective mechanisms. In our previous

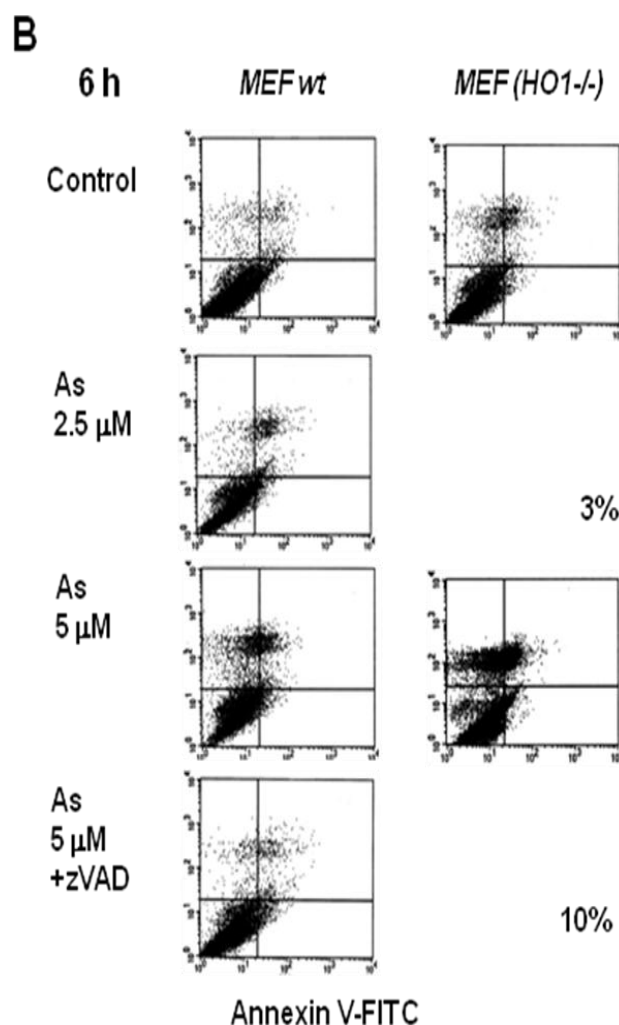
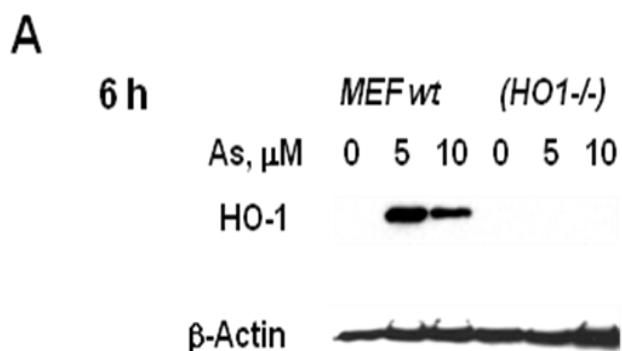


Figure 1. HO-1 deficient mouse embryonic fibroblasts (MEF) are extremely sensitive to sodium arsenite induced death. **A.** Western blot analysis of HO-1 induction by sodium arsenite in MEF wt. **B.** Apoptosis and the secondary necrosis levels following treatment with sodium arsenite (2.5-5 μ M) were determined using cell staining with Annexin-V-FITC + PI with the subsequent FACS analysis. A universal caspase inhibitor zVAD was used at dose 50 μ M.

investigations, we used sodium arsenite treatment (1-5 μM) for induction of apoptosis in human melanoma cells [4, 5]. However, the mitochondrial apoptotic pathway was induced by sodium arsenite treatment at relatively low levels in most melanoma lines, as well as in normal cells, and required an additional sensitization through the

specific suppression of cell survival pathways, such as MEK-ERK, PI3K-AKT or IKK-NF- κB , for efficient cancer cell. In the present study, we further elucidate a role of HO-1 suppression for dramatic upregulation of sodium arsenite-induced cell death in human melanoma cells.

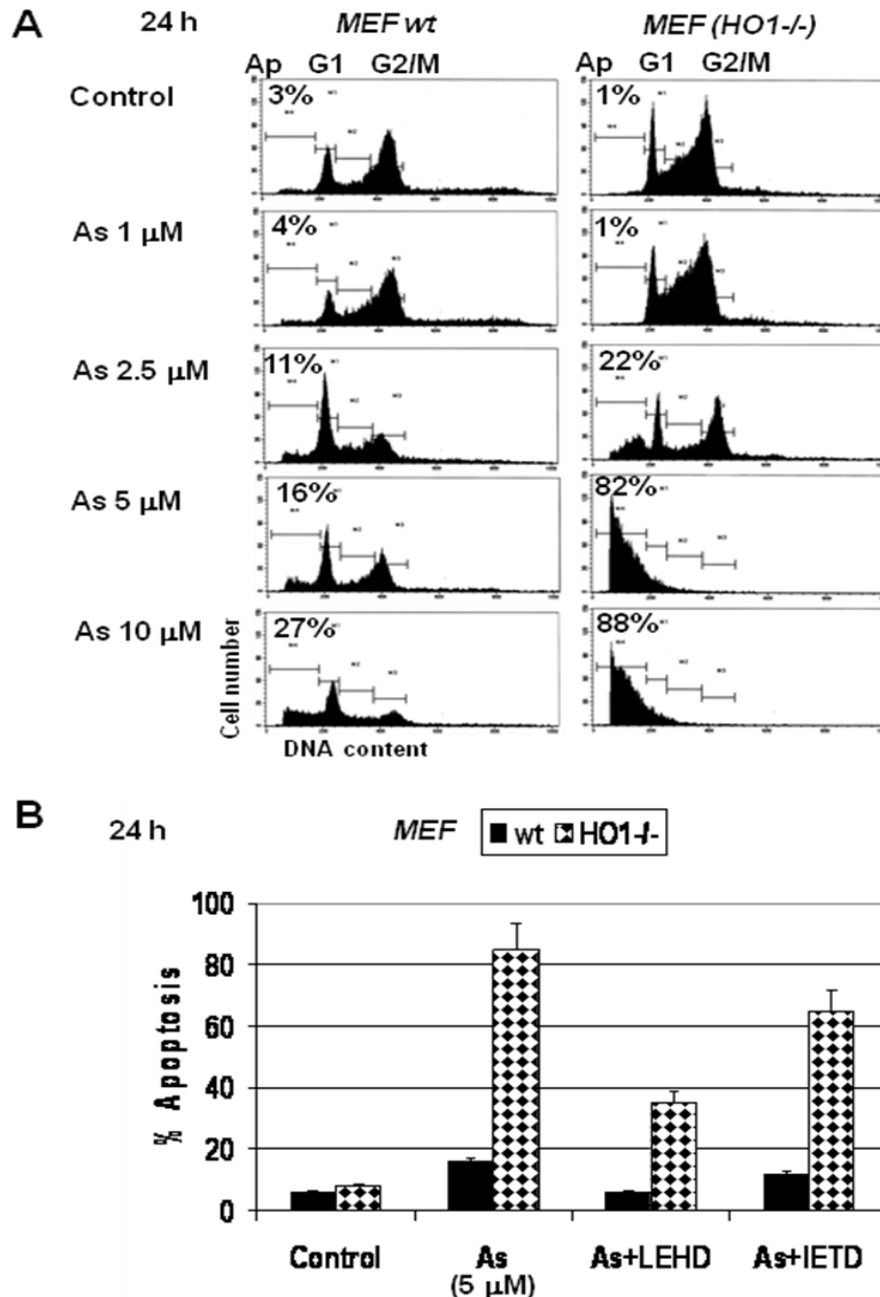


Figure 2. A. Cell cycle and apoptosis analysis of wt and HO-1-deficient MEF, which were treated with increased doses of sodium arsenite (1-10 μM), was performed using PI staining of DNA and the flow cytometry. Apoptosis (pre-G1) levels are indicated. B. Downregulation of arsenite-induced apoptosis by specific caspase inhibitors, LEHD and IETD (50 μM).

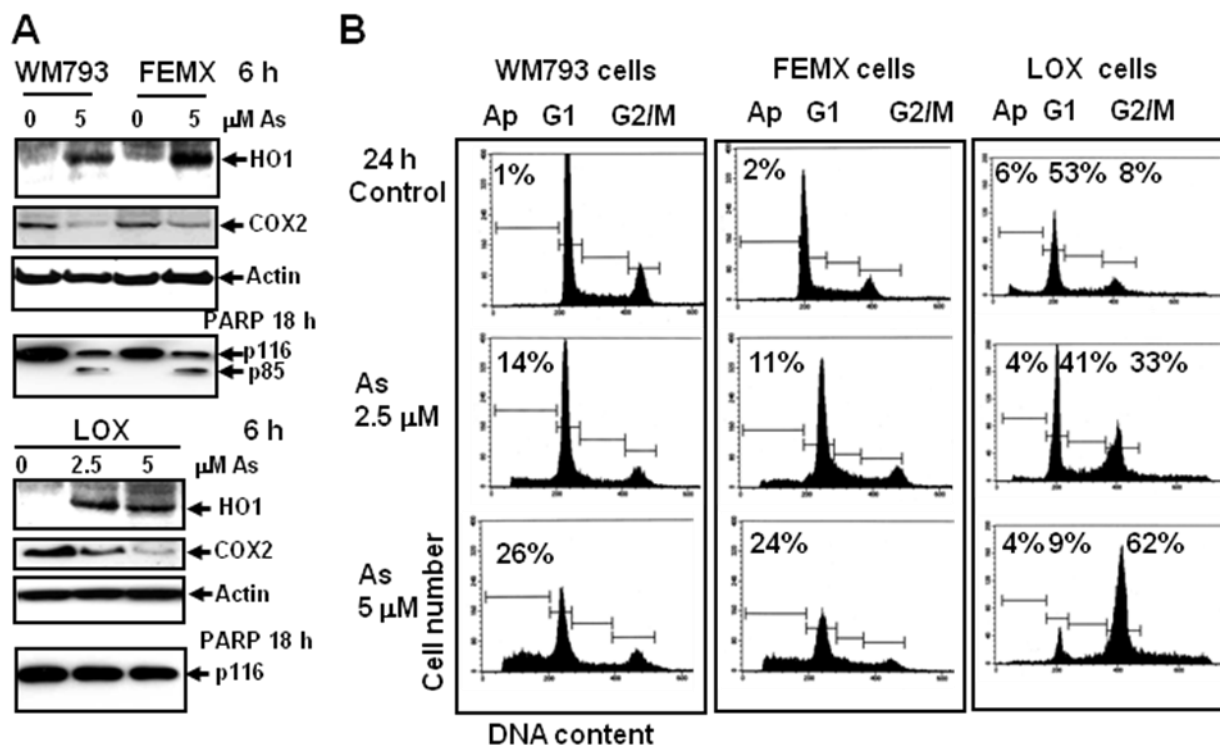


Figure 3. Induction of HO-1 expression and establishing apoptotic commitment in human melanoma cell lines after sodium arsenite treatment. **A.** Western blot analysis of protein levels of HO-1 and COX-2 6 h after sodium arsenite (5 μ M) treatment and PARP 18 h after treatment. **B.** Cell cycle and apoptosis analysis 24 h after sodium arsenite treatment using PI staining of DNA and the flow cytometry. Apoptosis (pre-G1) levels are indicated for WM793, FEMX and LOX melanoma cells. G1 and G2/M levels are indicated for LOX cells. Results of a typical experiment are shown. **C.** Cell death levels were determined 24 h after sodium arsenite (5-10 μ M) treatment in the presence or absence of caspase inhibitor zVAD (50 μ M) using PI staining of DNA and the flow cytometry.

To make a general assessment of HO-1 inducible expression for anti-apoptotic protection, we took advantage of HO-1 knock-out MEF, which were previously established in Solomon Snyder's lab [6]. We observed that HO-1 deficient MEF (Fig. 1A) were indeed more sensitive to sodium arsenite-induced apoptotic death, which was quickly converted to secondary necrosis even 6 h after treatment, compared to normal MEF (Fig. 1B). Using DNA staining and flow cytometry, we determined dramatic differences in apoptotic (pre-G1)

levels between HO1-deficient and normal MEF 24 h after sodium arsenite exposure (Fig. 2B). LEHD, a specific inhibitor of caspase-9, substantially suppressed levels of apoptosis, highlighting an activation of the mitochondrial apoptotic pathway, while the effect of IETD, a caspase-8 inhibitor, was relatively modest (Fig. 2B). Taken together, these results demonstrated a critical involvement of the mitochondrial apoptotic pathway and its dramatic acceleration in HO-1-deficient MEF following sodium arsenite treatment.

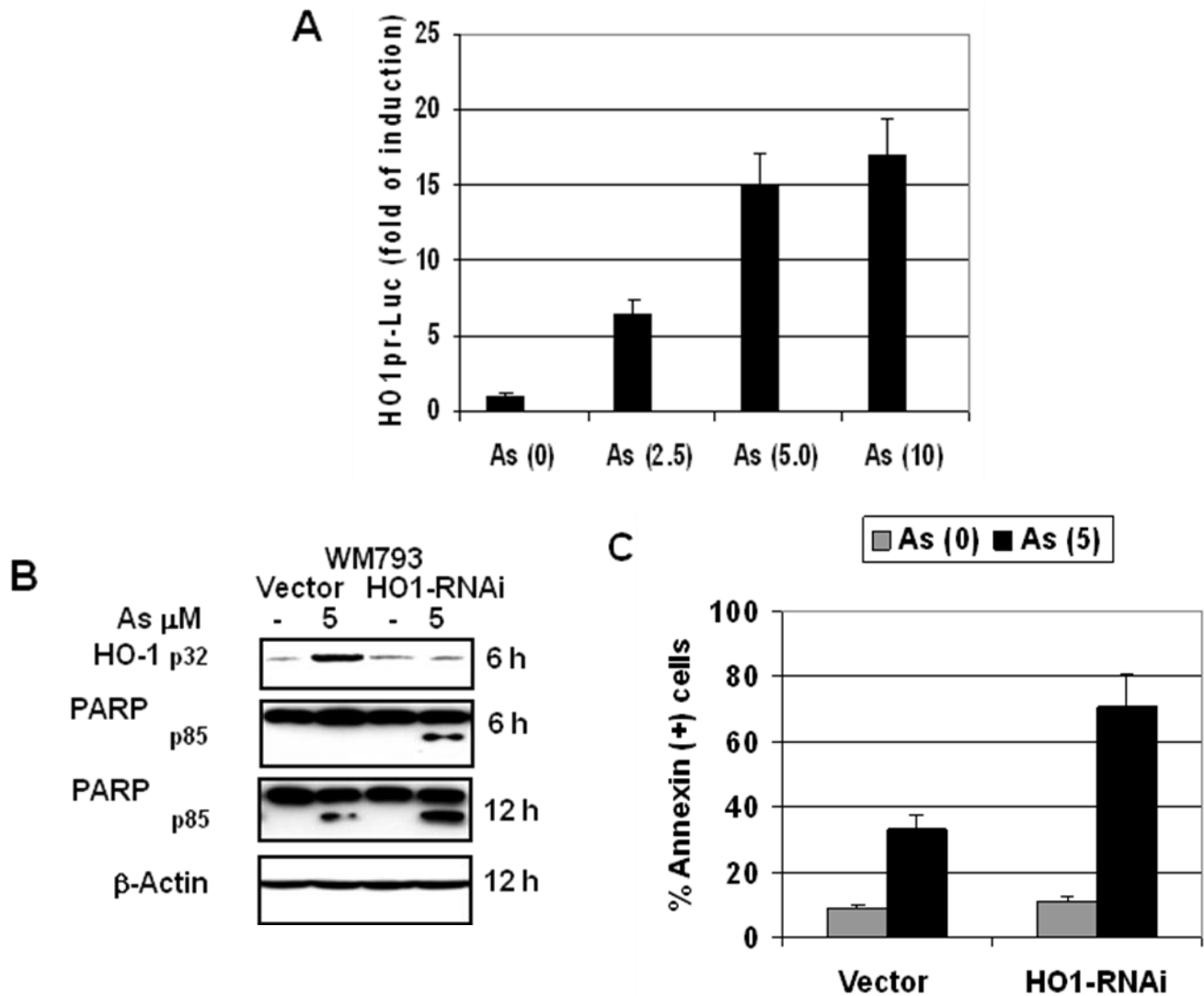


Figure 4. Inhibition of HO-1 expression by specific RNAi or inhibition of HO-1 enzymatic activity by PPIX(Zn) dramatically increased sodium arsenite-induced apoptosis in WM793 melanoma cells. **A.** An inducibility of the HO-1 promoter by sodium arsenite (2.5-10 μM) in WM793 cells. Melanoma cells were transiently transfected by HO1pr-Luc construct in the presence of β-Gal-expression vector. 24 h after transfection, cells were exposed to sodium arsenite for an additional 6 h. Luciferase reporter assay was performed and normalized ratio of Luc/β-gal activity was determined. **B.** WM793 cells were permanently transfected either with the empty vector or with the specific HO1-RNAi construct. Western blot analysis was performed for determination of HO-1 protein levels in the control and HO-1 deficient melanoma cells 6 h after sodium arsenite (As, 5 μM) treatment. PARP protein levels were determined 6 h and 12 h after treatment. Actin was used as a loading control. **C.** Annexin-V-PE (red) staining of WM793 cells permanently transfected with the empty vector or with HO1-RNAi (green) before and 6 h after sodium arsenite (5 μM) treatment.

Based on results obtained for MEF, a challenging question arose regarding further investigation of arsenite-induced apoptosis in melanoma cells sensitized by suppression of HO-1. Sodium arsenite treatment (2.5-5 μ M) strongly induced HO-1 protein levels, while downregulating COX-2 protein levels in human melanoma lines, WM793, FEMX and LOX. Caspase-3 driven cleavage of PARP, a characteristic feature of apoptotic commitment, was observed in WM793 and FEMX, but not in LOX cells (Fig. 3A) resulting in well

pronounced apoptosis for WM793 and FEMX cells, but G2/M arrest in LOX cells (Fig. 3B). A comprehensive analysis of normal melanocytes, normal fibroblasts IMR-90, several melanoma lines and neuroblastoma HTB-11 cells clearly demonstrated low and medium levels of apoptosis induced by 5-10 μ M sodium arsenite that could be partially blocked by zVAD, a universal caspase inhibitor (Fig. 3C).

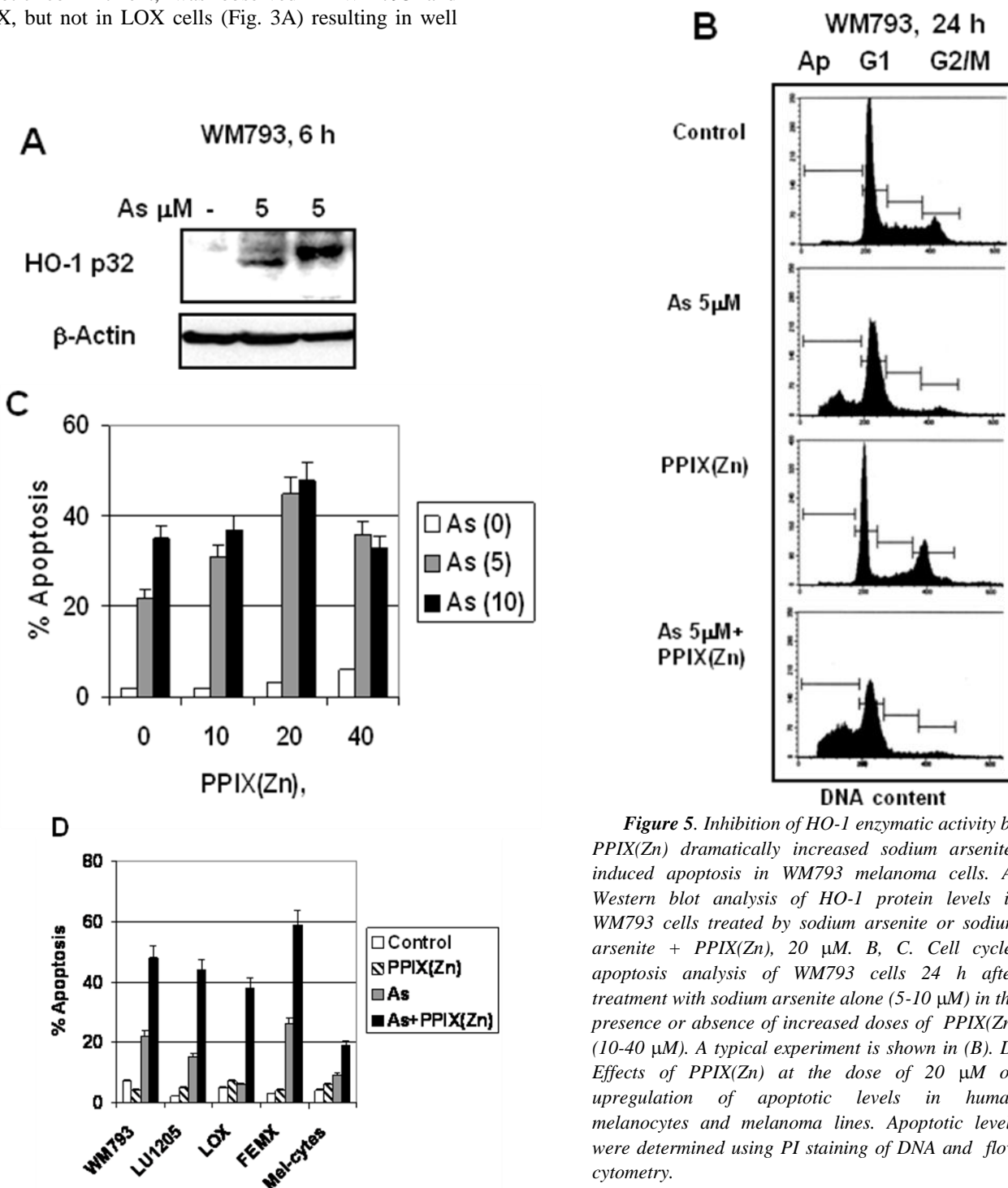


Figure 5. Inhibition of HO-1 enzymatic activity by PPIX(Zn) dramatically increased sodium arsenite-induced apoptosis in WM793 melanoma cells. **A.** Western blot analysis of HO-1 protein levels in WM793 cells treated by sodium arsenite or sodium arsenite + PPIX(Zn), 20 μ M. **B, C.** Cell cycle-apoptosis analysis of WM793 cells 24 h after treatment with sodium arsenite alone (5-10 μ M) in the presence or absence of increased doses of PPIX(Zn) (10-40 μ M). A typical experiment is shown in (B). **D.** Effects of PPIX(Zn) at the dose of 20 μ M on upregulation of apoptotic levels in human melanocytes and melanoma lines. Apoptotic levels were determined using PI staining of DNA and flow cytometry.

Since sodium arsenite regulates HO-1 promoter activity and HO-1 transcription (Fig. 4A), we used a HO1-RNAi construct for permanent transfection and suppression of HO-1 expression in WM793 melanoma cells; the control WM793 cells were transfected with the empty vector (Fig. 4B). Sodium arsenite induced PARP cleavage (that reflected caspase-3 activation) was substantially increased in WM793 with suppressed HO-1 expression (Fig. 4B). This was followed by significant upregulation of levels of apoptosis for HO-1 deficient cells positively stained with Annexin-V-PE (red) among GFP-positive permanently transfected WM793 cells (Fig. 4C).

As an alternative approach, we used an inhibitor of enzymatic activity of HO-1, Protoporphyrin IX Zn(II) [PPIX(Zn)] that also changed electrophoretic mobility of HO-1 after its binding of enzyme molecules (Fig. 5A). Sodium arsenite in a combination with PPIX(Zn) at dose of 20 μ M substantially increased (almost two-fold) apoptotic levels of WM9 cells 24 h after treatment (Fig. 5B). The most effective combination for apoptotic induction was 5 μ M sodium arsenite and 20 μ M PPIX(Zn), as we observed for several melanoma lines (Fig. 5C and D). Taken together, genetic and enzymatic inhibition of HO-1 demonstrated a substantially upregulated arsenite-induced apoptosis of human melanoma cells, while causing relatively mild effects in normal cells. Results obtained probably could improve therapeutic modalities for treatment of melanoma, one of the deadliest cancers, incident number of which progressively increased in USA and worldwide during the last fifty years [7].

References

1. X. Zhang, P. Shan, D. Jiang, P.W. Noble, N.G. Abraham, A. Kappas, P.J. Lee, Small interfering RNA targeting heme oxyg Fig. 5. Inhibition of HO-1 enzymatic activity by PPIX(Zn) dramatically increased sodium arsenite-induced apoptosis in WM793 melanoma cells. A. Western blot analysis of

HO-1 protein levels in WM793 cells treated by sodium arsenite or sodium arsenite + PPIX(Zn), 20 μ M. B, C. Cell cycle-apoptosis analysis of WM793 cells 24 h after treatment with sodium arsenite alone (5-10 μ M) in the presence or absence of increased doses of PPIX(Zn) (10-40 μ M). A typical experiment is shown in (B). D. Effects of PPIX(Zn) at the dose of 20 μ M on upregulation of apoptotic levels in human melanocytes and melanoma lines. Apoptotic levels were determined using PI staining of DNA and the flow cytometry. enase-1 enhances ischemia-reperfusion-induced lung apoptosis, J Biol Chem 279 (2004) 10677-10684.

2. D. Martin, A.I. Rojo, M. Salinas, R. Diaz, G. Gallardo, J. Alam, C.M. De Galarreta, A. Cuadrado, Regulation of heme oxygenase-1 expression through the phosphatidylinositol 3-kinase/Akt pathway and the Nrf2 transcription factor in response to the antioxidant phytochemical carnosol, J Biol Chem 279 (2004) 8919-8929.
3. W. Durante, Heme oxygenase-1 in growth control and its clinical application to vascular disease, J Cell Physiol 195 (2003) 373-382.
4. V.N. Ivanov, T.K. Hei, Arsenite sensitizes human melanomas to apoptosis via tumor necrosis factor alpha-mediated pathway, J Biol Chem 279 (2004) 22747-22758.
5. V.N. Ivanov, T.K. Hei, Combined treatment with EGFR inhibitors and arsenite upregulated apoptosis in human EGFR-positive melanomas: a role of suppression of the PI3K-AKT pathway, Oncogene 24 (2005) 616-626.
6. C.D. Ferris, S.R. Jaffrey, A. Sawa, M. Takahashi, S.D. Brady, R.K. Barrow, S.A. Tysoe, H. Wolosker, D.E. Baranano, S. Dore, K.D. Poss, S.H. Snyder, Haem oxygenase-1 prevents cell death by regulating cellular iron, Nat Cell Biol 1 (1999) 152-157.
7. C. Perlis, M. Herlyn, Recent advances in melanoma biology, Oncologist 9 (2004) 182-187. ■



2010 Annual Radiation Research Society Meeting, Maui, Hawaii (L-r): Dr. Sally Amundson, Dr. Guy Garty, Dr. Shanaz Ghandhi, Dr. Tadeo Ohnishi (President of JRRS), Dr. Tom Hei, Dr. Megumi Hada (NASA) and Dr. Frank Cucinotta (NASA).

Mitochondrial Alteration in Cytoplasmic Irradiation

Hongning Zhou, Sarah Huang, Alan Bigelow, and Tom K. Hei

Previous research indicated that cytoplasmic irradiation would induce DNA damage in both directly and non-irradiated cells, and reactive oxygen/nitrogen species play an essential role in the processing (1, 2). More recently, several studies demonstrated that mitochondria might play an important role in the

mutagenesis in directly irradiated cells without mitochondrial DNA (Figure 1). Furthermore, using real time quantitative PCR, we found that targeted cytoplasmic irradiation induced a transient increase in mitochondrial DNA content among human skin fibroblasts as a function of time post-irradiation as shown

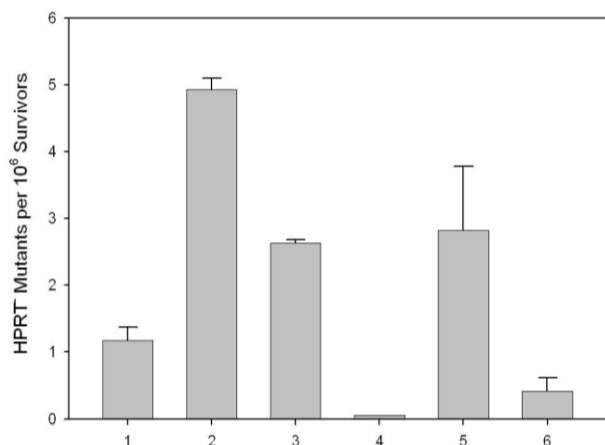


Figure 1. Alpha particle through cytoplasm or nucleus induced mutant fraction at the *hpert* locus in control as well as rho zero human fibroblasts without oxidative metabolism.

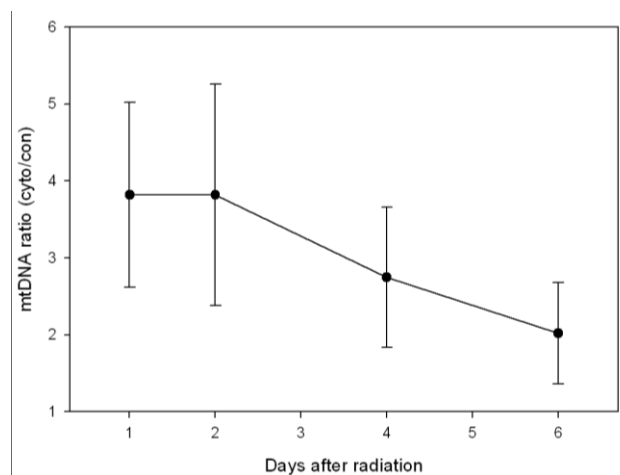


Figure 2. mtDNA/nuclear DNA ratio (cytoplasmic irradiated cells versus non-irradiated controls) as a function of time post-irradiation using quantitative RT-PCR.

regulation of radiation induced genotoxicities (3, 4). Using the Columbia University microbeam facility, we found that cytoplasmic irradiation could induce mutagenesis in mitochondrial functional human skin fibroblasts, although the mutation induction is relatively lower compared with nuclear irradiated cells. However, cytoplasmic irradiation could induce very little, if any,

in Figure 2. To detect mitochondrial alteration after cytoplasmic irradiation, a multiphoton imaging system was used. Small airway epithelia cells, labeled with GFP-glycoprotein linked to their mitochondrial membrane, were plated on a microbeam dish 24 hours before alpha particle irradiation through their cytoplasm. After irradiation, mitochondrial fusion was observed as

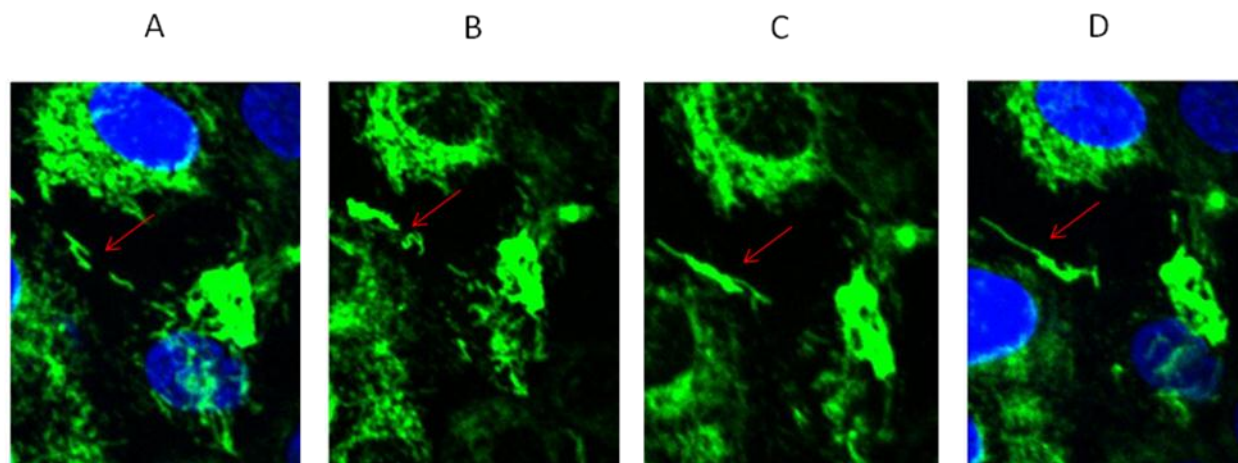


Figure 3: Mitochondrial changes after cytoplasmic irradiation. A. 0 minute after radiation; B. 10 minutes after radiation. C. 20 minutes after radiation. D. 30 minutes after radiation. Red arrow show the mitochondrial fusion site.

shown in Figure 3. One day post-irradiation with alpha particles through the cytoplasm, cells were stained with 3, 3-dihexyloxycarbocyanine iodine (DiOC6), a cell-permeant, green-fluorescent dye that is selective for the mitochondria of live cells. When compared to similarly-treated controls, irradiated cells show a significant reduction in mitochondrial membrane potential indicating a loss of function. These results indicated that mitochondria play a critical role in cytoplasmic irradiation induced genotoxicity, and impact on our understanding of the cellular response to DNA damage and low dose radiation risk assessment.

References

1. Morgan WF. Non-targeted and delayed effects of exposure to ionizing radiation: II. Radiation-induced genomic instability and bystander effects in vivo, clastogenic factors and transgenerational effects. *Radiat Res.* 2003; 159(5):581-96. Review.
2. Hei TK, Zhou H, Ivanov VN, Hong M, Lieberman HB, Brenner DJ, Amundson SA, Geard CR.

Mechanism of radiation-induced bystander effects: a unifying model. *J Pharm Pharmacol.* 2008; 60(8):943-50. Review.

3. Nugent S, Mothersill CE, Seymour C, McClean B, Lyng FM, Murphy JE. Altered mitochondrial function and genome frequency post exposure to gamma-radiation and bystander factors. *Int J Radiat Biol.* 2010; 86(10):829-41.
4. Zhou H, Ivanov VN, Lien YC, Davidson M, Hei TK. Mitochondrial function and nuclear factor-kappaB-mediated signaling in radiation-induced bystander effects. *Cancer Res.* 2008; 68(7):2233-40.

Acknowledgements

This research was supported by funding from the National Institutes of Health Grants CA 49062, ES 12888. The Radiological Research Accelerator Facility (RARAF) is an NIH supported Resource Center through grants EB-002033 (NIBIB). ■

The Role of Rad9 in Genomic Instability in Directly Irradiated and Bystander Cells

Brian Ponnaiya, Kevin M. Hopkins and Howard B. Lieberman

Rad9 has been implicated in a wide range of cellular processes (including the regulation of cell cycle checkpoints and DNA damage repair) that are thought to play roles in the development of tumors (reviewed in (1)). Previous studies have demonstrated that the deletion of *Rad9* can induce abnormal responses to DNA damage and genomic instability (2). In addition, Rad9 has been shown to play a role in radiation induced bystander responses (3). To further explore the link between genomic instability and bystander responses and the role of Rad9 in these phenomena, we examined the induction of genomic instability in bystander cells as a function of Rad9 status using an isogenic set of mouse embryonic stem cells. The three genotypes used in this study were

wild-type mouse ES cells, *Rad9*^{-/-} cells and *Rad9*^{-/-} cells ectopically expressing the mouse *Rad9* gene.

Populations of cells with the three genotypes were seeded onto double-ring mylar dishes as described previously (3) and irradiated with 1 Gy α -particles. Dishes were returned to the incubator for 24 hours following which irradiated and bystander populations were separated and reseeded into T25 flasks. Chromosome preparations were made at 7 day intervals and metaphases were analyzed for gross chromatid- and chromosome-type aberrations using Giemsa.

Frequencies of chromatid aberrations as a function of time post irradiation are presented in Figure 1.

BYSTANDER STUDIES

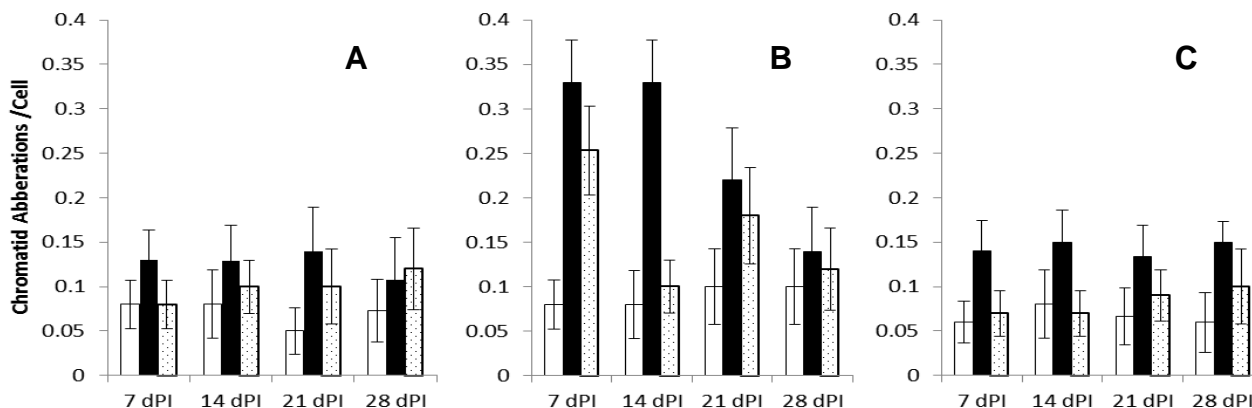


Figure 1. Chromatid aberration frequencies in control (clear bars), irradiated (filled bars) and bystander cells (stippled bars) in wild type (panel A), *Rad9*^{-/-} (panel B) and *Rad9*^{-/-} + *RAD9* (panel C) mouse embryonic stem cells.

As can be seen there were no differences in aberration yields in non-irradiated controls at all time points regardless of *Rad9* status. However, the *Rad9* status of the cells had a major impact on the induction of chromatid aberrations following exposure to α -particles. Wild-type irradiated and bystander cells did not have significantly higher yields of aberrations when compared to genotype matched controls over the course of the experiment. In

contrast, irradiated *Rad9*^{-/-} ES cells had ~4-5 fold higher levels at the early time points that returned to control levels by 28 days post irradiation. Bystander *Rad9* null cells also had higher yields at 7 days post irradiation. The reconstitution of *Rad9* status by ectopically expressing mouse *Rad9* seems to restore function in both irradiated and bystander cells; *Rad9*^{-/-}*Rad9* cells had aberration patterns similar to those observed for wild-type cells.

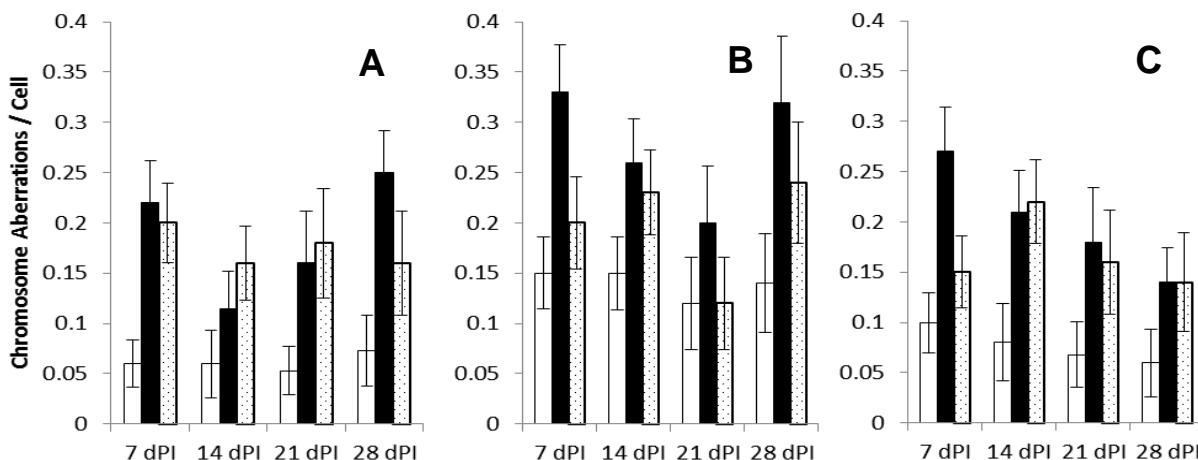


Figure 2. Chromosome-type aberration frequencies in control (clear bars), irradiated (filled bars) and bystander cells (stippled bars) in wild type (panel A), *Mrad9* knock-out (panel B) and *mRad9* knock-out+*HRAD9* (panel C) mouse embryonic stem cells.

Spontaneous chromosome aberrations were higher in *Rad9* knock-out cells as compared to wild-type or reconstituted cells at all time points (Figure 2). At 7 days post-irradiation, irradiated cells of all three genotypes had higher than control levels of chromosome-type aberrations. It is possible that these aberrations were induced by the irradiation and were in the process of being cleared from the populations. This possibility is supported by the fact that in irradiated wild-type and *Rad9*^{-/-} populations, aberration yields seemed to decrease and then increase with time post-irradiation (albeit with different kinetics). A similar decrease with time was observed in *Rad9*^{-/-} +RAD9 cells as well. However, the increases in yields of aberrations at later times would suggest that new aberrations are being formed at these delayed times. Chromosome aberration frequencies in both bystander wild-type and reconstituted populations were elevated over controls, up to 28 days post irradiation. However, in bystander *Rad9*^{-/-} cells, unlike the patterns for chromatid-type aberrations, chromosome-type aberration yields were for the most part similar to those of controls (with the possible exception of the last time point).

In conclusion, the data presented here supports previous findings of a role for Rad9 in both genomic instability and bystander responses. In addition, differential expression of chromatid- and chromosome-type aberrations as a function of Rad9 status suggests that the protein might play different roles in the appearance of delayed chromosomal aberrations in directly irradiated and bystander cells.

References

1. H. B. Lieberman, J. D. Bernstock, C. G. Broustas, K. M. Hopkins, C. Leloup and A. Zhu, The role of RAD9 in tumorigenesis. *J Mol Cell Biol* 3, 39-43 (2011).
2. K. M. Hopkins, W. Auerbach, X. Y. Wang, M. P. Hande, H. Hang, D. J. Wolgemuth, A. L. Joyner and H. B. Lieberman, Deletion of mouse rad9 causes abnormal cellular responses to DNA damage, genomic instability, and embryonic lethality. *Mol Cell Biol* 24, 7235-7248 (2004).
3. A. Zhu, H. Zhou, C. Leloup, S. A. Marino, C. R. Geard, T. K. Hei and H. B. Lieberman, Differential impact of mouse Rad9 deletion on ionizing radiation-induced bystander effects. *Radiat Res* 164, 655-661 (2005). ■

Induction of Genomic Instability in Bystander Cells via Media Transfer Following Si490 Irradiation

Brian Ponnaiya, Masao Suzuki^a, Chirzuru Tsuruoka^a, Yukio Uchihori^a and Tom K. Hei.

There is increasing evidence that biological responses to ionizing radiation are not confined to those cells that are directly hit, but may be seen in the progeny at subsequent generations (genomic instability) and in non-irradiated neighbors of irradiated cells (bystander responses). These so called non-targeted phenomena may have significant contributions to radiation-induced carcinogenesis especially at low doses where only a limited number of cells in a population are directly hit. Therefore, accurate risk assessments for exposures likely to be encountered in space (low dose/low dose rate exposures of high energy particles) must take into account these phenomena. One method used to study bystander responses has been the transfer of media from irradiated cells to non-hit cells, which has resulted in enhanced cell death (1, 2), chromosome damage (3) and increased cell proliferation (4) in the non-irradiated populations. It has been suggested that irradiated cells release factors into the media that result in the observed changes in recipient cells.

Here we assess the induction of chromosomal instability in bystander cells following media transfer from silicon ion irradiated human bronchial epithelial cells (HBEC-3kt). While the ability of high energy particles to induce either genomic instability (5-7) or bystander responses (8-11) have been examined independently, to our knowledge, the studies reported here are the first to examine the link between these phenomena as a consequence of high energy particle irradiation. Confluent cultures in T25 flasks were irradiated with 119 keV/μm silicon ions (490 MeV/nucleon), accelerated by the Heavy Ion Medical Accelerator in Chiba (HIMAC) at the National Institute of Radiological Sciences (NIRS), Chiba, Japan. Sham and irradiated flasks were returned to the incubator for 1 hour, following which media was removed, passed through a 0.2 μm filter and applied to non-irradiated cultures. One hour later, cells were trypsinized and reseeded onto 100 mm dishes single cell clone isolation. Between 12 and 24

BYSTANDER STUDIES

single cell clones were isolated from each population 14 days post irradiation. These clones were frozen down and 5-6 clones from each treatment population were randomly selected for expansion and further analyses by mFISH. Analyses of 5 clones isolated from the 2Gy irradiated population (known irradiated), and 5 clones from the population that received media from the 2 Gy flask (known bystanders), were performed.

mFISH karyotypes from clone Si8-B2 (irradiated with 2 Gy) are presented in Figure 1. A trio of translocations, t(17;3), t(5;17) and t(3;5), was detected in all the cells

analyzed. These translocations probably arose from a complex interchange at the time of irradiation. In addition, t(12;6) was present in 60% of cells. Interestingly, cells that did not have this particular aberration had only one copy of chromosome 6 (e.g. panel B). Additional translocations and fragments were also observed (eg. panels A and E). Since this clone came from a single irradiated cell, the appearance of particular aberrations in only a fraction of the cells would indicate that these occurred de novo as a function of time in culture – the definition of genomic instability.

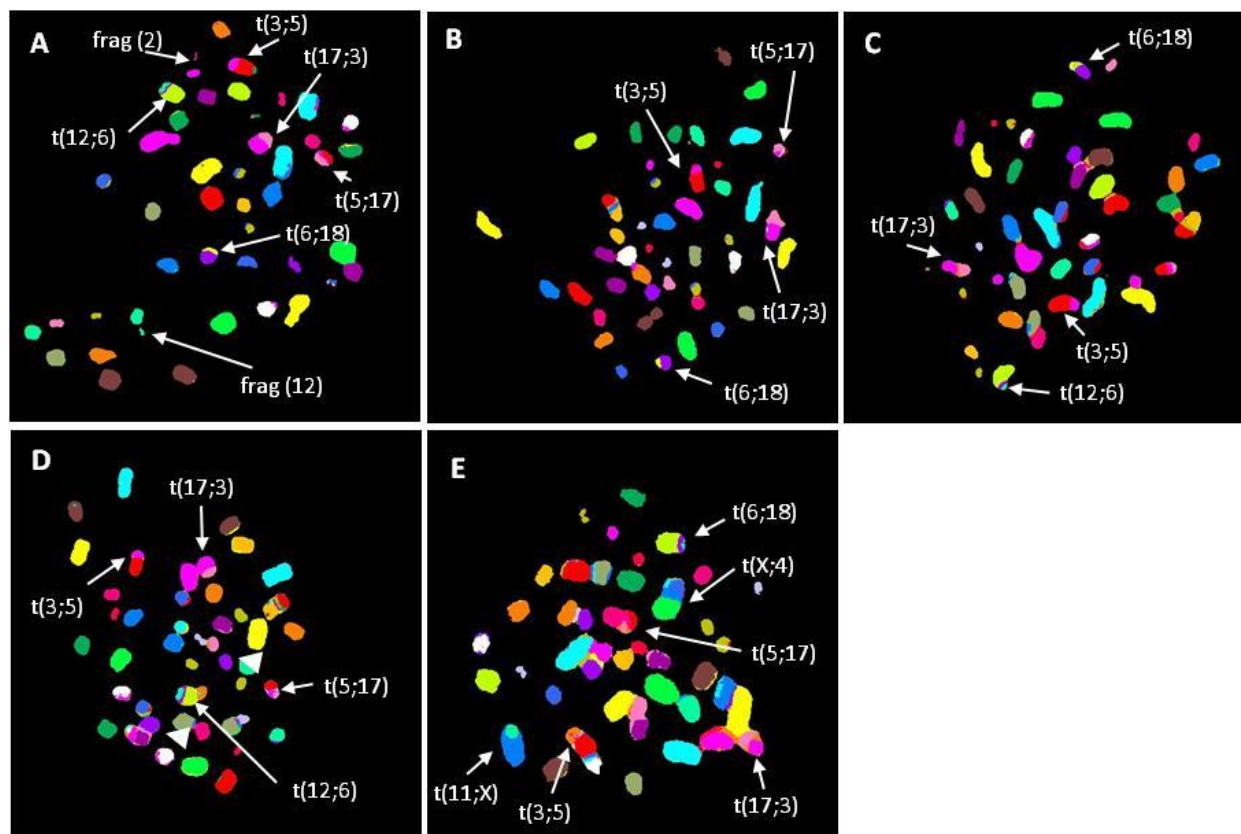


Figure 1. mFISH analyses of G2-PCCs from clone Si8-B2. This clone was isolated from the population that received 2 Gy Si490 ions.

The analyses of 5 clones isolated after irradiation with 2 Gy are summarized in Table 1. Using the standard criteria for defining the basis for chromosome instability (at least 5% of the cells were aberrant and if the clone was made up of at least 3 different subpopulations), all the clones were deemed to be unstable. It appears that the

degree of instability is variable with some clones demonstrating higher numbers of sub-populations than others.

^a National Institute of Radiological Sciences, Chiba, Japan

Table 1. Summary of mFISH results of single cell clones isolated from populations irradiated with 2 Gy Si490 ions.

Clone	% Normal Karyotype	% Aberrant Karyotype	# Subpopulations
Si8-A2	0	100	4
Si8-B2	0	100	7
Si8-C2	0	100	12
Si8-C3	0	100	5
Si8-C4	0	100	8

A representative sample of five different clones isolated from the population that received conditioned medium from 2 Gy irradiated culture were examined to define the karyotypes in bystander cells. As shown in Figure 2, 8.36% of the cells analyzed in one of the clone, Si12C1 had a normal karyotype (panel A). The other 64% of cells showed a variety of translocations including t(2;4) in 20% of cells (panel B), translocations involving chromosome 1 (32% of cells, panels C and E) and translocations involving chromosome 7 (16% of cells, panels D and E). Interestingly, in one instance,

chromosome 1 and chromosome 7 translocations were seen in the same cell (panel E). The presence of normal karyotypes would suggest that the original cell had a normal karyotype at least till the first cell division. The presence of chromosomal aberrations in fractions of the cells in the clone would suggest that they occurred later in culture and provides evidence for the induction of genomic instability in bystander cells that received media from irradiated culture.

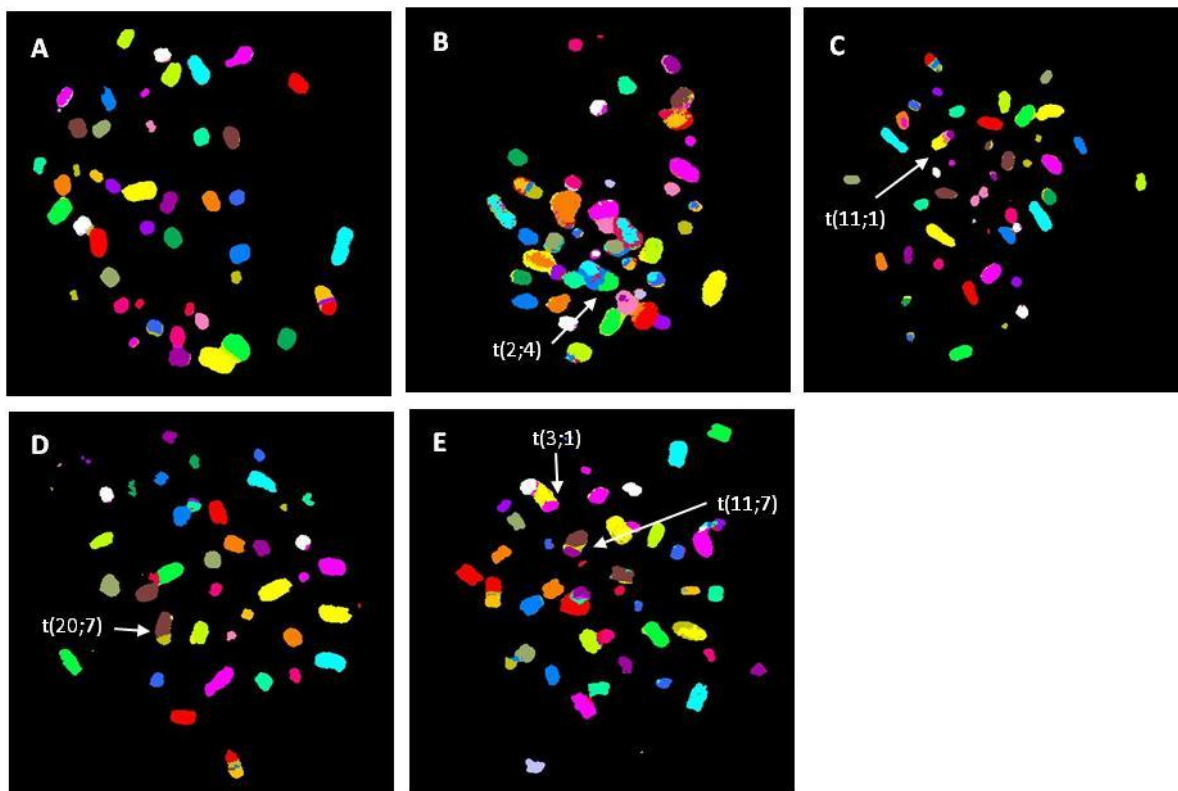


Figure 2. mFISH analyses of G2-PCCs from clone Si12-C1. This clone was isolated from a bystander population that received medium from a flask irradiated with 2 Gy Si490 ions.

The results for 5 bystander clones are presented in Table 2. Of the five clones, only two of them met our definition of chromosomal instability, i.e. had more than 3 subpopulations that made up at least 5% of the karyotypes analyzed (Si12-B4 and Si12-C1). Interestingly, from the

mFISH data of all the clones analyzed, there appears to be no correlation between the number of subpopulations and the number of aberrant cells in any given individual clone.

Table 2. Summary of mFISH results of single cell clones isolated from bystander populations that received media from cells irradiated with 2 Gy Si490 ions.

Clone	% Normal Karyotype	% Aberrant Karyotype	# Subpopulations
Si12-A2	100	0	1
Si12-B4	56	44	4
Si12-C1	36	64	6
Si12-C2	94	6	2
Si12-C4	80	20	2

In conclusion, the data presented here provide evidence that irradiation with high energy Si490 particles can induce genomic instability in clones of bystander cells via media borne factors. These data strengthen the link between the two phenomena that may be significant to radiation-induced carcinogenesis especially at low doses of ionizing radiation.

References

1. C. Mothersill and C. Seymour, Medium from irradiated human epithelial cells but not human fibroblasts reduces the clonogenic survival of unirradiated cells. *Int J Radiat Biol* 71, 421-427 (1997).
2. C. Mothersill and C. B. Seymour, Cell-cell contact during gamma irradiation is not required to induce a bystander effect in normal human keratinocytes: evidence for release during irradiation of a signal controlling survival into the medium. *Radiat Res* 149, 256-262 (1998).
3. B. E. Lehnert, E. H. Goodwin and A. Deshpande, Extracellular factor(s) following exposure to alpha particles can cause sister chromatid exchanges in normal human cells. *Cancer Res* 57, 2164-2171 (1997).
4. R. Iyer, B. E. Lehnert and R. Svensson, Factors underlying the cell growth-related bystander responses to alpha particles. *Cancer Res* 60, 1290-1298 (2000).
5. H. Hofman-Huther, H. Peuckert, S. Ritter and P.

Virsik-Kopp, Chromosomal instability and delayed apoptosis in long-term T-lymphocyte cultures irradiated with carbon ions and x rays. *Radiat Res* 166, 858-869 (2006).

6. C. L. Limoli, B. Ponnaiya, J. J. Corcoran, E. Giedzinski and W. F. Morgan, Chromosomal instability induced by heavy ion irradiation. *Int J Radiat Biol* 76, 1599-1606 (2000).
7. M. B. Martins, L. Sabatier, M. Ricoul, A. Pinton and B. Dutrillaux, Specific chromosome instability induced by heavy ions: a step towards transformation of human fibroblasts? *Mutat Res* 285, 229-237 (1993).
8. M. Buonanno, S. M. de Toledo, D. Pain and E. I. Azzam, Long-term consequences of radiation-induced bystander effects depend on radiation quality and dose and correlate with oxidative stress. *Radiat Res* 175, 405-415 (2011).
9. C. Fournier, D. Becker, M. Winter, P. Barberet, M. Heiss, B. Fischer, J. Topsch and G. Taucher-Scholz, Cell cycle-related bystander responses are not increased with LET after heavy-ion irradiation. *Radiat Res* 167, 194-206 (2007).
10. C. Shao, Y. Furusawa, Y. Kobayashi, T. Funayama and S. Wada, Bystander effect induced by counted high-LET particles in confluent human fibroblasts: a mechanistic study. *FASEB J* 17, 1422-1427 (2003).
11. H. Yang, V. Anzenberg and K. D. Held, The time dependence of bystander responses induced by iron-ion radiation in normal human skin fibroblasts. *Radiat Res* 168, 292-298 (2007). ■

Cox2 Expression in Irradiated and Bystander Mouse Mammary Tissues

Brian Ponnaiya, Yungfei Chai, Charles R. Geard and Tom K. Hei

There is now a significant amount of evidence supporting the induction of bystander responses following exposure to ionizing radiation. However, to date, most of these data come from cells in culture and only a few studies have investigated whether the phenomenon occurs *in vivo*. One such study has utilized the *gptΔ* mouse model to study bystander mutagenesis (1). Following irradiation of a 1cm² area in the lower abdomen of the mouse with 5 Gy X-rays, it was observed that the lungs (far removed from the site of irradiation and thereby bystander tissue) had elevated levels of *cox2* expression when compared to sham irradiated controls. Here we present data of *cox2* induction in the mammary glands from this *in vivo* model.

paraffin) and rehydrated with 100%, 90% and 70% ethanol. Slides were then immersed in Target Retrieval solution at 98°C for 20 minutes followed by cooling at RT for 20 minutes. The primary antibody was an anti-*cox2* rabbit polyclonal antibody (Genway Biotech, CA) and the secondary antibody was part of the Tyramide Signal Amplification Kit from Molecular Probes. Slides were counterstained with DAPI to visualize the nuclei. Pictures were taken of nuclei (blue) and *cox2* expression (red) in the ducts of the mammary glands and mean fluorescence intensities of individual cells were measured using ImageProPlus 6.0. A minimum of 200 cells were analyzed per sample.

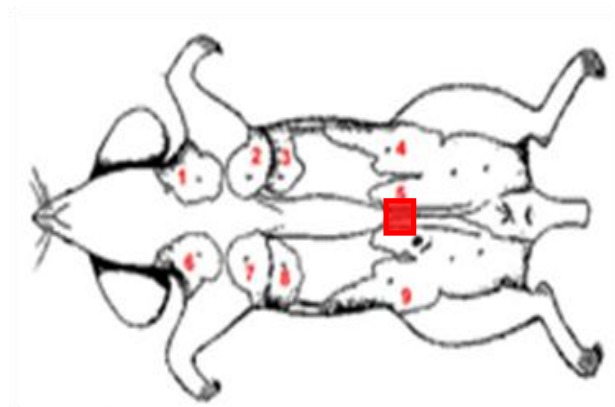


Figure 1. Distribution of mouse mammary glands (numbered 1-10) with respect to the zone of irradiation (red square).

10-12 week old female *gptΔ* mice were irradiated as previously described, i.e. 5 Gy X-rays delivered to a 1cm² area in the lower abdomen. For comparison purposes animals were also irradiated with either 5 Gy or 6 cGy (whole body irradiation). The 6cGy dose was selected based on calculations that found 6cGy was the scattering dose to organs in the thoracic cavity when 5 Gy was delivered to 1 cm² in the lower abdomen. One day post-irradiation, mice were sacrificed by cervical dislocation and mammary glands #1 (bystander tissue) and #5 (partially in the zone of irradiation) were isolated (see figure 1), briefly rinsed in PBS and fixed in 10% neutral buffered formalin for 24 hours. Tissues were then embedded in paraffin and 4 mm immunoblank sections were made (Histology facility).

To examine the expression of *cox2* in mammary tissues, slides were treated with Xylene (to remove

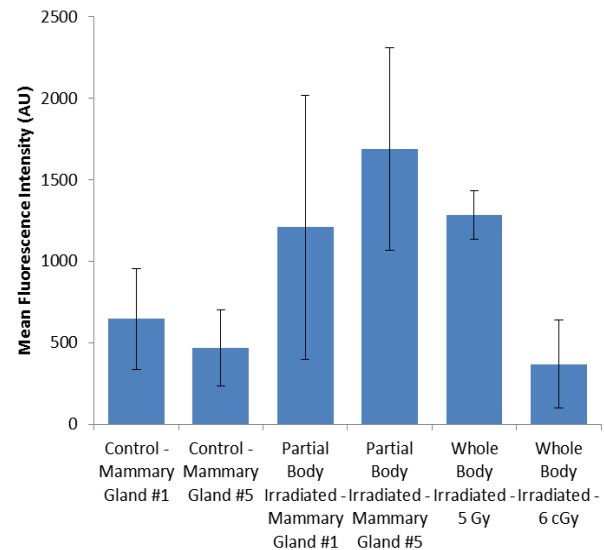


Figure 2. Expression of *cox2* in irradiated and bystander mammary tissues: Mean fluorescence intensity per nucleus in mammary glands of control and partial body irradiated mice. Each bar represents the mean of 3 animals.

As can be seen in Figure 2, *cox2* was expressed to similar levels in both glands 1 and 5 of sham irradiated mice. Further, following whole body irradiation with 5 Gy x-rays there was an induction of *cox2*; 2-3 fold higher than that of controls. Interestingly partial body irradiation also resulted in similar inductions. Both glands #1 and #5 from partially irradiated animals had elevated levels of *cox2* as compared to controls. Importantly, since gland #1 was far removed from the site of irradiation, it is

reasonable to conclude that induction of *cox2* in this gland occurred as a consequence of some sort of bystander signaling. Importantly, *cox2* levels in mammary glands of animals irradiated with 6 cGy were similar to those observed in controls. This would suggest that the alterations seen in the partial body irradiation were not due to scattered doses affecting the mammary glands. In addition, there was more variability among cells in both #1 and #5 glands in the partial body irradiation (as can be seen by the larger error bars). This would indicate that in the partial body irradiation not all cells are responsive to the bystander signaling, with some cells showing elevated levels of *cox2* while others have levels similar to those seen in control tissues. This is born out when the data are examined on a cell by cell basis. Figure 3 represents the frequency distribution of *cox2* expression levels in individual cells in control mammary gland, partial body irradiation gland #1 and partial body irradiation gland 5. The staining intensities have been binned at every 200 units.

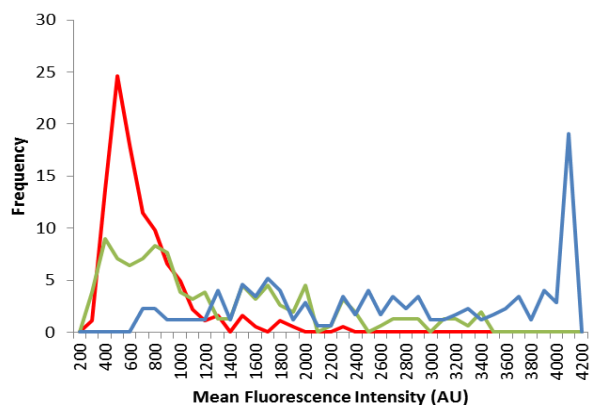


Figure 3. Frequency distribution of *cox2* expression in individual cells of control mammary gland (red line), partial body irradiation gland #1 (green line) and partial body irradiation gland #5 (blue line). Mean fluorescence intensities have been binned at every 200 units.

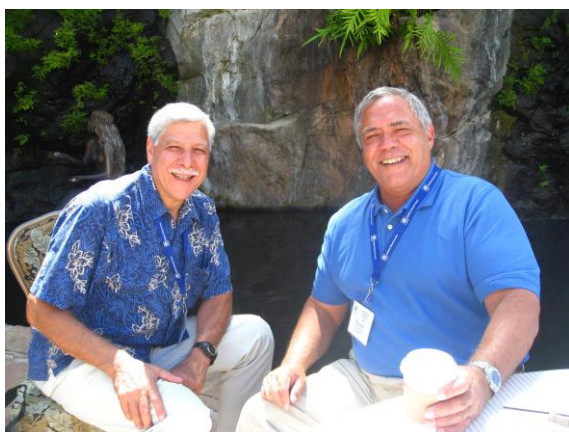
Expression levels in the control gland were for the most part uniformly low with almost 90% of the cells falling within a single peak between 400 and 1000 AU. In contrast, the distribution of the cells in gland #5 following partial body irradiation was more diverse, with about 25% of the cells having values between 3900 and 4200 AU (presumably directly irradiated cells) and a range of expression levels between 1200 and 3800 AU. Distribution in gland #1 from a partially irradiated animal was distinct from that of controls as well as gland #5. While 50% of the cells had values similar to those of controls (400-1000 AU), the rest of the cells had values between 1200 and 3400 AU. It might be argued that these intermediate values (between the lows seen in controls

and highs seen in gland #5) represent bystander cells that are responding to signals put out by the directly irradiated tissue.

In conclusion, the data presented here are further evidence of the bystander phenomenon in vivo and add support to the idea that bystander responses should be accounted for in risk estimation especially at low doses.

References

Y. Chai, S.X. Huang, G.M. Calaf and T.K. Hei. Radiation induced bystander mutagenesis in the gpt delta transgenic mouse model. *55th Annual Meeting of the Radiation Research Society, 2009.* ■



2010 Annual Radiation Research Society Meeting, Maui, Hawaii (L-r): Mr. Steve Marino, Dr. Richard Miller, Dr. Hongning Zhou, Dr. Yanping Xu and his wife, Sarah.

TGFBI Protentiates in Vitro Invasion Ability in Mesothelioma Cells

Gengyun Wen, Wupeng Liao^a, Vina Pulido^b and Tom K. Hei

Tumor metastasis, a complex, multistage process by which primary tumor cells migrate to and colonize distant tissues, is a critical step in the progression of cancer to

lethality (1). Understanding the mechanisms underlying this process is crucial to improve anti-metastatic therapies.

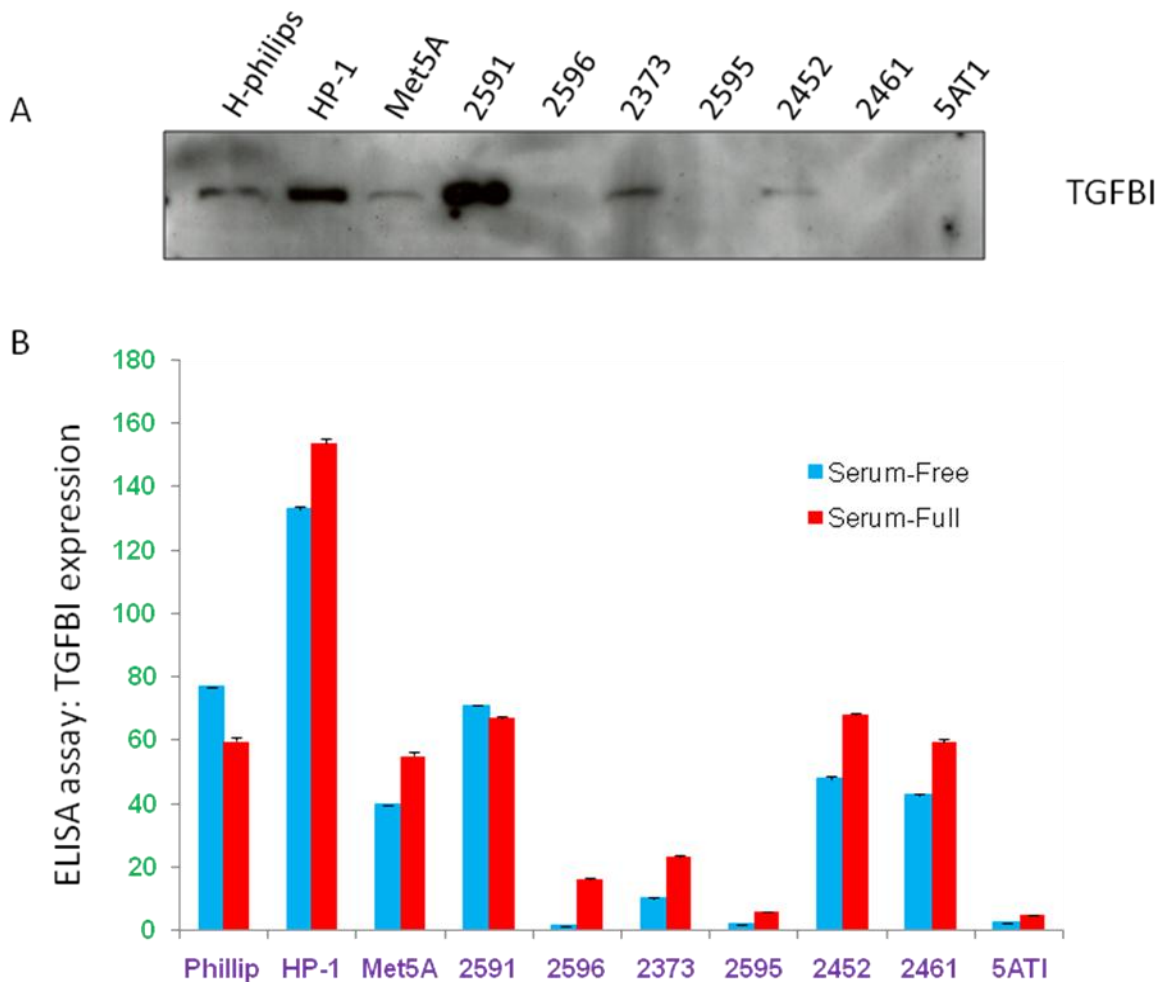


Figure 1. A) Expression of TGFBI in cell supernatant was determined by Western blotting. Media were harvested and concentrated 10-fold using SP Sepharose Fast Flow resin (GE Healthcare Bio-Sciences Corp. Piscataway, NJ) before Western blotting. TGFBI antibody was from R&D Systems (Minneapolis, MN). Experiments were performed three times and a representative immunoblot is shown here. B) TGFBI Duoset ELISA kit (R&D) was used to measure secreted TGFBI in culture media. Briefly, 96-well BD Falcon ELISA plates were coated overnight at 4°C with 4 µg/ml anti-human TGFBI capture antibody in a 100 µl volume. After washing for 3 times, wells were blocked with Reagent Diluent for 1 h at room temperature. 100 µl of culture media or TGFBI protein standards were added to the wells and incubated at room temperature for 2 h. After washing, the biotinylated anti-human TGFBI detection antibody (0.4 µg/ml) was then added and incubated for 1 h, followed by streptavidin-HRP conjugate working solution for 20 min. The plates were washed 5 times and developed with the tetramethylbenzidine (TMB) peroxidase EIA Substrate Solution. The reaction was stopped with Stop Solution, and the OD was read at 450 nm with 570 nm correction on a microplate reader.

Transforming growth factor-induced (TGFBI) protein, otherwise known as Betaig-h3, is detected in most of human tissues, as well as some types of tumor cell lines. TGFBI has been implicated in a number of pathological processes including tumorigenesis, angiogenesis, progression, etc. Deficiency of TGFBI has been linked with cell malignant transformation as well as tumorigenesis (2). However, the most extensive studies

on TGFBI have been directed toward understanding its role in corneal dystrophies, and a number of mutations in the gene have been shown to have a pathological manifestation (3, 4). Since TGFBI is a secreted protein and has been shown to serve as a “linker” between ECM and integrins (9), it was natural to associate its role with one of the most important traits of malignant tumors--metastasis.

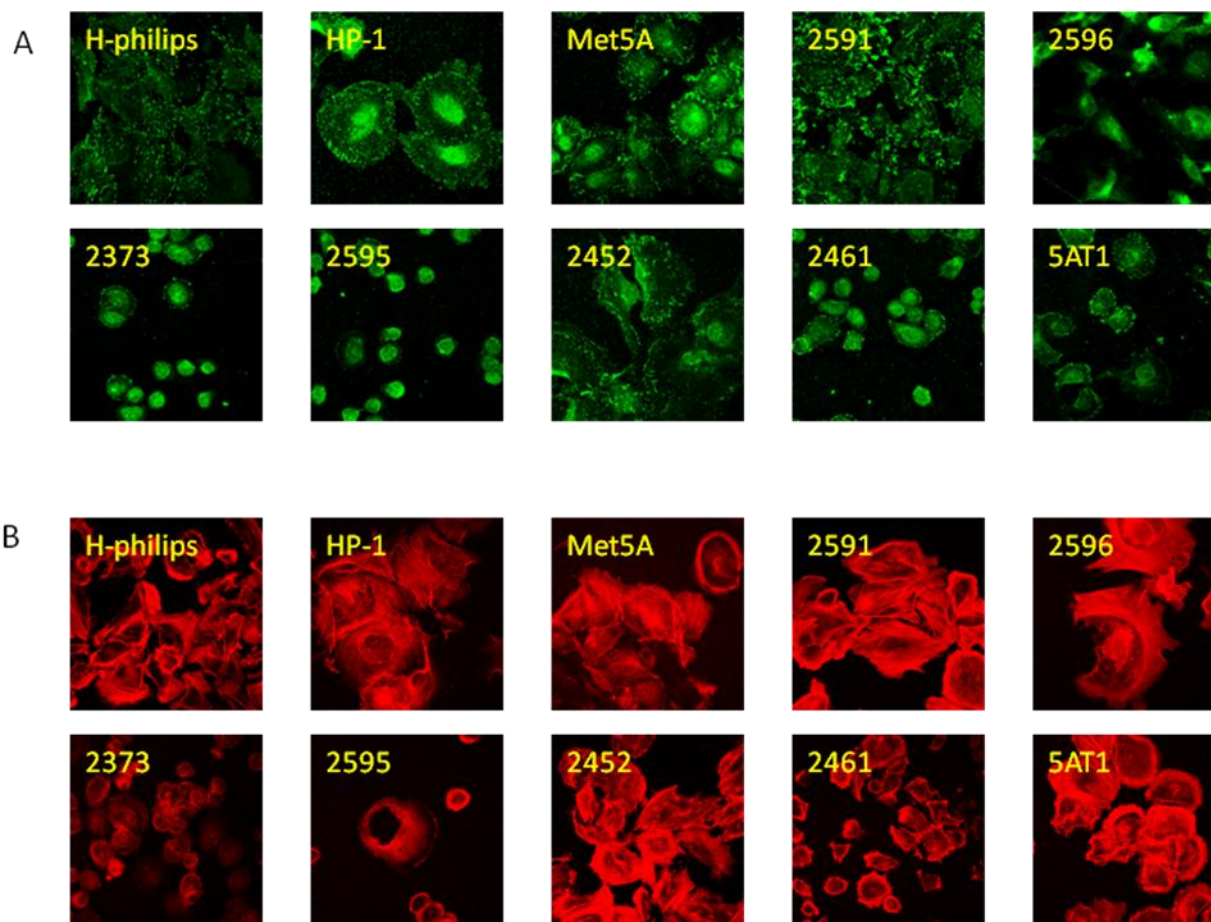


Figure 2. Alteration of focal adhesion and actin stress fiber formation with associated signaling activation in mesothelioma cells. Representative images display focal adhesion (A) and stress fiber formation (B) when cells spread on fibronectin, which are increased in cells expressing TGFBI. Cells were plated on fibronectin-coated coverslips in DMEM containing 2% bovine serum albumin and incubated at 37°C for 30 min. The adherent cells were then fixed and stained with rhodamine phalloidin (red) for stress fiber or antibody to vinculin (green) for focal adhesion (magnification 100x).

^a Department of Radiation Oncology, Columbia University

^b Department of Medicine, College of Physicians and Surgeons, Columbia University

Recently, however, a controversy has arisen as to the role of TGFBI in the control of tumor metastasis. Contradictory evidence obtained from different groups demonstrated that TGFBI either promotes or impedes this process (5, 6, and 7). Therefore, it is imperative to clarify whether this is a cell type-specific phenotype, or an incorrect conclusion based on the limited number of cell lines, or some other undiscovered facts.

In order to substantiate TGFBI's role in cancer metastasis, more cell lines were included in the study which are: eight different mesothelioma cell lines that have various TGFBI expression levels, one mesothelial cell line that expresses a certain amount of TGFBI along with its knockdown counterpart by TGFBI-selective siRNA (Figure 1A & B).

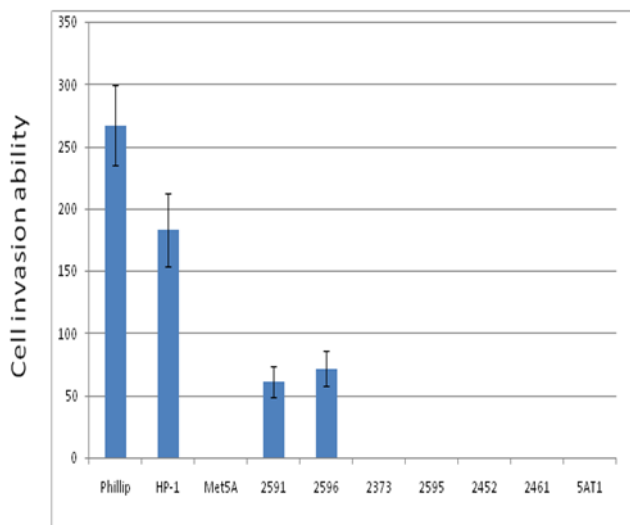


Figure 3. Invasion ability was measured using a matrigel invasion chamber. Cells in serum-free DMEM were seeded in invasion chambers and serum-containing DMEM was added to the lower wells. After incubation for 24 h, non-invading cells were removed from the upper surface. Cells at the bottom were fixed, stained with crystal violet and the number of cells was counted under microscopy. *In vitro* invasion activities are well correlated with the expression levels of TGFBI in mesothelioma cells. Data are mean±SD from three independent experiments with values for cells invading through Matrigel insert membrane given as a percentage of the cell migration through control insert membranes.

We assessed some of the most prominent *in vitro* characteristics associated with metastatic tumors, such as invasion ability, cell motility and adhesion dependent cellular morphology and signaling alterations. We found that cells expressing higher TGFBI generally, if not precisely, possess increased ability to adhere to ECM proteins, form cytoskeleton structures (Figure 2) and

activate adhesion-mediated downstream signaling molecules versus lower or undetectable TGFBI expressing cells; meanwhile, mesothelioma cells with higher TGFBI levels correlated well with enhanced abilities to penetrate matrix gels (*in vitro* invasion, Figure 3) and to migrate in chamber wells (*in vitro* motility). The latter one was also observed in TGFBI expressing mesothelial cells versus its TGFBI siRNA knockdown counterpart. By adding soluble TGFBI protein into the medium, lower or undetectable TGFBI expressing cells increased these abilities. Taken together, these data suggest that TGFBI expression in mesothelioma cells maybe associated with an increased metastatic potential, which is in disagreement with our previous findings in breast cancer and lung cancer cell lines that TGFBI moderates their metastatic potential. Ongoing work includes engineering these mesothelioma cells by changing TGFBI expression status, to find if these observed characteristics will change accordingly, and then further verifying the results *in vivo*.

References

1. Gupta GP, Massague J (2006) Cancer metastasis: building a framework. *Cell* 127 (4): 679-695
2. Zhang Y, Wen G, Shao G, Wang C, Lin C, Fang H, Balajee AS, Bhagat G, Hei TK, Zhao Y (2009) TGFBI deficiency predisposes mice to spontaneous tumor development. *Cancer Res.* 69 37-44
3. Thapa N, Lee BH, Kim IS (2007) TGFBIp/betaig-h3 protein: a versatile matrix molecule induced by TGF-beta. *Int. J. Biochem. Cell Biol.* 39: 2183-2194
4. Munier FL, Korvatska E, Djemai A, Le Paslier D, Zografos L, Pescia G, Schorderet DF (1997) Keratoepithelin mutations in four 5q31-linked corneal dystrophies, *Nat. Genet.* 15: 247-251.
5. Chaoyu Ma, Yu Rong, Daniel R. Radloff, Michael B. Datto, Barbara Centeno, Shideng Bao, Anthony Wai, Ming Cheng, Fumin Lin, Shibo Jiang, Timothy J. Yeatman, and Xiao-Fan Wang (2008) Extracellular matrix protein β ig-h3/TGFBI promotes metastasis of colon cancer by enhancing cell extravasation. *Genes & Dev.* 22: 308-321
6. Miranda P. Ween, Noor A. Lokman, Peter Hoffmann, Raymond J. Rodgers, Carmela Ricciardelli and Martin K. Oehler (2011) Transforming growth factor-beta-induced protein secreted by peritoneal cells increases the metastatic potential of ovarian cancer cells *Int. J. Cancer:* 128, 1570–1584
7. Gengyun Wen, Michael A. Partridge, Bingyan Li, Mei Hong, Wupeng Liao, Simon, K. Cheng, Gloria M. Calaf, Amish Shah, and Tom K. Hei (2011) TGFBI Expression Reduces *In Vitro* and *In Vivo* Metastatic Potential of Lung and Breast Tumor Cells. *Cancer Letters.* In press. ■

Epigenetic Inactivation of the TGFBI in Human Leukemia

Hongbo Fang, Tom K. Hei and Yongliang Zhao

TGFBI was first identified in a human lung adenocarcinoma cell line (A549) treated with transforming growth factor- β (1). It is ubiquitously expressed in human normal tissues; especially highly expressed in spleen and peripheral white blood cells. Downregulation of *TGFBI* in human tumor cells is a frequent event, and related to human tumorigenicity and decreasing the sensitivity of ovarian cancer cells to chemotherapeutic drugs (2). *TGFBI* disruption resulted in a dramatic predisposition to lymphomas and other cancer (3). The molecular mechanisms of absence of TGFBI in

tumor progression and whether the chemotherapy resistance in human leukemia is caused by TGFBI are unclear. DNA methylation of CpG islands plays an important role in silencing or inactivation of gene expression (4-5). It has been well-documented that some known tumor suppressor genes, such as cell cycle inhibitor (*p16INK4a*) and DNA repair genes (*hMLH1* and *BRCA1*), are modified and transcriptionally silenced by promoter hypermethylation (6).

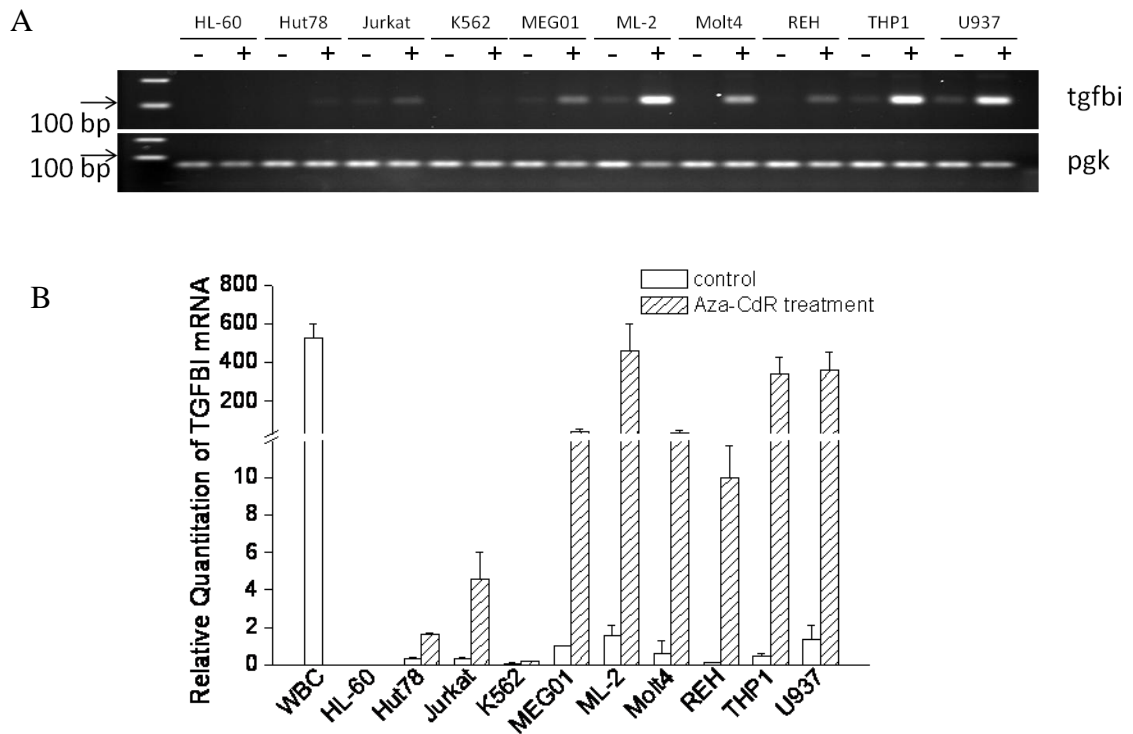


Figure 1. TGFBI mRNA level increased by Aza-CdR treatment. (A) PCR product of TGFBI mRNA level in leukemia cell lines. HL-60: human promyelocytic leukemia cell line, Hut 78: human T-cell leukemia line, Jurkat: human T cell lymphoblast-like cell line, K562: human erythromyeloblastoid leukemia cell line, MEG-01: human megakaryoblastic leukemia cell line, ML-2: human acute myelogenous leukemia cell line, Molt4: human acute lymphoblastic leukemia cell line, REH: human acute lymphocytic leukemia (non-T; non-B) cell line, THP-1: human acute monocytic leukemia cell line, U937: human leukemic monocyte lymphoma cell line. (B) Quantitative analysis of TGFBI mRNA level in normal white blood cell and human leukemia cell lines. WBC: Normal human peripheral white blood cell (control). Setting TGFBI mRNA expression of MEG-01 cell under normal culture condition 1. Aza-CdR changed TGFBI mRNA level in leukemia cells. “-”: Normal cultured cells; “+”: 10 μ M Aza-CdR induced for 4 days and changed medium for every day.

Our previous study showed that *TGFBI* was expressed at a relatively high level in normal and immortalized cell lines, whereas it was downregulated in most of the tumor cell lines. To test the *TGFBI* expression level in leukemia, we first used leukemia cell lines to detect its mRNA expression level with a PCR method. The results showed that the *TGFBI* was expressed at a high level in normal white blood cells, however it was dramatically downregulated in all of ten detected leukemia cell lines. To determine whether the *TGFBI* gene promoter methylation status of the leukemia cell lines was correlated with *TGFBI* mRNA expression change, the leukemia cell lines were treated with demethylating agent Aza-CdR (5-aza-2'-deoxycytidine) for 4 days. Eight of the leukemia cell lines were found to increase *TGFBI* mRNA level with Aza-CdR except for HL-60 and K562 cell lines (Figure 1). These results suggest a positive correlation between dense methylation of the *TGFBI* gene promoter and *TGFBI* mRNA level in leukemia cell lines.

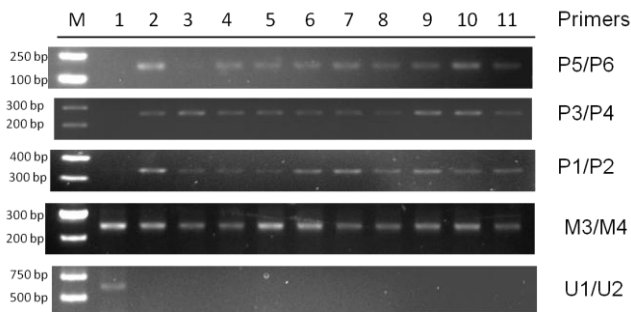


Figure 2. Methylation status of the *TGFBI* promoter in leukemia cell lines. M: DNA marker, Lanes 1-11: WBC, 293T, Hut78, Jurkat, K562, MEG01, ML-2, Molt-4, THP-1, REH, U937.

To determine whether downregulation of *TGFBI* gene resulted from promoter hypermethylation, gene promoter methylation status was characterized with nine leukemia cell lines by bisulfite treatment and MSP-based methylation screening method (7). Normal white blood cells and 293T cell lines were used as negative and positive controls respectively. As shown in Figure 2, Hut78, Jurkat, K562, MEG01, ML-2, Molt-4, THP-1,

REH and U937 cell lines were identified to harbor DNA methylation in *TGFBI* gene promoter region detected by primer sets P1/P2, P3/P4, P5/P6. The methylation frequencies of leukemia cell lines were almost 100%. These results were consistent with the findings in prostate cancer samples (7).

Taken together, the present study demonstrates that DNA hypermethylation of *TGFBI* gene promoter region correlates with silencing of *TGFBI* in leukemia tumor cell lines.

References

1. Skonier J, Neubauer M, Madisen L, Bennett K, Plowman GD, Purchio AF. cDNA cloning and sequence analysis of beta ig-h3, a novel gene induced in a human adenocarcinoma cell line after treatment with transforming growth factor-beta. *DNA Cell Biol.* 1992;11:511-22.
2. Shao G, Berenguer J, Borczuk AC, Powell CA, Hei TK, Zhao Y. Epigenetic inactivation of Betaig-h3 gene in human cancer cells. *Cancer Res.* 2006;66:4566-73.
3. Zhang Y, Wen G, Shao G, Wang C, Lin C, Fang H, et al. *TGFBI* deficiency predisposes mice to spontaneous tumor development. *Cancer Res.* 2009;69:37-44.
4. Li LC, Carroll PR, Dahiya R. Epigenetic changes in prostate cancer: implication for diagnosis and treatment. *J Natl Cancer Inst.* 2005;97:103-15.
5. Catto JW, Azzouzi AR, Rehman I, Feeley KM, Cross SS, Amira N, et al. Promoter hypermethylation is associated with tumor location, stage, and subsequent progression in transitional cell carcinoma. *J Clin Oncol.* 2005;23:2903-10.
6. Esteller M. CpG island hypermethylation and tumor suppressor genes: a booming present, a brighter future. *Oncogene.* 2002;21:5427-40.
7. Shah JN, Shao G, Hei TK, Zhao Y. Methylation screening of the *TGFBI* promoter in human lung and prostate cancer by methylation-specific PCR. *BMC Cancer.* 2008;8:284. ■



Dr. Howard B. Lieberman and Dr. Tom K. Hei.



Dr. Lubomir Smilenov and Ms. Monique Rey.

Differential Gene Expression in Nuclear and Cytoplasmic Microbeam Irradiated Normal Human Fibroblasts

Shanaz A. Ghandhi and Sally A. Amundson

We study the gene expression response of normal human fibroblast cells to α -particles. Previously we have focused our efforts on changes in gene expression at 30 minutes and 4 hours after α -particle irradiation and in bystander cells^{1,2}. This was achieved using the strip-dish format where cells are plated on two different thicknesses of Mylar and exposed to broad beam radiation using the track segment mode of RARAF. We were also interested in studying the gene expression response of microbeam-irradiated cells, after targeting the nucleus versus targeting only cytoplasm in cells. In our previous work done at 4 hr after irradiation, we found that genes predicted to be in TP53 and/or NF κ B networks responded in this time window. We reasoned that cells targeted in the nucleus and cytoplasm by microbeam radiation may

show a similar response at the 4 hr time point, and, we chose a previously confirmed 48-gene set to study after microbeam irradiation¹.

Cells were seeded on polypropylene dishes and irradiated as previously described³, at least 2 dishes were pooled (~1000 cells) and processed according to the Cells-to-Ct protocol (Ambion/Life technologies). An equivalent amount of RNA lysates from control, nuclear and cytoplasmic targeted samples were reverse transcribed to cDNA and loaded onto low density array cards (Applied Biosystems/Life Technologies). Gene expression levels were normalized to *ubiquitin C* and corresponding controls using the $2^{-\Delta\Delta C_t}$ method. A total of 4 biological replicates per condition were analyzed.

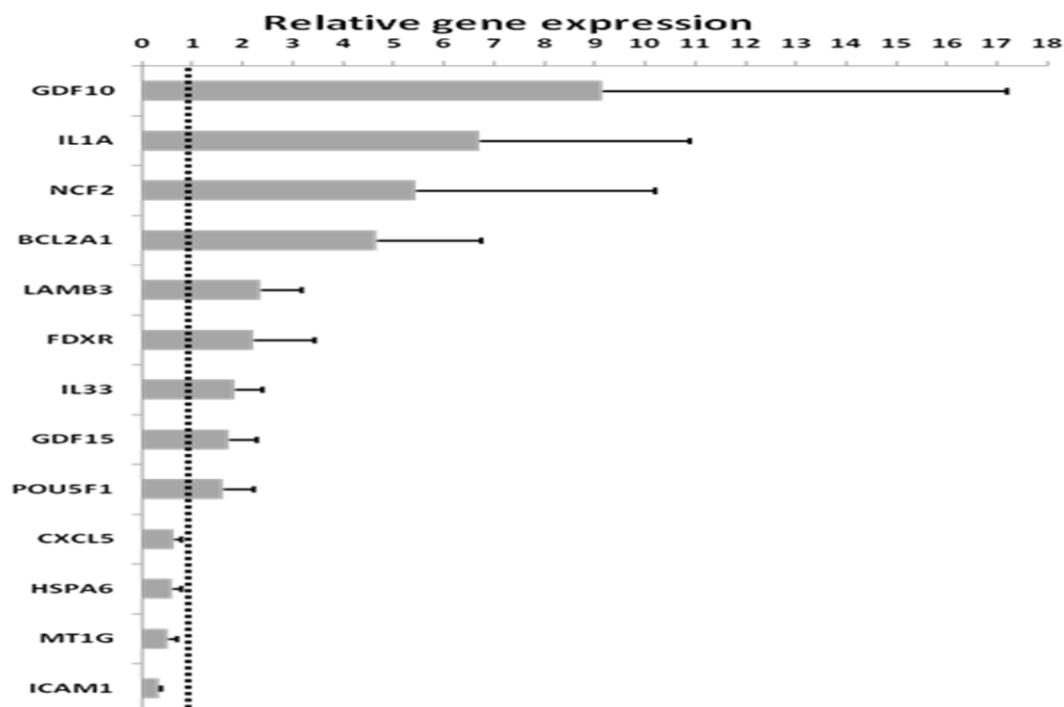


Figure 1. Nuclear-targeted microbeam-induced gene expression change.

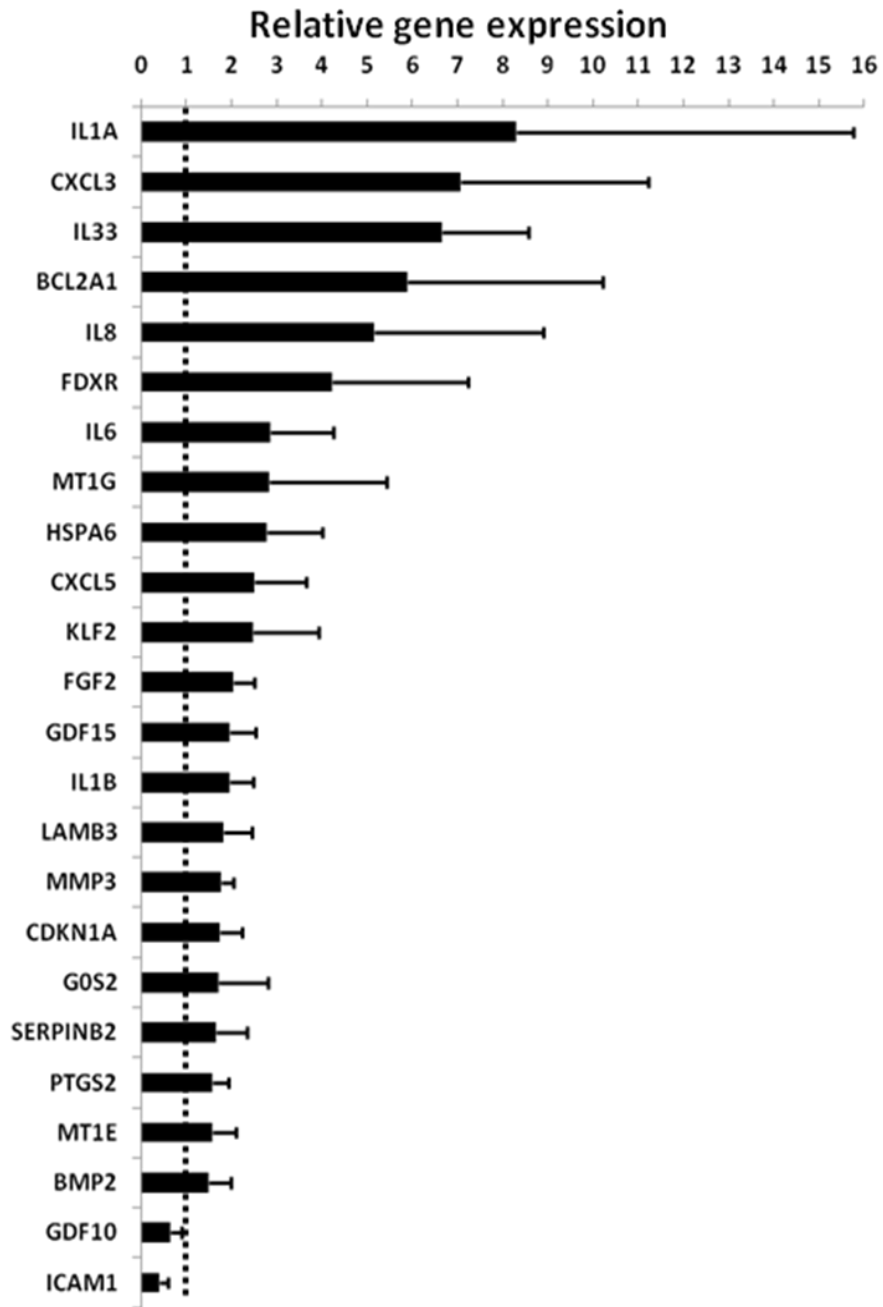


Figure 2. Cytoplasm-targeted microbeam-induced gene expression changes.

Nuclear- and cytoplasmic-targeted microbeam irradiation: gene expression response

We observed fewer genes responding (ratio cut-off ≥ 1.3 and ≤ 0.7), out of the 48-gene set, in cells whose nuclei were targeted (13 genes, Figure 1) than in cytoplasmic-targeted cells (24 genes, Figure 2). Although the genes were pre-selected to focus on genes in the TP53 and NF κ B signaling pathways that responded to broad beam irradiation at 4 hr after irradiation, they do not represent all possible genes in these pathways, so it is difficult to assess the preferential activation of either pathway based on these results. However, the results do indicate that cells that receive radiation only in the cytoplasm (Figure 2) do show significant responses related to cytokine and inflammatory signaling.

Comparing gene expression in nuclear- and cytoplasm-targeted cells, it was surprising that *CDKN1A* was not induced in cells whose nuclei were irradiated (mean fold change +1.2) and it may be possible that cytoplasmic irradiation triggers this gene more rapidly than when only nuclei of cells are hit. On the other hand, *FDXR* was induced in both conditions and is a known target of TP53 signaling. *IL1A* was also a top induced gene in both conditions but highly variable across experiments. Other cytokine/inflammatory pathway genes that were induced in cytoplasm-targeted cells were *IL1B*, *IL6*, *IL8*, *CXCL3*, *CXCL5*, *PTGS2* and *BCL2A1*, which

are all targets of NF κ B signaling. Interestingly, *ICAM1* was consistently down-regulated in both conditions.

This is the first report of the differential effect of targeted nuclear and cytoplasmic microbeam irradiation on gene expression in normal fibroblast cells. As expected, there were changes that were in common in the two types of treatment, but the surprising result was that targeting the cytoplasm using microbeam may be able to affect signaling and gene expression responses more than targeting of the smaller nucleus. It may be that the damage caused by the direct passage of several alpha particles through a nucleus actually retards the gene expression response. It remains to be seen if gene expression from targeted nuclear or cytoplasmic damage evolves in the same way as that responding to broad beam irradiation.

References

1. Ghandhi SA, Yaghoobian B, Amundson SA (2008) Global gene expression analyses of bystander and alpha particle irradiated normal human lung fibroblasts: Synchronous and differential responses. *BMC Medical Genomics*, **1**: 63.
2. Ghandhi SA, Ming L, Ivanov VN, Hei TK and Amundson SA (2010) Regulation of early signaling and gene expression in the alpha-particle and bystander response of IMR-90 human fibroblasts. *BMC Medical Genomics* **3**: 31. ■

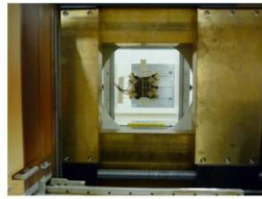
Heavy Ion Radiation-Induced Non-targeted Effects in Breast Tissues

Tony J.C. Wang, Yunfei Chai and Tom K. Hei

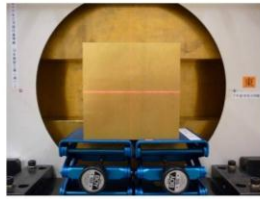
Ionizing radiation has been indispensable to medical diagnosis and cancer therapy. Over the last half-century, a central dogma in radiation biology has been that the effects of radiation occur only in directly irradiated cells and that nuclear DNA is the target for the biological action of radiation. Accordingly, it has long been presumed that no effect would be expected in cells that receive no radiation; however, this dogma has been challenged by the recent observation of radiation-induced non-targeted biological effects.¹⁻⁴ The recent resurgence of interest was stimulated from the findings of Nagasawa and Little who have demonstrated in 1992 that within monolayer cell cultures, a single alpha-particle traversal through <1% of the nuclei leads to the elevated frequency

of sister chromatid exchanges in more than 30% of cells.¹ Furthermore, it has been observed that COX-2, DNA double-stranded breaks, and oxidative stress appear to play a role in the non-targeted response.⁵⁻¹⁰ While most data reported on non-targeted effects have been obtained with in vitro culture systems, in vivo studies are now becoming available. Whole-body X-irradiation of radiosensitive *Ptch1*^{+/-} mice, with the head shielded, resulted in the induction of medulloblastoma, depicting the non-targeted effect. Most reports on radiation-induced non-targeted response utilize x-rays, yet there is little in vivo data on heavy ion radiation-induced non-targeted effects.

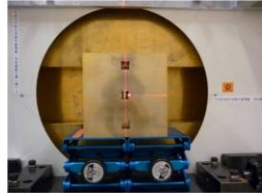
Heavy particles irradiation setup at HIMAC



Whole body irradiation (WBIR)



Full Shielding WBIR (Sham)



Partial body irradiation (PBIR)



Targeted area in PBIR

Figure 1. Experimental design at the NIRS. We exposed adult female transgenic *gpt delta* mice to carbon or argon particles under 4 conditions: Control, Sham-irradiated, WBIR, and PBIR.

Since 1994, over five thousand patients have been treated with heavy ion radiotherapy using the Heavy Ion Medical Accelerator in Chiba (HIMAC) at the National Institute of Radiological Sciences (NIRS) in Japan, primarily with carbon ions. Furthermore, there are several heavy-ion accelerator complexes in the world, and an increasing number of researchers are interested in using heavy-ion beams produced by NIRS for their research not only limited to carbon ions,¹² but also argon particles as well. Among several types of heavy ions, carbon ions were chosen for cancer therapy because they have superior physical and biological characteristics.^{13, 14} When the therapeutic effects of carbon ions are compared with those of X-rays, the carbon ions have an advantage of about three times the relative biological effectiveness (RBE) and an oxygen enhancement ratio (OER) of about half that of X-rays. In contrast to X-rays, carbon and argon ion beams can reduce damage to normal tissues by focusing the peak of the beam on the location of the tumor, as the beam becomes dramatically intense at a certain depth according to the energy applied but is weak before and after that depth. Clinical results have shown that carbon ion radiotherapy has the potential to provide a sufficient radiation dose to the tumor, while having acceptable morbidity in the surrounding normal tissues.¹⁵⁻¹⁹ By taking advantage of the unique properties of carbon ions, treatment with small fractions with higher doses within a short treatment period has been successfully carried out for a variety of tumors. This means that carbon ion radiotherapy can offer treatment for a larger number of patients than is possible with other modalities over the same time period. However, there is little information on heavy ion radiation-induced non-targeted effects and its potential benefits on tumor control outside

the radiation field as well as risks warrants further investigation. Therefore, continuing to investigate the consequences of heavy ion radiation-induced non-targeted response may lead to better understanding of both acute and late-side effects clinically.

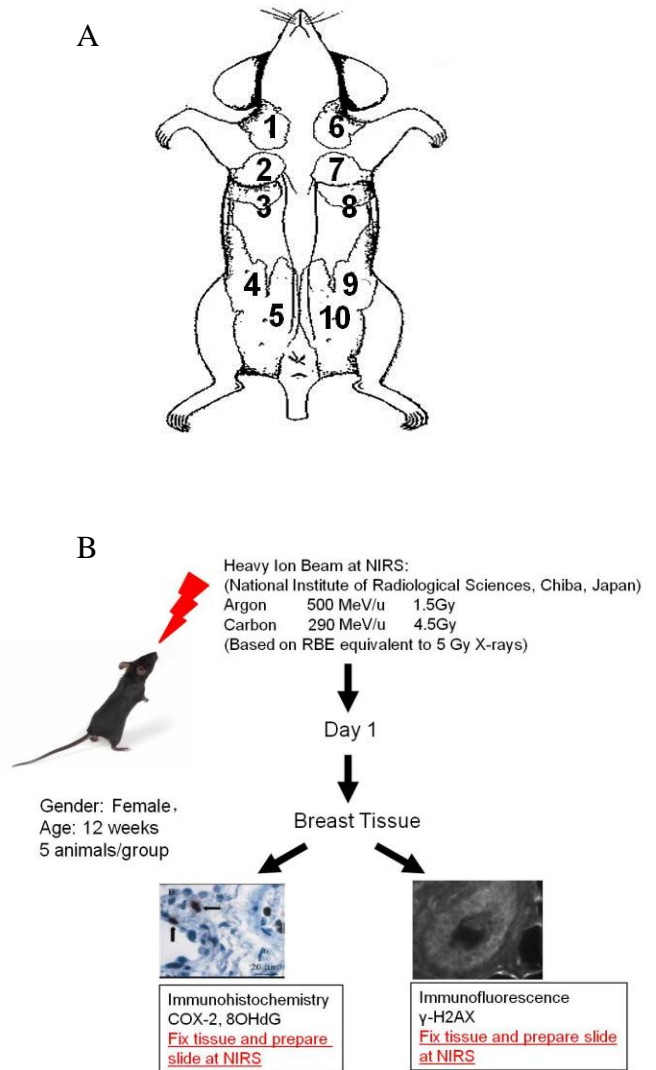


Figure 2. A) Mouse breast tissue anatomy, 5 pairs of breast tissue B) Adult female transgenic *gpt delta* mice are exposed to carbon or argon particles and sacrificed 24 hours post-radiation.

Experimental Design:

Using adult female transgenic *gpt* delta mice, we exposed the animals to an equitoxic dose of either carbon or argon particles using the HIMAC at the NIRS in Japan. The mice were stratified into 4 groups: non-treated control; animals irradiated under full shielding (Sham-irradiated); animals receiving whole body irradiation (WBIR); and animals receiving partial body irradiation (PBIR) to the lower abdomen with a 1 x 1 cm field. (Figure 1) Each group consisted of 5 animals. Dosimetric calculations performed showed similar background radiation levels between Sham-irradiated and PBIR. The doses used in the carbon ion (4.5 Gy) and in argon particle group (1.5 Gy) have a RBE equivalent to a 5 Gy dose of x-rays,(16-18) a dose which our laboratory has shown to be effective in the induction of non-targeted response in the *gpt* delta mouse model. 24 hours after radiation, the anterior 3 pairs of mouse breast tissue were harvested for analysis. (Figure 2) Using

immunohistochemistry (IHC) and immunofluorescence, we evaluated the expression of COX-2, 8-OHdG, γ -H2AX in mouse breast epithelial cells and examined relative levels.

COX-2, 8-OHdG, and γ -H2AX are induced in non-targeted breast tissues after heavy-ion partial body irradiation:

Expression of *COX-2* was examined in the four categories of breast tissues using IHC staining. In the carbon ion treatment groups, the relative fold increase (RFI) in *COX-2* expression was 1.01 in sham-irradiated group ($p > 0.05$), 3.07 in PBIR ($p < 0.05$) and 2.50 in WBIR ($p < 0.05$), respectively, when compared with controls. (Figure 3) In the argon ion treatment groups, the RFI in *COX-2* expression was 1.02 in sham-irradiated group ($p > 0.05$), 4.30 in PBIR ($p < 0.05$) and 2.97 in WBIR ($p < 0.05$), respectively, when compared with controls. The results are similar between both carbon and argon treated groups (data not shown).

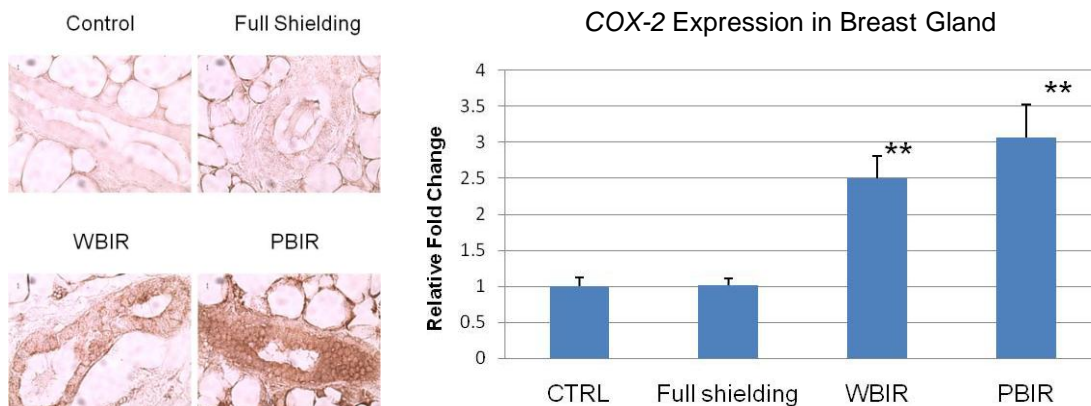


Figure 3. IHC staining for COX-2 in adult female transgenic *gpt* mice breast epithelial cells in the four categories treated with carbon ion radiation. These results are similar in the argon ion treated group.



Center for Radiological Research 2010 Picnic (L-r): Dr. Andrew Harken, Dr. Lubomir Smilenov, Dr. Erik Young, Dr. Guy Garty and Dr. Thomas Templin.

Expression of *8-OHdG* was examined in the four categories of breast tissues using immunohistochemical techniques. In the carbon ion treatment groups, the RFI in *8-OHdG* expression was 1.29 in sham-irradiated group ($p > 0.05$), 11.31 in PBIR ($p < 0.05$) and 11.79 in WBIR ($p < 0.05$), respectively, when compared with controls. (Figure 4) In the argon ion treatment groups, the RFI of *8-OHdG* expression as 1.30 in sham-irradiated group ($p > 0.05$), 3.85 in PBIR ($p < 0.05$) and 2.41 in WBIR ($p < 0.05$), respectively, when compared with controls. The results are similar between both carbon and argon treated groups (data not shown).

Expression of γ -H2AX (Cell Signaling Technology, Danvers, MA) was examined in the four categories of breast tissues using immunohistochemical techniques. Analysis was performed by comparing the foci number,

foci size, and foci intensity in different categories. In the carbon ion group, the RFI in γ -H2AX expression was 1.41 in sham-irradiated group ($p > 0.05$), 8.41 in PBIR ($p < 0.05$) and 10.59 in WBIR ($p < 0.05$), respectively, when compared with controls. (Figure 5) In the argon particle therapy group, the RFI of γ -H2AX expression was 0.80 in sham-irradiated group ($p > 0.05$), 1.75 in PBIR ($p < 0.05$) and 3.93 in WBIR ($p < 0.05$), respectively, when compared with controls. The data are consistent with the results using immunofluorescent staining in the carbon ion group, where the number of γ -H2AX foci per nucleus was 0.075 in the control group, 0.059 in the sham-irradiated group ($p > 0.05$), 0.224 in WBIR ($p < 0.05$), and 0.153 in PBIR ($p < 0.05$).

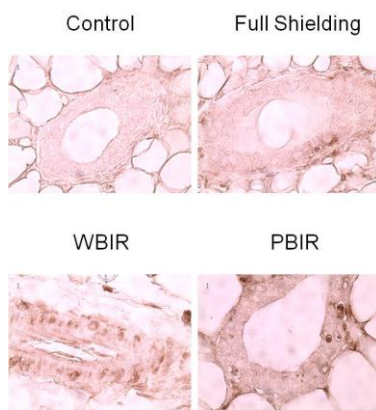


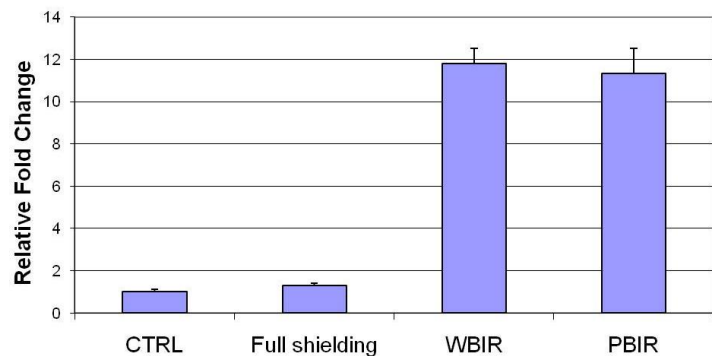
Figure 4. IHC staining for *8-OHdG* in adult female transgenic *gpt* mice breast epithelial cells in the four categories treated with carbon ion radiotherapy. These results are similar in the argon ion treated group.

In summary, our data show that heavy ions induce non-targeted induction of COX-2 and DNA damage in out-of-field breast tissues. These effects may pose new challenges to evaluate the risks associated with radiation exposure and understanding radiation-induced side effects.

References

1. Nagasawa, H., Little, J. B. Induction of sister chromatid exchanges by extremely low doses of alpha-particles. *Cancer Res.* 52:6394-6396, 1992.
2. Prise, K. M., O'Sullivan, J. M. Radiation-induced bystander signaling in cancer therapy. *Nat. Rev. Cancer* 9:351-360, 2009.
3. Mothersill, C., Seymour, C. B. Radiation-induced bystander effects – implications for cancer. *Nat. Rev. Cancer* 4:158-164, 2004.
4. Hamada, N. The bystander response to heavy-ion radiation: intercellular signaling between irradiated and non-irradiated cells. *Biol. Sci. Space* 23:195-202, 2009.

8-IGdG Expression in Breast Gland



5. Zhou, H., Ivanov, V. N., Gillespie, J., Geard, C. R., Amundson, S. A., Brenner, D. J., Yu, Z., Lieberman, H. B., Hei, T. K. Mechanism of radiation-induced bystander effect: role of the cyclooxygenase-2 signaling pathway. *Proc. Natl. Acad. Sci. USA* 102:14641-14646, 2005.
6. Hei, T. K., Zhou, H., Ivanov, V. N., Hong, M., Lieberman, H. B., Brenner, D. J., Amundson, S. A., Geard, C. R. Mechanism of radiation-induced bystander effects: a unifying model. *J. Pharm. Pharmacol.* 60:943-950, 2008.
7. Ermakov, A. V., Konkova, M. S., Kostyuk, S. V., Egolina, N. A., Efremova, L. V., Veiko, N. N. Oxidative stress as a significant factor for development of an adaptive response in irradiated and nonirradiated human lymphocytes after inducing the bystander effect by low-dose x-irradiation. *Mutat. Res.* 669:155-161, 2009.
8. Sokolov, M. V., Dickey, J. S., Bonner, W. M., Sedelnikova, O. A. gamma-H2AX in bystander cells: not just a radiation-triggered event, a cellular response to stress mediated by intracellular communication. *Cell Cycle* 6:2210-2212, 2007.

BYSTANDER STUDIES

9. Kashino, G., Kondoh, T., Nariyama, N., Umetani, K., Ohigashi, T., Shinohara, K., Kurihara, A., Fukumoto, M., Tanaka, H., Maruhashi, A., Suzuki, M., Kinashi, Y., Liu, Y., Masunaga, S., Watanabe, N., Ono, K. Induction of DNA double-strand breaks and cellular migration of bystander effects in cells irradiated with the slit-type microplanar beam of the spring-8 synchrotron. *Int. J. Radiat. Oncol. Biol. Phys.* 74:229-236, 2009.
10. Sedelnikova, O. A., Nakamura, A., Kovalchuk, O., Koturbash, I., Mitchell, S. A., Marino, S. A., Brenner, D. J., Bonner, W. M. DNA double-strand breaks form in bystander cells after microbeam irradiation of three-dimensional human tissue models. *Cancer Res.* 67:4295-4302, 2007.
11. Mancuso, M., Pasquali, E., Leonardi, S., Tanori, M., Rebessi, S., Di Majo, V., Pazzaglia, S., Toni, M. P., Pimpinella, M., Covelli, V., Saran, A. Oncogenic bystander radiation effects in Patched heterozygous mouse cerebellum. *Proc. Natl. Acad. Sci. USA* 105:12445-12450, 2008.
12. Okada, T., Kamada, T., Tsuji, H., Mizoe, J. E., Baba, M., Kato, S., Yamada, S., Sugahara, S., Yasuda, S., Yamamoto, N., Imai, R., Hasegawa, A., Imada, H., Kiyohara, H., Jingu, K., Shinoto, M., Tsujii, H. Carbon ion radiotherapy: clinical experiences at National Institute of Radiological Sciences (NIRS). *J. Radiat. Res.* 51:355-364, 2010.
13. Minohara, S., Fukuda, S., Kanematsu, N., Takei, Y., Furukawa, T., Inaniwa, T., Matsufuji, N., Mori, S., Noda, K. Recent innovations in carbon-ion radiotherapy. *J. Radiat. Res.* 51:385-392, 2010.
14. Hamada, N., Imaoka, T., Masunaga, S., Ogata, T., Okayasu, R., Takahashi, A., Kato, T. A., Kobayashi, Y., Ohnishi, T., Ono, K., Shimada, Y., Teshima, T. Recent advanced in the biology of heavy-ion cancer therapy. *J. Radiat. Res.* 51:361-383, 2010.
15. Mizoe, J. E., Tsujii, H., Kamada, T., Matsuoka, Y., Tsuji, H., Osaka, Y., Hasegawa, A., Yamamoto, N., Ebihara, S., Konno, A. Dose escalation study of carbon ion radiotherapy for locally advanced head-and-neck cancer. *Int. J. Radiat. Oncol. Biol. Phys.* 50:358-364, 2004.
16. Hasegawa, A., Mizoe, J. E., Mizota, A., Tsujii, H. Outcomes of visual acuity in carbon ion radiotherapy: analysis of dose-volume histograms and prognostic factors. *Int. J. Radiat. Oncol. Biol. Phys.* 64:396-401, 2006.
17. Kamada, T., Tsujii, H., Tsuji, H., Yanagi, T., Mizoe, J. E., Miyamoto, T., Kato, H., Yamada, S., Morita, S., Yoshikawa, K., Kandatsu, S., Tateishi, A. Efficacy and safety of carbon ion radiotherapy in bone and soft tissue sarcoma. *J. Clin. Oncol.* 20:4466-4471, 2002.
18. Imai, R., Kamada, T., Tsuji, J., Yanagi, T., Baba, M., Miyamoto, T., Kato, S., Kandatsu, S., Mizoe, J. E., Tsujii, H., Tazaki, S. Carbon ion radiotherapy for unresectable sacral chordomas. *Clin. Cancer Res.* 10:5741-5746, 2004.
19. Imai, R., Kamada, T., Tsuji, H., Tsujii, H., Tsuburai, Y., Tazaki, S. Cervical spine osteosarcoma treated with carbon ion radiotherapy. *Lancet Oncol.* 7:1034-1035, 2006.
20. Camphausen, K., Moses, M. A., Menard, C., Sproull, M., Beecken, W. D., Folkman, J., O'Reilly, M. S. Radiation abscopal antitumor effect is mediated through p53. *Cancer Res.* 63:1990-1993, 2003. ■



Center for Radiological Research 2010 Christmas Party (L-r): Mrs. Cui Xia Kuan, Ms. Yvette Acevedo, Dr. Shanaz Ghandhi and Dr. Tom Hei.

Rad9 Contributes to Prostate Cancer Cell Growth and Metastasis

Constantinos G. Broustas and Howard B. Lieberman

Introduction

Rad9 is a protein with an established role in DNA damage response and repair. As part of the Rad9-Hus1-Rad1 complex it acts as a sensor of DNA damage that recruits ATR kinase to the site of damage¹. In recent years, however, Rad9 has been implicated in pathways not directly related to the DNA damage/repair response. Moreover, it has been shown that Rad9 can act independently of its partners Hus1 and Rad1 to transactivate a number of genes including p21^{waf1/cip1} and mitogen activated protein kinase kinase 5 (MEK5)².

Previous reports showed that Rad9 is over-expressed in human prostate cancer specimens as well as prostate cancer cell lines³. Experiments designed to assess the

contribution of Rad9 in prostate tumor growth revealed that down-regulation of Rad9 in PC3 and DU145 xenografts injected in mice impaired their growth. Furthermore, immunohistochemical analysis showed that Rad9 expression increased along with cancer progression stages, suggesting a role of Rad9 in prostate malignant progression³.

The objective of this study was two-fold: (a) to assess the effect of Rad9 down-regulation on prostate cancer cell proliferation and survival, and (b) to investigate the impact of Rad9 down-regulation on three cell biological traits that are related to metastasis, namely migration, invasion, and anoikis sensitivity.

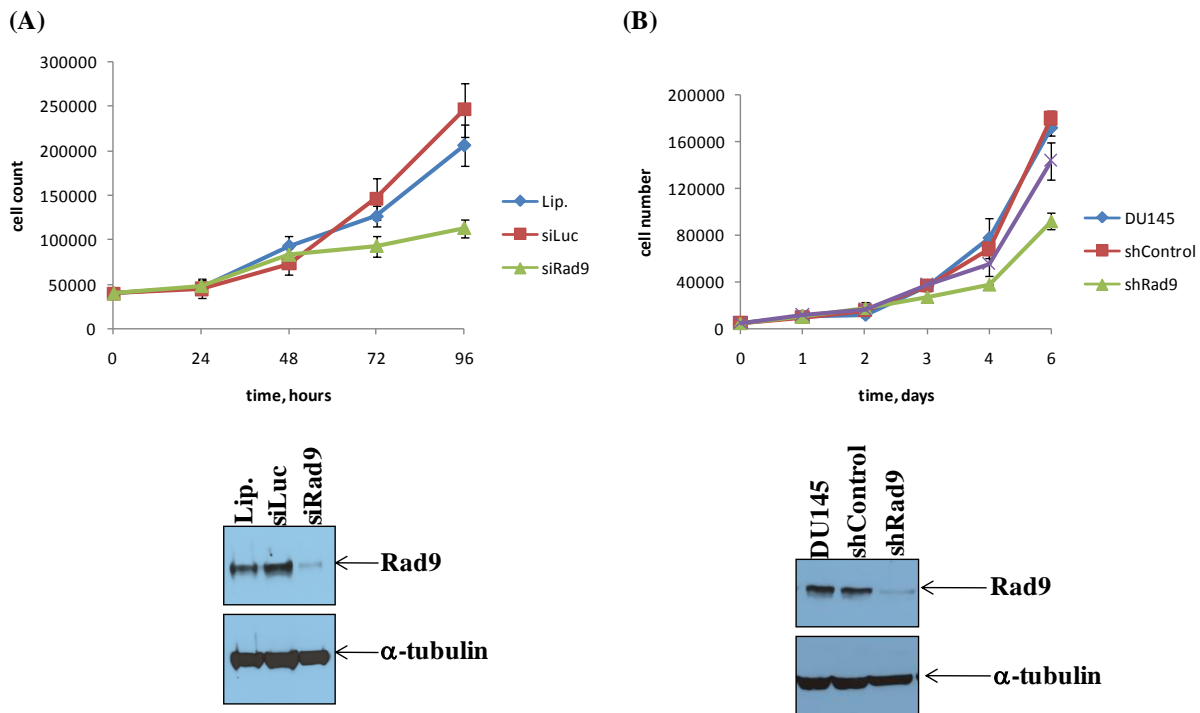


Figure 1. Cell proliferation assay. (A) upper panel, cell proliferation of DU145 cells transiently transfected with Lipofectamine only (Lip.), siControl (luciferase; siLuc), or Rad9 siRNA (siRad9) was analyzed by cell counting with a hemocytometer at the indicated time intervals after plating equal number of cells. Data are mean \pm SD of a representative experiment out of three independent experiments performed in duplicate. Lower panel, western blot analyses of Rad9 expression levels were assessed by immunoblotting with anti-Rad9 monoclonal antibodies or anti- α -tubulin monoclonal antibodies (loading control). (B) upper panel, cell proliferation of parental DU145 cells or cells stably expressing shRad9 or shControl (pSUPER-retro insertless vector) was analyzed by cell counting with a hemocytometer at the indicated time intervals after plating as equal number of cells. Data are mean \pm SD of a representative experiment out of two independent experiments performed in duplicate. Lower panel, western blot analyses of Rad9 expression levels were assessed by immunoblotting with anti-Rad9 monoclonal antibodies or anti- α -tubulin monoclonal antibodies (loading control).

Down-regulation of Rad9 decreases cell proliferation

To investigate the role of Rad9 in DU145 prostate cancer cell proliferation, we transiently silenced Rad9 by short interfering RNA (siRad9) or control siRNA (luciferase; siLuc) and examined the impact on cell proliferation over a period of 4d. Transfection with siRad9 resulted in more than 90% down-regulation in Rad9 protein expression compared with lipofectamine-only or siLuc transfected cells (Fig. 1A, lower panel). Cell proliferation was reduced in siRad9 expressing cells compared with control cells (Fig. 1A, upper panel). The reduction in cell proliferation in siRad9 expressing cells became apparent after 3d in culture and it was approximately 2.5-fold lower compared with the siLuc expressing cells by the end of the experiment at day 4. Similar results were obtained with another prostate cancer cell line, PC3 (data not shown). Likewise, we measured cell proliferation on DU145 cells stably transfected with short hairpin RNA against Rad9, insertless vector (pSUPER-retro-puro vector), or parental cells. Cells stably expressing shRad9 had reduced Rad9 protein expression by approximately 75% compared with Rad9

protein levels in either parental or shControl cells (Fig. 1B, lower panel). After 6d in culture, DU145/shRad9 cell number was approximately 3-fold lower than the DU145/shVector or DU145/parental cells (Fig. 1B, upper panel). Thus the *in vitro* cell proliferation assay recapitulated the *in vivo* results using the same cell lines. Cell proliferation results were also verified by colony formation for both PC3 and DU145 cells (not shown).

Rad9 knock-down reduces cell survival

To account for the reduced cell proliferation of DU145 cells with reduced Rad9 expression we examined cell viability by terminal deoxynucleotidyl transferase dUTP nick end labeling (TUNEL) assay (Fig. 2A). We found that transient down-regulation of Rad9 in DU145 cells (Fig. 2A, right panel) increased apoptosis from 5% in control (transfected with siLuc) cells expressing normal levels Rad9 to 35% in the siRad9 cells 4 days post-transfection (Fig. 2B). On the other hand, no difference in cell death was observed in the stable clones as measured by trypan blue exclusion assay (not shown).

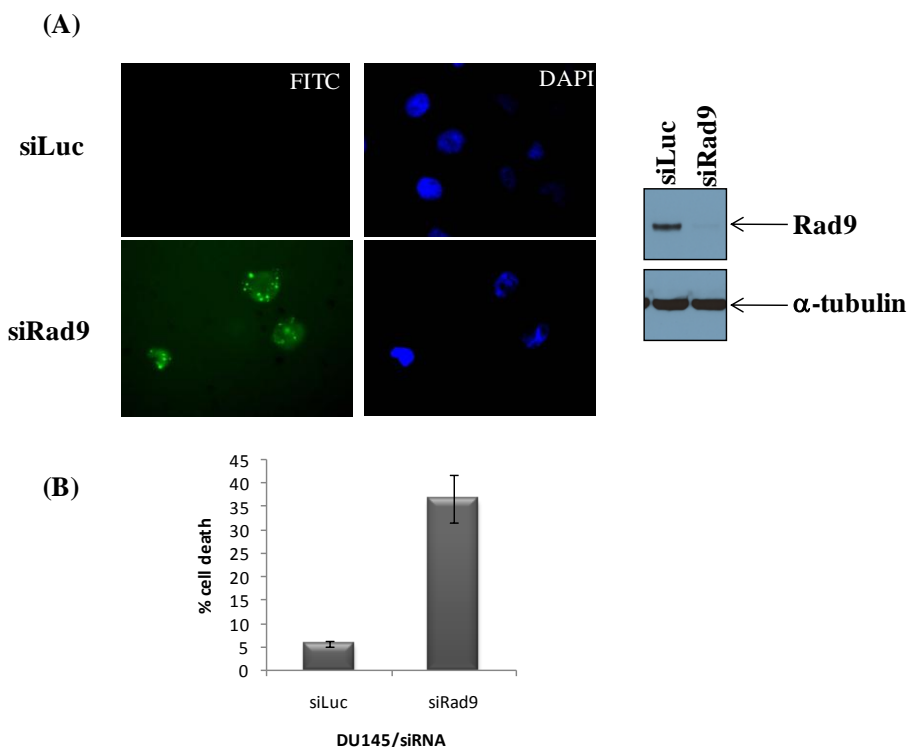


Figure 2. Apoptosis of DU145 cells transiently transfected with either siRad9 or siLuciferase was measured 3d post-transfection by TUNEL assay using the In Situ Cell Death Detection kit from Roche according to the manufacturer's instruction. (A) Shown are representative images of TUNEL-positive nuclei (green) counterstained with DAPI (blue). Right panel, expression of Rad9 in DU145 cells transfected with siLuc or siRad9 and analyzed by immunoblotting with anti-Rad9 monoclonal antibodies or anti- α -tubulin antibodies (loading control). (B) TUNEL positivity was quantified as percentage of TUNEL-positive nuclei divided by the total number of nuclei scored. The data represent the mean \pm SD from 3 independent experiments.

Suppression of migration, invasion and anoikis is mediated by Rad9 silencing

We showed previously that Rad9 expression levels may correlate with metastatic progression in prostate cancer. We thus examined the impact of Rad9 down-regulation on DU145 cell migration, invasion, and resistance to anoikis. These assays were conducted within 48h, when cell proliferation is similar in siRad9 and control cells. Consistent with a role in metastasis, when Rad9 was either transiently or stably down-regulated, DU145 cells showed impaired capacity to migrate or invade through matrigel. In these experiments, cells were added to the upper chamber of Boyden devices that were either un-coated (migration) or coated (invasion) with

matrigel and the lower chamber was filled with 10% fetal bovine serum that served as chemoattractant. A well filled with bovine serum albumin served as negative control (no chemoattractant). Quantitation showed that a 3-fold less migration and 5-fold less invasion was observed in the cells with diminished levels of Rad9 compared with cells (control or parental) expressing normal levels of Rad9. In agreement with the transient transfection results, migration was diminished by 2-fold in DU145/shRad9 cells compared with both controls DU145/parental and DU145/shVector (Fig. 3A, right panel). We thus conclude that Rad9 mediates tumor cell migration and invasion in vitro.

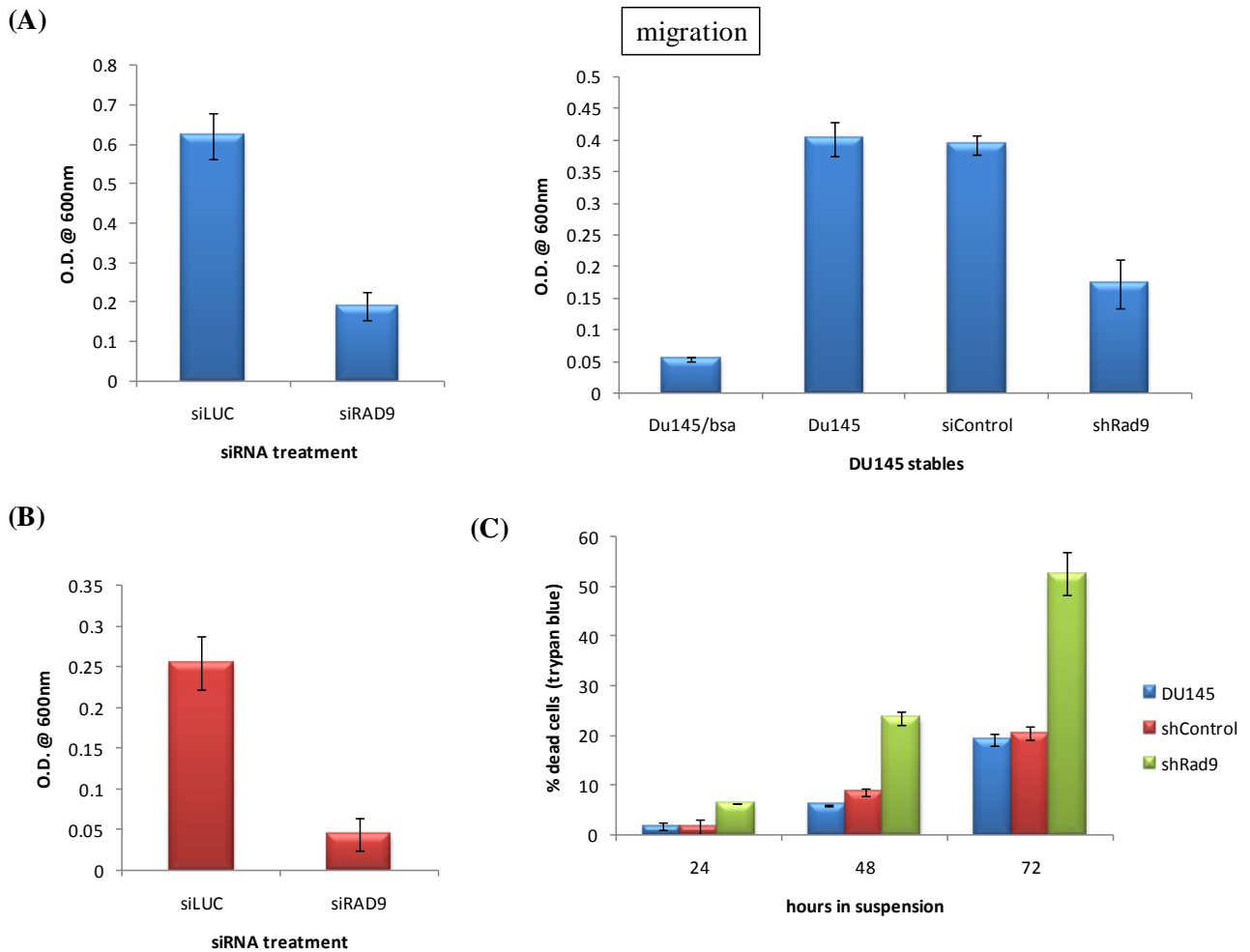


Figure 3. Rad9 regulation of DU145 cell migration and invasion. Cell migration (A) and invasion (B) assays were performed using 24-well Transwell inserts that were either un-coated (migration) or coated with matrigel (invasion). The lower chamber was filled with 10% fetal bovine serum that served as chemoattractant or 0.1% bovine serum albumin as negative control (DU145/bsa). After 16-22h (migration) or 48h (invasion) non-migrating cells were removed from the upper chamber and the cells that had migrated were fixed, stained with crystal violet, the stain was extracted in acetic acid and color was measured with a spectrophotometer at O.D. 600 nm. Data are mean \pm SD of a representative experiment out of three independent experiments performed in duplicate. (C) Anoikis assay. Equal numbers of cells were added to low cell attachment petri dishes and incubated for the indicated time. Cells were collected by centrifugation and viability was assayed by trypan blue exclusion. Data represent mean \pm SD from one experiment performed in duplicate.

Resistance to anoikis, that is induction of programmed cell death upon cell matrix detachment, is considered one of the *in vitro* markers of metastasis⁴. Anoikis resistance is a prerequisite for tumor cells to remain viable when they lose attachment to the extracellular matrix and it contributes to metastasis⁴. We thus cultured DU145 stable clones on suspension petri dishes to assess detachment-induced apoptosis (anoikis). In the absence of cell-matrix interaction, shRad9-expressing DU145 cells underwent anoikis, resulting in more than 50% dead cells after 3d of culturing as assessed by trypan blue exclusion assay compared with approximately 20% cell death in parental DU145 cells or DU145/shVector cells 72h in suspension (Fig. 3C). These findings point to a role of Rad9 in the protection of cancer cells from anoikis.

Conclusions

In this study we have presented data that Rad9 promotes prostate tumor cell growth and invasiveness. We base our conclusion on two findings: (a) Rad9 knock-down results in decreased cell proliferation and increased apoptosis and (b) Rad9 down-regulation impairs *in vitro* migration and invasion of DU145 cells and renders cells

more sensitive to anoikis. We are currently investigating the mechanistic details of the observed phenotype and trying to elucidate the pathway by which Rad9 may induce metastasis *in vivo*.

References

1. Lieberman HB, Bernstock JD, Broustas CG, Hopkins KM, Leloup C, Zhu A. (2011) The role of RAD9 in tumorigenesis. *J Mol Cell Biol.* **3**(1):39-43.
2. Yin Y, Zhu A, Jin YJ, Liu YX, Zhang X, Hopkins KM, Lieberman HB. (2004) Human RAD9 checkpoint control/proapoptotic protein can activate transcription of p21. *Proc Natl Acad Sci U S A.* **101**(24):8864-9
3. Zhu A, Zhang CX, Lieberman HB. (2008) Rad9 has a functional role in human prostate carcinogenesis. *Cancer Res.* **68**(5):1267-74.
4. Sakamoto S, Kyprianou N. (2010) Targeting anoikis resistance in prostate cancer metastasis. *Mol Aspects Med.* **31**(2):205-14. ■

***Mrad9*^{-/-} But Not *Mrad9b*^{-/-} Mouse Embryonic Stem Cells Are Sensitive To PARP-1 Inhibition Relative to Wild Type Controls**

Corinne Leloup, Adayabalam Balajee, Kevin M. Hopkins and Howard B. Lieberman

Background

RAD9 is a radiation resistance gene¹ and has multiple functions, including participation in DNA repair. RAD9 protein is recruited early in the DNA repair response to stalled replication forks as well as to DNA double strand breaks, where it plays a crucial role in delaying cell cycle progression². *RAD9* is also directly involved in various DNA repair mechanisms. The protein binds to several base excision repair proteins², to a homologous recombination repair protein³, and one involved in mismatch repair⁴, and influences the respective repair mechanisms.

Mrad9b, a *Mrad9* paralog⁵, confers resistance to ionizing radiation, ultraviolet light and mitomycin C in mouse embryonic stem (ES) cells⁶. It is not known yet by which mechanism *Mrad9b* exerts its protective effect, but the G2/M cell cycle checkpoint activated after ionizing

radiation exposure is normal in *Mrad9b*^{-/-} ES cells⁶. Therefore, we are investigating whether *Mrad9b* mediates resistance through activity in DNA repair.

Poly(ADP-ribose) polymerase-1 (*PARP-1*) is important for the repair of DNA single strand breaks (SSBs), base damage as well as double strand breaks (DSBs). It controls the recruitment and interaction of repair proteins by adding variably sized ADP-ribose polymers to them⁷. Earlier studies have shown that murine and human cells deficient in the homologous recombination repair (HRR) pathway are sensitive to PARP-1 inhibition^{8,9}. If *Mrad9*^{-/-} or *Mrad9b*^{-/-} cells are deficient in HRR, blocking PARP-1 activity in those cells is expected to render them more susceptible to DNA damage relative to wild type (WT) control cells.

Results

PARP-1 inhibition enhances sensitivity to ionizing radiation to the same extent in WT and *Mrad9*^{-/-} or *Mrad9b*^{-/-} mutant ES cells

Mrad9 and *Mrad9b* knock out mouse ES cells, previously produced in our laboratory^{10,6}, were used for these experiments. Both *Mrad9*^{-/-} and *Mrad9b*^{-/-} ES cells display increased sensitivity to ionizing radiation compared to WT ES cells (Fig. 1A), as expected^{10,6}. Blocking PARP-1 using PJ34 as an inhibitor hypersensitizes wild type as well as mutant ES cells to ionizing radiation, indicating that *PARP-1* is involved in the repair of damage caused by radiation in all the cells. The damage involves mainly single strand breaks, double

strand breaks and alterations in bases¹¹. This result in the WT cells is expected because *PARP-1* is involved in repair of all three types of damage⁶. However, the PARP-1 inhibitor radiosensitizing effect - as measured by IC₉₀ in the absence of PARP-1 inhibitor/IC₉₀ in the presence of PARP-1 inhibitor - is very similar for all three cell lines: 1.3 for WT and *Mrad9b*^{-/-} ES cells, and 1.0 for *Mrad9*^{-/-} ES cells, indicating that PARP inhibition does not lead to differentially enhanced radiosensitivity in either one of the mutant cell lines compared to the WT cells. These findings demonstrate that the functional loss of *Mrad9* and *Mrad9b* does not drastically alter the radiation sensitivity after PARP-1 inhibition.

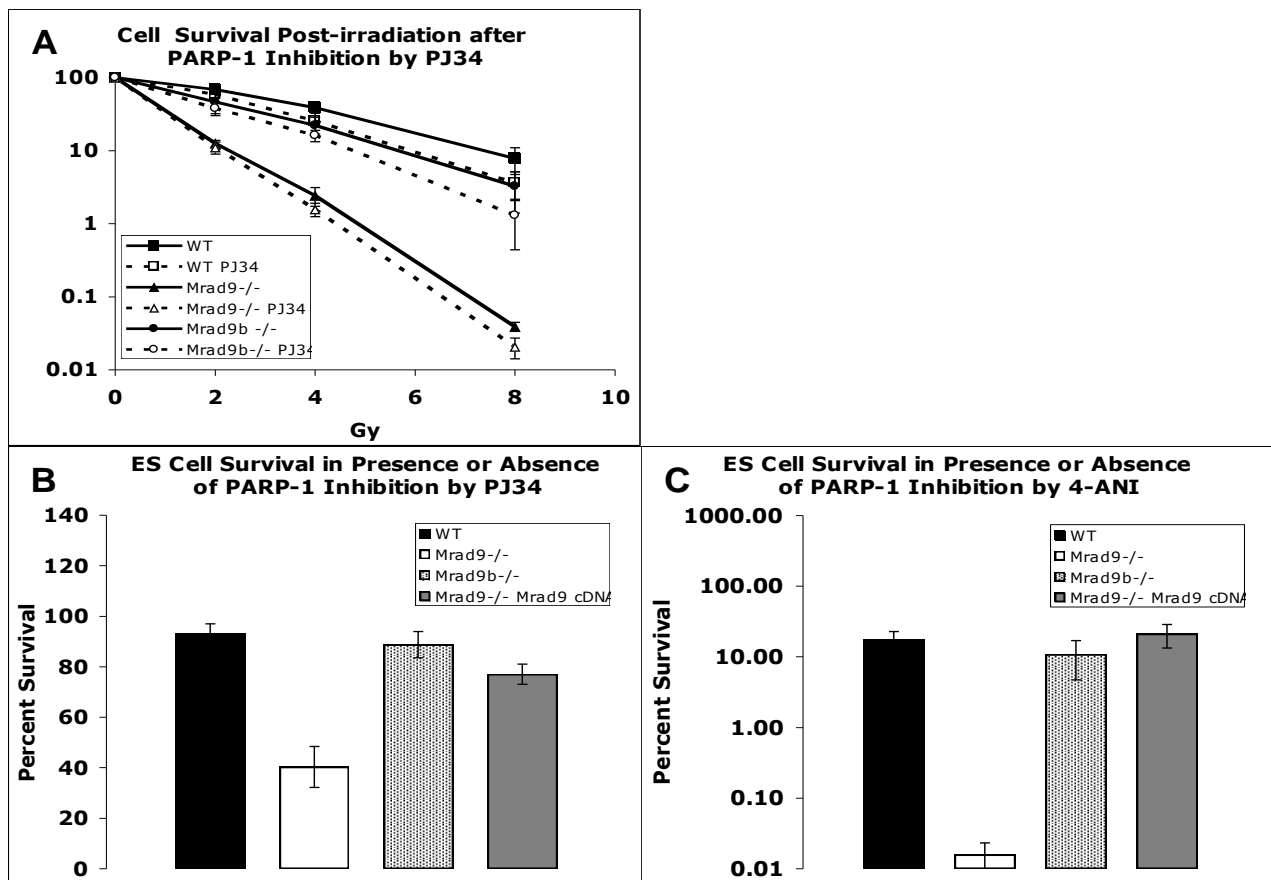


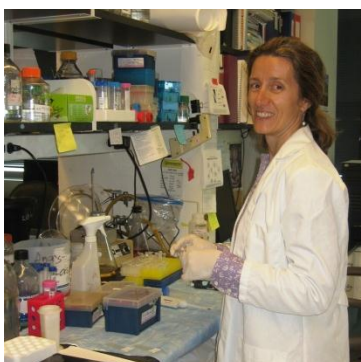
Figure 1. (A) Mouse ES cell survival after ionizing radiation exposure in the presence or absence of PARP-1 inhibition, as measured by a clonal survival assay. Mouse ES cells, wild type and mutant, were treated or not with 5 μ M PJ34 for one hour, and then irradiated or mock-irradiated with ¹³⁷Cs at a dose rate of 0.87 Gy/min. Medium was replaced in all dishes and 5 μ M of fresh PJ34 was added again when appropriate. Percent survival was calculated as 100 x (number of colonies in irradiated dishes/number of colonies in mock-irradiated control dishes). Data represent the average of at least four experiments. Error bars indicate standard deviation. **(B, C) Mouse ES cell survival in the presence or absence of PARP-1 inhibition, as measured by a clonal survival assay.** Mouse ES cells, wild type and mutant, were cultured in the presence or absence of 5 μ M PARP-1 inhibitor, PJ34 (B) or 4-ANI (C), for the duration of the experiment. Data are presented as 100 x (number of colonies with inhibitor/number of colonies without inhibitor), and represent the average of at least two experiments \pm standard deviation). * $p < 0.01$ compared to WT ES cells.

***Mrad9^{-/-}* but not *Mrad9b^{-/-}* mouse embryonic stem cells are sensitive to PARP-1 inhibition relative to wild type control cells**

In the absence of DNA damage induced by exogenous agents, *Mrad9^{-/-}* ES cells are more sensitive to PARP-1 inhibition than WT cells (Fig. 1B, C). Our results are consistent with previous reports demonstrating the sensitivity of HR defective cells to PARP-1 inhibition^{8,9}. On the basis of our finding we speculate that *Mrad9^{-/-}* cells may have an inherent deficiency in the HRR pathway for the repair of spontaneous DNA damage. Interestingly, we observed that the resistance was restored to WT levels by ectopic expression of *Mrad9⁺* in *Mrad9^{-/-}* ES cells. Our findings suggest that both *Mrad9* and *PARP-1* are essential for repair of spontaneous DNA damage. Therefore, inhibition of PARP-1-related activities in *Mrad9* knockout cells renders them very sensitive to spontaneous DNA damage. This assumption is further strengthened by the fact that *Mrad9b^{-/-}* cells do not display these characteristics, and are not genomically unstable⁶, indicate the importance of *Mrad9* in the protection of genomic integrity from spontaneous DNA damage.

References

1. Lieberman HB, Hopkins KM, Laverty M, Chu HM. 1992. Molecular cloning and analysis of *Schizosaccharomyces pombe rad9*, a gene involved in DNA repair and mutagenesis. *Mol Gen Genet* 232:367-376.
2. Lieberman HB. 2006. Rad9, an evolutionarily conserved gene with multiple functions for preserving genomic integrity. *J Cell Biochem* 97:690-697.
3. Pandita RK, Sharma GG, Laszlo A, Hopkins KM, Davey S, Chakhparonian M, Gupta A, Wellinger RJ, Zhang J, Powell SN, Roti Roti JL, Lieberman HB, Pandita TK. 2006. Mammalian Rad9 plays a role in telomere stability, S- and G2-phase specific cell survival, and homologous recombinational repair. *Mol Cell Biol* 26:1850-1864.
4. He W, Zhao Y, Zhang C, An L, Hu Z, Liu Y, Han L, Bi L, Xie Z, Xue P, Yang F, Hang H. 2008. Rad9 plays an important role in DNA mismatch repair through physical interaction with MLH1. *Nucleic Acids Res* 36: p. 6406-6417.
5. Hopkins KM, Wang X, Berlin A, Hang H, Thaker HM, Lieberman HB. 2003. Expression of mammalian paralogues of HRAD9 and Mrad9 checkpoint control genes in normal and cancerous testicular tissue. *Cancer Res* 63:5291-5298.
6. Leloup C, Hopkins KM, Wang X, Zhu A, Wolgemuth DJ, Lieberman HB. 2010. Mouse Rad9b is essential for embryonic development and promotes resistance to DNA damage. *Dev Dyn* 239:2837-2850.
7. Vidakovic M, Poznanovic G, Bode J. 2005. DNA break repair: refined rules of an already complicated game. *Biochem Cell Biol* 83:365-373.
8. Farmer, H, et al. 2005. Targeting the DNA repair defect in BRCA mutant cells as a therapeutic strategy. *Nature* 434: p. 917-921.
9. Mendes-Pereira AM, et al. 2009. Synthetic lethal targeting of PTEN mutant cells with PARP inhibitors. *EMBO Mol Med* 1:p. 315-322.
10. Hopkins KM, Auerbach W, Wang XY, Hande MP, Hang H, Wolgemuth DJ, Joyner AL, Lieberman HB. 2004. Deletion of mouse rad9 causes abnormal cellular responses to DNA damage, genomic instability, and embryonic lethality. *Mol Cell Biol* 24:7235-7248. ■



Members of Dr. Lieberman's Laboratory (L-r): Dr. Constantinos Broustas, Associate Research Scientist; Dr. Ana Vasileva, Associate Research Scientist and Mr. Kevin Hopkins, Senior Staff Associate.

DNMT3B Knockdown in Prostate Cancer Cells Reduces Tumor Formation in Nude Mice

Corinne Leloup, Aiping Zhu, Xiangyuan Wang^a and Howard B. Lieberman

Background

HRAD9 is overexpressed in human prostate tumor samples and cell lines. There is a strong correlation between *HRAD9* protein abundance and cancer stage. Furthermore, reducing *HRAD9* levels in DU145 and PC-3 prostate cancer cell lines using small interfering RNAs (shRNAs) correlates with reduced tumorigenicity in nude mice. In DU145, a prostate cancer cell line, there is

hypermethylation of CpG islands in a transcription suppresser site located in the second intron of *HRAD9*. Demethylation at this site using 5'-aza-2' deoxycytidine restores near-normal levels of methylation and reduces *HRAD9* protein levels, indicating that hypermethylation is the probable cause for increased *HRAD9* expression¹ in these cells.

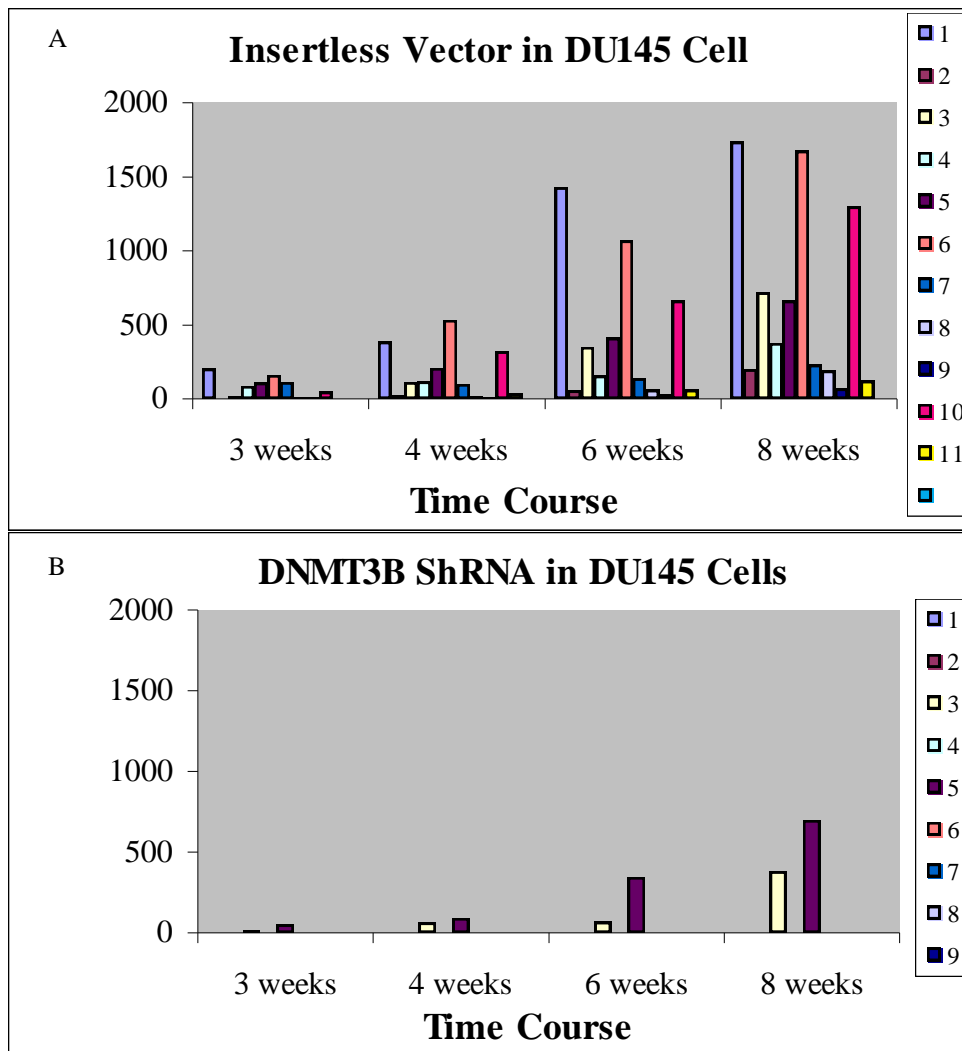


Figure 1. Tumor volume in nude mice after injection of DU145 prostate cancer cells infected with an insertless vector (A) or *DNMT3B* shRNA construct (B). Four sites were injected per mouse. Tumor volume was measured at various times after injection. Colored numbered squares correspond to different injection sites.

DNA methylation in mammalian cells is catalyzed by a family of DNA methyltransferases (*DNMTs*). Methylation is abnormal in cancer cell lines and tissues, and so far, the main players seem to be *DNMT1* and *DNMT3*². Zhu has shown that *DNMT1* knockdown in DU145 prostate cancer cells reduces *HRAD9* expression

and tumor formation in nude mice³. In this report, we show that *DNMT3B* knockdown in the same prostate cancer cells reduces tumor formation in nude mice as well. This is probably mediated via reduced methylation in *HRAD9* second intron and reduction in *HRAD9* expression.

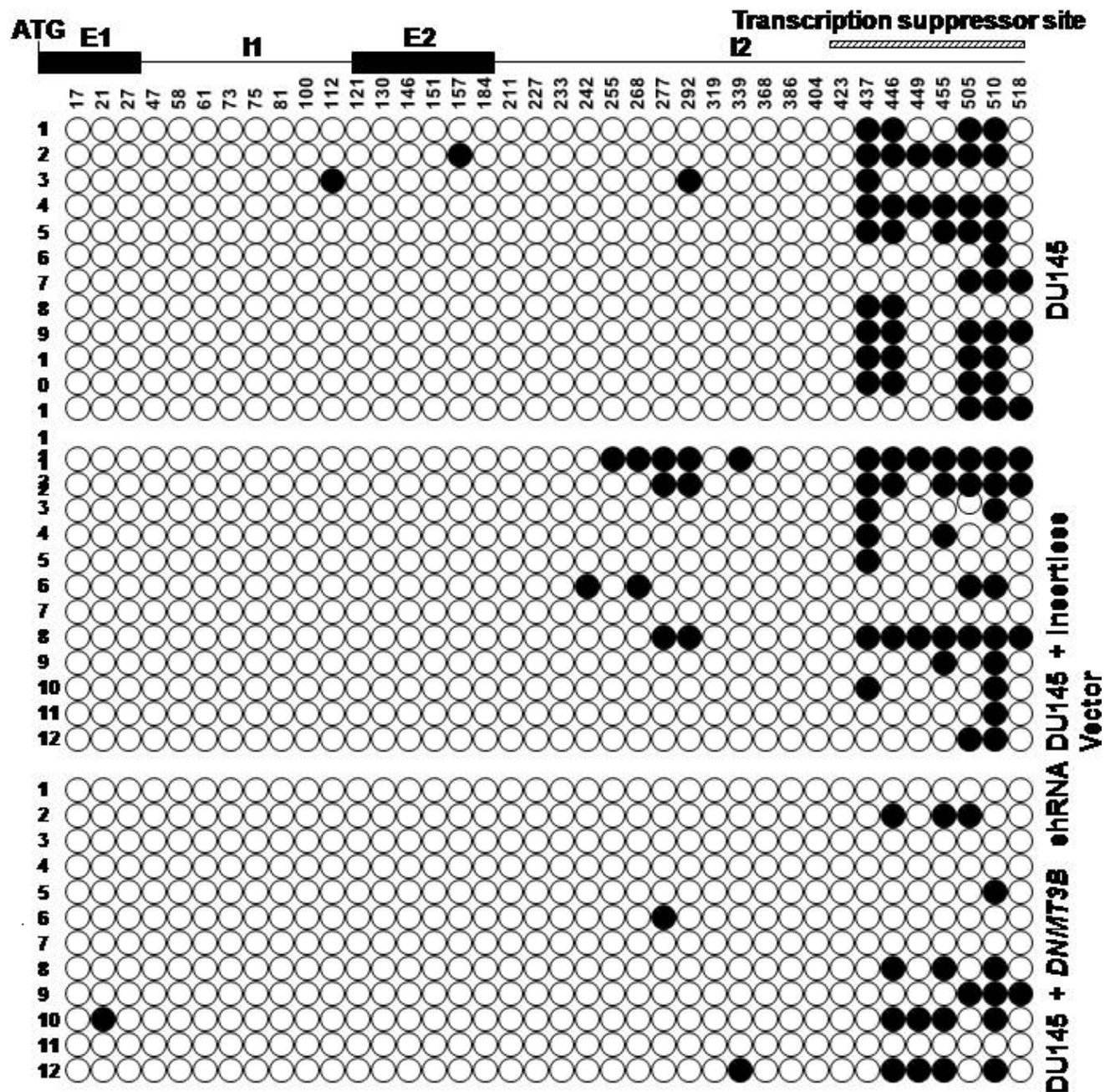


Figure 2. Methylation pattern in *HRAD9* CpG islands. Methylation was assed as described in Zhu et al.³. Filled circles correspond to methylated CpG islands. Open circles correspond to unmethylated CpG islands. ATG indicates the site for initiation of translation. E1, E2 correspond to exon1, exon 2. H, I2 correspond to intron 1, intron 2.

⁴Department of Genetics and Development,
College of Physicians and Surgeons,
Columbia University

Results

***DNMT3B* knockdown in prostate cancer cells reduces tumor formation in nude mice**

DU145, a prostate cancer cell line, was stably infected either with an insertless viral vector or with a *DNMT3B* shRNA construct in order to downregulate *DNMT3B* expression⁴. The cells were injected into nude mice. Tumor growth was monitored for two months. When DU145 cells containing the insertless vector were injected, a tumor formed in eleven of the twelve sites (Fig. 1A). When DU145 cells containing the *DNMT3B* shRNA construct were injected (Fig. 1B), only two sites out of nine harbored a tumor, indicating that DNMT3B aberrant activity is responsible for the tumor formation.

Downregulation of *DNMT3B* correlated with reduced methylation in a transcription suppressor site in *HRAD9* gene

We hypothesized that DNMT3B aberrant activity is responsible for hypermethylation of CpG islands in a transcription suppressor site in the second intron of *HRAD9*, leading to *HRAD9* overexpression. We have previously demonstrated that downregulating *DNMT3B* using shRNAs knocks down *HRAD9* expression in

DU145 cells⁴. We show here that downregulating *DNMT3B* using shRNAs reduces CpG island methylation in the transcription suppressor site in the second intron of *HRAD9* (Fig. 2). Therefore, *DNMT3B* is probably involved, together with *DNMT1*³, in tumor formation in nude mice via hypermethylation of a transcription suppressor site leading to *HRAD9* overexpression.

References

1. Zhu A, Zhang CX and Lieberman HB. Rad9 has a functional role in human prostate carcinogenesis. *Cancer Res* **68**:1267-74, 2008.
2. Kanai Y. Alterations of DNA methylation and clinicopathological diversity of human cancers. *Pathol Int* **58**:544-58, 2008.
3. Zhu A, Wang X and Lieberman HB. DNMT1 knockdown in prostate cancer cells reduces HRAD9 expression and tumor formation in nude mice. *CRR Annual Report* 39-41, 2009.
4. Leloup C, Zhu A and Lieberman HB. DNMT3B SiRNA downregulates HRAD9 expression in prostate cancer cells. *CRR Annual Report* 41-42, 2009. ■



2010 Department of Radiation Oncology Christmas Party Raffle Winners.

Mrad9 Plays an Important Role in Spermatogenesis

Ana Vasileva, Kevin M. Hopkins, Xiangyuan Wang^a, Melissa M. Weisbach^a, Aiping Zhu, Debra J. Wolgemuth^a and Howard B. Lieberman

Introduction

Mrad9 has multiple functions in several pathways responsive to DNA damage and for maintaining genomic integrity including homologous recombination. *Mrad9*-null mice die between E9.5 and E12.5, a phenotype accompanied by increased apoptotic activity and reduced cellular proliferation⁽¹⁾. All of these processes are critical for germ cell differentiation, spermatocyte development and function. Little is known about the role of Mrad9 in the germline. Therefore, to assess the activities of Mrad9 specifically during spermatogenesis, we constructed mice that conditionally lack Mrad9 in early lineage spermatogonia and monitored spermatogenesis.

Results

Characterization of *Mrad9* expression in mouse testis

In mice, spermatogenesis is initiated on day 3 postpartum (pp) and progresses as a synchronous wave during the first weeks of life (e.g., type B spermatogonia appear at 8 dpp; elongated spermatids appear after 22 dpp)⁽²⁾. We characterized the temporal pattern of *Mrad9*

expression in male gonads by northern analysis of total RNA from juvenile and adult mouse testes (Figure 1A, B). Total RNA from wild-type mouse embryonic stem cell (ESC) was used as positive control. Hybridization signal of expected size was detected as a 2.0 kb band. The relative amount of *Mrad9* mRNA was calculated as the ratio of Mrad9 band density to the band density representing the expression of ribosomal protein – a housekeeping gene used as loading control (Fig.1 B). *Mrad9* expression peaked at d7.5 testes which consist mainly of mostyspermatogonia. A slight reduction accompanied the appearance and accumulation of early spermatocytes by d12.5. Contrary to our expectations the *Mrad9* expression levels recovered by day 22.5 and remained at a similar level in the adult testis. These preliminary expression data suggest that Mrad9 RNA is present in pre-meiotic germ cells. To verify these results we will conduct qPCR expression assays that will include whole testis RNA from younger mice as well as RNA from isolated pure populations of germ cells.

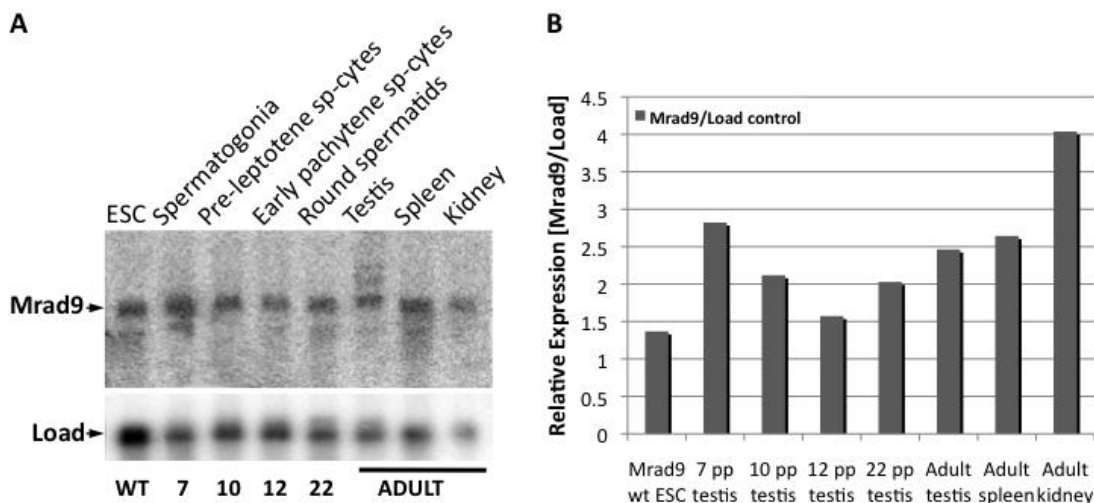


Figure 1. *Mrad9* expression in whole testis and purified germ cell populations. (A) Northern analysis of total RNA (30 µg/lane). Age (in days) is indicated at the bottom and latest corresponding germ cell type - on top. (B) Quantification of *Mrad9* mRNA expression relative to ribosomal protein loading control.

^a Department of Genetics and Development,
College of Physicians and Surgeons,
Columbia University

We examined the localization of Mrad9 in testis by immunostaining with anti-hRad9 antibodies that cross-react with the mouse protein. The protein appeared in the nucleus of undifferentiated A-type spermatogonia, which are present at the basal membrane of the tubule at various stages of the seminiferous cycle. Examples of Mrad9 localization in spermatogonia are shown in Fig. 2A (Stage

I tubule). At later stages, e.g. spermatogonial differentiation, Mrad9 seems to translocate to the cytoplasm as observed in intermediate and B-type spermatogonia as well as pre-leptotenespermatocytes (Fig. 2B). These data are consistent with the early peak of *Mrad9* expression observed by Northern hybridization.

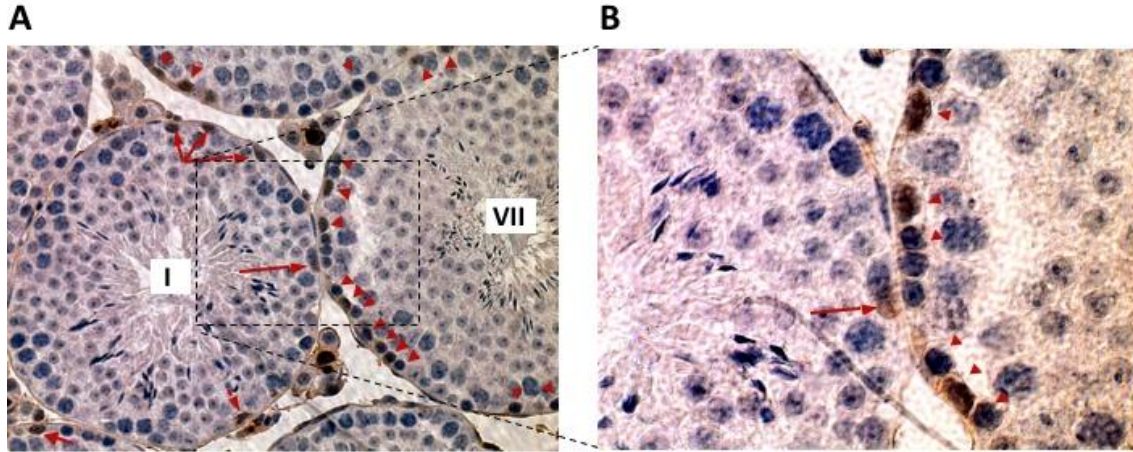


Figure 2: Mrad9 protein localization in adult mouse testis. Immunostaining of paraffin embedded adult mouse testicular sections at 40x (A) or 100x (B) magnification. Mrad9 signal (brown) in undifferentiated A-type spermatogonia (red arrows), Stage I tubule, and B-type spermatogonia and pre-leptotenespermatocytes (red arrowheads) at Stage VII. Hematoxylin (blue) marks the nuclei.

Generation of mice with conditional deletion of Mrad9 in the testis

We found that mice null for *Mrad9* are embryonic lethal⁽¹⁾. It was essential to make animals with a cell-specific, conditional deletion we have reported previously⁽³⁾. *Mrad9^{fl/fl}* mice (*Mrad9^f* denotes the “floxed” allele) were viable and healthy, consistent with our expectation that this allele is functionally wild-type. Homozygous *Mrad9^{fl/fl}* mice were crossed with a strain where Cre expression is driven by the neurogenin-3 promoter in undifferentiated spermatogonia and pancreas (*Ngn3Cre^{+/-}* mice),⁽⁴⁾. *Mrad9^{fl/+} Ngn3-Cre^{+/-}* progeny were back-crossed with *Mrad9^{fl/fl}* mice.

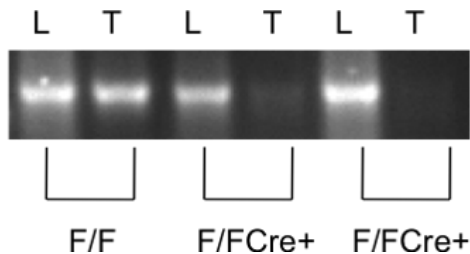


Figure 3. Deletion of *Mrad9* in the testes (T) but not liver (L) of progeny mice bearing *Mrad9^{fl/fl}Cre⁺*. Mouse with just the floxed version of *Mrad9* (F/F) was a positive control for testis DNA.

From these matings, we confirmed by genotyping that we produced a *Mrad9^{fl/del} Ngn3-Cre^{+/-}* mouse. Using PCR with primers corresponding to *Mrad9⁽¹⁾*, we initially examined DNA from testes with expected expression of the *Ngn3-Cre* transgene, and from liver where *Ngn3 Cre* is not normally expressed. As predicted and indicated in Fig. 3, the *Mrad9^{fl/fl}* progeny have *Mrad9* in both liver and testes specimens.

Mrad9^{fl/fl}Cre⁺ progeny have *Mrad9* DNA essentially only in liver. Given the dramatic weakness of the *Mrad9* bands in testis DNA, it appears that most if not all cells lack the “floxed” allele. Other tissues will be examined to demonstrate that, as expected, only testes and perhaps pancreas have a deletion of *Mrad9*.

Characterization of spermatogenesis in testes with conditional Mrad9 deletion

We tested if deletion of both *Mrad9* alleles in the testis has an effect on male fertility. Three rounds of mating of each *Mrad9^{fl/del} Ngn3-Cre⁺* male (n=11) with two wild-type CD1 females resulted in a wide variation of mutant male fertility. Three out of eleven (27%) males produced no progeny over the course of three months (Table 1). The number of pups sired by four males (36.3%) was close to the litter size expected for wild-type animals, while the remaining four males exhibited declining fertility as they only sired pups only during the first or the first and the second rounds of mating.

Table 1. Summary of the *Mrad9^{fl/del}*, *Ngn3-Cre* fertility study

Genotype	Sperm Count [$\times 10^5$]	Pups & Embryos			Testis weight [mg]
		First Mating	Second mating	Third mating	
#1 <i>Mrad9 fl/del</i> , <i>Cre</i> +	0.9	0	0	0	23
#2 <i>Mrad9 fl/del</i> , <i>Cre</i> +	16.9	0	0	0	53
#3 <i>Mrad9 fl/del</i> , <i>Cre</i> +	14.1	0	0	0	41.9
#4 <i>Mrad9 fl/del</i> , <i>Cre</i> +	9.3	6	0	0	53.5
#5 <i>Mrad9 fl/del</i> , <i>Cre</i> +	10.6	6	0	0	41
#6 <i>Mrad9 fl/del</i> , <i>Cre</i> +	7.3	10	5	0	48
#7 <i>Mrad9 fl/del</i> , <i>Cre</i> +	27.8	7	13	0	51
#8 <i>Mrad9 fl/del</i> , <i>Cre</i> +	23.5	7	5	9	51.5
#9 <i>Mrad9 fl/del</i> , <i>Cre</i> +	38.7	12	11	10	87
#10 <i>Mrad9 fl/del</i> , <i>Cre</i> +	59	10	11	14	56.2
#11 <i>Mrad9 fl/del</i> , <i>Cre</i> +	69.5	11	10	14	63.8
#1 <i>Mrad9 fl/+</i> , <i>Cre</i> -	173.8	13	12	14	80
#2 <i>Mrad9 fl/+</i> , <i>Cre</i> -	183.5	12	10	12	110

At 5.5 months of age, mated males were sacrificed and their reproductive tract compared to that of matched *Mrad9^{fl/+}* controls. Gross morphological evaluation revealed reduction in the testis size of the *Mrad9^{fl/del}* *Ngn3-Cre* males to various degrees, suggestive of reduction or elimination of germ cell numbers.

Histological analysis of epididymides from homozygous mutants showed few sperm relative to controls consistent with the reduction in sperm count. Examination of testis sections revealed a range of unusual seminiferous tubule phenotypes in the *Mrad9^{fl/del}* *Ngn3-Cre* mutants (Fig. 4A, B and C) that were absent in controls (Fig. 4D). Most frequently we found reduced number of germ cell layers and aberrant localization of elongated spermatids near the basal membrane, as well as vacuolization (Fig. 4A, B, C). Lack of one or more germ cell generations presumably occurred via loss of spermatogonial stem cells. Apoptotic germ cells or morphologically abnormal cells were not observed at the time points examined. Lack of *Mrad9* does not disrupt spermatogenesis per se, as tubules with germ cells produce morphologically normal and fertilization-competent spermatozoa.

It is quite unusual for such high proportion of mutants to be fertile and present with “close-to-normal” morphology in the majority of testis tubules. Inefficient excision of the *Mrad9fl* allele or expression of *Ngn3-Cre* only in the fraction of spermatogonia that contribute to adult spermatogenesis may provide viable explanation. To overcome this limitation we crossed *Mrad9fl/+* line with mice with *Cre* expression driven by a *Stra8* promoter specific for spermatogonia⁽⁵⁾. We hypothesize that the resulting *Mrad9fl/del* *Stra8-Cre* + males will also present with reduced fertility or will be completely infertile.

To assess the efficiency of *Cre*-recombinase excision, a second line of mice is also being generated by crossing

the *Mrad9 +/f* *Ngn3Cre +/-* male mice with female Td-tomato transgenics and reciprocally by crossing Td-tomato male mice with *Mrad9f/f* *Ngn3Cre +/-* females. The F1 progeny will carry both tomato transgene and a *Mrad9* floxed allele. The efficiency of *Mrad9fl* allele excision will be assessed in the testis of tomato positive mice selected from the crosses of the F1 progeny. In *Cre*-expressing cells, efficient excision of the “floxed” Td-tomato transgene showed give rise to a functional EGFP transgene turning fluorescence of positive cells from red to green. It is also possible that cells are double positive if only one allele is excised in Td-tomato^{+/+} animals.

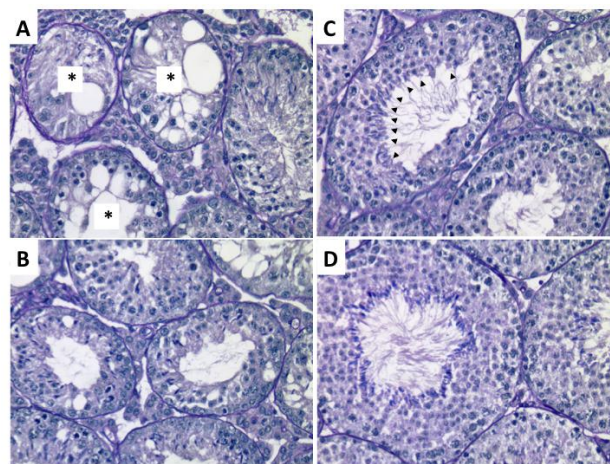


Figure 4. *Mrad9^{fl/del}*, *Ngn3-Cre* testis histology. (A) A sterile *Mrad9^{fl/del}* *Ngn3-Cre* male with mostly agametic tubules (asterisks); (B) Tubules with two or fewer layers of cells, instead of four; (C) Partially fertile *Mrad9^{fl/del}* *Ngn3-Cre* mutant - arrowheads point to sperm absent in the opposite end of the tubule; (D) Normal testis from a control *Mrad9^{fl/+}* mouse. Paraffin embedded tests from adult littermates were sectioned and stained with periodic acid-Schiff (PAS) reagent and hematoxylin.

Our results to date, together with the previously described pattern of expression of *Mrad9*, suggest an essential function for *Mrad9* in the mitotic cell divisions of spermatogonia and possibly in the transition from mitosis to meiosis. Further examination of the cellular and biochemical causes for the effect of targeted conditional mutagenesis of *Mrad9* in spermatogonia is underway. The consequences of *Mrad9* loss in pre-leptoten spermatocytes, possibly during progression from G/S phase, remain to be elucidated by excising the conditional allele with Cre-driver onset occurring at a later specific sate of spermatogenic.

References

1. Hopkins, K.M., Auerbach, W., Wang, X.Y., Hande, M.P., Hang, H., Wolgemuth, D.J., Joyner, A.L., and Lieberman, H.B. (2004) Deletion of mouse *Mrad9* causes abnormal cellular responses to DNA damage, genomic instability, and embryonic lethality. *Mol. Cell. Biol.* 16, 7235-7248.
2. Bellve, A.R., Millette, C.F., Bhatnagar, Y.M., and O'Brien, D.A. (1977). Dissociation of the mouse testis and characterization of isolated spermatogenic cells. *J. Histochem. Cytochem.* 25, 480-494.
3. Hu, Z., Liu, Y., Zhang, C., Zhao, Y., He, W., Han, L., Yang, L., Hopkins, K. M., Yang, X., Lieberman, H. B., and Hang, H. (2008) Targeted deletion of *Mrad9* in mouse skin keratinocytes enhances genotoxin-induced tumor development. *Cancer Res.* 68, 5552-5561.
4. Yoshida, S., Takakura, A., Ohbo, K., Abe, K., Wakabayashi, J., Yamamoto, M., Suda, T., and Nabeshima, Y. (2004). Neurogenin3 delineates the earliest stages of spermatogenesis in the mouse testis. *Dev. Biol.* 269, 447-458.
5. Sadate-Ngatchou, P. I., Payne, C. J., Dearth, A. T. & Braun, R. E. (2008) Cre recombinase activity specific to postnatal, premeiotic male germ cells in transgenic mice. *Genesis* 46, 738-742. ■

Human Rad9 Subcellular Localization as Induced by Microirradiation

Joshua D. Bernstock, Kevin M. Hopkins, Aiping Zhu, Constantinos G. Broustas and Howard B. Lieberman

Introduction

RAD9 regulates multiple cellular processes that influence genomic integrity, and for at least some of its functions the protein acts as part of a heterotrimeric complex bound to HUS1 and RAD1 proteins. RAD9 participates in DNA repair, including base excision repair, homologous recombination repair and mismatch repair, multiple cell cycle phase checkpoints, apoptosis, etc. Aberrant *RAD9* expression has been linked to breast, lung, thyroid, skin and prostate tumorigenesis, and a cause-effect relationship has been demonstrated for the latter two. Interestingly, human RAD9 overproduction correlates with prostate cancer whereas deletion of *Mrad9*, the corresponding mouse gene, in keratinocytes leads to skin cancer. These results reveal that RAD9 protein can function as an oncogene or tumor suppressor, and aberrantly high or low levels can have deleterious health consequences.¹ Nevertheless, the exact functions of RAD9 responsible for the development of cancer have not been defined and it is therefore of the utmost importance that the structural, functional and regulatory relationships of Rad9 be mapped out in detail.

To define the function of Rad9 with respect to the cellular response to DNA damage, this project concerns

the creation of localized double-strand breaks in DNA and analysis of the kinetics of Rad9 focus formation alone/in conjunction with known protein binding partners. The response to damage will be monitored by fluorescence imaging of live HEK 293T cells stably expressing a fluorescently tagged Rad9 fusion protein as well as other proteins similarly labeled.

Experiment background and procedure

Creation of GFP-Tagged Protein Constructs: Human cDNA was generated and cloned into fluorescent protein vectors via standard PCR/restriction enzyme digestions/religation methods. Plasmids encoding an in frame sequence of GFP, YFP, CFP or RFP and the cDNA of interest were constructed. A neomycin resistance cassette for selection is contained within the Evrogen fluorescent vectors [GFP (G), YFP (Y), CFP (C), RFP (R)], thereby allowing for the selection of stable clones. To date the following cDNAs have been fused into vectors encoding all four fluorescent colors: *Rad9* (C,G,R,Y), *Rad9b* (C,G,R,Y), *Hus1* (C,G,R,Y), *Hus1b* (C,G,R,Y), *PCNA* (C,G,R,Y), *Rad17* (C,G,R,Y), *Rad1* (C,G,R,Y), *Bcl-2* (C,G,R,Y), *Bcl-xl* (C,G,R,Y), and Androgen Receptor (C,G,R,Y), which will permit tracking of the respective proteins within cells.

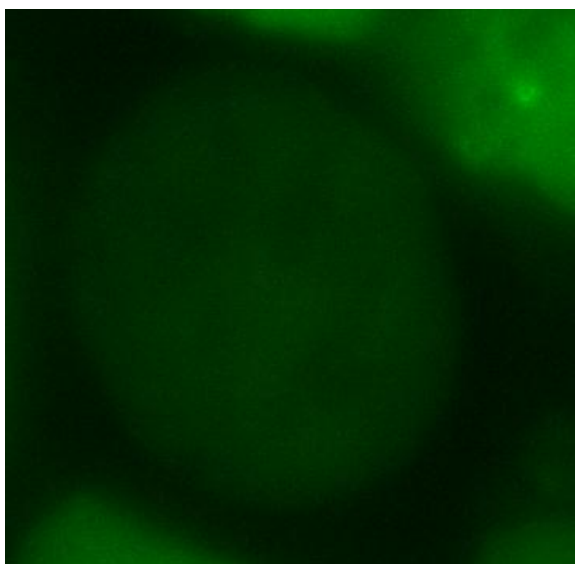


Figure 1. Target HEK293T cell pre 355-nm solid-state UV laser microirradiation

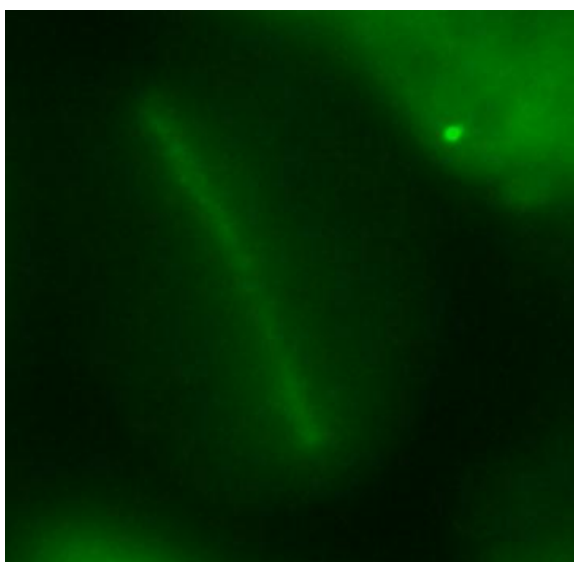


Figure 2. Target HEK293T cell nuclei (GFP-hRad9 fusion) 2 minutes post irradiation

Generation of Cell Lines Stably Expressing GFP-Tagged Proteins: We initially focused on the construct that has Rad9 fused to GFP. We stably transfected human embryonic kidney (HEK) 293T cells, using 1000 $\mu\text{g}/\text{mL}$ G418 as the selective agent.

Formation of DNA DSBs in Partial Nuclear Volumes: DNA DSBs were induced in cells by adapting the methods of Lukas et al. and Davey et al.^{2,3} Live cells stably expressing GFP-hRad9 were grown in MatTek 35mm Glass Bottom Culture Dishes at a density 1.75×10^5 cells/dish in the presence of $10 \mu\text{M}$ BrdU for 24hr. Prior to irradiation, asynchronously dividing HEK 293T cells were stained with Hoechst 33342 dye at a concentration of $1 \mu\text{g}/\text{ml}$ for 30min. Cells were visualized using the PALM MicroBeam IV microscope (Herbert Irving Comprehensive Cancer Center) using a 40x lens. Immediately after irradiation, localization of GFP-hRad9 was followed for 10 min in 2-min intervals.

Future direction and goals

FRET (Forster [Fluorescence] Resonance Energy Transfer) experiments will be performed. The aforementioned will be designed to elucidate specific/subtle details of the dynamic molecular interactions between Rad9 and its binding partners.

References

1. Lieberman HB, Bernstock JD, Broustas CG, Hopkins KM, Leloup C, and Zhu A. The role of RAD9 in tumorigenesis. *J. Mol. Cell Biol.* 3: 39-43, 2011.
2. Bekker-Jensen S, Lukas C, Melander F, Bartek J, and Lukas J. Dynamic assembly and sustained retention of 53BP1 at the sites of DNA damage are controlled by Mdc1/NFBD1. *J. Cell Biol.* 170: 201-211, 2005.
3. Greer DA, Besley BD, Kennedy KB, and Davey S. hRad9 rapidly binds DNA containing double-strand breaks and is required for damage-dependent topoisomerase II beta binding protein 1 focus formation. *Cancer Res.* 63: 4829-4835, 2003. ■

Genetic Control of the Trigger for the G2/M Checkpoint

Erik F. Young, Lubomir Smilenov and Eric Hall

At high radiation doses (0.5Gy- 2Gy) there is good evidence that radiation can induce many types of cancer; the best evidence coming from the study of the A-bomb survivors.

Present controversy surrounds cancer risks at lower doses below 100 mGy where unequivocal results from epidemiological studies are not available. Radiation protection agencies, such as ICRP and NCRP suggest that risk at low doses should be estimated using a linear, no threshold extrapolation from the risks at higher doses. This simple assumption may not be valid if different radiation response programs are operational at high versus low doses. An important radiation response is the activation of the G2/M checkpoint.

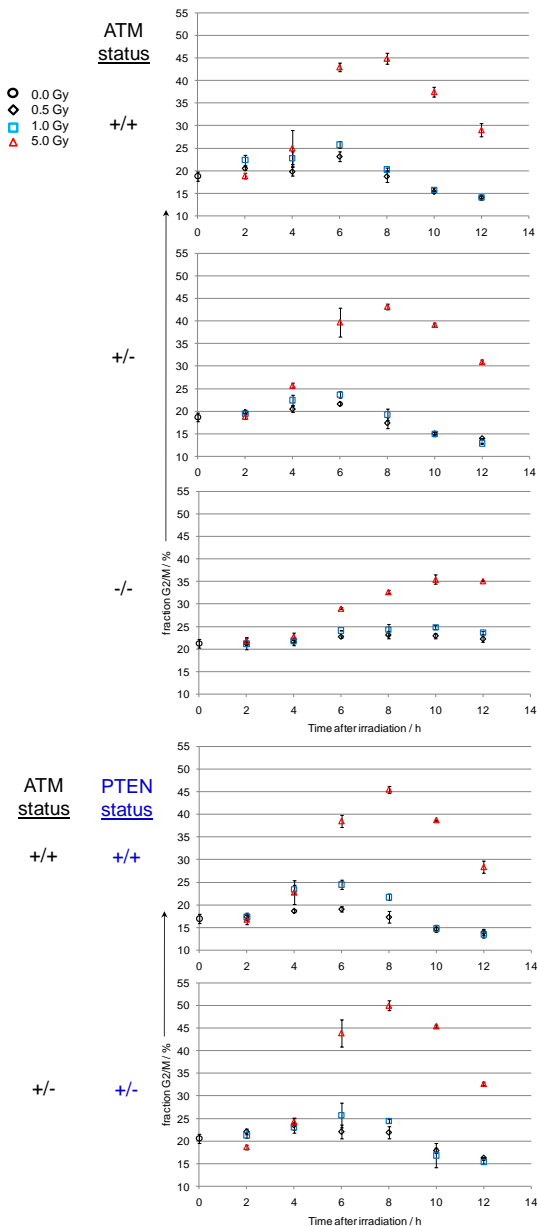


Figure 1. G2/M arrest kinetics in irradiated mouse embryo fibroblasts (MEFs). MEFs were irradiated at 0.5, 1.0 and 5.0 Gy and harvested over a 12 hr time course as shown. Cells were stained for cell cycle analysis with propidium iodide. The mean and standard deviation of technical triplicates are shown.

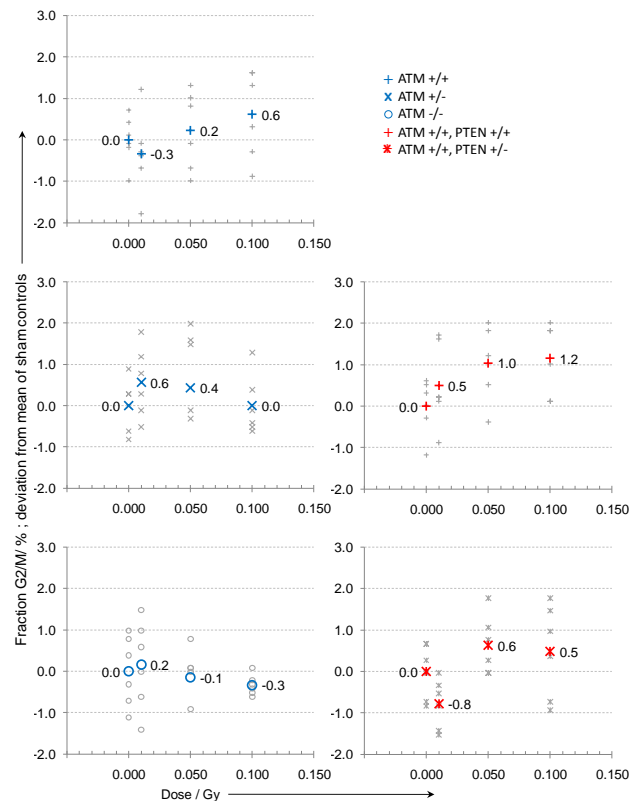


Figure 2. G2/M arrest kinetics in irradiated mouse embryo fibroblasts (MEFs). MEFs were irradiated at very low doses shown at a uniform 6 hour time after irradiation. The mean (bold symbols) and acquired data (gray symbols) are plotted.

When normal cells are exposed to a dose of radiation large enough to cause significant DNA damage, they become arrested at the G2/M checkpoint, and it is assumed that this delay allows repair of damage before the complex task of mitosis is attempted. While this is true in normal cells, cells homozygous for mutations in *ATM* do not possess a competent G2/M checkpoint, which may be one reason for their exquisite radiosensitivity, though, in addition, they are not proficient in the repair of DNA damage.

Employing proliferating mouse embryo fibroblasts, we chose to investigate the function of the G2/M checkpoint at high and low doses, and also to analyze the influence of mutations in a number of genes involved in DNA repair and checkpoint control

MEFs were isolated from embryos resulting from the pairing of parents, haploinsufficient for either *PTEN* or *ATM*. Progeny represented all possible genotypes from the cross, with wild type, doubly hemizygous and singly hemizygous embryos represented as verified by PCR. Cells of each genetic background were irradiated with doses of gamma-rays from 50 mGy to 5 Gy, and the function of the G2/M checkpoint analyzed by measuring the percentage of cells in G2/M as a function of time after

irradiation, using flow cytometry. The results are shown in Figures 1. The G2/M arrest kinetics for all cell types at the lowest doses (0 to 150 mGy) are shown in Figure 2.

Discussion

A number of conclusions are evident from the data.

1) In wild type cells, a G2/M checkpoint is evident following a dose of 5Gy, but there is little evidence of a significant checkpoint at a dose of around 10 mGy.

2) In cells homozygous for *ATM*, the G2/M checkpoint is greatly reduced and delayed even at a dose as high as 5 Gy.

3) To our surprise, cells haploinsufficient for *ATM*, and even cells haploinsufficient for both *ATM* and *PTEN*, exhibit a pattern of G2/M arrest that is indistinguishable from wild type cells.

Acknowledgements

We are thankful to Ramon Parsons for providing *PTEN* mutant mice.

This work was supported by DOE grant DE-FG02-09ER64809. ■

Generation of a Low Cost Live Cell Imaging Capability

Erik F. Young

Introduction

One of the fundamental endpoints for a variety of studies in radiation biology is the division or cycling of cells in culture. Several assays to measure this process have transcended great spans of time owing to their simplicity, low cost and ease of use. These assays include the common propidium iodide cell cycle analysis in which staining of cells for their DNA content is followed by population analysis by flow cytometry. Limitations of this method can include small variations in staining intensity or stain uptake and the inevitable error introduced by manual gating or adjustment of voltage across the photo detector to an extent that is visually pleasing, but perhaps statistically variable. There is also the clonogenic dilution assay which reports the ability of a cell to survive and proliferate used exhaustively in the generation of survival curves. Clonogenic assays can be time and resource consuming and overlapping colonies can be difficult to score. A common theme among all of

these tried and true methods, along with many others not mentioned here, is a component of uncertainty and error.

A requirement arose in our work for a method that reported, with absolute fidelity, the division of cells over a given time course. We considered direct observation of cells but realized that there are operator associated limitations of endurance which would impact the accuracy and precision of data acquired in this way. Further, a large quantity of cultureware would be required to sample cells over a timecourse as the biology of the culture would become altered in a high oxygen, reduced temperature environment outside the culture incubator. Changes in temperature and oxygen concentration have been known for some time to have significant effects on radiation response biology (1-5). To address this need, a brief search was mounted for existing equipment that could be used to generate an appliance that could record cell cultures over a prolonged timecourse.

Components and Assembly

Existing components

The laboratory is equipped with a CK-2 inverted microscope used for routine surveillance of growing cultures in the lab. This microscope is equipped with adapters allowing for the attachment of a C4040Z consumer grade digital camera. The camera is accompanied by a type RM-1 infrared remote to allow for self portraiture and remote triggering. With these two components, the requirement for a triggering mechanism became apparent. The triggering mechanism would need to be programmable since time studies of dividing cells would understandably vary according to cell type. A suitable solution presented itself in an inexpensive and commercially available microcontroller, the Arduino Duemilanove.

Timing and Control

The Arduino is a small circuit board with digital and analog outputs supported by the 128bit ATMEGA processor at its core. The microcontroller is powered by a barrel type DC input plug commonly delivering 5-12V from a wall mounted adaptor. Such adaptors can be found in the lab as charging stations for rechargeable pipette aids used with serological pipettes. The microcontroller can be linked to any laptop PC via a USB type B connector. In this way, control over the precise timed delivery of power to the trigger mechanism could be achieved, but transmission of the infrared signal to the camera from the RM-1 remote under this timing scheme was required.

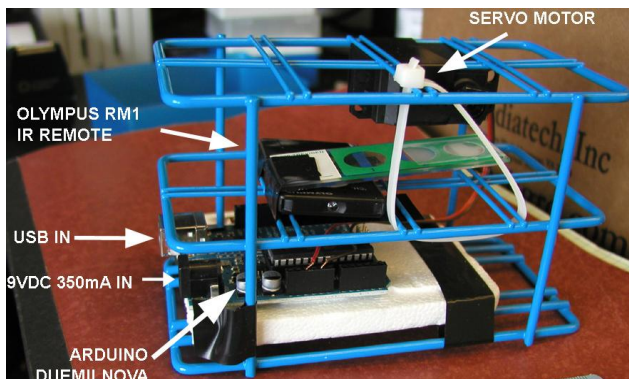


Figure 1. Arduino based trigger mechanism for live imaging.

Internet-available code for the interaction of the Arduino with a low power servo motor was uploaded into the memory of the controller and the timing of sweeps of the servo motor could be adjusted by making adjustments to the code. The RM-1 remote control is a fairly inexpensive item to replace, but in the interests of preserving the remote control for use in other applications, the remote controller was not disassembled to facilitate linkage to the Arduino’s electronics. Instead, the remote controller was lashed to a stand and the servo

motor was positioned so as to depress the button on the controller (Fig. 1).

Illumination

Exceptional thermal insulation is a property of tissue culture incubators, prohibiting sustained illumination of cultures with the high wattage halogen bulb in the microscope. Powering this lamp would also be difficult from outside the incubator. As such, an inexpensive Dot-it™ light emitting diode (LED) based lamp (Osram-Sylvania, Danvers, MA) was cannibalized for its array of three white LEDs which were soldered to jumper wire and connected to the Arduino providing for programmable, intermittent illumination only during the

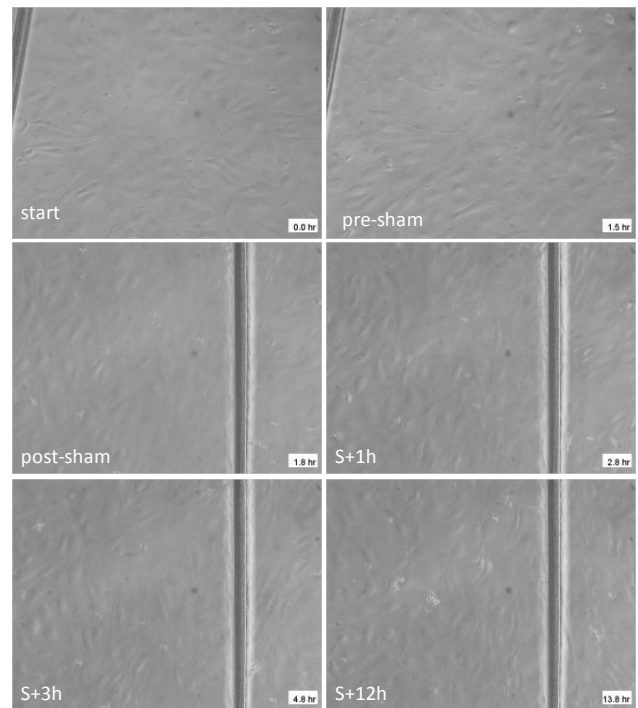


Figure 2. Human umbilical vein endothelial cells were seeded on collagen coated culture ware and allowed to recover for 20 hours before a sham irradiation. Cells were recorded over a subsequent 12 hour span of time.

sweep of the servo and photography proper. Powered through the Arduino, the quantity of electrical wiring strung through the incubator door was now also reduced to two lines: one for the camera and one for the trigger. While the strength of the illuminator array was not great enough to mount directly into the light path of the microscope’s optics, we found that placement of the illuminator array atop the cultureware provided very sufficient illumination. While we did observe a significant loss of phase contrast in the process, orthogonal placement of the illuminator array did cast cell features into sharper contrast.

Environment

Establishment of an optimized culture environment for the system is relatively easy as the entire assembly fit easily into an incubator cabinet devoid of shelving. While the humidity and temperature conditions associated with standard culture fell within the operating limits of the camera we considered that many exposures over time would be deleterious to the electronics and optical components of our system. To this end, we removed the pan of water in the bottom of the incubator and instead performed all imaging sessions in a 24 well dish cluster with the outer wells filled with sterile water and a single inner well filled with culture media.

Use

With the largest capacity memory card available and altering the settings of the camera to collect lower quality images, we were able to collect 640 images per time course. After the length of the time span to be photographed, arithmetic was used to determine the spacing of photographs. These values were programmed into the code commanding the triggering mechanism and then uploaded into the memory of the Arduino. The experiment was transferred to the incubator and the camera's reverse screen display activated and focused on the cells to be studied. While the plane of focus was established, illumination was provided by temporarily shorting the connection to the illuminator array directly between 5V supply and ground pins on the Arduino. Focus was ensured by scratching the culture surface providing a bold target for the autofocus feature of the camera to home on. Once established, the experiment was left to photograph itself.

After completion of the experiment, images were converted en masse to an 8 bit, black and white format to economize file size and compiled into an AVI format movie playing at 8 frames per second using Internet-available Image J software. Frames from a sample time course of human umbilical vein endothelial cells are shown in Fig. 2. A separate example is available for viewing on the Internet (6).

Improvement

The present is a time of great ferment in the discipline of automated image processing. Indeed the development of modalities to minimize the requirement of expensive, experienced, highly trained pathologists in the pursuit of digital diagnosis is well under way. Pattern recognition algorithms are being developed intramurally as well for high throughput quantitation of phospho- γ -H2AX foci (7, 8). As this field advances, surveillance of cell divisions in such movies should be more readily quantitated.

References

1. E. I. Azzam, I. George, G. P. Raaphorst, *Radiat Res* 90, 644 (Jun, 1982).
2. B. Palcic, B. Faddegon, L. D. Skarsgard, *Radiat Res* 100, 340 (Nov, 1984).
3. B. Palcic, L. D. Skarsgard, *Radiat Res* 100, 328 (Nov, 1984).
4. G. P. Raaphorst, E. I. Azzam, *Int J Radiat Oncol Biol Phys* 8, 1947 (Nov, 1982).
5. G. P. Raaphorst, E. I. Azzam, M. D. Sargent, M. Einspinner, J. Borsa, *Br J Radiol* 54, 638 (Jul, 1981).
6. E. F. Young,
<http://www.youtube.com/watch?v=063AvJ2mWNc>.
7. G. Garty et al., *Health Phys* 98, 209 (Feb).
8. H. C. Turner et al., *Radiat Res* 175, 282 (Mar). ■



October 2010 University Senate meeting: Senators (L-r) Ronald Breslow (Chemistry, Tenured Faculty), James Applegate (Astronomy, Tenured Faculty), Ruairidh McLeod (Teachers College, Student) and Guy Garty (CRR, Professional Research Officer), watch a virtual walk through of the newly finished North West Corner Science building.

Effects of Ionizing Radiation on DNA Repair Dynamics in 3-Dimensional Human Vessel Models: Differential Effects According to Radiation Quality

Peter W. Grabham, Burong Hu*, Alan W. Bigelow and Charles R. Geard

Several proteins involved in DNA repair and DNA damage signaling such as phosphorylated histone 2A family member X (γ -H2AX) and the tumor suppressor TP53 binding protein 1 (53BP1) have been shown to

produce discrete foci that are believed to co-localize to DSB. Here we have examined the kinetics of DNA repair in human vessel tissue models in which the cell components are now differentiated and post-mitotic. We wanted to find out the kinetics of DNA repair in these tissues and determine whether it was different relative to replicating monolayers. We used High energy and LET Fe ions, low LET high energy protons and Gamma photons.

*Key Laboratory of Heavy Ion Radiation Biology and Medicine, Institute of Modern Physics, Chinese Academy of Sciences, Lanzhou, P.R. China.

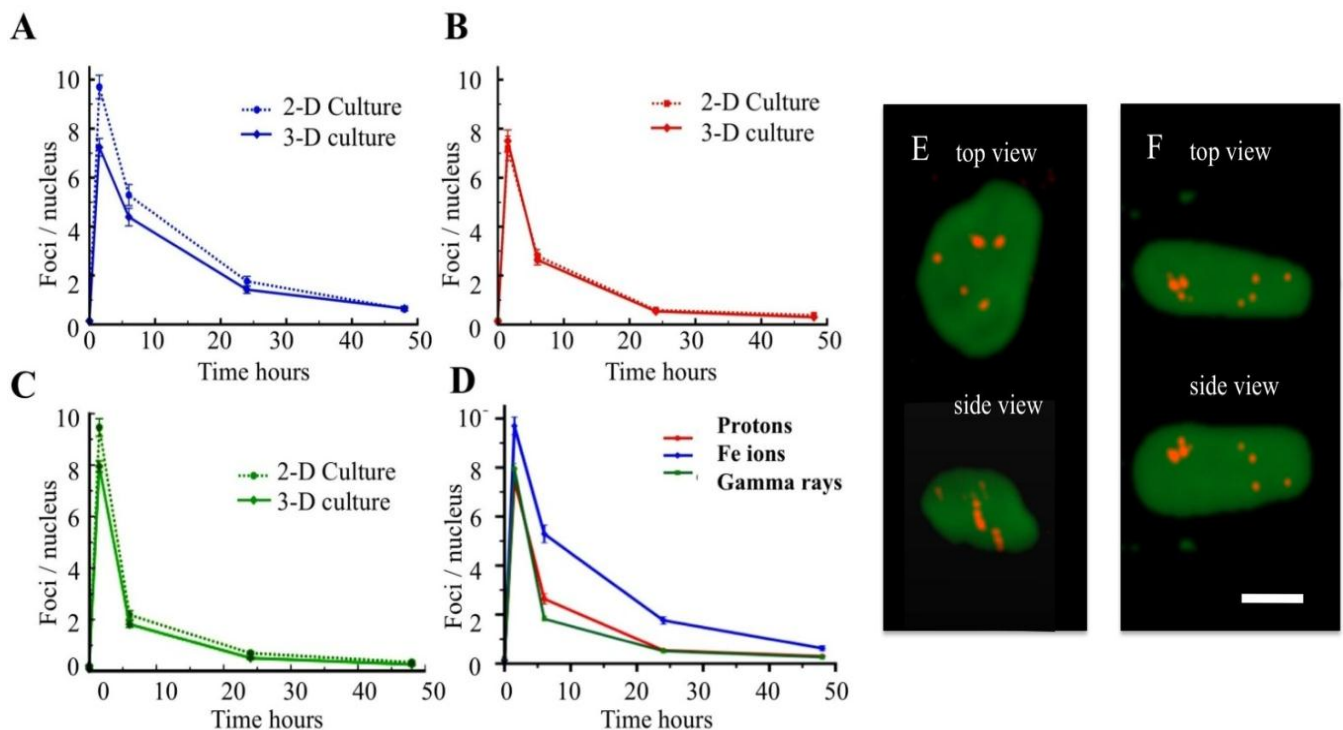


Figure 1. Kinetics of 53BP1 focus formation and decline in irradiated cells and in capillary-like structures. Cultures were exposed to 80 cGy of 1GeV Fe ions (A), 1Gev protons (B) and gamma radiation (C) then immunostained for 53BP1 and the number of foci per nucleus determined. Bars indicate the standard errors of the means. At 1h 30 min all three types of radiation induced similar numbers of foci per nucleus in 2-D and 3-D cultures. Foci then rapidly declined over 24 hours. A plot of all three in 3-D cultures superimposed (D) shows the relative kinetics of foci formation and decline for each ionizing radiation. (E) and (F) 3-D rendered images from 2-photon microscopy. Immunostaining of cell nuclei (green) and 53BP1 foci (red) show that Fe ions induce tracks of DNA repair (E) but protons do not (F). Bar = 10 μ m.

Kinetics of foci formation and DNA repair in 2 and 3-Dimensional cultures.

We carried out dose response experiments using HZE particles and photons to determine an appropriate dose to examine foci formation and DNA repair kinetics (not shown). 80cGy was found to give around 8-10 foci per nucleus 1 hour 30 min after exposure for all three types of radiation. We therefore used this dose to examine the kinetics of 53BP1 nuclear foci in post-mitotic 2-dimensional cultures and in 3-dimensional vessel models following irradiation, by Fe ions (1GeV), protons (1GeV) and gamma rays. 1h 30min after exposure each ionizing radiation produced a comparable number of foci per nucleus in this assay at the time point of 1h 30min (Figure 1). There was little difference between the number of foci in 2-Dimensional dividing monolayers and the number in 3-Dimensional capillary-like vessels except in the cells irradiated with high-energy Fe ions (Figure 1A). One explanation for this is that the Fe ions produce tracks of DNA repair foci whereas protons do not. When we used image analysis of foci captured using 2-photon microscopy, tracks of DNA repair were observed in Fe ion irradiated vessels although not all foci seen through the plane of the particle beam were part of repair tracks (Figures 1E and F). Thus, a top view in the plane of the particle beam superimposes foci along a particle track. Correspondingly, the target area (nucleus) for 2-D cultures is larger but thinner than 3-D cultures so more ion particles fall upon the nuclei of 2-D cultures.

Following the reduction of foci with time, we observed that Fe ions, protons and gamma rays have different rates of decline (successful repair), with high LET exhibiting slowest repair and gamma rays the fastest repair (Figure 1 A-D). Furthermore, as DNA is repaired the difference between foci produced by Fe ions in 2-D compared to 3-D cultures is diminished.

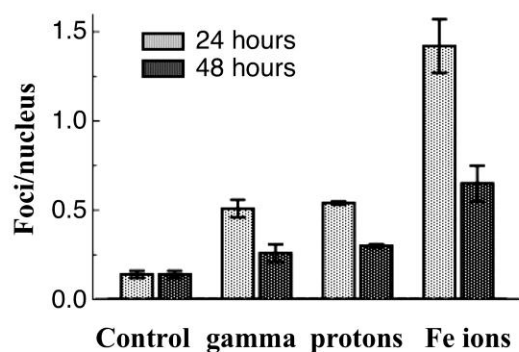


Figure 2. Frequency of repair foci in nuclei 24 and 48 hours after irradiation. Data from Figure 2 is represented as a histogram showing similar kinetics for foci induced by protons and gamma irradiations whereas foci caused by Fe ions are more persistent.

After 48 hours the number of foci induced by protons and gamma rays has reduced to almost control levels (Figure 2). As expected, high LET Fe particles produced more persistent damage. At 48 hours the number of foci was still greater than 0.5 per cell. In contrast high-energy protons and gamma photons both with an LET of less than 1 KeV μ m showed almost complete repair after 48 hours (Figure 2).

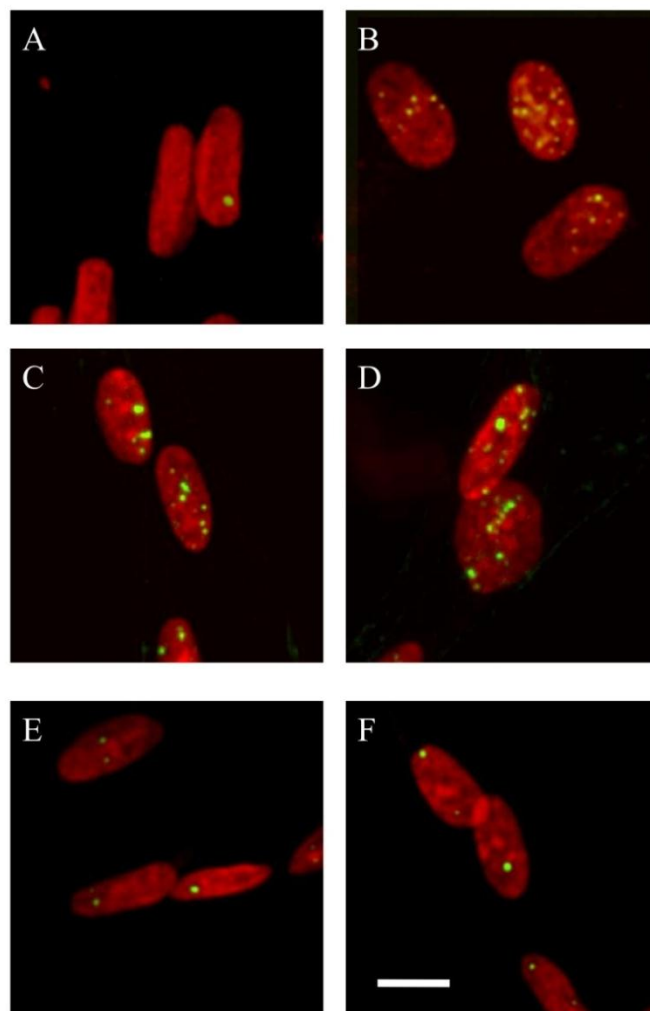


Figure 3. Size and frequency of 53BP1 foci in irradiated 3-D human vessel models. Nuclei are stained red and 53BP1 foci are stained green. A. Unirradiated control sowing few but large foci. B. 1 hr 30 min after 80 cGy gamma irradiation small foci have formed. C. Vessels exposed to 80 cGy Fe ions show foci of different sizes 1 hr 30 min after irradiation. D. Vessels exposed to protons also show foci of different sizes 1 hr 30 min after irradiation. E and F. Cultures exposed to Fe ions and protons respectively show that both large and small foci remain after considerable repair.

Distribution of foci size.

We examined the DNA repair foci induced by these types of radiation in more detail by analyzing the size of repair foci over time. Foci were binned and the frequency of each bin determined (Figures 3 and 4). Foci in unirradiated nuclei appear in vessel cultures at a frequency of around 0.1 per nucleus and many are characteristically large (Figures 3A and 4). More than 40% of the foci have an area larger than $1 \mu\text{m}^2$ (Figure 5). Following exposure to ionizing irradiation the cell nuclei exhibit repair foci within minutes of exposure. By 1 hour 30 minutes foci have fully formed and the foci size distribution is different for gamma photons than for ion particles (Figures 3 and 4). Nuclei irradiated with gamma photons have many small foci and very few foci larger than $0.6 \mu\text{m}^2$. Nuclei irradiated with high-energy protons or Fe ions have fewer small foci and more substantially

larger foci. At this early time the size profiles of foci induced by Fe ions and protons were indistinguishable. 24 hours later after much successful repair the foci size profiles showed differences between all three irradiations (Figures 3 and 4). For gamma irradiation, the foci size profile changed appreciably and became similar to the control with fewer small foci and more foci larger than $1 \mu\text{m}^2$. High-energy particles did not show such a change in foci size profiles indicating that a different type of damage is occurring with particle radiation (Figures 3 and 4). Size distribution of foci induced by Fe ions and protons was similar at 1 hour 30 minutes and 24 hours even though considerable repair had taken place (Figure 1). There was little difference at 1 hour 30 minutes but a slight increase in larger foci at 24 hours after irradiation with protons.

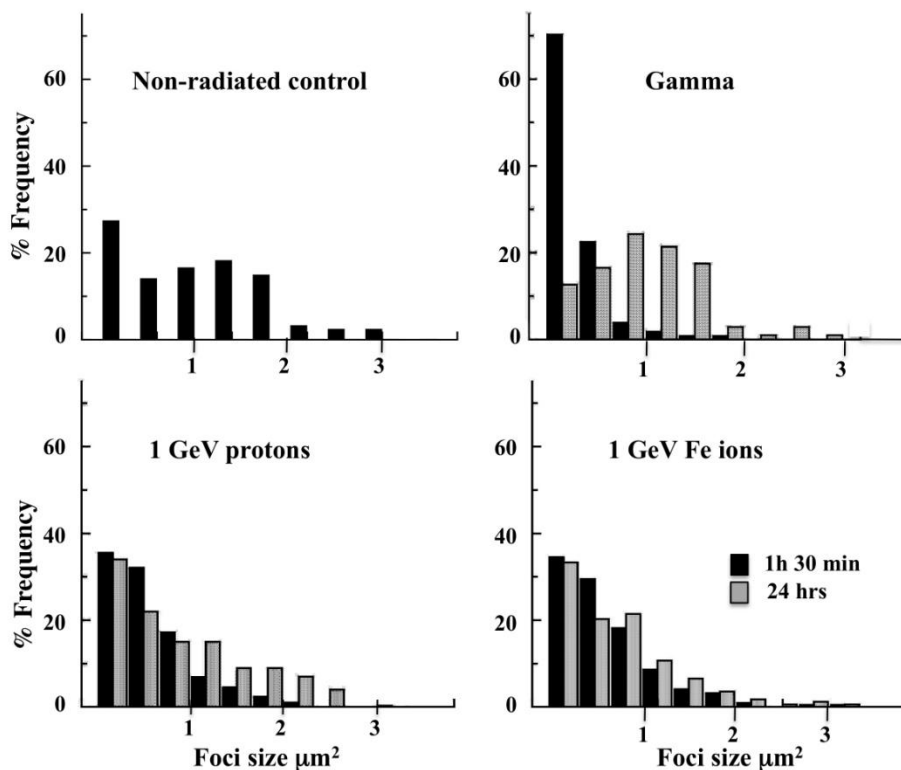


Figure 4. Size distribution of 53BP1 foci induced by particle and photon irradiation. Foci were imaged and sorted into $0.33 \mu\text{m}^2$ bins. At least 150 foci for each condition were measured. Small foci induced by gamma irradiation mostly disappear after 24 hour leaving large foci similar to the non-irradiated control. Fe ions and proton irradiations induce a range of foci sizes. 24 hours after irradiation size profiles remain largely the same except for an increase in the proportion of larger foci after proton irradiation.

Each ionizing radiation produced a comparable number of foci per nucleus in this assay at the time point of 1h 30min (Figure 3). Cells exposed to the high LET (LET = 150) Fe ions are expected to receive 6.9 particle hits per nucleus and the count of foci was an average of 7.1 indicating that Fe ions are efficient at inducing repair and that secondary effects might be present. Cells exposed to the low LET protons (LET = 0.2225) are expected to receive 4269 particle hits per nucleus and the count of foci was an average of 9.0. Thus, particle for particle protons are less efficient at inducing DNA repair foci.

Following the reduction of foci with time, we observed that Fe ions, protons and gamma rays have different rates of decline (successful repair), with high LET exhibiting slowest repair and gamma rays the fastest repair (Figure 2). High LET, as in dividing cells, probably produces more complex damage that is difficult to repair. Comparisons of DNA damage and repair

between 2D differentiated cells and 3D tissue culture models show no difference in the case of protons or gamma rays. Fe ions however, show more damage (foci) in 2D cultures than 3D models. One explanation is that 2D cell nuclei present a larger flatter not thinner target than rounder 3D nuclei. After 48 hours of repair the remaining foci in each case is now the same. If Fe ions produce ionizing tracks then analysis by projecting depth slices on to one frame will render multiple damage sites onto one focus. After repair however, the remaining foci, which are now only less than 20% of the original, are represented more accurately by this kind of analysis. Studies on particle size show that when foci size is binned, Fe ions induce a profile of large and small foci that is the same 1h 30 min after exposure as it is 24 hours after exposure.

Acknowledgement

This work was supported by NASA grant NNX10AB38G. ■

Development of Human 3-Dimensional Brain Tissue Culture Model for the Study of Space Radiation Effects on the Degeneration of the Central Nervous System

Preety Sharma and Peter Grabham

Human space exploration is associated with a significant risk of exposure to ionizing galactic cosmic rays (GCR) and solar particle events (SPE). GCR radiation consists of particles from protons to iron nuclei with broad energy spectra ranging from 10MeV/n to 1012MeV/n (3). The potential risks resulting from exposure to space radiation include significant hazard to the central nervous system (CNS) of space flight crews that could impair cognitive functions and compromise mission operation, potentiate late degenerative conditions affecting the quality of life. Considerable studies have shown that space radiation can have adverse effects on cognition and behavior (1, 2). Still, estimating CNS and degenerative risks from space radiation is difficult due to limited human epidemiology data and scarcity of experimental data on threshold doses for effects on CNS functions (3).

The CNS consists of neurons, and supporting cells called neuroglia. The neuroglia consist of astrocytes, oligodendroglia and microglia. These cells provide scaffold support binding the CNS together. The astrocytes make up about half the brain and are arranged in networks. The brain endothelial cells forming the blood vasculature and astrocytes are sensitive to radiation induced damage (4). In a degenerative disease condition like Alzheimer's loss of neurons and synaptic

dysfunctioning may result in neurofibrillary tangling and neuritic plaques. The plaques are formed due to extracellular deposition of the secreted form of the amyloid precursor protein (APP). The amyloid protein that is not cleared by vessels may compromise vessel function due to vessel changes and inflammation further degenerating the tissue (5). Compromise of the blood brain barrier may result in leakage of serine proteases and other deleterious blood proteins into the brain triggering inflammation and severe pathways in neurons and other cells. Activation of glial cells may result in overproduction of inflammatory cytokines such as TNF alpha and IL-6. These cytokines may result in neurodegenerative cascade. Studies indicate that high LET radiation has a significant effect on neurogenic population that involves cell loss and microenvironment changes (3).

The primary objective of the research project was to advance the understanding of space radiation effects on human central nervous system. Cell-cell and cell-matrix interactions are influenced by the local microenvironment. Studies have shown that cells cultured in 3D environment represent in vivo phenotypic behavior and interactions better than 2D monolayer cultures for several cell types including neural cells. We have attempted to engineer a 3-D tissue model consisting of the

three major cell types in the brain- endothelial cells,

The cells were differentiated separately and combined together in 3D matrix at different time points to represent the mature and developing neurovascular units. We started with at least two different sources for each cell type. These were grown in 3D gel with matrigel in combination with rat tail collagen type I. Different combination of the matrix proteins and media additives such as brain derived growth factor, fibroblast growth factor, phorbol ester with or without serum were used to determine the optimal growth conditions of the neuronal and astrocyte cultures. Then, cultures were set up as two culture systems consisting of a) neurons and astrocytes b) astrocytes and endothelial vessel. After few days of

astrocytes and neurons to produce a “neurovascular unit”. culturing the third cell component was added to form a three cell system. 3D cultures can be used to determine the effects of space radiation by assaying for morphology and specific degeneration markers using cell imaging and detection of secreted proteins. The presence of extracellular matrix proteins such as collagen, laminin and the multicellular nature of the system make it more closely resembling in vivo conditions than 2-dimensional culture of single cell types. The cells tend to retain the cytoarchitecture, gene expression, cellular signaling, differentiation status and pathological susceptibility more similar to the tissue response as a whole.

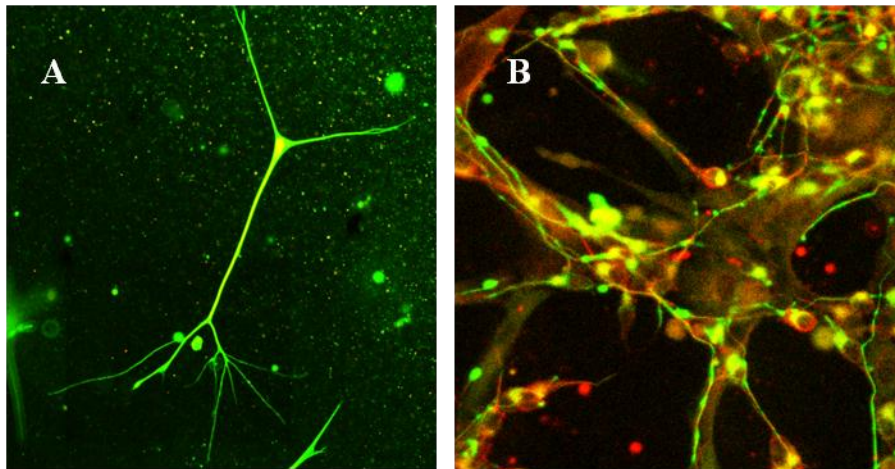


Figure 1. A) Human mesenchymal stem cell line derived neurons stained with rabbit anti-APP antibody and mouse anti-tubulin 3 antibody. Coculture of three cell types in 3D matrices. B) Human brain microvessel cells formed into tubes, astrocytes stained with GFAP (green) and neurons stained with APP (red).

Preliminary studies in our laboratory have shown we can differentiate human mesenchymal stem cell line hADSC into neurons and once plating them into collagen/matrigel matrices they extend multiple long axonal processes. These neurons stain positive for two neuronal markers APP protein and tau (Fig. 1A). Normal human astrocytes were differentiated to characteristic stellate morphology in 3D gel and stained positive for specific astrocyte marker GFAP protein. Once the protocol for both neuronal and astrocyte differentiation was developed the differentiated cells were pooled with the endothelial cells in a 3D matrigel to form the three cell 3D culture (Fig 1B).

References

1. Denisova NA, Shukitt-Hale B, Rabin BM, Joseph JA. 2002. Brain signaling and behavioral responses induced by exposure to (56) Fe-particle radiation. *Radiat Res.* Dec; 158(6):725-34.
2. Rabin BM, Shukitt-Hale B, Joseph JA, Carrihill-

Knoll KL, Carey AN, Cheng V. 2007 Relative effectiveness of different particles and energies in disrupting behavioral performance. *Radiat Environ Biophys.*, 46(2):173-7.

3. NCRP Report No. 153, Information Needed to Make Radiation Protection Recommendations for Space Missions Beyond Low-Earth Orbit
4. Grabham P, Hu B, Sharma P and Geard C., 2011. Effects of ionizing radiation on three-dimensional human vessel models: differential effects according to radiation quality and cellular development. *Radiat Res.*, 175(1): 21-8
5. Haass C, Selkoe DJ. 2007. Soluble protein oligomers in neurodegeneration: lessons from the Alzheimer's amyloid beta-peptide. *Nat Rev Mol Cell Biol.* Feb; 8(2):101-12.

Acknowledgements

This work was supported by NASA grant NNX10AB38G. ■

Effect of Ionizing Radiation on Endothelial Monolayer Permeability and Barrier Function

Preety Sharma and Peter Grabham

Exposure to high charge and energy space radiation is a major health concern for astronauts during long term space mission [1]. Increase in permeability of vascular endothelium is the most common and immediate event to radiation injury. At clinically relevant doses, acute vascular damage in the form of hyperpermeability, apoptosis, and edema is visible within hours of irradiation in normal tissue [2]. The endothelium monolayer integrity *in vivo* is regulated by two specialized intercellular junctions the adherens junction (AJ) and the tight junctions (TJ). The tight junctions components include transmembrane proteins claudins, occludins and junctional adhesion molecules (JAMs). Cytoplasmic components of TJ such as ZO-1, ZO-2 and ZO-3 among others link the transmembrane TJ components to the actin cytoskeleton. Adherens junctions are composed of transmembrane glycoproteins of the cadherin superfamily of which vascular endothelial (VE)-cadherin is found in human endothelial cells. Redistribution or changes in the components of tight and adherens junction proteins such as occludin, VE-cadherin, claudin, ZO-1, ZO-2 has been shown to mediate permeability changes in endothelial cells. These changes may occur in response to inflammatory mediators such as histamine or thrombin during pathologic conditions [3, 4] or during the normal process of proliferation and angiogenesis in response to vascular endothelial growth factor (VEGF) [5]. The blood brain barrier (BBB) is mainly formed by tightly associated brain microvascular endothelial cells interacting with different cell components such as pericytes, astrocytes, and neurons. Astrocytes are known to induce and maintain the BBB properties through the secretion of soluble factors and cell-cell to contact [6, 7].

The aim of the present experiments was to evaluate the effects of ionizing space radiation on the brain endothelial barrier properties by studying the transport of fluorescently labeled tracer molecules across the endothelial monolayer cultures grown on transwell inserts under different growth conditions. Radiation effects on the adhesion proteins and actin cytoskeleton were also visualized on endothelial cultures using immunocytochemistry and confocal microscopy.

Measurement of transendothelial electrical resistance (TEER) using human brain microvascular endothelial cells in different growth conditions

In order to optimize the conditions appropriate for BBB permeability studies we initially performed TEER measurements on human brain microvascular endothelial cells (HBMVEC) in different media conditions over time using electric cell-substrate impedance sensing (ECIS) (Applied BioPhysics, Rochester, NY). Media commonly used for growth of endothelial cells, the endothelial growth media (EGM) and for differentiation endothelial growth media 2 (EGM2) were used. The difference between the EGM-2 and EGM media is presence of angiogenic factors, such as VEGF and human fibroblast growth factor (hFGF). In the presence of the EGM, HBMVEC at two different densities (0.24×10^5 and 1×10^5) reached the maximum resistance of 600 ohms by day 4. TEER values were markedly higher reaching 800 ohms on day 2 for HBMVEC grown in EGM2 or when the medium was switched from EGM to EGM2 (Fig.1).

According to model of Giaever and Keese [8] the ECIS resistance data can be resolved into components that distinguish the resistance to current flow beneath the cell layer (α) from the resistance to current flow between adjacent cells (R_b). α depends on the characteristics of the cell-matrix adhesion and R_b represents the true barrier function of endothelial cells [9]. The resistance values in our experiment represent the total resistance measured. VEGF is known to control cell surface expression of class of adhesion proteins-integrins. Integrins are involved in mediating adhesion of cell to extracellular matrix and sometimes to other cells. VEGF and FGF, in coordination with integrins, play a central role in development and differentiation of the vasculature during angiogenesis [10]. The resistance values for endothelial cells grown in EGM were higher than for the astrocytes grown in the same media. HBMVEC are known to develop tighter cell-to-cell junctions essential for their role as CNS barrier supporting the higher resistance observed. The resistance values reached high when HBMVEC were grown in EGM2 medium. One possible explanation for that is additional supply of growth factors VEGF and FGF by the medium. These factors may have stimulated integrin expression on the cell surface resulting in better cell adhesion to ECM increasing the α component and thus overall resistance indicating the importance of both cell-to cell contacts and the cell-matrix adhesion in complete development of the tighter junctions and monolayer.

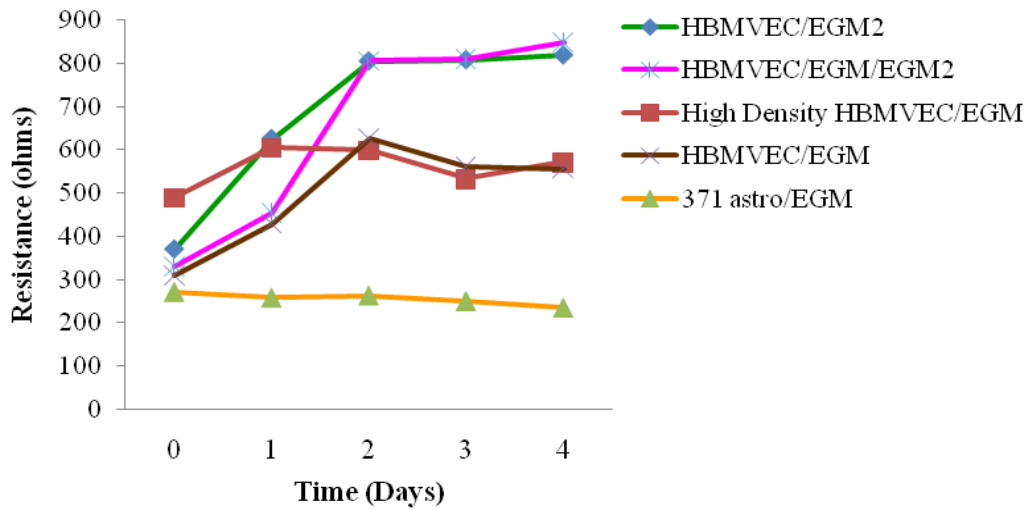


Figure 1. Measurement of transendothelial resistance using human brain microvascular endothelial cells in different growth conditions.

Effect of space radiation on permeability of human endothelial transwell cultures

Space radiation consists of a range of high charge and energy particles with varying linear energy transfer (LET). Previous studies in our laboratory had shown the sensitivity of human umbilical vein endothelial cells (HUVEC) to space radiation according to LET of the charged particle and developmental stage of the 3D vessel tissue model [11]. To follow up on the events leading to the breakdown or reduction of the vessel structure as observed with Fe ions (1GeV) at 0.8 Gy in mature vessels or low LET protons (1GeV) at 0.4 Gy, we investigated the permeability characteristics of the endothelial cells using a human blood brain barrier model. HBMVEC were grown on permeable membrane transwell inserts placed in 24 well plate, in EGM or EGM2. The top well represents the luminal (blood) and bottom well abluminal (brain)

side of the blood brain barrier. Alexaflour 488 ovalbumin tracer molecule was added to the media in the top well immediately before exposure to high energy iron ion (1GeV) and proton (1GeV) radiation. A fixed volume (50ul) of medium from the bottom well was collected at hourly intervals up to 3 hours on the day of irradiation or 24 hours later after radiation. The samples were read at 485nm using Biotek ELISA plate reader with Gen4 software. This was initially performed on cells grown in EGM media commonly used in assays investigating the effects of inflammatory mediators such as histamine or thrombin during pathologic conditions. A dose response curve indicated no change in permeability of the HBMVEC in response to space radiation (protons and iron ion) irrespective of dose, radiation type, or radiation quality up to 28 hours after irradiation (Fig. 2a). Similar results were obtained when cells were grown in EGM2.

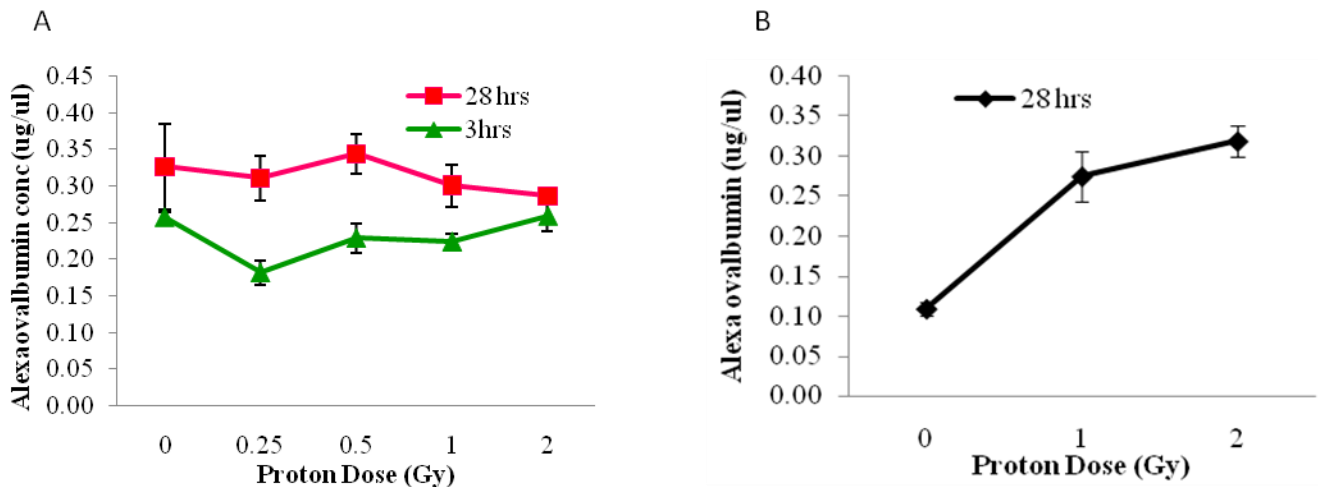


Figure 2. Effect of HZE ionizing radiation at different doses on endothelial permeability monitored by transport of carrier molecule Alexaflour ovalbumin through human endothelial 2D transwell monolayer cultures over time using a) EGM growth medium and b) EGM2 differentiation medium with astrocytes.

The control levels of permeability in these cultures were found to be high when compared to the levels in published mice studies using tracer molecules and brain histology, indicating that a fully impermeable barrier was not produced. This particular assay is useful for determining the effects of agents like inflammatory mediators that cause large changes in the cell shape but is not sensitive enough for more subtle changes in the permeability of the BBB. One of the key features of the endothelial cells in the blood brain barrier is presence of extremely tight 'tight junctions' minimizing the exchange of polar solutes between blood plasma into the brain [4]. *In vivo* the brain endothelial cells are known to interact with astrocytes and it has been shown that the endothelial tight junctions are enhanced when co-cultured with astrocytes or in the presence of ACM. There is still debate

as to whether direct contact between the two cell types is required for complete endothelial cell differentiation or soluble factors secreted by astrocytes are sufficient [7, 12]. In order to replicate *in vivo* conditions more closely, donor matched astrocytes were added to the bottom wells that had HBMVEC growing on the top of the membrane insert. Cells were grown in EGM-2 and here the serum was removed immediately prior to irradiation with 1GeV protons.

The monolayer developed tighter junctions in the presence of astrocytes and the absence of serum as indicated by a 3-fold lower permeability in controls (Fig. 2b). Results so far indicate an increase in permeability in response to proton dose at 28 hours. Ongoing studies will examine the effects of other ion species and energies.

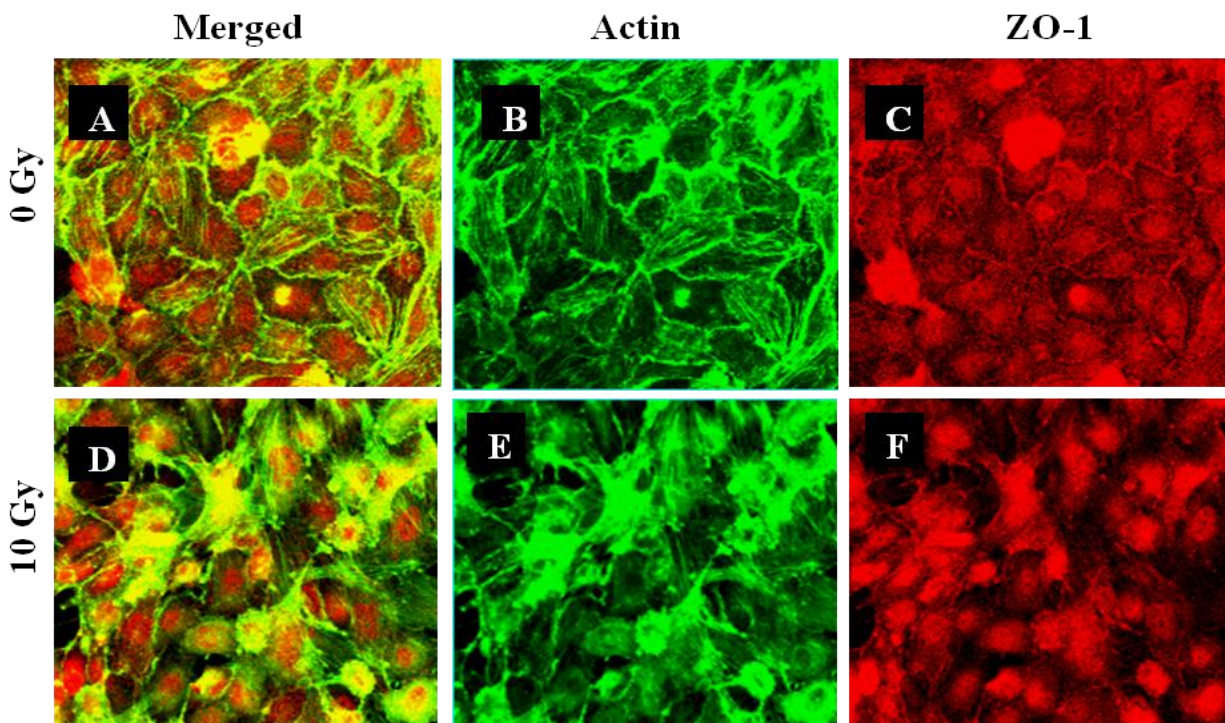


Figure 3. 2D HBMVEC monolayer transwell cultures were irradiated with 10Gy gamma source or unirradiated. Actin was found to relocate from cell periphery (B, 0Gy) and form stress fibers (E, 10Gy); ZO-1 was found to localize from cell to cell contact (C, 0Gy) to perinuclear area (F, 10Gy). Panels A and D are merged images of (B, C) and (E, F) respectively.

Gamma radiation effects on endothelial adhesion proteins

Preliminary studies indicated an increase in permeability of the endothelial cells grown in EGM media in response to 10Gy gamma rays unit as measured using fluorescent ovalbumin tracer diffusion (not shown). Immunocytochemistry of the exposed cells were performed to identify changes in actin organization and ZO-1. In non irradiated HBMVEC, F-actin stained using rabbit Alexa 488 anti-phalloidin was found to be strongly localized at the cell margin and few actin bundles were present within the cell body (Fig. 3a). Irradiation with 10Gy gamma led to reorganization of actin cytoskeleton

as indicated by disappearance of the thick peripheral F-actin band and appearance of stress fibers. The tight junction scaffolding protein ZO-1 was visualized and found to be strongly localized at the areas of cell-to-cell contact with minimal peri-nuclear staining. Marked ZO-1 redistribution was observed at 3 hours after 10 Gy and ZO-1 appeared to localize from areas of cell-to-cell contact to the perinucleus region. Based on these results, studies are in progress to characterize the response of actin, ZO-1 and other adhesion molecules to space radiation in endothelial cells grown in differentiation medium and to correlate these changes with alterations in permeability.

References

1. Nelson, G.A., Fundamental space radiobiology. *Gravit Space Biol Bull*, 2003. 16(2): p. 29-36.
2. Gabrys, D., et al., Radiation effects on the cytoskeleton of endothelial cells and endothelial monolayer permeability. *Int J Radiat Oncol Biol Phys*, 2007. 69(5): p. 1553-62.
3. Bazzoni, G.B., et al., In vivo effect of aluminium upon the physical properties of the erythrocyte membrane. *J Inorg Biochem*, 2005. 99(3): p. 822-7.
4. Abbott, N.J., et al., Structure and function of the blood-brain barrier. *Neurobiol Dis*, 2010. 37(1): p. 13-25.
5. Petty, M.A. and E.H. Lo, Junctional complexes of the blood-brain barrier: permeability changes in neuroinflammation. *Prog Neurobiol*, 2002. 68(5): p. 311-23.
6. Dohgu, S., et al., Transforming growth factor-beta1 upregulates the tight junction and P-glycoprotein of brain microvascular endothelial cells. *Cell Mol Neurobiol*, 2004. 24(3): p. 491-7.
7. Siddharthan, V., et al., Human astrocytes/astrocyte-conditioned medium and shear stress enhance the barrier properties of human brain microvascular endothelial cells. *Brain Res*, 2007. 1147: p. 39-50.
8. Giaever, I. and C. R. Keese (1991). "Micromotion of mammalian cells measured electrically." *Proc Natl Acad Sci U S A* 88(17): 7896-7900
9. Di Cello, F., et al., Divergent effects of zinc depletion in brain vs non-brain endothelial cells. *Biochem Biophys Res Commun*, 2005. 335(2): p. 373-6.
10. Hynes, R.O., B.L. Bader, and K. Hodivala-Dilke, Integrins in vascular development. *Braz J Med Biol Res*, 1999. 32(5): p. 501-10.
11. Grabham, P., et al., Effects of ionizing radiation on three-dimensional human vessel models: differential effects according to radiation quality and cellular development. *Radiat Res*, 2011. 175(1): p. 21-8.
12. Ma, S.H., et al., An endothelial and astrocyte co-culture model of the blood-brain barrier utilizing an ultra-thin, nanofabricated silicon nitride membrane. *Lab Chip*, 2005. 5(1): p. 74-85.

Acknowledgement

This work was supported by NASA grant NNX10AB38G. ■



CRR members (L-r): Dr. Peter Grabham, Dr. Preety Sharma, Dr. Charles Geard, Mr. Gary Johnson and Dr. Gerhard Randers-Pehrson.

Ultraviolet Light Exposure Influences Skin Cancer in Association with Latitude

Miguel Rivas^a, María C. Araya^b, Fresia Caba^c, Elisa Rojas^a and Gloria M. Calaf^d

The increase in the amount of ultraviolet (UV) light that reaches the earth due to the destruction of the ozone layer is considered to be responsible for the worldwide increase in skin cancer. For physical and biological reasons, UV light has been divided into three regions: UVA (320-400 nm), UVB (290-320 nm) and UVC (100-290 nm). UV light has very high energy, and although human exposure to UV radiation causes a few beneficial health effects such as vitamin D3 formation, it causes many detrimental health effects such as sunburn, ocular damage, photoaging, immune suppression and skin cancer (1). Ozone depletion, the level of UV light, elevation, latitude, altitude and weather conditions influence the emission of UV radiation reaching the surface of the earth. Skin cancer has been associated with prolonged exposure to UVB. It has been reported that excessive levels of UVA and UVB lights have multiple effects, which can be harmful to humans (2-9). The amount of light that reaches the earth is strongly dependent on the ozone layer, with absorption increasing with shorter wavelengths. UVA light has high atmospheric transmission (3), while short-wavelength UVC light is completely absorbed and does not reach the surface of the earth (9). Solar UVB light (290-320 nm) has multiple effects that can be harmful to humans. Even if a small amount of UVB light reaches the surface of the earth, it can be the most dangerous of the UV light types (3).

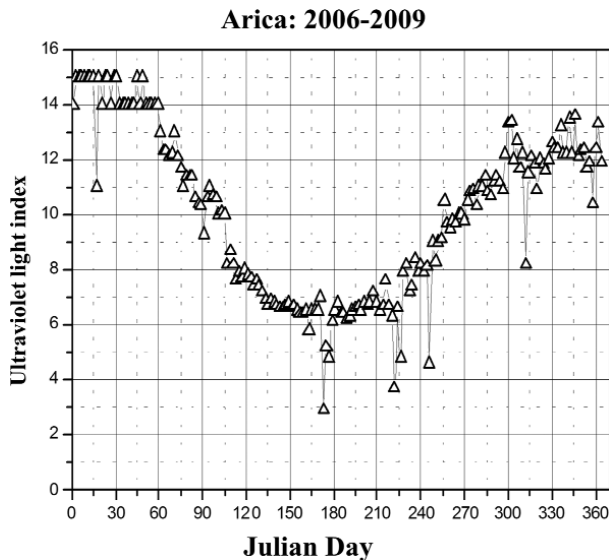


Figure 1. Daily mean values of ultraviolet solar light index (UVI) obtained between 2006 and 2009 in Arica.

The risk of skin cancer varies with altitude, latitude and skin pigmentation, which are all modified by overexposure to UV light (3). As the incidence of skin cancer in fair-skinned individuals is increasing at an alarming rate each year around the world, it is important to know the UV doses that people around the world are exposed to throughout their lives. In countries with fair-skinned populations, skin cancer is the most diagnosed of all cancers. It has been reported that in the United States

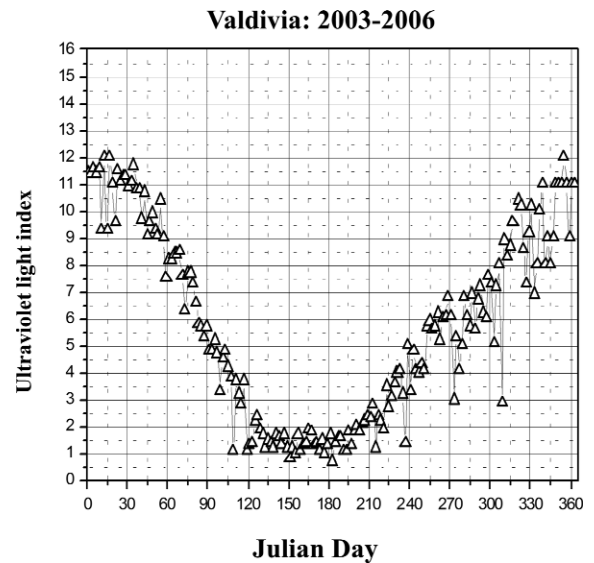


Figure 2. Daily mean values of ultraviolet solar light index (UVI) obtained between 2003 and 2006 in Valdivia.

there were over one million new skin cancer cases in 2002 (10). UV doses increase with increasing altitude and decreasing latitude. It is estimated that most indoor-working adult Europeans are exposed to 10,000-20,000 J/m² per year, Americans to 20,000-30,000 J/m² per year and Australians to 20,000-50,000 J/m² per year (excluding vacation, which can increase the dose by $\geq 30\%$). The outdoor UV doses are weighted for different biological effects, the time that people spend outdoors, their ambient exposures and the terrestrial and personal UV doses of adult outdoor and indoor workers as well as children and adolescents around the world. Ionizing radiation, environmental pollutants, chemical carcinogens and work-related exposures have been associated with skin cancers. Exposure to artificial UV radiation (tanning beds and lamps), aging, skin color, diet and smoking are considered important risk factors. Consequently, the interest in the prevention of sun overexposure is

increasing, as is the knowledge of photo-protection methods and radiation levels. The UVI is a well-known tool recommended by the World Health Organization (WHO) to avoid the harmful effects of UV sunlight. UVI forecasts are provided by many national meteorological services, but local UVI measurements can provide a more realistic and appropriate evaluation of radiation exposure levels.

Ultraviolet radiation exposure, latitude and skin cancer are important factors to analyze. In this study,

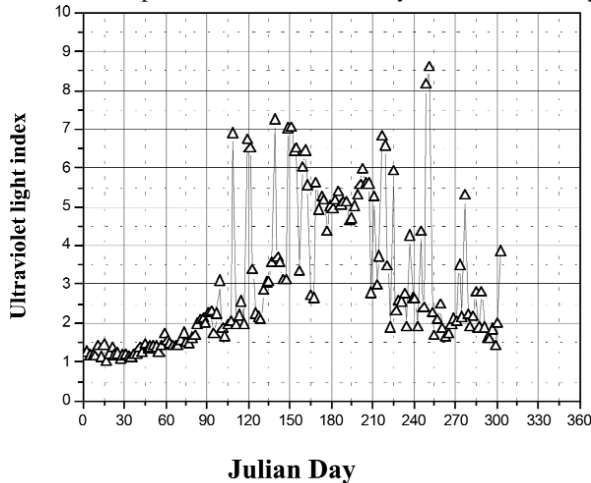


Figure 3. Quotient of maximum mean daily values of ultraviolet solar light index (UVI) obtained between 2006 and 2009 in Arica and between 2003 and 2009 in Valdivia.

comparative UVI values from Arica and Valdivia were considered. Arica is a city located in the subtropical zone of northern Chile, 25 meters above sea level, with latitude of 18°49'S and a longitude of 70°19'W. It has a microclimate characterized by stable meteorological conditions throughout the year, including low precipitation (<5 mm per decade), predictable winds, a high percentage of clear sky days and high ground reflectivity due to the presence of light sand. Due to its location near sea level, the population performs a great number of outdoor activities. Valdivia is a city located in the southern part of Chile, 19 meters above sea level with latitude of 39°38'S and a longitude of 73°5'W. The aim of the present study was to determine the relationship between latitude and the risk of skin cancer in two cities with different latitudes.

A national UV network exists in Chile that informs the population regarding the daily value of UVI from the city of Arica to Antarctica. Experimental measurements from Arica were obtained using a wide-band solar light biometer YES between 2006 and 2009. Experimental measurements from Valdivia were obtained by using a wide-band solar light biometer YES from 2003 to 2006. UVI measurements were classified according to the WHO parameters. Both instruments were calibrated according to the regulations of the World Meteorological Organization (WMO) and to an agreement with Tarapacá University and the Chilean Meteorological Organization (Dirección

Meteorológica de Chile, DMC) UV network. To explain the possible effect of radiation on skin cancer, revised pathological reports were analyzed in men and women from Arica and Valdivia, Chile. In Arica, data were collected between the periods 1997-2000 and 2001-2007, and in Valdivia between 1993-1997 and 1998-2002. In the present study, we investigated the characteristics of UV light in relation to skin cancer in populations from Arica and Valdivia, Chile. In this study, comparative values of UVI were considered to explain the possible effect of radiation on skin cancer in pathological reports from men and women. Figs. 1 and 2 show the daily mean values of UVI obtained from 2006-2009 in Arica, and from 2003-2006 in Valdivia. The UVI fluctuated from 6-15 between 2006 and 2009 in Arica. However, the UVI fluctuated from 1-12 between 2003 and 2009 in Valdivia. Fig. 3 corresponds to the quotient of maximum mean daily experimental values of UVI obtained between 2006-2009 in Arica and 2003-2006 in Valdivia, where the maximum quotient values were observed during the winter period. In Arica, cancer data were collected between the periods 1997-2000 and 2001-2007 and in Valdivia between the periods 1993-1997 and 1998-2002. When the distribution of several types of cancer was compared between Arica and Valdivia, the results showed that the incidence of skin cancer in Arica per 100,000

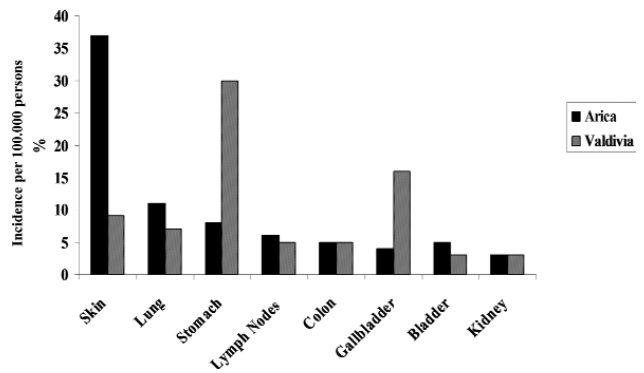


Figure 4. Incidence of several types of cancer registered in Arica and Valdivia. Data show the percentage of cases per 100,000 persons.

persons was the highest among other types, as shown in Fig. 4. Other types of cancer analyzed were lung, stomach, lymphatic nodes, bile ducts, colon, bladder and kidney, being 37% in Arica and only 9.1% in Valdivia. The incidence of the different types of skin cancer found in both cities is shown in Fig. 5. It can be seen that basocellular (69%) and espinocellular (28%) carcinomas, and melanomas (3%) were more predominant in Arica than in Valdivia (45%, 43% and 11 %, respectively). Fig. 6 shows the distribution of the different types of skin cancer in both cities in relation to gender. It can be seen that basocellular carcinoma was more predominant in men (70%) in Arica than in Valdivia. However, espinocellular carcinomas and melanomas were higher in women in Valdivia than in Arica, whereas melanomas were frequent in Valdivia. Fig. 7 shows an increase in the

incidence of skin cancer in men and women in Arica (Fig. 7A) and a slight increase in women between 1997-2000 and 2001-2007 in Valdivia and a decrease in men between 1997-2000 and 2001-2007 (Fig. 7B). It can be concluded that Arica received greater UV than the rest of

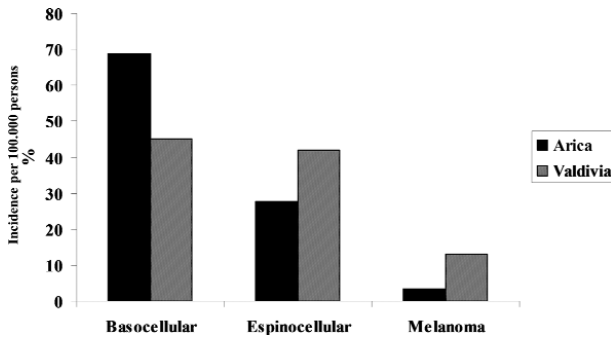


Figure 5. Incidence of several types of skin cancer registered in Arica and Valdivia. Data show the percentage of cases per 100,000 persons.

the country. Arica has registered the highest values of UVI in comparison to Valdivia, thus explaining the high prevalence of skin cancer in that population. The quotient of maximum mean daily values of UVI obtained from these two cities gave an indication that latitude played a role in the incidence of skin cancer. Very high levels were noted throughout the year due to the subtropical location of this city, which has a microclimate with a high number of clear sky days and it is also a desert adjacent to the Pacific Ocean, causing ground reflectivity. However, Valdivia presented the lowest UVI levels, especially in winter, in comparison to Arica. Skin cancers have been found in dermatoses and various types of keratoses, chronically injured or non-healing wounds and scars. In the present study, we analyzed the incidence of skin cancer in Arica and Valdivia according to pathological type and gender. Pathological reports of skin cancer indicated the possible effects of latitude in relation to radiation in these two cities. A greater percentage of basocellular carcinomas were found in Arica than in Valdivia, being more common in men than women,

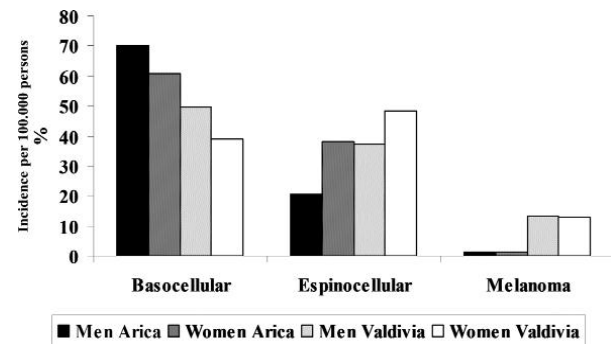


Figure 6. Incidence of skin cancer registered in Arica and Valdivia in relation to gender. Data show the percentage of cases per 100,000 persons.

whereas espinocellular carcinomas and melanomas were higher in Valdivia than in Arica.

The results of this study also indicate a steady increase in the incidence of skin cancer in Arica, most probably due to the high levels of UV light to which individuals are exposed throughout the year, as well as the cumulative effect of this type of radiation on the skin. Therefore, skin cancer incidence increased from 7.4-18.7 in men and from 10.0-21.7 in women in Arica between the periods 1997-2000 and 2001-2007. However, skin cancer incidence in Valdivia was 8.9 between 1993-1997 and 1998-2002 and was similar between men and women. Recreational sun exposure and sunburn are strong predictors of melanoma at all latitudes, whereas measures of occupational and total sun exposure predict melanoma predominately at low latitudes. Grant investigated risk variation by tumor site and latitude (10). Melanoma risk was related to sun exposure. A pooled analysis of 15 case-control studies (7216 controls and 5700 melanoma cases) was performed, correlating patterns of sun exposure, sunburn and solar keratoses with melanoma risk. The results indicated that recreational sun exposure was a risk factor for melanoma on the trunk and limbs, but not on the head and neck at various latitudes. Occupational sun exposure was associated with the risk of melanoma on the head and neck at low latitudes. Total sun exposure was associated with the increased risk of melanoma on the limbs at low latitudes, but not on other body sites or at other latitudes. Sunburn in children associated with melanoma on the trunk, limbs, and head and neck showed little variation across latitudes. As the presence of head and neck solar keratoses was associated with the increased risk of melanoma on the head and limbs, it was concluded that melanoma risk at different body sites was associated with different amounts and patterns of sun exposure. It has been reported that melanoma risk at different body sites is associated with different amounts and patterns of sun exposure (11).

Recreational sun exposure and sunburn are strong predictors of melanoma at all latitudes, whereas measures of occupational and total sun exposure predict melanoma predominately at low latitudes. As shown by Krishnamurthy, ultraviolet light from sunlight is implicated in the etiology of non-ocular malignant melanoma (12). Krishnamurthy reported the relation of such melanomas from seven cancer registries in different parts of India with latitude, altitude, ozone levels and ultraviolet (UV) light exposure. The results showed slight negative associations of melanoma with latitude, and statistically non significant ones with atmospheric ozone levels, and a positive association with UV. Lee and Scotto found that linked temporal and latitude changes rise in the incidence of and mortality from melanoma of the skin and they found that this is slowing down in younger age groups in the United States (13). In many white

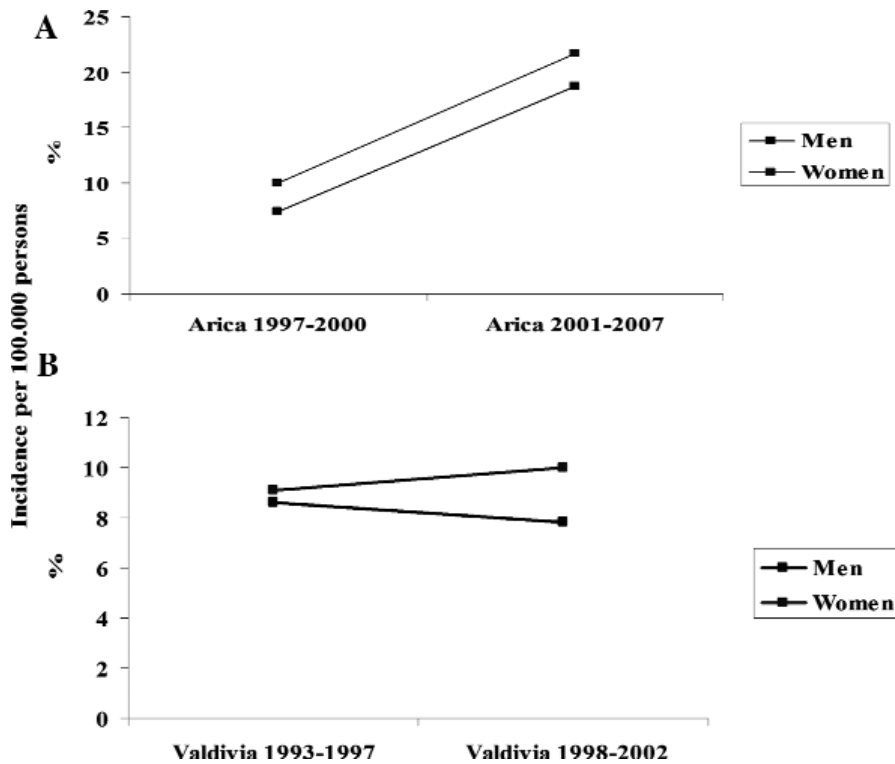


Figure 7. Incidence of skin cancer registered in Arica and Valdivia in relation to gender. In Arica, data were collected between 1997-2000 and 2001-2007, and in Valdivia between 1993-1997 and 1998-2002. Data show the percentage of cases per 100,000 persons.

populations, including those of the United States, melanoma incidence and mortality rates increased according to proximity of residence to the equator. Variations with age in this gradient do not seem to have been examined. They examined the influence of latitude on melanoma rates and found that it varied with age and found a decline from old age to youth in the influence of latitude for both the incidence of and mortality from melanoma of the skin in men, and for mortality in women. Furthermore, these changes in the relationship to latitude with age correlated with the changes in time trends with age.

The link with exposure suggests that the time trends in melanoma are driven by variations in damage to melanocytes during the early year of life which increases sensitivity to sunlight. This has implications for the general understanding of melanoma etiology and for health education. Our previous study showed that the basocellular and espinocellular carcinomas among the

malignant skin tumor types were more common in men (44.4 and 16.6%, respectively) than in women (24.9 and 10.7%, respectively) (14). Basocellular carcinoma was observed in individuals between 40 and 79 years of age. The incidence of skin cancer significantly increased between 2000 and 2006 per 100,000 persons. The factor of incidence of skin cancer per 100,000 populations significantly increased between 1980 and 2000 in both genders, but was higher in men (0.79-1.99) than in women (0.63-1.56). The results of this study indicate a steady increase in the incidence of skin cancer in Arica, Chile, most probably due to the high levels of ultraviolet light to which individuals are exposed throughout the year, as well as the cumulative effect of this type of radiation on the skin.

^aDepartamento de Física, Facultad de Ciencias, Universidad de Tarapacá;

^bHospital Juan Noé Arica;

^cDepartamento de Ciencias Clínicas, Universidad de Tarapacá;

^dInstituto de Alta Investigación, Universidad de Tarapacá, Arica, Chile;

References

1. Parrish JA, Anderson F, Urbach F and Pitts D: UVA: Biological Effects of Radiation with Emphasis on Human Response to Longwave Ultraviolet. Plenum Press, New York, p151, 1978.
2. Van der Leun JC, De Gruijl FR, Tevini M and Worrest RC: Ultraviolet carcinogenesis: environmental effects of ozone depletion. *Recent Results Cancer Res* 128: 263-267, 1993.
3. Madronich S, Mckenzie RI, Bjorn LO and Caldwell MM: Changes in biologically active ultraviolet radiation reaching the Earth's surface. *J Photochem Photobiol* 46: 5-19, 1998.
4. Jagger J: Solar UV. *Actions Living Cells*. Praeger, 1985.
5. Godlee F: Dangers of ozone depletion. *BMJ* 303: 1326-1328, 1992.
6. Jones RR: Ozone depletion and cancer risk. *Lancet* 2: 443-446, 1987.
7. Pathak MA, Riley FC and Fitzpatrick TB: Melanogenesis in human skin following exposure to long-wave ultraviolet and visible light. *Invest Dermatol* 39: 435-443, 1962.
8. Sánchez F: Consideraciones sobre la capa de ozono y su relación con el cáncer de piel. *Revista Méd Chile* 134: 1185-1190, 2006.
9. WMO: Report of the WMO Meeting of Experts on B Measurements, Data quality and Standardization of UV indices. No. 36, 1994.
10. Grant WB: Risk of internal cancer after diagnosis of skin cancer depends on latitude, smoking status and type of skin cancer. *Int J Cancer* 124: 1741-1742, 2009.
11. Chang YM, Barrett JH, Bishop DT, Armstrong BK, Bataille V, Bergman W, Berwick M, Bracci PM, Elwood JM, Ernstoff MS, Gallagher RP, Green AC, Gruis NA, Holly EA, Ingvar C, Kanetsky PA, Karagas MR, Lee TK, Le Marchand L, Mackie RM, Olsson H, Østerlind A, Rebbeck TR, Sasieni P, Siskind V, Swerdlow AJ, Titus-Ernstoff L, Zens MS and Newton-Bishop JA: Sun exposure and melanoma risk at different latitudes: a pooled analysis of 5700 cases and 7216 controls. *Int J Epidemiol* 38: 814-830, 2009.
12. Krishnamurthy S: The geography of non-ocular malignant melanoma in India: its association with latitude, ozone levels and UV light exposure. *Int J Cancer* 51: 169-172, 1992.
13. Lee JA and Scotto J: Melanoma: linked temporal and latitude changes in the United States. *Cancer Causes Control* 4: 413-418, 1993.
14. Rivas M, Araya MC, Durán V, Rojas E, Cortes J and Calaf GM: Ultraviolet light exposure and skin cancer in the city of Arica, Chile. *Mol Med Rep* 2: 567-572, 2009. ■



Visiting Professor Dr. Tadashi Kamada (middle), director of charged particle therapy at the NIRS in Japan with Drs. Clifford Chao (left) and Tom K. Hei (right) before his Grand Round lecture.



Visiting Professor Dr. Tadashi Kamada (right) with Dr. Eric J. Hall (left), Higgins Professor Emeritus of Radiation Oncology.

The Balance between Initiation and Promotion In Radiation-Induced Murine Carcinogenesis

Igor Shuryak, Robert L. Ullrich^a, Rainer K. Sachs^b and David J. Brenner

Studies of radiation carcinogenesis in animals allow detailed investigation of how the risk depends on age at exposure and time since exposure, and of the mechanisms which determine this risk, e.g. induction of new pre-malignant cells (initiation) and enhanced proliferation of already existing pre-malignant cells (promotion). To assist the interpretation of these patterns, we apply a newly-developed biologically-based mathematical model^(1, 2) to data on several types of solid tumors induced by acute whole-body radiation in mice^(3, 4).

The model includes both initiation and promotion and analyzes pre-malignant cell dynamics on two different time scales: comparatively short-term during irradiation, and long-term during the entire life span. The detailed assumptions and mathematical implementation of our model were described elsewhere⁽²⁾. Briefly, the model assumes that normal organ-specific stem cells, which reside in stem cell niches or compartments, referred to generically as “niches”, can be initiated to a pre-malignant state, either spontaneously or by radiation, and can then be transformed into fully malignant cells, which form tumors after some lag time. The parameters needed to apply this formalism to the selected data sets (discussed below), where a single acute radiation dose was administered, are presented in Table 1. To reduce the number of adjustable constants, we restricted some parameters to biologically plausible values or ranges (Table 1).

The equation for the mean expected number of new fully malignant cells per individual per unit time under

background conditions (A_{bac} , units = time^{-1}), which is an approximation for the cancer hazard function L time units later, was derived previously^(1, 2). It is repeated below, using the notation where age is defined as the sum of age at exposure (T_x) and the time after exposure (T_y):

$$A_{bac} = (a/b) (\exp[b (T_x + T_y)] - 1) \exp[-c (T_x + T_y)^2]$$

The expression for the radiation-induced excess relative risk (ERR) after a single acute radiation dose D is:

$$\text{ERR} = [(Q_1 Q_2 + Q_3)/Q_4] - 1, \text{ where: } Q_1 = (1 + Y D)/(1 + Y D (1 - \exp[-\delta T_y]));$$

$$Q_2 = [(\exp[b T_x] - 1) (1 - (1 - \exp[-\alpha D - \beta D^2])^2) + b X (D \exp[-\alpha D - \beta D^2])] \exp[b T_y];$$

$$Q_3 = \exp[b T_y] - 1; \quad Q_4 = \exp[b (T_x + T_y)] - 1$$

Our results suggest general mechanistic similarities between radiation carcinogenesis in mice and in human atomic bomb survivors (Fig. 1). The excess relative risk (ERR) decreases with age at exposure up to an exposure age of one year, which corresponds to mid-adulthood in humans; the pattern for older ages at exposure, for which there is some evidence of increasing ERRs in atomic bomb survivors, cannot be evaluated using the data set analyzed here. Also similar to findings in humans, initiation dominates the ERR at young ages, when there are few background pre-malignant cells, and promotion becomes important at older ages (Fig. 2).

Table 1. Summary of model parameters

Parameter	Units	Interpretation	Restrictions
a	time^{-2}	Spontaneous stem cell initiation and transformation	none
b	time^{-1}	Pre-malignant niche replication	none
c	time^{-2}	Pre-malignant cell aging	none
δ	time^{-1}	Homeostatic regulation of pre-malignant cell number per niche	none
Z	cells/niche	Carrying capacity for pre-malignant cells per niche	$Z = 1$
X	time/dose	Radiation-induced initiation	none
Y	dose ⁻¹	Radiation-induced promotion	none
α , β	dose ⁻¹ , dose ⁻²	Stem cell inactivation by radiation	$0.2 < \alpha < 0.6 \text{ Gy}^{-1}$; $\beta = 0$
L	time	Lag period between the first fully malignant cell and cancer	$L = 100$ days for cancer incidence, 200 for mortality

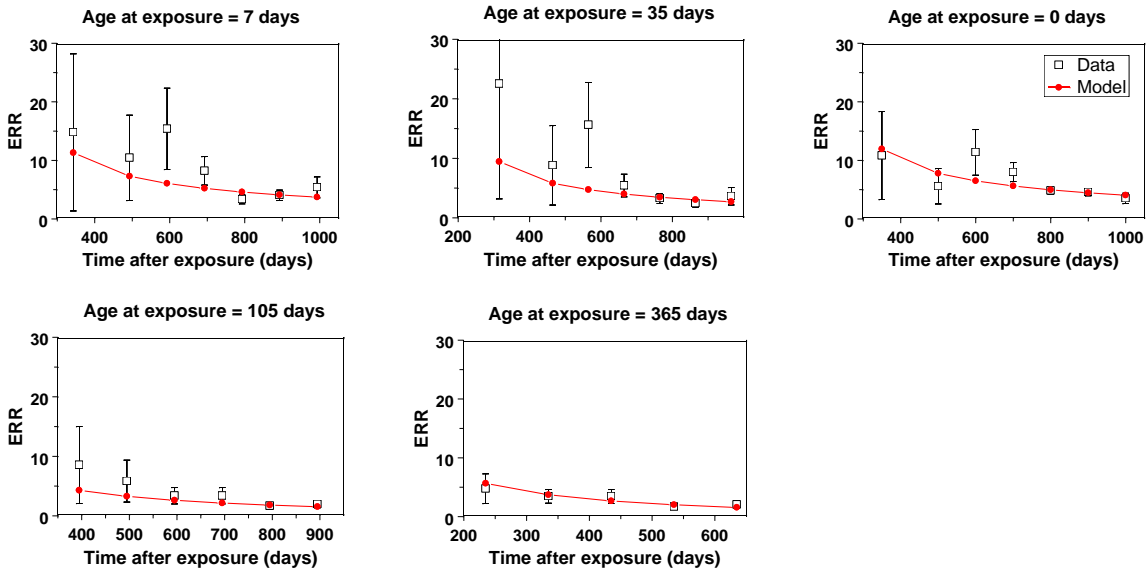


Figure 1. The data and best-fit model predictions for the excess relative risk (ERR) for mortality from all solid tumors combined at a dose of 1.9 Gy. The model predictions corresponding to the data points are represented by points (filled circles), which were generated using the corresponding combinations of dose, age at exposure, and time since exposure. The lines connecting the predicted points are shown for convenience only.

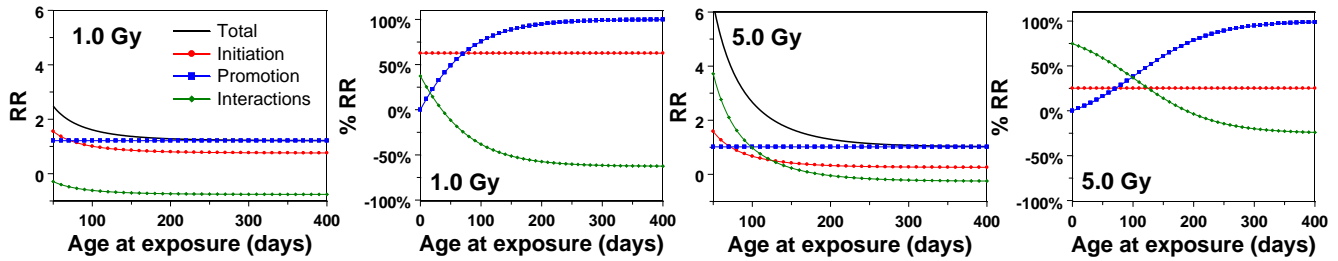


Figure 2. Contributions of initiation, promotion, and initiation-promotion interactions (i.e. promotion of radiation-initiated pre-malignant cells), all influenced by cell killing, to predicted liver tumor relative risk (RR) just after irradiation.

References

1. I. Shuryak, P. Hahnfeldt, L. Hlatky, R. K. Sachs and D. J. Brenner, A new view of radiation-induced cancer: integrating short- and long-term processes. Part II: second cancer risk estimation. *Radiat Environ Biophys* 48, 275-286 (2009).
2. I. Shuryak, P. Hahnfeldt, L. Hlatky, R. K. Sachs and D. J. Brenner, A new view of radiation-induced cancer: integrating short- and long-term processes.

- Part I: approach. *Radiat Environ Biophys* 48, 263-274 (2009).
3. S. Sasaki and N. Fukuda, Dose-response relationship for induction of solid tumors in female B6C3F1 mice irradiated neonatally with a single dose of gamma rays. *J Radiat Res (Tokyo)* 40, 229-241 (1999).
4. S. Sasaki and N. Fukuda, Temporal variation of excess mortality rate from solid tumors in mice irradiated at various ages with gamma rays. *J Radiat Res (Tokyo)* 46, 1-19 (2005). ■

^a Department of Radiation Oncology, University of Texas Medical Branch

^b Department of Math, University of California, Berkeley

Effects of Radiation Quality on Interactions between Oxidative Stress, Protein and DNA Damage in *Deinococcus Radiodurans*

Igor Shuryak and David J. Brenner

Ionizing radiation damages DNA and also induces oxidative stress, which can affect the function of proteins involved in DNA repair, thereby causing repair of DNA damage to become less efficient. We previously developed a mathematical model of this potentially synergistic relationship and applied it to γ -ray exposure data on the radiation-resistant bacterium *Deinococcus radiodurans* ⁽¹⁾. The next step, presented here, was to investigate the effects of radiation quality on these processes by applying the model to data on exposures of *D. radiodurans* to heavy ions with linear energy transfer (LET) of 18.5–11,300 keV/ μm ⁽²⁾.

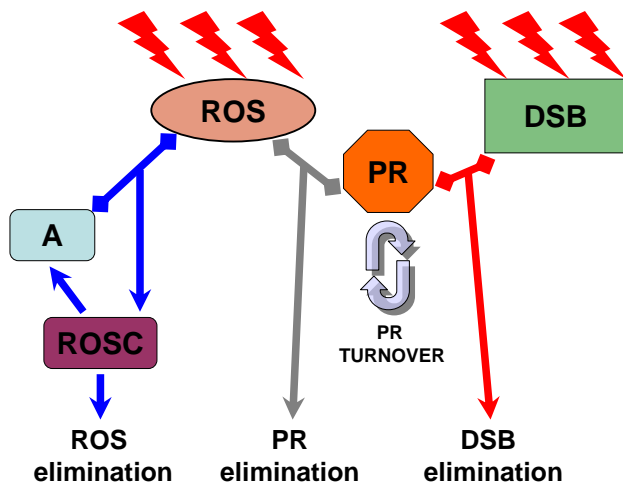


Figure 1. Schematic representation of model assumptions: Radiation (lightning symbols) produces reactive oxygen species (ROS) and DNA double strand breaks (DSB). ROS can react with antioxidants (A) to form a complex (ROSC), which then decays, resulting in elimination of ROS and regeneration of the antioxidants. DSBs are eliminated by repair involving specific proteins (PR), which are produced and degraded at a certain turnover rate. Importantly, ROS can damage these proteins, resulting in elimination of their repair capacity. Consequently, those ROS that are not removed by antioxidants damage DNA repair machinery and hinder correct repair of DSBs.

The main model assumptions are presented schematically in Fig. 1. The predicted cell survival probability (S) was calculated using equations 7 and 9 in the previous article ⁽¹⁾. Survival after a dose D of acute irradiation (i.e. when the irradiation time is short

compared with the characteristic DSB repair time) can be approximated as follows:

$$S = \exp[-c_8 D \exp[-k_{23} \exp[-k_1 D]]]$$

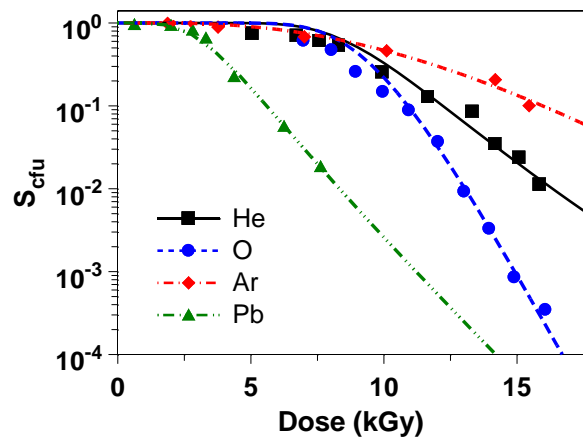


Figure 2. Typical *D. radiodurans* colony forming unit (CFU) survival curves for acute irradiation with ions of different LET. The symbols are data points, and the lines are corresponding model fits. Legend: black squares = He ions, LET = 18.5 keV/ μm ⁽³⁾; blue circles = O ions, LET = 290 keV/ μm ⁽³⁾; red diamonds = Ar ions, LET = 2010 keV/ μm ⁽⁴⁾; green triangles = Pb ions, LET = 11,300 keV/ μm ⁽⁴⁾.

Therefore, cell survival depends mainly on three parameter combinations: 1) DSB induction by radiation (c_8 , units = dose⁻¹), 2) repair protein inactivation by radiation (k_1), and 3) generalized DSB repair capacity of the cell (k_{23}). Only the first two of these are assumed to be radiation-related (c_8 and k_1); the third depends on culture conditions and cell properties (e.g. genetic background, exponential or stationary phase of culture growth, type of growth medium, oxygenation, etc.), but not on radiation (although different radiation types can produce different types of DSBs, here we neglect this for model simplicity).

The model adequately describes the observed cell survival data after heavy ion exposure using these three parameters combinations (Fig. 2). Although statistical uncertainties around best-fit parameter estimates are substantial, the behaviors of model parameters are consistent with current knowledge of LET effects (Fig. 3): inactivation cross-sections for both DNA and proteins

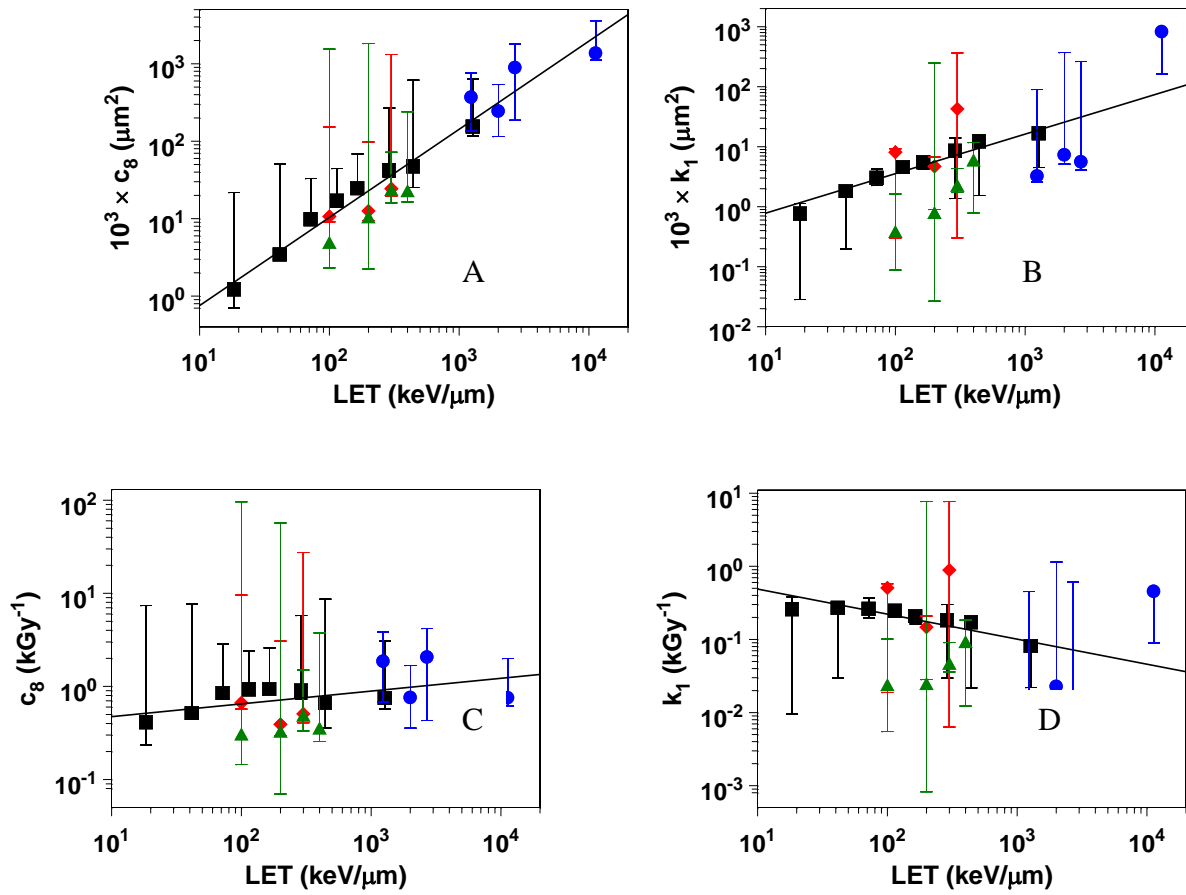


Figure 3: Best-fit values for DSB induction (parameter c_8) and for repair protein inactivation (parameter k_1) for each radiation type, as function of LET. Both parameters are shown per unit of radiation dose (kGy^{-1}) and as inactivation cross-sections (μm^2). Legend: black squares = reference⁽³⁾; blue circles =⁽⁴⁾; red diamonds =⁽⁵⁾, irradiation in physiological state; green triangles =⁽⁵⁾, irradiation in dry state. The lines represent best-fit regression equations with the form $\log(y) = a + b \log(x)$, where x is LET in $\text{keV}/\mu\text{m}$. The constants a and b , their 95% confidence intervals, and regression r^2 values are: Panel A = -1.257 ($-1.624, -0.890$), 1.137 ($0.998, 1.277$), 0.96 ; Panel B = -0.765 ($-1.774, 0.243$), 0.658 ($0.275, 1.042$), 0.51 . For panels C and D the r^2 values are 0.26 and 0.22 , and the slopes b and their confidence intervals are, by definition, the same as in panels A and B, respectively, minus unity. The four data points for irradiation of dry cells (green triangles) were not included in the regressions.

increase with increasing LET; DNA damage yield per unit of radiation dose also increases with LET; protein damage per unit dose tends to decrease with LET; DNA and especially protein damage yields are reduced when cells are irradiated in the dry state. These results suggest that synergism between oxidative stress and DNA damage may play an important role not only during γ -ray exposure, but during high-LET radiation exposure as well.

References

1. Shuryak and D. J. Brenner, A model of interactions between radiation-induced oxidative stress, protein and DNA damage in *Deinococcus radiodurans*. *J Theor Biol* 261, 305-317 (2009).

2. Shuryak and D. J. Brenner, Effects of radiation quality on interactions between oxidative stress, protein and DNA damage in *Deinococcus radiodurans*. *Radiat Environ Biophys* 49, 693-703.
3. D. L. Dewey, The survival of *Micrococcus radiodurans* irradiated at high LET and the effect of acridine orange. *Int J Radiat Biol Relat Stud Phys Chem Med* 16, 583-592 (1969).
4. H. Zimmermann, M. Schafer, C. Schmitz and H. Bucker, Effects of heavy ions on inactivation and DNA double strand breaks in *Deinococcus radiodurans* R1. *Adv Space Res* 14, 213-216 (1994).
5. M. Imamura, S. Sawada, M. Kasahara-Imamura, K. Harima and K. Harada, Synergistic cell-killing effect of a combination of hyperthermia and heavy ion beam irradiation: in expectation of a breakthrough in the treatment of refractory cancers (review). *Int J Mol Med* 9, 11-18 (2002). ■

Identify Urinary Biomarkers in Response to Radiation Using NMR Spectroscopy

Congju Chen, Truman R. Brown^a and David J. Brenner

As the threat of terrorism increases globally, the possibility of a radiological attack in a public place is of great concern. The range of possible scenarios for such events is wide, with as few as zero and as many as tens of thousands of individuals potentially exposed to high doses of radiation. How best to address the health effects of such a radiation exposure is a serious problem. In some situations it is clear that appropriate medical care can substantially shift the lethal dose at 60 days (LD50/60) to higher doses(1). Thus, in the context of such an attack, rapid, early screening of exposed individuals will be critical to identify the individuals who need urgent medical intervention and to reassure (in most scenarios) the majority of individuals who received minimal or low

radiation exposure. There is a pressing need for new high-throughput non-invasive biodosimetry methodologies for massive population screening scenarios(2). Here we suggest a high-throughput, non-invasive approach to identify radiation biomarkers in urine and demonstrate a proof of principle in mice.

Another issue we are addressing in the present work is the metabolism changes in response to partial-body radiation. This is based on the fact that most exposure will not be homogeneous whole body, but will be inhomogeneous, either because of shielding, or because radioactive material was ingested. We have demonstrated, for the first time, urinary biomarkers can be used to characterize partial-body radiation exposures

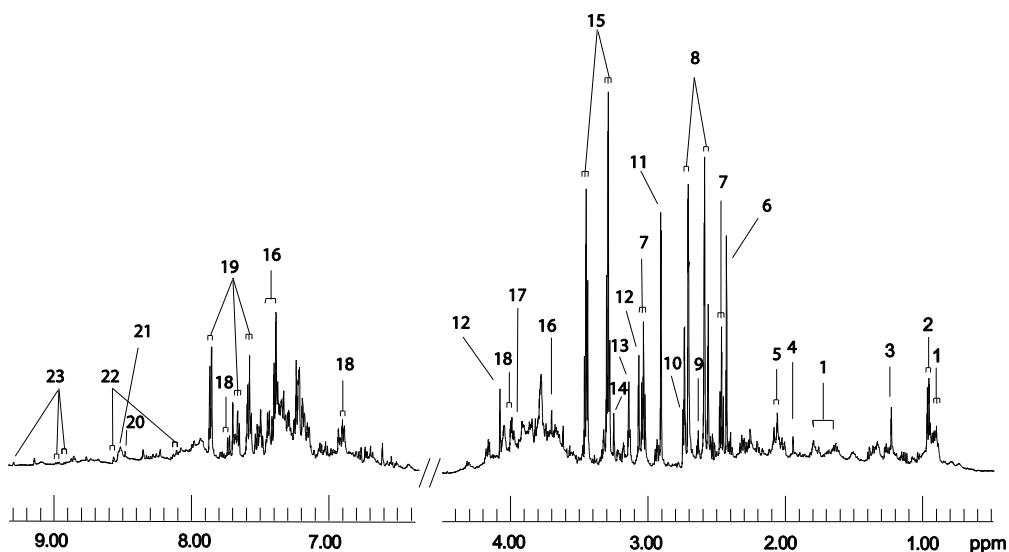


Figure 1. A typical 600 MHz ^1H NMR spectrum of mouse urine. The spectra region (4.5-6.4 ppm) containing imperfect water suppression and large urea peak was removed for display and analysis. The spectra in the aromatic region (6.4-9.3 ppm) were magnified 4 times compared with the region 0.5-4.5 ppm. Assignments: 1, 2-hydroxybutyrate; 2, 2-oxoisocaproate; 3, unknown singlet; 4, acetate; 5, N-acetyl group; 6, succinate; 7, 2-oxoglutarate; 8, citrate; 9, methylamine; 10, dimethylamine; 11, trimethylamine; 12, creatine; 13, malonate; 14, choline; 15, taurine and trimethylamine-N-oxide; 16, phenylacetylglycine; 17, creatinine; 18, 4-aminohippurate; 19, hippurate; 20, formate; 21, N-methyl-4-pyridone-5-carboxamide (4PY); 22, N-methylnicotinate (NMN acid); 23, N-methylnicotinamide (NMN amide).

^a Department of Radiology and Radiological Science,
Center for Advanced Imaging Research (CAIR),
Medical University of South Carolina, Charleston

Whole-body irradiation

For whole-body irradiation, mice were irradiated to 8 Gy X rays. Urine samples were collected for 7 days after exposure, from both irradiated and control mice. ^1H Nuclear Magnetic Resonance (NMR) spectra of all the urine samples were acquired on a spectrometer operating at a proton frequency of 600 MHz. A representative ^1H NMR spectrum and assignments of major resonances, are shown in Fig. 1. The spectral region (4.5-6.4 ppm) containing the residual water and large urea peaks was excluded from analysis. The multivariate data were analyzed by Principal Component Analysis (PCA) method in house-developed software HiRes (3).

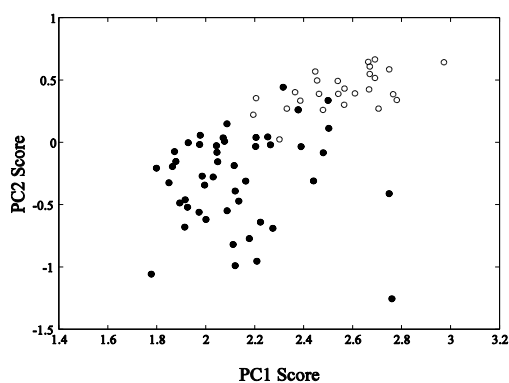


Figure 2: An example of PCA analysis from ^1H NMR spectra of urine from irradiated (filled circle) and control mice (open circle).

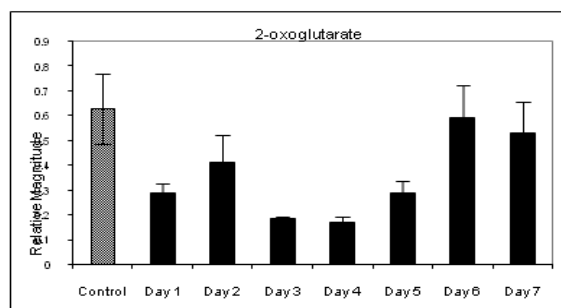


Figure 3. Relative magnitude on average representing citrate in urine samples from control mice (grey bar) and irradiated mice (black bar) for different post-irradiation period.

PCA analysis revealed a broad ranges of metabolism changes in response to radiation, which include creatine, succinate, methylamine, citrate, 2-oxoglutarate, taurine, N-methyl-nicotinamide, hippurate and choline. An example of PCA results is displayed in Fig. 2. Among those metabolites identified, most exhibited reduced levels after radiation exposure, with the most significant reduction coming from those metabolites involved in energy metabolism, i.e., succinate, citrate, 2-oxoglutarate. The temporal dependence of several biomarkers on radiation exposure has also been explored. The temporal

dependence of citrate level in irradiated mice is shown in Fig. 3. Since the temporal dependence is not the same for different biomarkers, combining several metabolomic biomarkers with different temporal dependence could provide an estimate of when the radiation exposure occurred (Fig. 4).

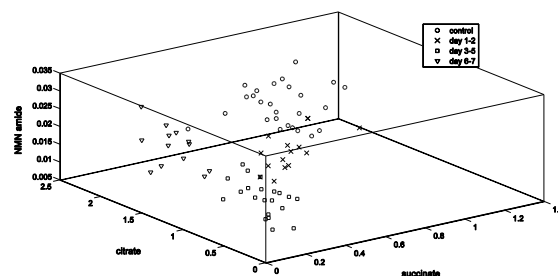


Figure 4. Three-dimensional display of PCA scores for citrate, succinate and NMN amide in the urine samples from the irradiated and control mice. The different symbols represent urine samples at different post-exposure period.

In summary, the responses of mice to a high radiation dose were characterized by broad ranges of metabolism changes, including slowed energy metabolism, damaged liver and kidney, and altered gut microbes. Among the many biomarkers identified in the present work, urinary levels of succinate, citrate and 2-oxoglutarate appear excellent candidates to serve as urine-based radiation biomarkers. Combining several biomarkers with different temporal dependence could provide useful information on when the radiation exposure occurred. This NMR-based work, along with the studies based on MS(4-6), provide a near-complete profile of radiation metabolomics in the rodent model.

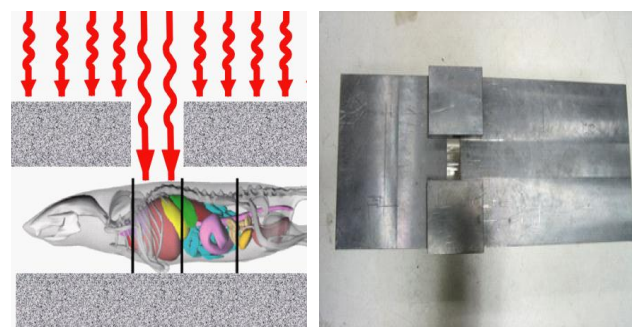


Figure 5. Left: The scheme to partially irradiate mouse. Four partial-body exposure scenarios were designed: head, cardiac/pulmonary, gastro-intestinal and reproduction organs irradiations. Right: The fully adjustable rectangular slot in the lead slab, which allowing us to select the region of the mouse to be irradiated.

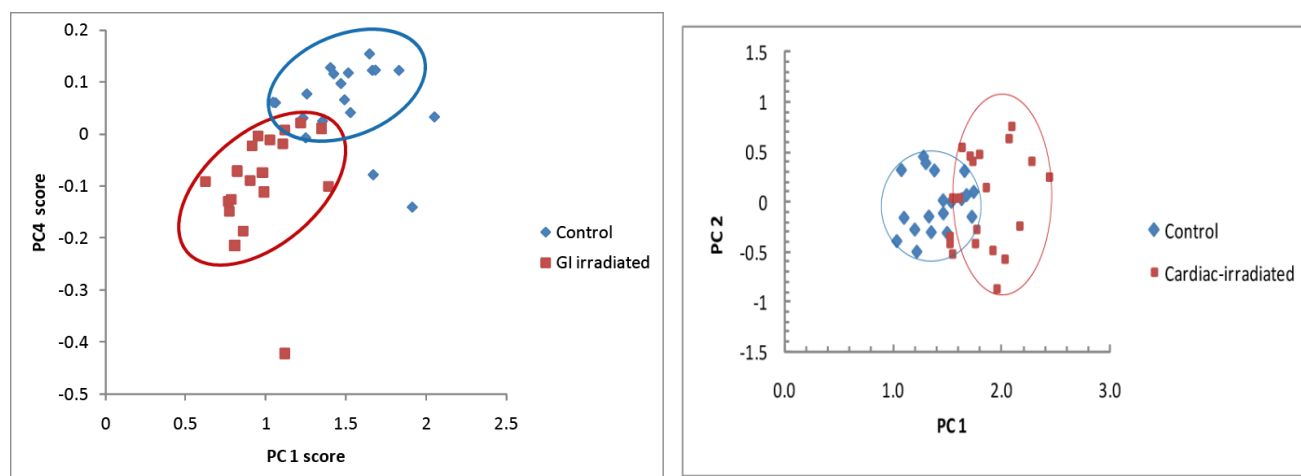


Figure 6. Example of PCA results on selected region of urine NMR spectra from GI- (left panel) and cardiac-irradiated (right panel) mice with 16 Gy X-ray.

Table 1. The identified biomarkers and their change directions in urines from irradiated mice (16 Gy) for different partial-body exposure scenarios compared with control group. TMAO: trimethylamine-N-oxide

Gastrointestinal		Cardiac/Pulmonary		Head	
Metabolites	Change	Metabolites	Change	Metabolites	Change
2-oxoisocaproate	↓	taurine	↑	taurine	↑
unknown (1.21ppm)	↓	TMAO	↑		
acetate	↓				
succinate	↓				
trimethylamine	↓				
creatine	↑				

Partial-body Irradiation

For partial-body irradiation, mice were partially exposed to two doses of X-ray irradiation (8 Gy and 16 Gy). As shown in Fig. 5, four partial-body exposure scenarios were designed to include head, cardiac/pulmonary, gastro-intestinal and reproduction organs irradiations. Urine collection protocol, NMR spectral acquiring and PCA analysis were the same as those described in whole-body irradiation section.

Preliminary PCA analysis indicated that we can distinguish partial-body irradiated mice from the control ones (Fig. 6). More importantly, different radiation scenarios showed different metabolism response phenotypes (Fig. 6). In other words, the urinary biomarkers in response to X-ray radiation exposures are specific to the nature of the partial body exposure. The identified biomarkers and their change directions in urines

from irradiated mice (16 Gy) for different partial-body exposure scenarios are summarized in Table 1. More experiments on different exposure scenarios with various dosages need to be done to characterize the specific partial body exposure.

Acknowledgements

We would like to thank Dr. Arthur G. Palmer III and his group (Department of Biochemistry and Molecular Biophysics, Columbia University) for their help in acquiring the NMR spectra. This work is supported by grant HDTRA1-07-1-0025 from the Defense Threat Reduction Agency (DTRA).

References

1. G. H. Anno, R. W. Young, R. M. Bloom and J. R. Mercier, Dose response relationships for acute ionizing-radiation lethality. *Health Phys* 84, 565-575 (2003).
2. G. Garty, Y. Chen, A. Salerno, H. Turner, J. Zhang, O. Lyulko, A. Bertucci, Y. Xu, H. Wang, et al., The RABIT: a rapid automated biodosimetry tool for radiological triage. *Health Phys* 98, 209-217 (2010).
3. Q. Zhao, R. Stoyanova, S. Du, P. Sajda and T. R. Brown, HiRes--a tool for comprehensive assessment and interpretation of metabolomic data. *Bioinformatics* 22, 2562-2564 (2006).
4. C. Lanz, A. D. Patterson, J. Slavik, K. W. Krausz, M. Ledermann, F. J. Gonzalez and J. R. Idle, Radiation metabolomics. 3. Biomarker discovery in the urine of gamma-irradiated rats using a simplified metabolomics protocol of gas chromatography-mass spectrometry combined with random forests machine learning algorithm. *Radiat Res* 172, 198-212 (2009).
5. J. B. Tyburski, A. D. Patterson, K. W. Krausz, J. Slavik, A. J. Fornace, Jr., F. J. Gonzalez and J. R. Idle, Radiation metabolomics. 1. Identification of minimally invasive urine biomarkers for gamma-radiation exposure in mice. *Radiat Res* 170, 1-14 (2008).
6. J. B. Tyburski, A. D. Patterson, K. W. Krausz, J. Slavik, A. J. Fornace, Jr., F. J. Gonzalez and J. R. Idle, Radiation metabolomics. 2. Dose- and time-dependent urinary excretion of deaminated purines and pyrimidines after sublethal gamma-radiation exposure in mice. *Radiat Res* 172, 42-57 (2009). ■



Dr. Gloria Calaf (left and right), Adjunct Associate Research Scientist, a Full Professor from Universidad de Tarapacá, Arica, Chile and her colleagues (middle).

Progress in Adapting the X-ray Machine to Low Dose Rate Studies

*Carl D. Elliston, Sally A. Amundson, Sunirmal Paul, Gary W. Johnson,
Lubomir Smilenov and David J. Brenner*

Most research in radiation biodosimetry has focused on acute exposure to radiation. Our own Center for High Throughput Minimally Invasive Radiation Biodosimetry has focused on determination and quantitation of biomarkers of radiation response. Exciting progress has been made on this front. Yet, it is also well established that there is a dose rate effect in humans, and how this dose rate effect may manifest biodosimetrically has yet to be established. In this context we are planning a series of experiments to investigate the effects of dose rate on biodosimetric endpoints in mice exposed *in vivo* and human blood samples exposed *in vitro*. These experiments will involve delivering the same dose ~4 Gy

to samples at dose rates ranging from 1 Gy/min to 4 Gy/day.

XRad 320

Experiments will be performed in our X-Rad 320 Biological Irradiator (Precision X-Ray, North Branford, CT). This device provides a system for precise delivery of radiation doses to specimens in a self-contained, shielded cabinet. The system features an adjustable shelf, exchangeable beam hardening filters, and a programmable control panel that allows tube current ranging from 0.1 to 12.5 mA at its maximum 320 kVp. Exposures for up to 24 hours are possible.

Dose Uniformity

Ideally, in this study, all samples would receive the same dose, and each sample would receive a uniform dose throughout its volume, without being subjected to other forms of stress. The X-Rad 320 has excellent planar dose uniformity for a biological irradiator, however, there is still a variation of about 13% across the 25cm x 25cm area of the fields. Dose homogeneity can be much better

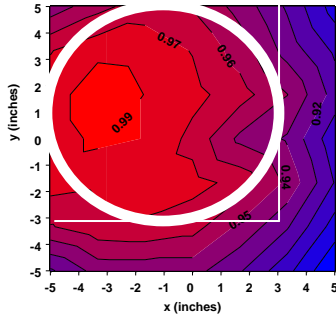


Figure 1

in a smaller area, however, with the area to be used constraining the number of samples to be irradiated per experiment. In addition, there is a reduction in dose as a function of depth through the sample. For a mouse 2 cm thick, there will be a reduction in dose of 5% just due to the inverse square law. Actual dose reduction due to attenuation and scatter may be greater.

Custom Beam Filter

An additional requirement is that both acute and low dose rate irradiations should be performed using the same quality of x rays. This requires that we can perform 1 Gy/minute for acute studies, yet be able to obtain 3-4 Gy/day for low dose rate studies. This must be achieved while changing only the mA and source to surface distance (SSD). The strongest manufacturer provided filter gives ~1.1 Gy/min at 50 cm SSD but a minimum of 7 Gy/day at maximum SSD. Therefore, we have created a custom Thoraeus filter (1.25 mm Sn, 0.25 mm Cu, 1.5 mm Al). This filter provides a dose rate of ~4 Gy/day at the maximum SSD, and a dose rate of ~ 1Gy/min at 40 cm SSD.

Additional Requirements for Blood Irradiations

For blood samples temperature, humidity, and carbon dioxide content need to be maintained. Additionally, we do not want any metal in the x-ray beam because the increased scatter would affect dose homogeneity. In order to do this, we have created an all plastic incubator (Figure 2). Blood is incubated in 50 ml conical tubes angled to keep the blood within about a 20 cm diameter in order to minimize planar dose variation. The samples are rotated to further minimize any dose inhomogeneity. Temperature is controlled through solid state heaters on a feedback loop attached to carbon fiber walls to distribute the heat evenly. A data logger monitors carbon monoxide, humidity and temperature within the incubator. The incubator holds 12 samples.

A commercial incubator's temperature is stable to 0.1° C (assuming the door is not opened). Tests have shown

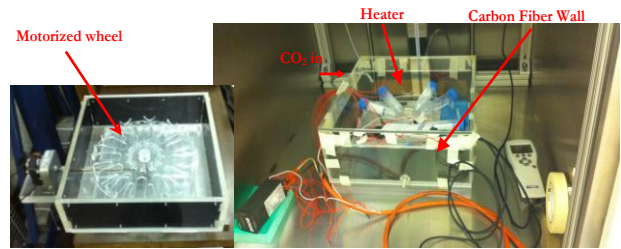


Figure 2

that the temperature within our custom incubator fluctuates about 0.5 – 1.5° C over 24 hours. We investigated whether this temperature variation was likely to confound any gene expression assays of radiation response by measuring expression of two heat shock (HSPA1L and HSPH1) and 1 cold shock (CIRBP) gene using quantitative real-time RT-PCR. We looked for heat or cold shock response in blood samples kept in our custom incubator at 37° C for 24 hours. Negative controls were kept in a commercial incubator for 24 hours (with the door never opened). Blood was heated to 42° C in a circulating water bath for 4 hours to provide a positive heat shock control. Cold shock controls were held at 32° C for 24 hours in our custom incubator with analysis performed afterwards. With the temperature maintained at a nominal 37° C, there was no difference in gene expression between our custom incubator and a commercial incubator.

Additional Requirements for Mouse Irradiations

For studies in mice with endpoints up to 24 hours, IACUC rules require that mice have a 12 hour light/dark cycle. Additionally, each mouse must have a minimum of 77 cm² and a height of 5". Further, the temperature must be maintained between 18-24° C to meet IACUC requirements and to assure that the mice do not undergo unintended stress, particularly important for metabolomic studies. Within these constraints, we would like to irradiate as many mice at a time as possible while maintaining

as uniform a dose as possible. We also require that no metal be in the beam and cannot use gel packs to replace water for mice as this would compromise metabolomic studies.



Figure 3

We have therefore built custom mouse housing (Figure 3) that can hold up to 8 mice, provides water from all-plastic bottles, and conforms to IACUC standards. The greatest challenge in this endeavor was to maintain the temperature inside the mouse housing within the 18-24° C

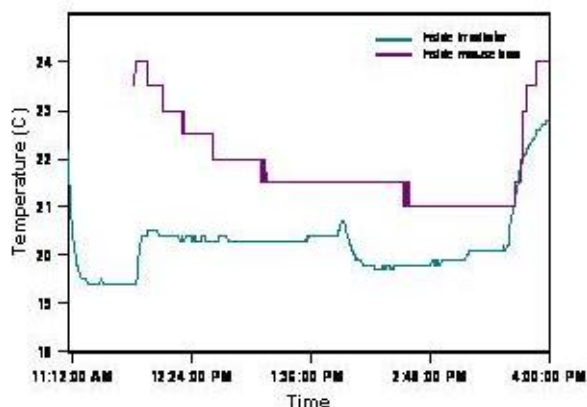


Figure 4

range. To accomplish this, we have designed and constructed a mouse air conditioner consisting of a CPU cooling fan, a water pump with cooling element, and an ice bath. The CPU cooling fan is a double fan with a

radiator between the two fans. Cold water circulates through the radiator, cooling the blown air. Measurements (Figure 4) show that this design adequately cools both the inside of the irradiator and the inside of the mouse housing.

Conclusions

In summary, we have encountered a number of technical challenges in designing systems for our planned low dose rate irradiations. We have designed and built a blood sample incubator, which is in the final stages of assembly. After assembly, we will perform final dosimetry measurements and reaffirm that there are no issues with gene expression from heat or cold shock. The mouse housing is complete and ready for biology.

Acknowledgements

We would like to thank Drs. Gerhard Randers-Pehrson and Guy Garty for their helpful insights, and Dr. Congju Chen for her help with irradiation of animals. The support of Dr. Lieberman's lab and the medical physics team in radiation oncology were also instrumental in this work. This work is supported by the Center for High-Throughput Minimally-Invasive Radiation Biodosimetry, National Institute of Allergy and Infectious Diseases grant number U19 AI067773. ■

Predicting the Risk of Secondary Lung Malignancy Associated with Breast Radiation Therapy

John Ng^a, Igor Shuryak, Yanguang Xu, KS Clifford Chao^a, Ryan J. Burri, Tom K. Hei, and David J. Brenner

Introduction

The risk of secondary lung malignancy (SLM) is a significant concern for women treated with whole breast radiation therapy after breast conserving surgery for early stage breast cancer. This concern has gained prominence as the use of adjuvant breast radiation has increased and as prognosis has steadily improved over the past decade (1). Furthermore, the latency period of radiation-induced second cancers is often greater than 10 years, and the risk persists 30 to 40 years after therapy (2). It would be particularly valuable to comparatively estimate the risk of secondary lung malignancies between two clinically

acceptable whole breast irradiation techniques such as supine whole breast irradiation, the current standard adjuvant radiotherapy technique, and the clinically accepted alternative techniques of prone breast irradiation and hypofractionated breast irradiation (3,4). A comparative analysis of the risk estimates between these techniques may impact treatment decision-making.

In this study, a novel biologically-based mathematical model of spontaneous and radiation-induced carcinogenesis (5, 6) was used to quantitatively predict the lifetime absolute and relative risks of secondary lung malignancy for women who were planned for breast radiation treatment in both the standard supine position and the alternative prone position, using both the standard fractionation schedule and the alternative hypofractionated schedule.

^a Department of Radiation Oncology, Columbia University Medical Center

Methods and Materials

Patient Characteristics

The treatment plans of fifteen patients with early stage breast cancer treated with whole breast radiotherapy at Columbia University Medical Center (CUMC) were retrospectively assessed. All had biopsy-proven node-negative breast carcinoma.

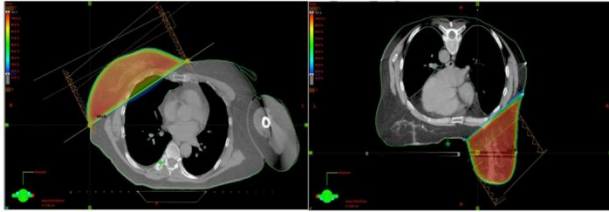


Figure 1. Sample Dose Color Map of the Same Patient in the Supine (left) and Prone (right) Position

Treatment Planning Methods

All patients were simulated by computed tomography (CT) for radiotherapy in both the prone and

the supine positions. Standard whole breast treatment plans were designed for each patient in each treatment position. An example of a typical patient treatment plan pair is shown in Figure 1.

Four plans were generated for each patient (n = 60 total plans): a standard fractionation plan in the supine position, a hypofractionated plan in the supine position, a standard fractionation plan in the prone position, and a hypofractionated plan in the prone position. The prescription dose for the standard fractionation schedule was 5000 cGy in 25 fractions. For the hypofractionated schedule, the prescribed dose was 4256 cGy in 16 fractions (4). All plans were normalized so that 95% of the breast target volume received 95% of the prescribed dose. Dose volume histograms (DVHs) of the target and normal tissues were calculated for each treatment plan. Figure 2 shows a typical matched dose-volume histogram for a patient simulated in both the supine and the prone positions with a standard fractionation schedule and a hypofractionated schedule used for each position.

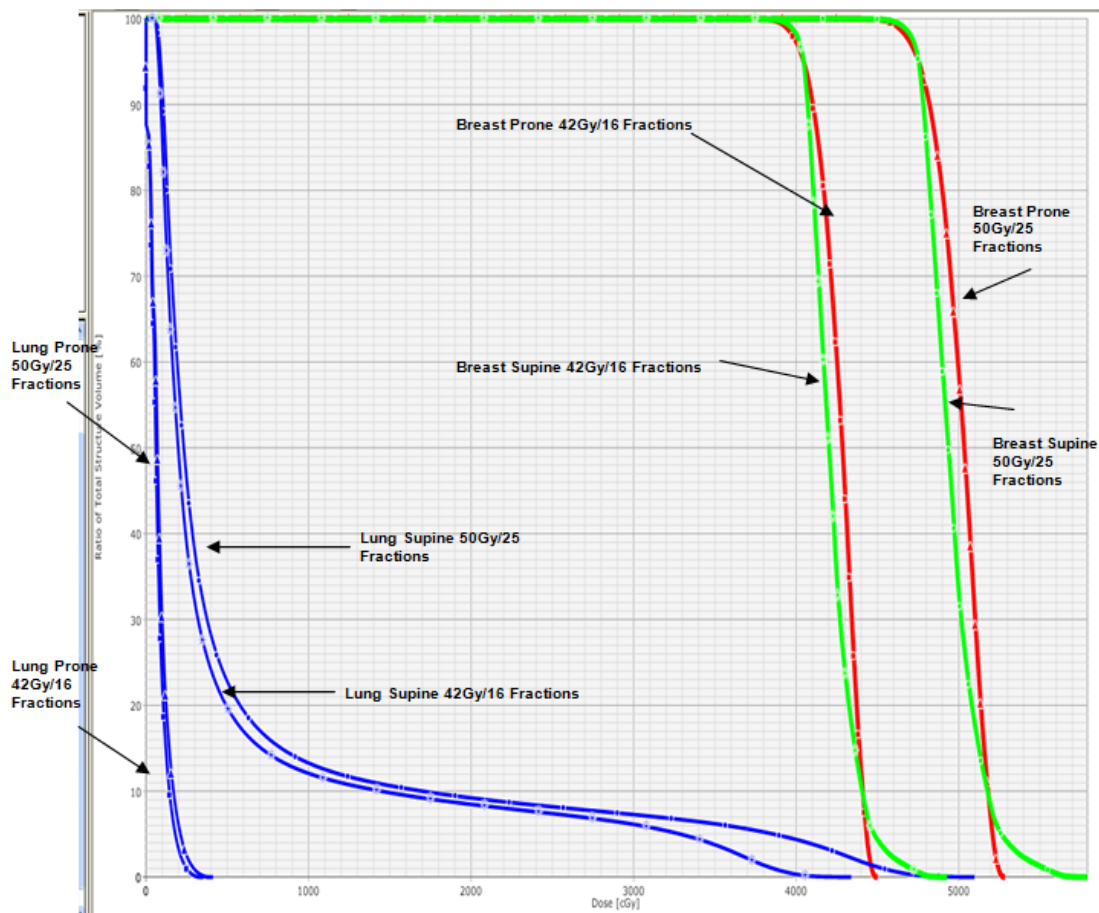


Figure 2. Sample DVH of the same patient in the prone and supine position for both the standard fractionation and hypofractionation schedules. Abbreviations: gy: Gray; DVH: Dose Volume Histogram

Differential DVH data for the ipsilateral lung from each treatment plan were then analyzed using a Fortran program that utilizes a biologically-based mathematical model of spontaneous and radiation-induced carcinogenesis (5,6). The carcinogenesis model (5,6) employed in the estimation of the risk of SLMs emphasizes the different kinetics of radiation-induced cancer initiation and promotion and tracks the yields of premalignant cells before, during, shortly after, and long after radiation exposure. In earlier work, this model was shown to reproduce the main dose-dependent features of radiation-induced second cancers after radiotherapy (6,7).

Expected Lifetime Absolute Risk (Prone vs. Supine)

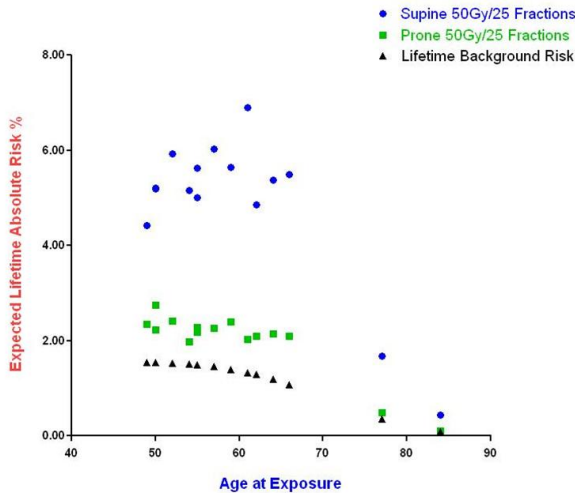


Figure 3. Predicted lifetime absolute risk of lung malignancy vs. supine (blue) breast irradiation for standard fractionation.

Abbreviations: Gy: Gray

Model-predicted absolute risks of lung cancer for each year after radiotherapy were adjusted by the probability of the patient to survive up to the given year, and all of these results were summed to obtain lifetime absolute risk. The lifetime absolute risks associated with each plan were averaged and compared with average lifetime absolute risks for individuals of the same age receiving no radiotherapy. This procedure allowed lifetime absolute risks of lung cancer, as well as the relative risks of SLMs of the different treatment techniques, to be estimated.

Results

There was statistically significantly less radiation dose delivered to the ipsilateral lung for each of the fifteen patients in the prone position when compared to the supine position. For the standard fractionation schedule of 5000 cGy in 25 fractions, the average mean lung dose (MLD) was measured to be 54.2 cGy +/- 5.2 cGy (standard error (SE)) in the prone position vs. 645.5

Mean Expected Lifetime Risk by Technique

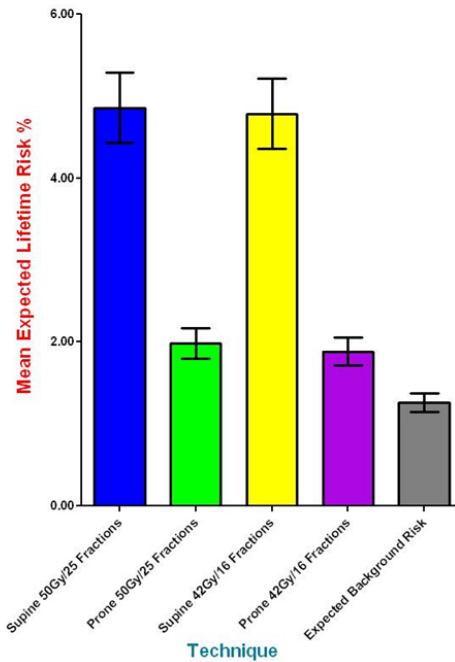


Figure 4. Mean predicted lifetime absolute risk of lung malignancy by breast irradiation technique.

Bars indicate standard error.

Abbreviations: Gy: Gray.

cGy +/-43.5 cGy in the supine position (p < 0.001, paired t-test).

The predicted lifetime absolute risks of lung cancer for each patient are shown as a scatter plot for treatment with standard fractionation in both the prone and supine positions in Figure 3. The mean predicted lifetime absolute risk of lung cancer for standard fractionation was 4.86% +/- 0.43% in the supine position and 1.99% +/- 0.18% in the prone position for a mean difference of 2.87% (95% confidence interval (CI) 2.28 to 3.47%; p<0.001). As illustrated in Figure 3, this risk difference was greater with younger patient age.

There was no significant difference in lifetime absolute lung cancer risk when comparing the two fractionation schedules for the supine position (p=0.18). The mean difference in absolute risk between the fractionation schedules was 0.10% (95% CI 0.08 to 0.13%; p<0.001) in the prone position. However, there was no difference in the relative risk (RR) of SLMs between standard fractionation and hypofractionated schedules in either the supine (RR 1.05, 95% CI 0.97 to 1.14) or prone positions (RR 1.01, 95% CI 0.88 to 1.15). A higher risk of SLMs was predicted for supine breast irradiation when compared with prone breast irradiation for both the standard fractionation and hypofractionation schedules (Relative Risk (RR) 2.59, 95% confidence interval (CI) 2.30 to 2.88, and RR 2.68, 95% CI 2.39 to 2.98, respectively).

Finally, the relative risks of SLMs for the various treatment techniques compared to background risk were

as follows: supine standard fractionation, RR 4.04, 95% CI 3.62 to 4.46; supine hypofractionation, RR 3.98, 95% CI 3.56 to 4.40; prone standard fractionation, RR 1.56, 95% CI 1.46 to 1.66; and prone hypofractionation, RR 1.48, 95% CI 1.40 to 1.57.

The mean expected lifetime absolute risks of lung cancer associated with all four treatment techniques and the background risk are shown in Figure 4.

Discussion

Several epidemiological studies with long-term follow-up have documented an increased risk of SLMs in women who have been treated with post-mastectomy radiotherapy (8) or supine whole breast radiotherapy (9). This standard of care technique, however, has been known to result in substantial levels of radiation delivered to nearby organs including the ipsilateral lung and the heart (10).

In recent years, alternative techniques of breast irradiation have emerged for patients with early stage breast cancer. Prone breast irradiation was initially developed to improve dose homogeneity in woman with larger breasts (11). The technique also typically results in decreased dose to normal tissues, including the heart and lungs, as the breast tissue tends to fall away from the chest wall. Many studies have confirmed the improved dosimetric results of prone breast irradiation by showing consistently decreased radiation dose to the lungs (10). However, there have been no studies published to date that quantify, or have attempted to quantify, the excess relative risk of secondary lung malignancy when a breast cancer patient is treated with radiotherapy in the supine position compared with the prone position.

Another alternative technique, using a hypofractionated schedule, has been shown to be equivalent to standard fractionated whole breast RT in a recently updated randomized controlled trial with 10-year median follow-up (4). Due to the relatively recent acceptance of this fractionation schedule, there have been no studies published to date that have quantified, or attempted to quantify, the relative risk of secondary lung malignancy when a breast cancer patient is treated with hypofractionated breast radiotherapy compared with standard fractionated breast radiotherapy.

The relative risk estimates for SLMs from the present study are comparable with the relative risks of secondary lung malignancies estimated from several retrospective series on patients treated with supine whole breast irradiation (9,12). A study from the Institut Curie examined the risk for different secondary malignancies after breast radiotherapy and noted a statistically significant increase for lung cancers, a risk that persisted after 10 years of follow-up from radiation treatment (9). In a large cohort study of patients from the Connecticut Tumor Registry, the estimated relative risk of secondary lung malignancy after breast radiotherapy was 2.8 after 15 years of follow-up (12).

Finally, a separate SEER analysis focusing on mortality showed a long-term increased risk of lung cancer mortality in patients treated with whole breast RT compared to the general population with a relative risk of 2.7 after 15 years (13).

The current study suggests that the predicted lifetime risk of radiotherapy-induced lung cancer is significantly lower when women are treated in the prone position with whole breast radiotherapy compared to the more commonly utilized supine position. According to these estimates, the relative risk of secondary lung malignancies may be decreased more than two-fold using the prone breast technique. On the other hand, hypofractionated breast radiotherapy did not appear to clinically significantly affect the secondary lung malignancy risk when compared with standard fractionation for a given treatment position. The predicted benefits of prone breast radiotherapy with respect to secondary lung malignancy risks are likely to be even greater for younger patients, as the predicted absolute risk of secondary lung malignancy increases with younger age.

Partial breast irradiation, a newer technique currently the subject of a large-scale randomized trial, NSABP B-39 (14), may result in an even lower risk of secondary lung malignancy than prone breast radiation. This topic is currently being studied at our institution in a separate modeling analysis.

Conclusions:

Patient position during whole breast radiation treatment is an important factor in determining the associated risk of secondary lung malignancy. Treatment in the prone position produces a substantially lower risk of secondary lung malignancy than treatment in the more common supine position. Quantifying this risk may be useful for clinicians as they counsel women with early stage breast cancer about their treatment options.

References

1. Jemal A, Siegel R, Xu J, et al. Cancer statistics, 2010. *CA Cancer J Clin* 2010;60:277-300.
2. Preston DL, Ron E, Tokuoka S, et al. Solid cancer incidence in atomic bomb survivors: 1958-1998. *Radiat Res* 2007;168:1-64.
3. Formenti SC, Gidea-Addeo D, Goldberg JD, et al. Phase I-II trial of prone accelerated intensity modulated radiation therapy to the breast to optimally spare normal tissue. *J Clin Oncol* 2007;25:2236-2242.
4. Whelan TJ, Pignol JP, Levine MN, et al. Long-term results of hypofractionated radiation therapy for breast cancer. *N Engl J Med* 2010;362:513-520.
5. Shuryak I, Hahnfeldt P, Hlatky L, et al. A new view of radiation-induced cancer: integrating short- and

- long-term processes. Part I: approach. *Radiat Environ Biophys*, 2009; 48:263-74.
6. Shuryak I, Hahnfeldt P, Hlatky L, et al. A new view of radiation-induced cancer: integrating short- and long-term processes. Part II: second cancer risk estimation. *Radiat Environ Biophys* 2009;48:275-286.
 7. Shuryak I, Sachs RK, Brenner DJ. A new view of radiation-induced cancer. *Radiat Prot Dosimetry* 2011;143:358-364.
 8. Woodward WA, Strom EA, McNeese MD, et al. Cardiovascular death and second non-breast cancer malignancy after postmastectomy radiation and doxorubicin-based chemotherapy. *Int J Radiat Oncol Biol Phys* 2003;57:327-335.
 9. Kirova YM, Gambotti L, De Rycke Y, et al. Risk of second malignancies after adjuvant radiotherapy for breast cancer: a large-scale, single-institution review. *Int J Radiat Oncol Biol Phys* 2007;68:359-363.
 10. Griem KL, Fetherston P, Kuznetsova M, et al. Three-dimensional photon dosimetry: a comparison of treatment of the intact breast in the supine and prone position. *Int J Radiat Oncol Biol Phys* 2003;57:891-899.
 11. Merchant TE, McCormick B. Prone position breast irradiation. *Int J Radiat Oncol Biol Phys* 1994;30:197-203.
 12. Inskip PD, Stovall M, Flannery JT. Lung cancer risk and radiation dose among women treated for breast cancer. *J Natl Cancer Inst* 1994;86:983-988.
 13. Darby SC, McGale P, Taylor CW, et al. Long-term mortality from heart disease and lung cancer after radiotherapy for early breast cancer: prospective cohort study of about 300,000 women in US SEER cancer registries. *Lancet Oncol* 2005;6:557-565.
 14. National Surgical Adjuvant Breast and Bowel Project (NSABP). Protocol B-39/RTOG 0413. A Randomized Phase III Study of Conventional Whole Breast Irradiation (WBI) Versus Partial Breast Irradiation (PBI) for Women with Stage 0, I, or II Breast Cancer. <http://www.nsabp.pitt.edu/B-39.asp> ■



Center for Radiological Research 2010 Christmas Party: Dr. Igor Shuryak (top left), Mr. Steve Marino (top right), Mr. David Cuniberti, Dr. Thomas Templin, Mr. Robert Morton (bottom left) and Dr. Preety Sharma (bottom right).

New Directions for the Center for High Throughput Minimally Invasive Radiation Biodosimetry

Guy Garty, Sally A. Amundson, Albert J. Fornace^a and David J. Brenner

In 2010 The Columbia Center for High Throughput Minimally Invasive Radiation Biodosimetry was funded for an additional 5 years. In the first 5 years the center has focused on development of biodosimetry assays and the required technologies for performing them at high throughputs, as would be required for response to a mass radiation event in a large city.

With this renewal, the overriding theme of the center remains high-throughput biodosimetry and the technology to achieve it. It is well established that this is a central and necessary component of any effective response to a large scale radiological event [1], and in the 5+ years that the Centers for Medical Countermeasures against Radiation (CMCR) program has been in existence, we have increased the potential biodosimetry throughput that may be achieved after a large-scale event from <100 / day to thousands per day using the Rapid Automated Biodosimetry Tool (RABiT) [2, 3]. We have developed gene expression signatures for biodosimetry [4, 5] and a nanofluidic platform for their rapid measurement [6], and have established the new field of radiation metabolomics [7, 8]. We have also partnered with the New York City Department of Health to investigate integrating biodosimetry into their emergency response plan [9].

The current 5-year cycle, however, takes a more “scientific” and less “technological” approach, utilizing the tools we have developed so far to answer key questions in biodosimetry.

“Beyond Simple Exposures”: Our initial proposal focused exclusively on external whole-body acute photon irradiation. The first main theme, over the next 5 years, is to assess the significance of the variety of other radiation scenarios that are likely to occur, in particular the effects of *low dose rate protracted exposure, partial-body exposure, internal emitters, and neutron exposure*.

To investigate these questions we have developed a low dose rate x-ray irradiator [10] for blood samples as well as for small animals. We are also developing a novel neutron source, based on the RARAF accelerator, which will mimic the neutron spectra expected from an improvised nuclear device (IND)[11]

We have also partnered with the Lovelace Respiratory Research Institute in Albuquerque, NM. We will use our biodosimetry endpoints to quantify radiation exposure in mice exposed to internal emitters, absorbed by inhalation, injection or ingestion.

“Beyond Dose: Towards Individual Radiosensitivity”: In that we have developed high-throughput systems for using various biomarkers for biodosimetry, we are in a unique position to probe the application of these biomarkers for *predicting inter-individual sensitivity to acute radiation syndromes* – our second major renewal theme. We have two interlaced motivations here: The first is to investigate correlations between our high-throughput biomarkers and individual acute radiation sensitivity, and the second is to probe the associated mechanisms. Both of these approaches build on – and would not be possible without – the high-throughput biodosimetry work that we have accomplished to date.

We will employ several models of inter-individual variability of radiation sensitivity to assess potential associations with our various biodosimetric endpoints. Using a human model, we will assess potential associations between high-throughput RABiT radiation response biomarkers and radiation-induced erythema, a model for acute radiation response, in 500 women undergoing post-lumpectomy radiotherapy.

We will also use a murine model consisting of eight inbred mouse strains representing a range of published LD50 values from 5.6 to 9.4 Gy. We will compare basic gene expression profiles and high-throughput RABiT radiation response biomarkers among these inbred strains to look for correlations with their LD50 values. A subset of these mouse strains will also be used to look for stochastic differences in gene expression and metabolomic markers between individual genetically identical mice exposed to the LD50. Early evidence suggests that such differences can identify the specific animals that will die as a result of such an exposure at very early times (1-3 days) after irradiation.

References

1. Pellmar, T.C. and S. Rockwell, and the Radiological/Nuclear Threat Countermeasures Working Group: Priority list of research areas for radiological nuclear threat countermeasures. *Radiat Res*, 2005. 163(1): p. 115-23.
2. Garty, G., et al., The RABiT: A Rapid Automated Biodosimetry Tool for radiological triage. *Health Physics*, 2010. 98: p. 209-217.
3. Garty, G., et al., The RABiT: A Rapid Automated Biodosimetry Tool For Radiological Triage II. Technological Developments International Journal of Radiation Biology, 2011. In Press.

4. Paul, S. and S.A. Amundson, Development of gene expression signatures for practical radiation biodosimetry. *International Journal of Radiation Oncology Biology Physics*, 2008. 71(4): p. 1236-1244.
5. Paul, S., et al., Prediction of In Vivo Radiation Dose Status in Radiotherapy Patients using Ex Vivo and In Vivo Gene Expression Signatures. *Radiation Research*, 2011. 175(3): p. 257-265.
6. Brengues, M., et al., Biodosimetry on small blood volume using gene expression assay. *Health Physics*, 2010. 98(2): p. 179-185.
7. Tyburski, J.B., et al., Radiation metabolomics. 1. Identification of minimally invasive urine biomarkers for gamma-radiation exposure in mice. *Radiation Research*, 2008. 170(1): p. 1-14.
8. Patterson, A.D., et al., The Role of Mass spectrometry-based metabolomics in medical countermeasures against radiation. *Mass Spectrometry Reviews*, 2010. 29(3): p. 503-521.
9. Garty, G., P.A. Karam, and D.J. Brenner, Infrastructure to Support Ultra High Throughput Biodosimetry Screening after a Radiological Event. *International Journal of Radiation Biology*, 2011. In Press.
10. Carl D. Elliston, Sally A. Amundson, Sunirmal Paul, Gary W. Johnson, Lubomir Smilenov and David J. Brenner, Progress in Adapting the X-ray Machine to Low Dose Rate Studies, *CRR Annual Report 87-9*, 2010.
11. Xu, Y., Neutron Microbeam, *CRR Annual Report 19-20*, 2010. ■

^aDepartment of Radiation Oncology, Biochemistry and Molecular & Cellular Biology, Lombardi Comprehensive Cancer Center, Georgetown University

Advances in the Lymphocyte Harvesting Module on the RABIT

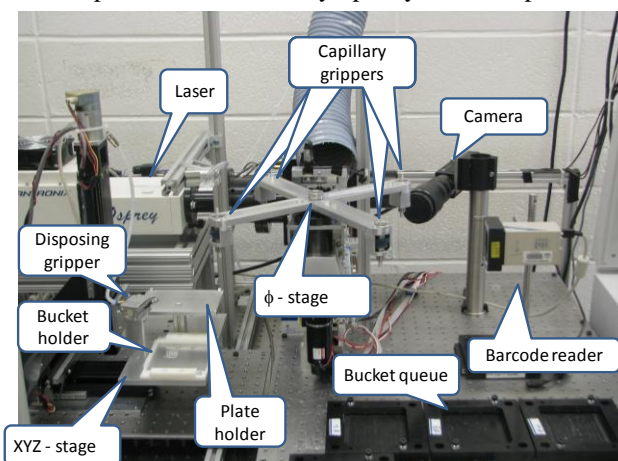
Guy Garty, Youhua Chen^a, Jian Zhang,^a Hongliang Wang,^a Nabil Simaan^a, Y. Lawrence Yao,^a and David J. Brenner

The RABiT (Rapid Automated Biodosimetry Tool) [1, 2] developed at the Columbia Center for High Throughput, Minimally Invasive Radiation Biososimetry is an automated, ultra-high throughput biodosimetry workstation. The RABiT analyzes fingerstick-derived blood samples (~30 μ l), either to estimate past radiation dose, or to identify individuals exposed above / below a cutoff dose.

One of the main challenges in rapid lymphocyte processing in the RABiT is the harvesting of lymphocytes from blood-filled capillaries. In order to transfer these lymphocytes to a multi-well plate, we must first successfully extract the capillary from the centrifuge bucket, then cut the capillary and finally dispense the lymphocytes into the well. Previously [2] the capillaries were handled individually, by the central SCARA robot, which greatly limited throughput (~6,000 samples per day or 12 sec/sample). To increase throughput, we subsequently we have developed a streamlined system based on parallel processing of four samples at once, using a custom designed Robotic station [1].

New Lymphocyte Harvesting Station

- (i) The new Lymphocyte harvest station (see figure) contains:
- (ii) A Cartesian three-dimensional XYZ-stage serving as a movable platform for the centrifuge buckets, containing capillaries and the 96 well plate into which the lymphocytes are dispensed.



- (iii) A CCD camera which images the capillary to locate the boundary between red blood cells and separation medium.
- (iv) A barcode reader (BR), which registers the bar code identifier on each capillary.
- (v) A cutting station where a 2 Watt UV laser, is used to cut the capillaries, 9 mm above the boundary identified in B.
- (vi) A motorized carousel with four rotating arms and four capillary grippers, rotates 90 degrees anticlockwise at each step to transfer capillaries to the four work stations (A-D above)

This new scheme also involved an upgrade to the capillary-cutting laser and can process up to 96 capillaries without requiring assistance from the SCARA robot, freeing the latter to handle plates and centrifuge buckets exclusively. This serves to increase throughput at the other RABiT subsystems as they no longer have to compete for resources.

Reliability of Capillary picking

For the new setup, we have tested the reliability of pulling capillaries out of the centrifuge bucket for various speeds of the handling robot and for various picking depths. Initial tests showed that >93% of the capillaries were successfully picked for all system settings tested. The residual unsuccessful picks are typically due to small misalignments between the capillary and the gripper. An online rapid failure detection system is being developed to trap this error and perform a second attempt at picking the capillary in case of failure. Since the capillary picking time is still shorter than the cutting time, this has no impact on throughput.

Success Rate of Laser Cutting
(Out of 32 capillaries for each condition.)

		Sweep speed [mm/sec]					
		0.5	0.75	0.8	0.9	1	1.5
Rotation speed [RPM]	40	32	32	20	25	32	20
	45		25	25	25	32	
	50		20	25	25	32	
	55		25	32	32	32	
	60	20	32	20	25	32	32
	80	32	32			32	20

Reliability of Capillary Cutting

For a given laser power (1.9 W) and cutting time (1.7 sec) we have tested various laser sweeping and capillary rotation speeds. Based on these measurements, we have selected operational settings of 55 rpm and 0.9 mm/s. Overall, using the new, higher laser power, the swept beam, and the assisting gripper, we have reduced the

cutting time from 3.5 sec to 1.7 sec while improving the success rate to >99%. (see table)

Although the new lymphocyte handling robot is slower than the SCARA robot at picking capillaries, the reliability of capillary picking has been significantly improved, with 1-5% of capillaries not picked on the first attempt (compared to almost a half with the old design)

Sample integrity

A major concern in RABiT design was to avoid blood leakage from the capillaries both during shipping and during processing in the RABiT. This is important to prevent cross contamination and loss of samples, as well as being a safety issue for the RABiT operator and maintenance personnel. In theory, because the bottom of the capillary is sealed, the blood and separation medium cannot leak out of the top during shipping due to surface tension. Our tests have confirmed this both in the lab and in the field.

To demonstrate this, we have tested leakage during blood shipping [2], by collecting 32 (unirradiated) blood samples and shipping them, using a commercial carrier from Arizona to New York, as well as from the CRR to Nevis and back. None of the samples leaked during shipping and all samples maintained the required layering of blood and separation medium, allowing efficient separation of lymphocytes from red blood cells. The lymphocytes were then cultured to division and formed binucleated cells.

Another aspect of sample integrity is that of the viability of lymphocytes during shipping, in particularly for the CBMN assay where the lymphocytes must be healthy enough to divide. Additionally, the yield of phosphorylated H2AX was seen in many studies to decrease with time [3, 4] due to repair of the DNA double strand breaks. While this cannot be prevented prior to the blood draw, it can be greatly reduced by storing the blood at low temperatures [5]. We therefore envision shipping the blood samples chilled, in containers similar to those used for shipping vaccines [6]. This is currently being tested [7].

References

1. Garty, G., et al., The RABiT: A Rapid Automated Biodosimetry Tool For Radiological Triage II. Technological Developments International Journal of Radiation Biology, 2011. In Press.
2. Garty, G., et al., The RABiT: A Rapid Automated Biodosimetry Tool for radiological triage. Health Physics, 2010. 98: p. 209-217.
3. Redon, C.E., et al., g-H2AX as a biomarker of DNA damage induced by ionizing radiation in human peripheral blood lymphocytes and artificial skin. Advances in Space Research, 2009. 43(8): p. 1171-1178.

4. Redon, C.E., et al., The Use of gamma-H2AX as a Biosimeter for Total-Body Radiation Exposure in Non-Human Primates. PLoS ONE, 2010. 5(11): p. e15544.
5. Moroni, M.M., et al. (2008) Does Cell Culture Type And Blood Transport Temperature Affect Dicentric Yield And Radiation Dose Assessment? Journal of Medical, Chemical, Biological and Radiological Defense 6.
6. Kendal, A.P., R. Snyder, and P.J. Garrison, Validation of cold chain procedures suitable for distribution of vaccines by public health programs in the USA. Vaccine, 1997. 15(12-13): p. 1459-1465.
7. Taveras, M., Garty, G, Brenner, DJ and Turner H, γ -H2AX Signal Preservation in Blood samples Shipped for Biosimetry Analysis. CRR annual Rept 101-04, 2010. ■

^a Department of Mechanical Engineering, Columbia University

Effects of *ex vivo* Culture on Gene Expression in Human Peripheral Blood Cells

Sunirmal Paul and Sally A. Amundson

Microarray gene expression assays for biomarker discovery are increasingly attractive because they are both quantitative and robust. One can measure all of the genes in the genome simultaneously, using microarray gene expression profiling, and small perturbations in the levels of single transcripts do not obscure the overall picture. Recently, the potential risk of radiation exposure as part of a terrorist attack has been identified as a national security threat^[1,2]. In such an event, one approach to achieve faster and potentially highly sensitive measurement of radiation exposure would be the utilization of high-throughput gene expression biosimetry that can predict radiation exposure or provide radiation dose estimates. Most such approaches use peripheral blood (PB) cells as a radiosensitive and relatively accessible tissue. Our lab and other research groups have measured the radiation induced gene expression in whole blood^[3,4,5,6], isolated lymphocytes^[7,8], or specific blood cell subsets^[9]. The utility of the gene expression approach depends largely on the reproducibility of responses among individuals and the specificity of those responses for radiation exposure.

In vivo gene expression profiling with radiotherapy patients has been shown to predict radiation exposure and provide radiation dose estimates^[9]. Such in vivo human exposures are probably the best basis for the development of practical radiation biosimetry. However, the utility of this approach is largely limited by radiotherapy protocols, such as fractionation and partial body exposures. Thus *ex vivo* gene expression profiling with human PB cells remains an attractive option to investigate gene expression signatures that would be relevant to radiation dose exposure in vivo. Using *ex vivo* gene expression profiling in human PB, we have previously

identified a 74-gene signature^[5] that can predict radiation exposure across a broad dose range (0, 0.5, 2, 5 and 8 Gy) throughout a window of time (6 to 24 hr). The 74-gene signature has also been shown to predict radiation dose exposure in radiotherapy patients in vivo with high accuracy^[6], and the accuracy of radiation dose determination was unaffected by variation in gender or smoking associated stress^[9].

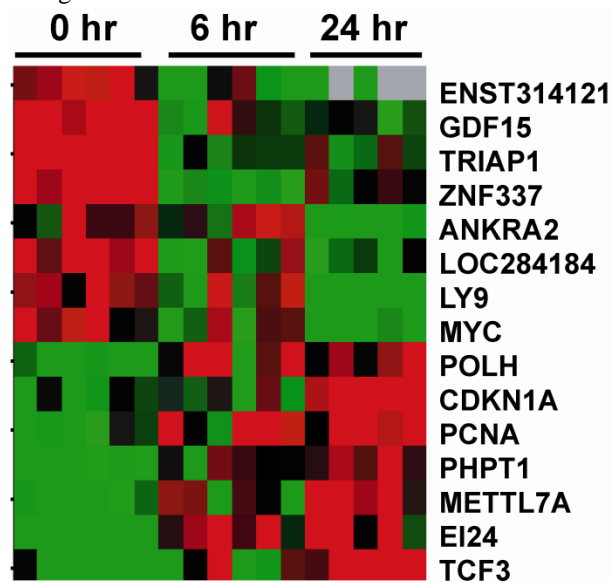


Figure 1. Average linkage clustering of 15 genes showing *ex vivo* culture effects as a function of incubation time. Length of incubation (in hours) is shown across the top. Gene names are indicated along the right edge. High expression as measured by microarray is depicted as red, and low expression is depicted as green.

Despite the high fidelity of the 74-gene set in determining dose exposure, an effect of ex vivo culture was also evident at all doses, both in irradiated samples and in unirradiated controls^[5]. Previous studies have indicated that expression levels of many genes are sensitive to ex vivo incubation in human peripheral blood cells^[10] and in primary human lymphocyte cultures^[11]. The influence of this ex vivo culture effect on the signatures being developed for radiation biodosimetry has not been thoroughly investigated to date, however. In this report, we have investigated the impact of ex vivo incubation on gene expression following radiation exposure. Our results suggest that only a few genes of our previously defined 74-gene signature are influenced by ex vivo culture and exclusion of these genes from the 74-gene set diminishes the previously demonstrated effects of time in culture without significant loss of dose discrimination.

Microarray analysis using BRB-ArrayTools

Whole genome measurements of gene expression were carried out using Agilent One-color Quick Amp labeling kit (Santa Clara, CA). Background corrected hybridization signal intensities were imported into BRB-ArrayTools, version 4.1^[12] log₂ transformed and median normalized. Non-uniform outliers or features not significantly above background intensity in 25% or more of the hybridizations, and features not changing in at least 10% of the hybridizations were filtered out. This yielded 17,392 features that were used in subsequent analyses. Class comparison was conducted using BRB-ArrayTools to identify genes that were differentially expressed between groups. Genes with p values <0.001 were considered statistically significant. The false discovery rate (FDR) was also estimated for each gene to control for false-positive results. Multidimensional scaling (MDS) was performed in BRB-ArrayTools to create a low-dimensional graphic representation of the high-dimensional data comprising the identified gene

expression signature. The Euclidian distance metric was used to compute a distance matrix and the principal components of the gene expression signature. Data was also visualized using hierarchical clustering in BRB-ArrayTools. The Euclidean distance metric and average linkage were used to cluster genes and generate a heat map.

Results and discussion

The main goal of this study was to identify genes in human peripheral blood cells that were sensitive to ex vivo incubation that might influence the accuracy of radiation biodosimetric assessment. We performed a class comparison in BRB-ArrayTools to identify differentially expressed genes across the time points using data from the un-irradiated control samples at all time points studied. This analysis identified 4,851 genes differentially expressed (at p <0.001 and FDR <4%) after both 6 and 24 hr in ex vivo culture. Fifteen of these genes overlapped with the 74-gene set^[5]. To visualize expression over time of the ex vivo sensitive gene set, a heat map was plotted (Fig. 1).

The focal point of this study was to identify the genes from the 74-gene set that have an ex vivo culture effect and to determine the genes responsible for the previously observed horizontal separation between 6-hr and 24-hr irradiated and unirradiated control samples (Fig. 2a). If unexposed control level gene expression differs between samples as an effect of exposure to the ex vivo environment, such an effect could cause separation between time points irrespective of radiation doses. To test this theory, we excluded from the 74-gene set the 15 genes that showed differential expression due to ex vivo incubation. We then used MDS to visualize the expression of this refined 59-gene signature in samples taken after 6 hr and 24 hr. Interestingly, the horizontal separation between 6-hr and 24-hr samples was largely diminished irrespective of radiation dose (Fig. 2b), suggesting that this approach did identify the major contributors to the time-in-culture effect.

In summary, these analyses demonstrate that expression levels of a large number of genes in human peripheral blood can be influenced by ex vivo incubation and that a small subset of these ex vivo sensitive genes also respond to radiation exposure. However, a careful investigation to address such issues should improve the fidelity of the ex vivo model for developing gene expression for radiation biodosimetry.

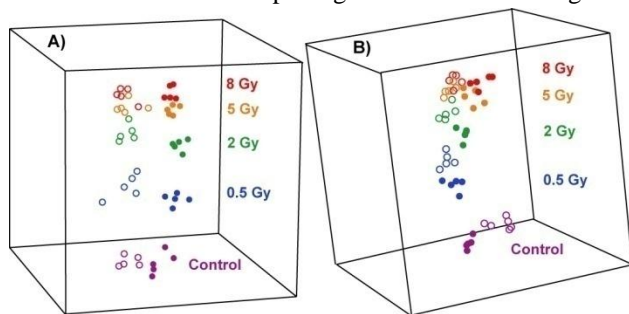


Figure 2. MDS plots of 6-hour (open circles) and 24-hr (filled circles) samples using A) the 74-gene signature^[8] and B) the refined 59-gene signature. Axes represent the first three principal components of gene expression. Each point represents the relative gene expression of either the 74-gene signature (A) or the refined 59-gene signature (B). Red symbols: 8 Gy samples, gold: 5 Gy, green: 2 Gy, blue: 0.5 Gy, purple: controls.

3. "Medical management of the acute radiation

References

1. Mettler FA Jr, V. G. (2002). "Major radiation exposure--what to expect and how to respond." *N Engl J Med.* 346(20): 1554-1561.
2. Waselenko JK, M. T., Blakely WF, Pesik N, Wiley AL, Dickerson WE, Tsu H, Confer DL, Coleman CN, Seed T, Lowry P, Armitage JO, Dainiak N (2004). syndrome recommendations of the Strategic National

- Stockpile Radiation Working Group." *Ann Intern Med.* 140(12): 1037-1051.
4. Amundson SA, G. M., McLeland CB, Epperly MW, Yeager A, Zhan Q, Greenberger JS, Fornace AJ Jr. (2004). "Human *in vivo* radiation-induced biomarkers: gene expression changes in radiotherapy patients." *Cancer Res.* 64(18): 6368-6371.
 5. Dressman HK, M. G., Chao NJ, Meadows S, Marshall D, Ginsburg GS, Nevins JR, Chute JP (2007). "Gene expression signatures that predict radiation exposure in mice and humans." *PLoS Med* 4(4): e106.
 6. Paul S, A. S. (2008). "Development of gene expression signatures for practical radiation biodosimetry." *Int J Radiat Oncol Biol Phys* 71(4): 1236-1244.
 7. Paul S, A. S. (2011). "Gene expression signatures of radiation exposure in peripheral white blood cells of smokers and non-smokers." *International Journal of Radiation Biology* (In press).
 8. Amundson SA, D. K., Shahab S, Bittner M, Meltzer P, Trent J, Fornace AJ Jr (2000). "Identification of potential mRNA biomarkers in peripheral blood lymphocytes for human exposure to ionizing radiation." *Radiat Res* 154(3): 342-346.
 9. Mori M, B. M., Tirone I, Hooghe-Peters EL, Desaintes C (2005). "Transcriptional response to ionizing radiation in lymphocyte subsets" *Cellular and Molecular Life Sciences* 62: 1489-1501.
 10. Paul S, B. C., Turner HC, McLane A, Wolden SL and Amundson SA (2011). "Prediction of *In Vivo* Radiation Dose Status in Radiotherapy Patients using *Ex Vivo* and *In Vivo* Gene Expression Signatures." *Radiat Res.* 175(3): 257-265.
 11. Baechler EC, B. F., Karypis G, Gaffney PM, Moser K, Ortmann WA, Espe KJ, Balasubramanian S, Hughes KM, Chan JP, Begovich A, Chang SY, Gregersen PK, Behrens TW (2004). "Expression levels for many genes in human peripheral blood cells are highly sensitive to *ex vivo* incubation." *Genes Immun.* 5(5): 347-353.
 12. Falt S, H. K., Lambert B, Wennborg A. (2003). "Long-term global gene expression patterns in irradiated human lymphocytes." *Carcinogenesis* 24: 1837-1845.
 13. Simon R, L. A., Li MC, Ngan M, Menenzes S, Zhao Y (2007). "Analysis of Gene Expression Data Using BRB-Array Tools." *Cancer Inform.* 2007 Feb 4;3:11-7 3: 11-17. ■

Post-irradiation Kinetics of γ -H2AX in Peripheral Lymphocytes after Radiotherapy Treatment

Helen C. Turner, Guy Garty, Maria Taveras, Antonella Bertucci, Israel Deutsch^a and David J. Brenner

Molecular biological markers of radiation response could potentially be of use for monitoring the progress of radiation therapy, and even for predicting outcome early in a treatment regimen. Currently, the best established radiation exposure biomarkers are those based on cytogenetic assays. The γ -H2AX assay is widely used in radiation biodosimetry and has been shown to be highly sensitive and specific for the detection of double strand breaks (DSBs). Immunofluorescence microscopy has shown that phosphorylated H2AX (γ -H2AX) forms visible, discrete nuclear γ -H2AX foci at DNA DSB sites after exposure to ionizing radiation (1, 2). The number of γ -H2AX foci has been shown to closely correspond to the number of DSBs, with each DSB yielding one focus (3). The advantage of the γ -H2AX assay is that the formation of γ -H2AX foci at the DNA damage site is fast, with γ -H2AX foci forming within 3–15 min and reaching their maximum within 30 min of irradiation (5). It is well known that γ -H2AX levels change rapidly following

ionizing radiation exposure, particularly during the first 24 h, leaving residual γ -H2AX levels by 24–48 h (6). Recent studies have shown that residual levels of γ -H2AX *in vivo* demonstrate a dose response more than 48 h after irradiation in mouse skin (7) and in blood lymphocytes and hair samples from non-human primates (8).

The objective of this study was to assess the persistence of the γ -H2AX signal after *in-vivo* irradiation in blood lymphocyte samples collected from volunteer patients currently undergoing radiotherapy treatments. To date, we have recruited 8 cancer patients who have received a targeted radiotherapy regimen of 1.8-2 Gy per dose to the pelvic and head and neck regions. The mean total blood dose was calculated to be in the range 2-4 Gy. To examine the kinetics of *in-vivo* induction expression of the γ -H2AX protein in blood lymphocytes, peripheral blood samples were collected before the start of the radiotherapy therapy treatment, after the 1st irradiation fraction, and 24 hrs after 1st fraction. To determine the

decay kinetics after radiotherapy, blood samples were drawn immediately after the radiotherapy treatment ended, at 2 days and at 1 week post exposure.

γ -H2AX Analysis

Peripheral whole blood samples were diluted with RPMI-1640 medium in the ratio 1:1 and layered over an equal volume of lymphocyte separation media (Histopaque 1077) and spun at 1200 for 40 min. The isolated lymphocytes were washed twice with phosphate buffered saline (PBS) and fixed with ice-cold methanol and immuno-labeled with anti-human γ -H2AX monoclonal antibody. The γ -H2AX protein was visualized using an Alexa Fluor 555 (AF555) secondary antibody, counterstained with the nuclear stain DAPI. Images were captured using an Olympus epifluorescence microscope (Olympus BH2-RFCA) and stored as 8-bit grayscale images using MicroSuite™ Five software. Fluorescent images of DAPI-labeled nuclei and AF555-

labeled γ -H2AX were captured separately for each time point using a 63X oil immersion objective. Quantification of γ -H2AX yields was determined by measuring the total γ -H2AX nuclear fluorescence per lymphocyte (9) at a fixed exposure time of 2s. The figure below shows analyses of γ -H2AX yields of the first 7 patients after the first and last radiotherapy fractions, with two additional time points, 2 and 7 days after treatment. Patients 1 to 4 and patient 7 received targeted radiotherapy fractions to the pelvic region whereas patients 5 and 6 received targeted treatments to the head and neck region. Patient 1 was reported to have received prior multiple hormone therapy and chemotherapy more than 1 month prior to radiation treatments whereas Patient 2 received chemotherapy less than 1 month before the radiotherapy start date. Patients 3 to 7 did not receive chemotherapy within 1 month of starting radiotherapy. None of the patients had received prior radiation treatments.

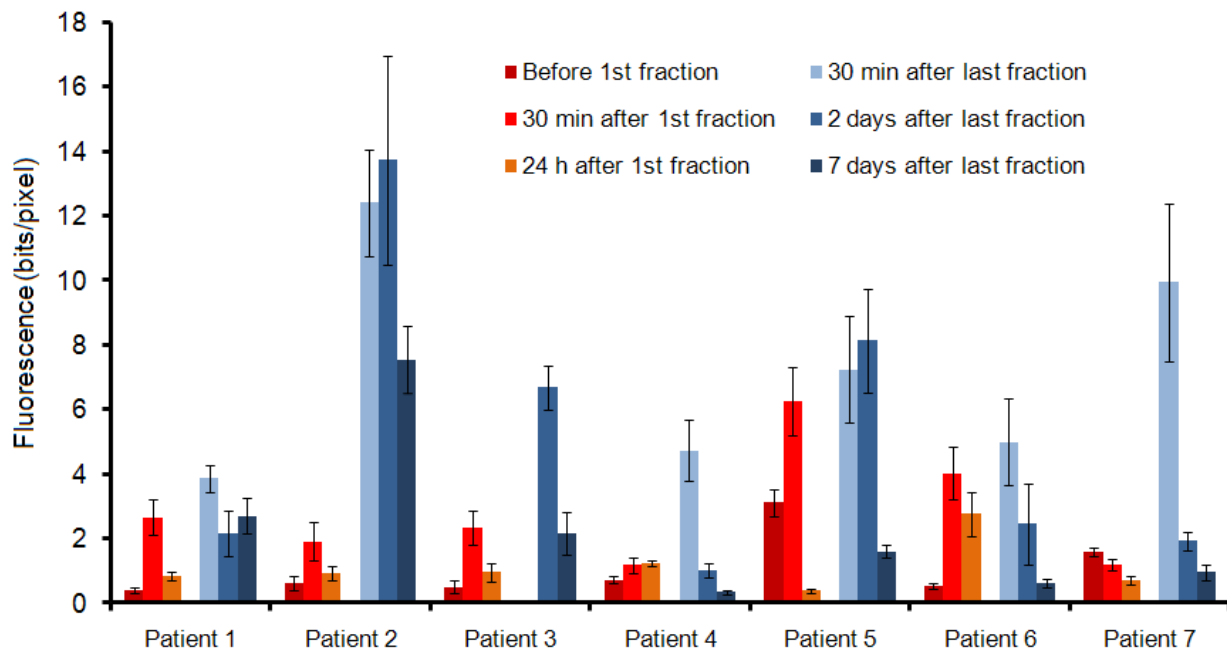


Figure 1. γ -H2AX yields in patients undergoing radiotherapy treatments. Lymphocytes were isolated from blood samples collected before the 1st fraction, 30 min and 24 h (red shades) after the 1st fraction and 30 min, 2 and 7 days after the last fraction (blue shades).

After the first fraction of radiotherapy, quantitative analyses showed a significant ($P < 0.05$) induction of γ -H2AX expression in blood lymphocytes in patients 1,2,3,5 and 6. These results highlight that the γ -H2AX assay is sensitive enough to quantifiably detect small changes in γ -H2AX induction *in vivo*; in particular in blood samples collected ~ 30 min after the 1st radiotherapy fraction where the mean blood dose per fraction was calculated to be in the range in the range 0.069 to 0.1 Gy. Post-irradiation kinetics revealed variability in the decay of γ -H2AX signal, with some patients showing a slower decay of the γ -H2AX signal

between days 2 and 7 with some patients showing a faster rate of decay between these time points. For example, patients 2 and 5 showed an increase in γ -H2AX yields in lymphocytes isolated on day 2 following the end of treatment. With the exception of Patient’s 4 and 6, the results show the persistence of a quantifiable and measurable γ -H2AX signal up to 7 days post exposure after doses of 2 to 4 Gy.

In summary, the present report measured γ -H2AX total fluorescence levels in lymphocytes using γ -H2AX specific antibodies to evaluate post-exposure decay

kinetics of γ -H2AX in cancer patients receiving conventional fractionated radiotherapy. The results show apparent inter-patient differences in the rate of γ -H2AX decay *in vivo*. To determine whether individual variability is a factor in the efficiency of DNA double strand repair, we will continue to accrue new patient volunteers receiving radiotherapy to pelvic and head/neck regions and examine in more detail the kinetics of γ -H2AX dissolution after radiation treatment.

References

1. A. Nakamura, O. A. Sedelnikova, C. Redon, D. R. Pilch, N. I. Sinogeeva, R. Shroff, M. Lichten and W. M. Bonner, Techniques for gamma-H2AX detection. *Methods Enzymol.* 409, 236–250 (2006).
2. N. Bhogal, F. Jalali and R. G. Bristow, Microscopic imaging of DNA repair foci in irradiated normal tissues. *Int. J. Radiat. Biol.* 85, 732–746 (2009).
3. O. A. Sedelnikova, E. P. Rogakou, I. G. Panyutin and W. M. Bonner, Quantitative detection of 125IdU-induced DNA doublestrand breaks with gamma-H2AX antibody. *Radiat. Res.* 158, 486–492 (2002).
4. O. A. Sedelnikova, D. R. Pilch, C. Redon and W. M. Bonner, Histone H2AX in DNA damage and repair. *Cancer Biol. Ther.* 2, 233–235 (2003).
5. F. Antonelli, M. Belli, G. Cuttone, V. Dini, G. Esposito, G. Simone, E. Sorrentino and M. A. Tabocchini, Induction and repair of DNA double-strand breaks in human cells: dephosphorylation of histone H2AX and its inhibition by calyculin A. *Radiat. Res.* 164, 514–517 (2005).
6. C. E. Redon, J. S. Dickey, W. M. Bonner and O. A. Sedelnikova, gamma-H2AX as a biomarker of DNA damage induced by ionizing radiation in human peripheral lymphocytes and artificial skin. *Adv. Space Res.* 43, 1171–1178 (2009).
7. N. Bhogal, P. Kasppler, F. Jalali, O. Hyrien, R. Chen, R. P. Hill, and R. G. Bristow, Late residual gamma-H2AX foci in murine skin are dose responsive and predict radiosensitivity *in vivo*. *Radiat. Res.* 173, 1–9 (2010).
8. Redon CE, Nakamura AJ, Gouliava K, Rahman A, Blakely WF, Bonner WM. The use of gamma-H2AX as a biodosimeter for total-body radiation exposure in non-human primates. *PLoS One.* 5(11):e15544 (2010).
9. Turner HC, Brenner DJ, Chen Y, Bertucci A, Zhang J, Wang H, Lyulko OV, Xu Y, Shuryak I, Schaefer J, Simaan N, Randers-Pehrson G, Yao YL, Amundson SA, Garty G. Adapting the γ -H2AX Assay for Automated Processing in Human Lymphocytes. 1. *Technological Aspects. Radiat Res.* 175(3):282-90 (2011). ■

^a*Department of Radiation Oncology, New York Presbyterian Hospital and Columbia University Medical Center, New York, NY 10032*

γ -H2AX Signal Preservation in Blood Samples Shipped for Biodosimetry Analysis

Maria Taveras, Guy Garty, David J. Brenner and Helen C. Turner

After a large-scale radiological event, there will be a major need to assess, within a few days, the radiation doses received by tens or hundreds of thousands of individuals, both in order to assess radiation risk in what is sure to be a resource-limited scenario [1,2]; as well as to reduce panic by reassuring those who were not significantly exposed. At the Center for High-Throughput Minimally Invasive Radiation Biodosimetry, we have developed the Rapid Automated Biodosimetry Tool

(RABiT), a fully automated, ultra-high throughput (6,000-30,000 samples per day per machine) robotically-based biodosimetry workstation [3,4]. The RABiT is based on complete automation of two well-characterized biodosimetric assays, the γ -H2AX assay [5] and the micronucleus assay [6].

In response to a large scale radiological event, 30 μ l fingerstick of blood samples will be collected in heparin-coated capillaries at specific collection sites and

transported to the RABIT for screening. Whilst the γ -H2AX assay provides a rapid, same day dose estimate and would be the preferred assay of choice for high throughput analyses, it is well known that γ -H2AX foci levels change rapidly over time, particularly during the first 24 hours post exposure, with residual levels detected up to 48 hours. The current operational concept of use for the RABIT is that samples arriving at the RABIT system within 24–36 hours of radiation exposure will be analyzed using the γ -H2AX assay, with all subsequent samples analyzed using the micronucleus assay [4]. Previous research has shown that γ -H2AX repair can be delayed by cooling the blood immediately post radiation exposure [7]. In the present study, we measured γ -H2AX yields in peripheral blood samples irradiated *ex vivo* with gamma rays between 0 to 7.5 Gy at post exposure times of 0.5 and 24 hours. The objective was to determine whether cooling the blood lymphocytes to temperatures between 4-14°C would better preserve the γ -H2AX signal post exposure compared to maintaining the samples at ambient temperatures. This would allow extending the RABIT processing of samples using the (faster) γ -H2AX assay to samples collected within 24-36 hours post exposure rather than just those delivered to the RABIT at those times.

Sample preparation

Peripheral blood samples were collected from healthy volunteers and irradiated *ex vivo* with 0 to 7.5 Gy γ -rays. To induce γ -H2AX foci formation in human lymphocytes, the blood samples were incubated at 37°C for 30 minutes to allow foci formation. For each dose, blood-filled capillaries containing lymphocyte separation medium were prepared, sealed with a capillary sealant and inserted into a RABIT sample holder as shown in Figure 1. The sample holder has been designed to hold 32 blood-filled capillaries in total. For transport, the capillary holder is supported within a foam segment and for extra impact protection; the capillary ends are sandwiched under a foam insert. To explore methods to optimally preserve the γ -H2AX signal during shipping, the irradiated blood samples were packaged as described above and stored in the following 3 simulated shipping conditions: (i) room temperature in ambient laboratory conditions; (ii) using a temperature assured commercial shipping box for biological materials or (iii) a conventional/standard insulated Styrofoam™ box.

The Nomadic Pre-Qualified Shipper, Model E24A (Thermosafe Brands, Arlington Heights, IL), was selected for our commercial shipping scenario due to its manufacturer-guaranteed shipping temperatures of 2-8°C

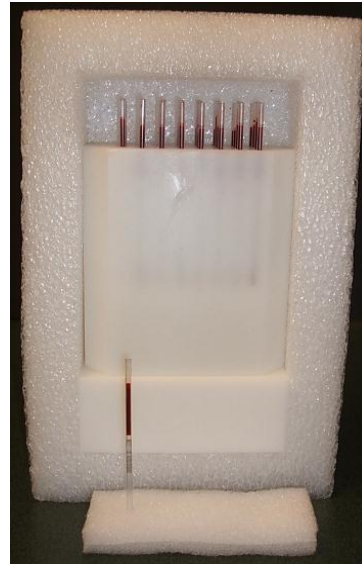


Figure 1. RABIT sample holder filled with capillaries

for 48 hours for refrigerated goods and biological specimens. Briefly, this sophisticated shipping box maintains good temperature control by inserting the sample into a small, inner cardboard box (7½ x 5 x 3¾ inches) which is sealed and placed inside a medium box (10½ x 8 x 6½) fitted with eight refrigerated gel packs (typically at 4°C). This medium-sized box is then placed into an expanded polystyrene box (EPS) where one ice-pack (typically at -20°C) lies at the base of the box and two ice packs on the top and sealed. The insulated box is then finally placed inside a large cardboard box for shipping. As a faster, more economical and readily accessible method for shipping, we packed the blood samples in an insulated Styrofoam™ box (11.5 x 1.4 x 8.5) using pre-chilled refrigerated gel packs fitting snugly around the blood samples. For samples stored at room temperature, the capillaries were packed in an insulated Styrofoam™ container and placed on the laboratory bench. A USB temperature data logger was included with each blood sample in order to generate a temperature profile. The temperature logger was programmed to record temperature readings every half hour during 0 to 48 hour time period. In Figure 2, Panel A displays the range of the temperatures recorded for the 3 different storage conditions, and Panel B represents the average temperatures of the two chilled conditions in a line graph.

A

Conditions/ Time Range	0-12 h	12-24 h	24-36 h	36-48 h
Room Temperature	25 - 23°C $\bar{T} = 23.7^\circ\text{C}$	23 - 24°C $\bar{T} = 23.2^\circ\text{C}$		
Thermosafe Shipper	23.3±2.7 - 7.4±1.1°C $\bar{T} = 9.5^\circ\text{C}$	7.6±0.9 - 7.0±0.5°C $\bar{T} = 7.3^\circ\text{C}$	6.8±0.7 - 6.0±0.7°C $\bar{T} = 6.8^\circ\text{C}$	6.8 - 7.5°C $\bar{T} = 7.2^\circ\text{C}$
Styrofoam™ Box	24.0±0.5 - 11°C $\bar{T} = 11.2^\circ\text{C}$	11±1.0 - 12.5±1.5°C $\bar{T} = 11.8^\circ\text{C}$	14 - 14.5°C $\bar{T} = 14.3^\circ\text{C}$	14.5 - 16°C $\bar{T} = 15.3^\circ\text{C}$

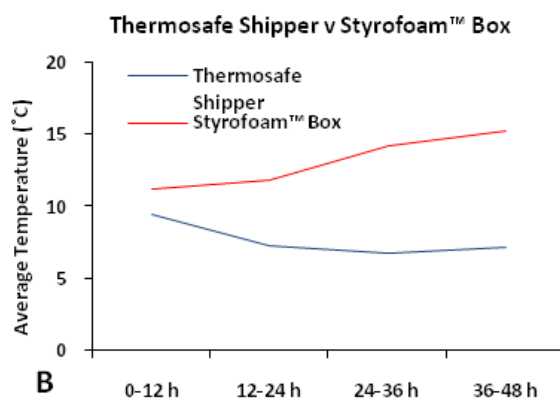


Figure 2. Panel A, a Temperature Profile Table for blood storage conditions; and Panel B a graph comparing the Thermosafe Shipper to the Styrofoam™ box.

These results show that the Thermosafe Shipper maintains the blood samples at around 7 °C for up to 48 hours. The time taken to reach internal temperatures of ~ 9.5°C was about 3-3.5 hours. In contrast, the Styrofoam™ box cooled quickly to ~11°C within one hour, since, due to limited internal space, the pre-chilled fridge packs were placed in direct contact with the sample and probe. Overall, the Styrofoam™ box maintained temperatures of ~ 11.5°C for 24 hours before gradually warming up to 15°C by 48 hours.

γ-H2AX Analysis

Quantitative analyses of total γ-H2AX fluorescent yields in isolated blood lymphocytes were determined by immunolabeling isolated lymphocytes using an anti-human monoclonal γ-H2AX antibody and visualized using an Alexa Fluor 555 (AF555) secondary antibody, counterstained with the nuclear stain DAPI [8]. Figure 3 shows the γ-H2AX yields in human lymphocytes isolated

from 30 μl whole blood samples at 30 minutes and 24 hours post exposure. The results showed that cooling the irradiated blood lymphocytes to temperatures below ~ 13°C appeared to better preserve the γ-H2AX signal 24 hours post exposure compared to the capillary blood samples stored at ambient temperatures. Samples stored in the Thermosafe Shipper packing system showed a higher retention of the γ-H2AX signal across the doses compared to the samples stored in the more conventional Styrofoam™ box. To assess whether cooling conditions affected lymphocyte survival during 24 hour storage, viability was determined by trypan blue exclusion, and differential cell counts were performed using a Neubauer-Levy Hemacytometer. The percentage of viable cells under chilled conditions (Thermosafe and Styrofoam™ boxes) dropped down to ~ 75%, while the room temperature samples maintained > 80% viability, with additional decreases below 80% at the 5Gy dose.

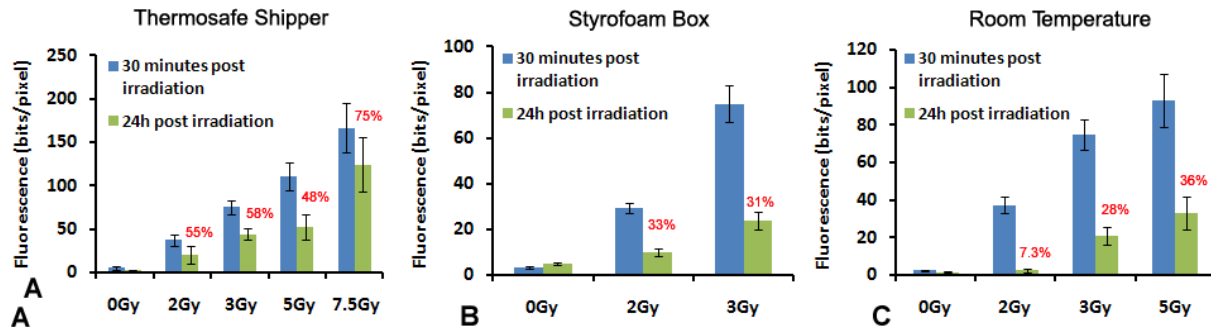


Figure 3. γ -H2AX preservation in irradiated blood lymphocytes after storage in Thermosafe box (Panel A), Styrofoam box (Panel B) and at room temperature (Panel C) 24 hours post exposure. γ -H2AX yields are presented as the average total γ -H2AX fluorescence values in bits per pixel (green bars) with the percent (%) γ -H2AX retention values (in red) calculated from the maximal induction of γ -H2AX foci after 30 minutes of exposure (blue bars). Error bars represent \pm SEM.

In summary, we have demonstrated that it is possible to reduce the rate of γ -H2AX signal decay 24 hours post exposure if the blood lymphocytes are maintained at cooler temperatures during this time. Blood samples stored in the Thermosafe Shipper maintained a constant, cooler temperature over a longer period of time, which appeared better designed to preserve the γ -H2AX signal post irradiation. The results show that blood samples packaged in a more economical and conventional set up using insulated Styrofoam™ boxes may also provide a good alternative for shipping blood samples for γ -H2AX analyses. Future studies will look to investigate the effect of chilling blood samples beyond 24 hours (36-48 hours) to more accurately determine the assay switch over time for samples arriving at the RABiT post irradiation.

References

1. Flynn DF, & Goans RE. Nuclear terrorism: triage and medical management of radiation and combined-injury casualties. *Surg Clin North Am.* 86:601-636; 2006
2. Kumar P, & Jagetia GC. A review of triage and management of burns victims following a nuclear disaster. *Burns.* 20: 397-402; 1994.
3. Garty G, Chen Y, Salerno A, Turner H, Zhang J, Lyulko O, Bertucci A, Xu Y, Wang H, Simaan N, Randers-Pehrson G, Yao YL, Amundson SA, Brenner DJ. The rabbit: a rapid automated

biodosimetry tool for radiological triage. *Health Phys.* 98:209-217; 2010.

4. Garty G, Chen Y, Turner H, Zhang J, Lyulko O, Bertucci A, Xu Y, Wang H, Simaan N, Randers-Pehrson G, Yao YL, & Brenner DJ. The rabbit: a rapid automated biodosimetry tool for radiological triage. ii. technological developments. *Int J Radiat Biol.* 87:1-15; 2011. In press.
5. Redon CE, Nakamura AJ, Gouliava K, Rahman A, Blakely WF, Bonner WM. The use of gamma-H2AX as a biodosimeter for total-body radiation exposure in non-human primates. *PLoS One.* 23: e15544; 2010.
6. Fenech M, Chang WP, Kirsch-Volders M, Holland N, Bonassi S, and Zeiger E, HUMN project: detailed description of the scoring criteria for the cytokinesis-block micronucleus assay using isolated human lymphocyte cultures. *Mutat Res,* 534:65-75; 2003.
7. Ismail I H, Wadhra T I & Hammarsten O. An optimized method for detecting gamma-H2AX response among humans. *Nucleic Acids Res.,* 35:1-10; 2007.
8. Turner HC, Brenner DJ, Chen Y, Bertucci A, Zhang J, Wang H, Lyulko OV, Xu Y, Shuryak I, Schaefer J, Simaan N, Randers-Pehrson G, Yao YL, Amundson SA, Garty G. Adapting the γ -h2ax assay for automated processing in human lymphocytes. 1. technological aspects. *Radiat Res,* 175:282-290; 2011. ■

Automated Image Analysis for Micronucleus Assay in RABiT

Oleksandra V. Lyulko, Guy Garty, Helen C. Turner, Gerhard Randers-Pehrson and David J. Brenner

Image analysis module for RABiT.

At the Center for High-Throughput Minimally Invasive Radiation Biodosimetry we have developed the Rapid Automated Biodosimetry Tool (RABiT) – a completely automated robotic-based ultra-high-throughput biodosimetry workstation (1, 2, 3 and 4). In case of a large-scale radiological event, hundreds of thousands of people may need to be screened using the RABiT in a short period of time to estimate the doses received by individuals. The estimation of the dose is based on the analysis of peripheral blood lymphocytes obtained from a single fingerstick. The lymphocytes undergo the cytokinesis-block micronucleus assay (5) and the images of cytoplasm and nuclei of the cells are analyzed to estimate the frequency of micronuclei (MNi) in binucleated cells as a biomarker of DNA-damage

events. We have developed software to automatically localize binucleated cells, detect MNi and calculate their frequency in the sample.

The RABiT utilizes dual staining of the nuclei and cytoplasm and images them simultaneously with multiple cameras, allowing for high throughput. The advantage of the dual staining approach for the automated image analysis is that it enables nuclei to be matched with their corresponding cells, allowing for more precise identification of binucleated cells. Since the nuclei and cell images are analyzed separately, the artifacts from the cytoplasm staining are not misinterpreted as MNi.

The image analysis software is written in C using Matrox Imaging Library (MIL). The scoring algorithm is based on the protocol for the CBMN assay developed by M. Fenech (5, 6).

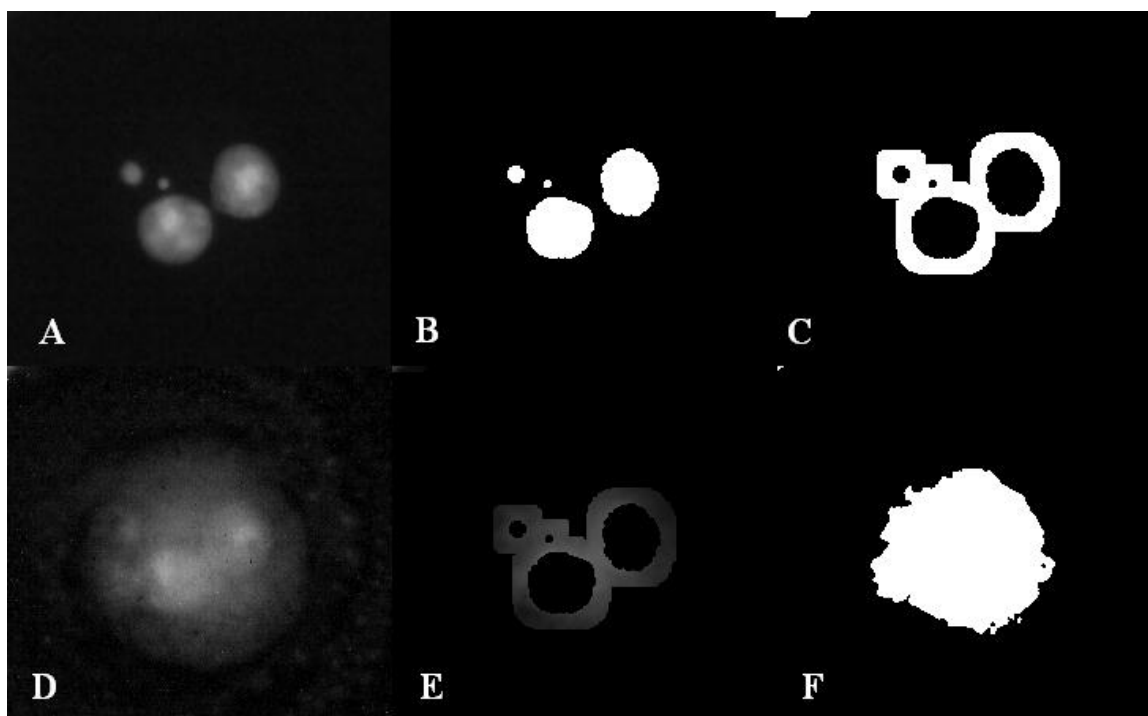


Fig. 1. Automated thresholding procedure for segmentation of the cytoplasm. A: grayscale DAPI image; B: binarized image of nuclei; C: vicinity of the nuclei is selected; D: grayscale image of cytoplasm; E: pixel intensities of the cytoplasm will be averaged to find the threshold; F: binarized image of the cytoplasm.

Image processing.

The two images, corresponding to nuclei and cytoplasm, are first subject to background subtraction followed by application of the median filter to remove “salt-and-pepper” noise.

Segmentation of the nuclei from the cytoplasm. The next step is binarization. When standard thresholding procedure (based on image histogram) is applied, it may not detect some micronuclei, because they often appear dimmer than the main nuclei, especially at higher doses (4-8 Gy).

To make the detection of MNi less dependent on variations of staining intensity, we developed a procedure, based on an iterative application of standard thresholding of the image. With each iteration, the areas that were just detected are masked, and areas with lower intensity appear on the binarized image. At a certain point (pre-set number of iterations), this iterative process stops for the nuclei and continues only for smaller objects. This way the effective threshold for micronuclei is lower than that for nuclei. After binarization, touching nuclei are separated using a watershed method.

Segmentation of cytoplasm from the background. The ability of the standard binarization technique to differentiate whole cells from the background is limited when the nuclei have higher intensity than the surrounding cytoplasm and when there is residual staining of the background.

To calculate the correct threshold intensity for cell segmentation, we use the binarized image of the nuclei to localize the cells. A mask image, allowing only the outside vicinities of the nuclei to be visible, is overlaid on the cell image (Fig.1). The intensities of the pixels of the cell image, corresponding to the areas around the nuclei, are averaged. The average value approximates the intensity of the cell boundaries and is used as a threshold for binarization of the cell image.

Selecting viable cells. To include only viable cells into the analysis, we characterize the objects in the cell image by size and shape. Cells with intact cytoplasm should be approximately circular in shape and with relatively smooth edges. To characterize the shape of the cell, we use the following object parameters: compactness, roughness, elongation and Feret elongation. Combined

with the information about the area of an object, this ensures effective differentiation of the viable cells from clusters, aggregations of platelets, staining artifacts, apoptotic cells etc. Similar analysis is performed with respect to the nuclei.

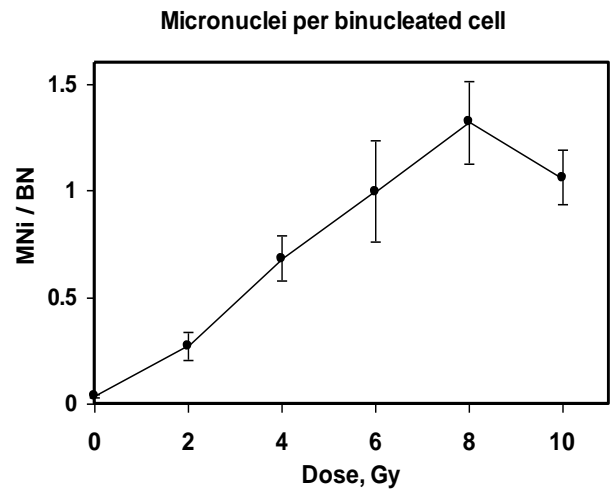


Fig. 2. Average number of micronuclei in binucleated cells.

Identifying and scoring micronuclei.

After cells have been selected for analysis based on their size and compactness, they are analyzed one-by-one. The coordinates of the centers of the nuclei are determined and matched with the outlines of the cell. The nuclei which do not belong to the cell are excluded from the analysis.

The number of nuclei in a single cell and their areas are calculated and the nuclei are sorted by size and divided into two categories: the main nuclei and the MNi. The area of a micronucleus in binucleated human lymphocytes varies between 1/256 and 1/9 of the area of the main nuclei (5). Information about the number of binucleated cells and number of MNi is accumulated while the analysis is carried on to the next image. The analysis of the sample terminates either when a preset number of binucleated cells are scored or when all available images are analyzed.



Members of Dr. David Brenner’s group (L-r): Dr. Guy Garty, Research Scientist, Dr. Maggie Chen, Associate Research Scientist, Mr. Carl Elliston, Senior Staff Associate and Dr. Andrew Harken, Postdoctoral Research Scientist.

Validation.

The performance of the developed automated module was validated by producing dose response curves. Blood samples from several healthy donors were irradiated in the dose range from 0 to 10 Gy. Series of 250 images from each dose and each donor were collected and analyzed. Fig. 2 shows the mean number of micronuclei per binucleated lymphocyte across all the donors. The error bars represent standard error and show expected significant inter-individual variability (7). The automatically generated yield of micronuclei demonstrates dose dependence very close to linear from 0 to 8 Gy. Above 8 Gy the number of micronuclei decreases due to inability of the cells with severally damaged DNA to enter mitosis (8).

Currently the software is being integrated into the RABiT imaging system.

References

1. Salerno, J. Zhang, A. Bhatla, O. V. Lyulko, A. Dutta, G. Garty, N. Simaan, G. Randers-Pehrson, Y. L. Yao and J. Nie, Design considerations for a minimally invasive high-throughput automation system for radiation biodosimetry. In *IEEE Int. Conf. Automation Science and Engineering*, pp. 846-852. 2007.
2. G. Garty, Y. Chen, A. Salerno, H. C. Turner, J. Zhang, O. V. Lyulko, Y. Xu, H. Wang, N. Simaan and D. J. Brenner, The RABiT: A rapid automated biodosimetry tool for radiological triage. *Health Phys.*, **98**(2), 209-17 (2010).
3. Y. Chen, J. Zhang, H. Wang, G. Garty, Y. Xu, O. V. Lyulko, H. C. Turner, G. Randers-Pehrson, N. Simaan and D. J. Brenner, Development of a robotically-based automated biodosimetry tool for high-throughput radiological triage. *Int. J. Biomechatronics and Biomedical Robotics*, **1**(2), 115-125 (2010).
4. Y. Chen, J. Zhang, H. Wang, G. Garty, Y. Xu, O. V. Lyulko, H. C. Turner, G. Randers-Pehrson, N. Simaan and D. J. Brenner, Design and preliminary validation of a rapid automated biodosimetry tool for high-throughput radiological triage. In *Proc. ASME Int. Design Engineering Technical Conferences & Computers and Information in Engineering Conference*, paper no. DETC2009-86425, San Diego, 2009.
5. M. Fenech, Cytokinesis-block micronucleus cytochrome assay. *Nat. Protoc.* **2**, 1084-104 (2007).
6. M. Fenech, W. P. Chang, M. Kirsch-Volders, N. Holland, S. Bonassi and E. Zeiger, HUMN project: detailed description of the scoring criteria for the cytokinesis-block micronucleus assay using isolated human lymphocyte cultures. *Mutat. Res.* **564**, 65-75 (2006).
7. H.-W. Gantenberg, K. Wuttke, C. Streffer, W.-U. Müller, Micronuclei in Human Lymphocytes Irradiated in Vitro or in Vivo. *Rad. Res.* **128**(3), 276-281 (1991).
8. W.-U. Müller, A. Rode, The micronucleus assay in human lymphocytes after high radiation doses (5-15 Gy). *Mutat. Res.* **502**, 47-51 (2002). ■



Fourth Annual Scientific Retreat for the Center for High-Throughput Minimally-Invasive Radiation Biodosimetry on April 1 -2, 2010, New York.

Gene Expression Responses to Low-dose Radiation Exposure in Human Peripheral Blood

Sally A. Amundson and Sunirmal Paul

We have used *ex vivo* irradiation of peripheral blood from healthy donors as one model for the development of gene expression signatures for radiation biodosimetry (1, 2). In this work, we have spanned the range of exposures between 0.1 and 8 Gy. Here we focus on the response to the lowest dose investigated, 0.1 Gy, and compare these responses to those at a moderately high dose, 2 Gy.

Whole blood was diluted 1:1 with RPMI1640 medium containing 10% heat-inactivated fetal bovine serum, and exposed to gamma-rays using the AEC Gammacell-40 cesium irradiator. RNA was extracted after incubating the blood for 6 hours, and was labeled and hybridized to Agilent whole-genome microarrays using standard protocols. After washing, microarray slides were immediately scanned with the Agilent Scanner (G2404B) using the recommended settings. The scanned images were analyzed with Agilent Technologies Feature Extraction 9.1 using default parameters for background correction and flagging of non-uniform features.

Background corrected hybridization intensities were imported into BRB ArrayTools v.3.8.1 (3), log₂ transformed and normalized to the median array. Features that were non-uniform outliers, invariant or non-expressed in 25% or more of the samples were filtered out and not used in further analysis. At the p<0.005 level of significance, 268 genes responded to the 0.1 Gy dose. However, the false discovery rate (FDR) climbed to just over 20% for some of these genes. Of these genes, 112 had a FDR <5%. Many more genes were significantly altered by the 2 Gy dose, with 1793 responding at the p<0.005 level of significance, all with FDR < 5%.

The sets of genes responding to either 0.1 or 2 Gy radiation were uploaded into DAVID, (the database for annotation, visualization and integrated discovery) (4) and gene ontology analysis was performed. The p53 signaling pathway was the most strongly enriched pathway function among genes responding to both doses. Biological processes significantly enriched in the response to 0.1 Gy

centered on regulation of apoptosis and signaling functions. These functions were also enriched in the response to 2 Gy, however, additional processes were also enhanced at the higher dose. Biological processes engaged after 2 Gy but not 0.1 Gy included immune response functions and cell proliferation (Table 1).

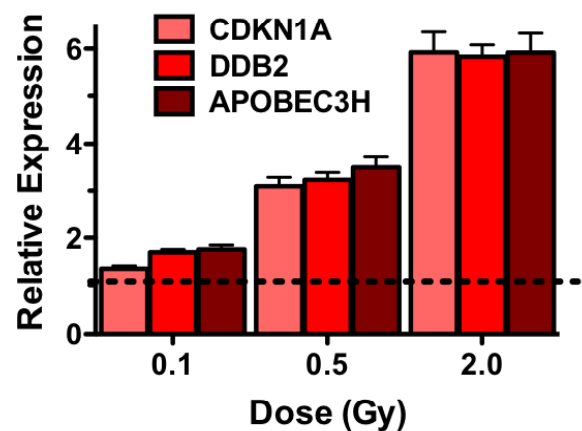


Figure 1. Real-time PCR measurements of gene expression 6 hours after exposure. Bars are the mean and SEM of measurements on 24 independent donors.

We used quantitative real-time RT-PCR to compare the expression of three p53-regulated genes, *CDKN1A*, a major regulator of cell cycle arrest, *DDB2*, which codes for a DNA damage repair protein, and *APOBEC3H*, a mediator of apoptosis, after exposure to 0.1, 0.5 and 2 Gy (Figure 1). All three genes were up-regulated by radiation exposure, even following the lowest dose, and the magnitude of change increased with increasing dose.

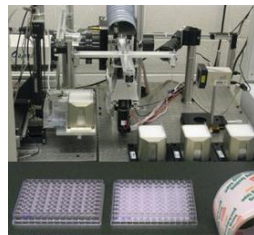


Table 1. Gene Ontology analysis of response to 0.1 and 2 Gy gamma-rays

0.1 Gy			
Term	# genes	Fold Enrichment	Benjamini p-value
hsa04115:p53 signaling pathway	12	16.0	5.98E-09
GO:0006974~response to DNA damage stimulus	18	4.6	4.86E-04
GO:0008629~induction of apoptosis by intracellular signals	8	14.0	9.29E-04
GO:0010942~positive regulation of cell death	16	3.5	0.006
GO:0042770~DNA damage response, signal transduction	7	8.3	0.018
GO:0007242~intracellular signaling cascade	27	2.0	0.039
2 Gy			
Term	# genes	Fold Enrichment	Benjamini p-value
BP00148:Immunity and defense	140	1.7	7.17E-08
GO:0042127~regulation of cell proliferation	100	1.9	4.58E-06
GO:0044459~plasma membrane part	206	1.4	5.65E-06
GO:0006955~immune response	88	1.9	2.26E-05
GO:0006954~inflammatory response	49	2.2	3.44E-04
hsa04115:p53 signaling pathway	18	3.6	8.07E-04
GO:0008285~negative regulation of cell proliferation	50	2.0	0.001
GO:0009611~response to wounding	66	1.8	0.001
GO:0042981~regulation of apoptosis	89	1.6	0.002
BP00102:Signal transduction	268	1.2	0.006
GO:0007242~intracellular signaling cascade	123	1.4	0.009
GO:0043066~negative regulation of apoptosis	46	1.9	0.011
BP00176:Blood clotting	17	2.9	0.011
BP00274:Cell communication	108	1.4	0.013
BP00253:Induction of apoptosis	23	2.2	0.026
GO:0002250~adaptive immune response	16	3.0	0.032
BP00152:B-cell- and antibody-mediated immunity	16	2.6	0.033

In conclusion, we find that peripheral blood is very sensitive to even relatively low doses of ionizing radiation, and can provide consistent gene expression readout relative to dose. These findings may help to extend downward the range of doses that can be detected using gene expression biodosimetry.

References

1. S. Paul and S. A. Amundson, Development of gene expression signatures for practical radiation biodosimetry. *Int J Radiat Oncol Biol Phys* 71, 1236-1244 (2008).
2. S. Paul and S. A. Amundson, Gene expression signatures of radiation exposure in peripheral white blood cells of smokers and non-smokers. *Int J Radiat Biol*, in press.
3. R. Simon, A. Lam, M.-C. Li, M. Ngan, S. Meneses and Y. Zhao, Analysis of gene expression data using BRB-Array Tools. *Cancer Informatics* 2, 11-17 (2007).
4. D. W. Huang, B. T. Sherman and R. A. Lempicki, Systematic and integrative analysis of large gene lists using DAVID bioinformatics resources. *Nat Protoc* 4, 44-57 (2009). ■

Whole Mouse Blood MicroRNAs as Biomarkers for Exposure to γ -rays and ^{56}Fe Ions

Thomas Templin, Sally A. Amundson, David J. Brenner, and Lubomir B. Smilenov

Biomarkers of ionizing radiation exposure are useful in a variety of scenarios, such as medical diagnostic imaging, occupational exposures, and spaceflight. Recently, high-throughput methodologies have been used to estimate the extent of radiation-induced functional changes. Comparisons of gene expression between irradiated and control samples effectively discriminate irradiated from nonirradiated samples, as well as samples exposed to low doses of radiation from samples exposed to high doses. Additionally, functional analyses of the differentially expressed genes show that radiation induces changes in many cellular processes.¹⁻⁵ These studies demonstrate the feasibility of using gene expression to estimate both radiation dose and the physiological effects of ionizing radiation.

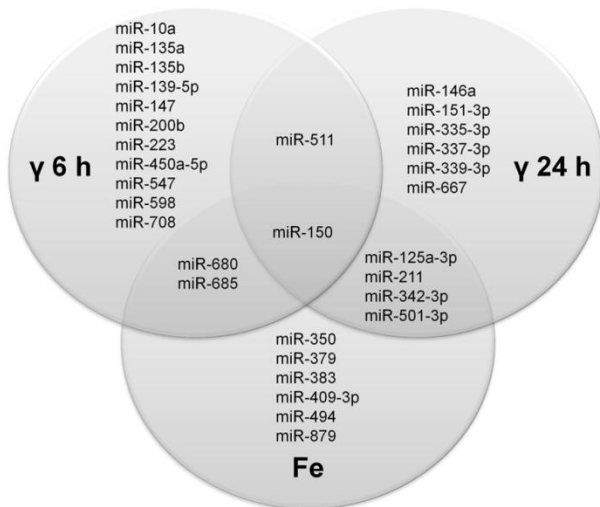


Fig.1. Venn diagram showing miRNAs differentially expressed in the indicated irradiation conditions. Areas of overlap among different circles depict miRNAs differentially expressed in multiple conditions. For simplicity, miRNAs expression at different doses of irradiation is not distinguished in the diagram, and miRNAs that are differentially expressed at any dose corresponding to the respective radiation type and time point are shown. Both time points are combined for miRNAs differentially expressed upon ^{56}Fe irradiation.

In the present study, we validated miRNAs as biomarkers for exposure to low-LET γ -rays and high-LET ^{56}Fe ions. ^{56}Fe and other heavy ions are components of galactic cosmic rays which pose a health threat to astronauts, particularly on missions beyond low earth orbit. Our investigation is an *in vivo* proof-of-principle study, in which we exposed C57BL/6 mice to various

doses of γ -ray or ^{56}Fe -ion total body irradiation and measured miRNA expression levels in the blood of the irradiated and control mice. Due to its easy accessibility and the relative non-invasiveness of phlebotomy, blood is an excellent tissue for biomarker tests.

Mice were irradiated with doses of 0.5, 1.5, or 5.0 Gy γ -rays (dose rate of 0.0136 Gy/s) or with doses of 0.1, or 0.5 Gy ^{56}Fe ions (dose rate of 0.00208 Gy/s). Total RNA was isolated from whole blood at 6 h or 24 h after irradiation. Three animals per irradiation condition were used. Differentially expressed miRNAs were determined by means of quantitative real-time PCR.

Our main finding is that ionizing radiation induces changes in the miRNA signature of whole blood and that these changes depend on the irradiation parameters. Overall we found that 31 miRNAs (19% of all detected miRNAs) were differentially expressed after irradiation (Fig. 1). Noticeably, the differentially expressed miRNAs and their numbers differ among the various irradiation conditions. More miRNAs are generally differentially expressed at high radiation doses, compared to low doses. However, for the low doses (0.5 Gy and 1.5 Gy γ -rays and 0.1 Gy ^{56}Fe ions) the numbers of miRNAs whose expression levels changed upon radiation exposure were lower at 24 h after irradiation compared to the earlier time point. This decrease may be explained by the repair of radiation damage. For the high doses (5.0 Gy γ -rays and 0.5 Gy ^{56}Fe ions) the numbers of differentially expressed miRNAs were approximately the same for both time points.

Table 1. Accuracy, sensitivity, and specificity of the class-prediction classifiers for predicting the irradiation type or dose, based on miRNA expression signatures.

Irradiation condition	Accuracy	Sensitivity	Specificity
γ		0.667	0.833
^{56}Fe	75%	0.75	0.875
Control		0.833	0.917
γ 0.0 Gy		1	0.889
0.5 Gy		0.833	0.944
1.5 Gy	88%	0.667	1
5.0 Gy		1	1
^{56}Fe 0.0 Gy		1	1
0.1 Gy	100%	1	1
0.5 Gy		1	1

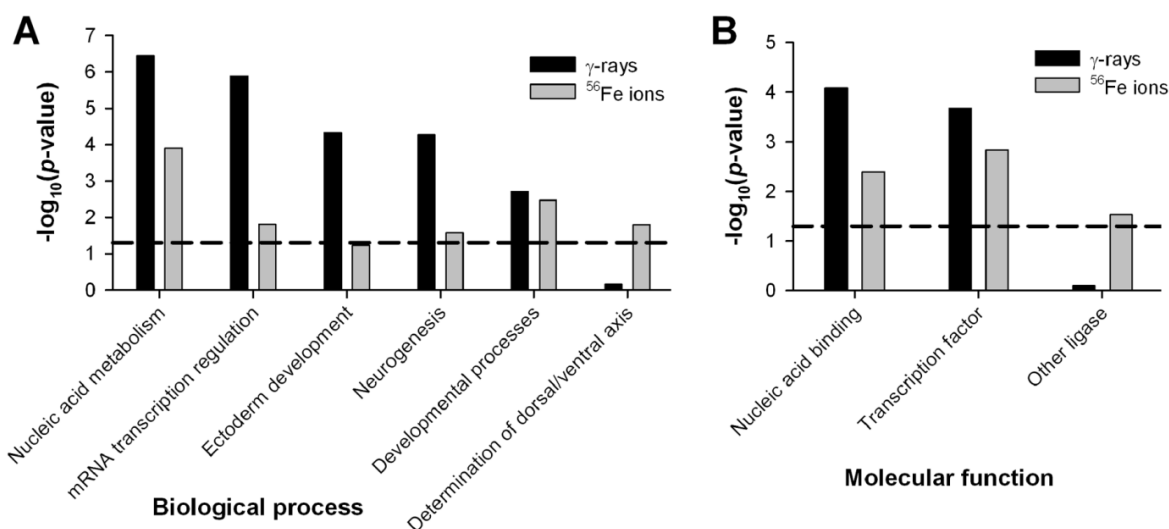


Fig. 2. Biological processes and molecular functions with increased miRNA control after irradiation. The GO analysis is based on genes targeted only by miRNAs that were switched on by irradiation. The target genes were determined using TargetScanMouse v. 5.⁶ and then uploaded to the PANTHER GO database v. 6.0⁷ to determine the biological processes (A) and molecular functions (B) in which the target genes are overrepresented. The mouse AB1700 gene list (Applied Biosystems) was used as the reference genome. Processes and functions above the horizontal dashed line exhibit significant enrichment at a Bonferroni-corrected p-value of < 0.05.

Since miRNA expression signatures contain information about the regulation of hundreds to thousands of target genes, it is very reasonable to use them for the development of radiation classifiers. Based on the detected differences in miRNA expression signatures, we developed such classifiers and showed that miRNAs can be used, in principle, as predictors of radiation exposure. Our classifiers performed with variable accuracy: they classified the samples reasonably well according to radiation type (accuracy of 75%) and were very exact for dose estimation (accuracy of 88% for γ -rays and of 100% for ⁵⁶Fe ions) (Table 1). An advantage of our classifiers is that they encompass various scenarios that require predictions about received radiation exposures. It is possible to run two predictors in sequence. For example, if neither the radiation type nor the dose of exposure is known, the classifier predicting radiation type can be applied first, and, after the radiation type has been determined, a γ - or ⁵⁶Fe-specific classifier can be used to estimate the dose of exposure. A further advantage is that the classifiers do not require pre-exposure control samples because 1) all samples that were used to develop the classifiers were derived from separate, independent organisms and 2) the nearest-centroid classifiers that we developed are able to assign a radiation type and a radiation dose to a sample with unknown radiation status based on the absolute normalized expression values (ΔC_T values) of the miRNAs contained in the classifier.

We also analyzed the functions of the genes targeted by the differentially expressed miRNAs in order to obtain information on the physiological changes in mouse blood induced by γ or ⁵⁶Fe irradiation. The numbers of the target genes of the differentially expressed miRNAs per irradiation condition are considerable. For example, 6 h

after γ irradiation with 1.5 Gy, 515 genes (conserved targets only) are targeted by the differentially expressed miRNAs, using our context-score cut-off criterion. As a result, the effects of the radiation-responsive miRNAs on cellular processes could be quite substantial. The GO analysis results show that irradiation changes miRNA control of specific biological processes, such as nucleic acid metabolism, transcription regulation, and development (Fig. 2).

References

- Fachin AL, Mello SS, Sandrin-Garcia P, Junta CM, Donadi EA, Passos GA, Sakamoto-Hojo ET. 2007. Gene expression profiles in human lymphocytes irradiated in vitro with low doses of gamma rays. *Radiation Research* 168:650-665.
- Amundson SA. 2008. Functional genomics in radiation biology: a gateway to cellular systems-level studies. *Radiation and Environmental Biophysics* 47:25-31.
- Paul S, Amundson SA. 2008. Development of gene expression signatures for practical radiation biodosimetry. *International Journal of Radiation Oncology Biology Physics* 71:1236-1244.
- Roy L, Gruel G, Vaurijoux A. 2009. Cell response to ionising radiation analysed by gene expression patterns. *Annali dell Istituto Superiore di Sanita* 45:272-277.
- Brengues M, Paap B, Bittner M, Amundson S, Seligmann B, Korn R, Lenigk R, Zenhausern F. 2010. Biodosimetry on small blood volume using gene expression assay. *Health Physics* 98:179-185.
- Grimson A, Farh KK, Johnston WK, Garrett-Engele P, Lim LP, Bartel DP. 2007. MicroRNA targeting

specificity in mammals: determinants beyond seed pairing. *Molecular Cell* 27:91-105.

7. Thomas PD, Campbell MJ, Kejariwal A, Mi H, Karlak B, Daverman R, Diemer K, Muruganujan A,

Narechania A. 2003. PANTHER: a library of protein families and subfamilies indexed by function. *Genome Research* 13:2129-2141. 1. ■

Radiation-induced MicroRNA Expression Changes in Peripheral Blood Cells of Radiotherapy Patients

Thomas Templin, Sunirmal Paul, Sally A. Amundson, Erik F. Young, Christopher A. Barker^a, Suzanne L. Wolden^a, and Lubomir B. Smilenov

MicroRNAs (miRNAs) are a class of small noncoding RNAs that have been identified as potent regulators of gene expression. Sequencing and functional analysis show that miRNAs control the expression of more than 50% of human genes by mRNA destabilization and translational repression.¹ At the same time, *in vivo* and *in vitro* studies have found that miRNA control is essential for the proper execution of many processes active in normal cells, including cell metabolism, cell differentiation, and cell signaling.² Moreover, numerous analyses of miRNA expression signatures in tumors have found that they are highly specific and can be correlated with tumor state and tumor prognosis.^{3, 4} miRNA dysregulation has also been identified in many other diseases.⁵⁻⁹

Recently, it has been shown that ionizing radiation can induce changes in miRNA expression profiles in normal human fibroblasts¹⁰ and immortalized cell lines^{11, 12}. Since exposure to medical sources of radiation^{13, 14} or to radiation emitted by an improvised radiological or nuclear device¹⁵ poses a health risk to the exposed population, we investigated to what degree human-blood miRNA signatures can be used as biomarkers for radiation exposure.

Blood from 8 radiotherapy patients in complete remission CR 1 or 2 was collected immediately prior to and at 4 h after total body irradiation with 1.25 Gy X-rays. Both miRNA and gene expression changes were measured by means of quantitative PCR and microarray hybridization, respectively. Hierarchical clustering, multidimensional scaling, class prediction, and gene ontology analysis were performed to investigate the potential of miRNAs to serve as radiation biomarkers and to elucidate their likely physiological roles in the radiation response.

We found that 45 miRNAs (23% of all miRNAs detected in blood cells) exhibited statistically significant changes in expression levels at 4 hours after irradiation with a dose of 1.25 Gy X-rays when compared to pre-

irradiation controls (Fig. 1). This result indicates an extensive shift in miRNA expression, with important consequences for cell functions. Notably, all differentially expressed miRNAs exhibited increased expression levels after irradiation. We did detect underexpressed miRNAs in every patient, but they were not statistically significantly downregulated across all patients. The predominance of upregulated miRNAs could be a characteristic of the early radiation response in blood cells. Importantly, 27 of the 45 radiation-induced miRNAs were upregulated in every patient. When one patient who had a markedly different miRNA expression profile than the other patients was excluded from the analysis, the number of miRNAs upregulated across all patients increased to 39. The high consistency of miRNA expression changes in human blood cells across individuals emphasizes the great value of miRNA signatures as radiation biomarkers.

A major concern for any comparative analysis of data derived from total blood cell populations before and after irradiation is that blood cell subsets may change after irradiation due to the radiation sensitivity of white blood cells (WBCs). According to estimates of the effect of irradiation on blood cell counts, the lymphocyte depletion rate constant is very low for doses of up to 1 Gy, and the decrease in the number of WBCs has been estimated to be 6% at 12 hours after irradiation.^{16,17} Based on these data, we assumed that a dose of 1.25 Gy would not induce a significant change in the numbers of blood cells for the 4-h time point that we used. This implies that the miRNA and gene expression changes we observe are due to functional changes in the irradiated cells and not the consequence of cell-subset depletion. Although workable biomarkers can be developed for class prediction even when blood-cell subsets change in response to irradiation, the postulation of subset constancy substantially facilitates the interpretation of the results of the gene ontology (GO) analysis.

Because of the high number of differentially expressed miRNAs identified in our study, we developed radiation classifiers that can predict the irradiation status of blood samples. Both paired and unpaired classifiers constructed from all differentially expressed miRNAs performed with an accuracy of 100%. The robust

performance of the unpaired classifiers is especially important because their functioning does not require pre-exposure control samples. These results encourage the pursuit of additional studies that further investigate the potential of miRNAs to serve as reliable biomarkers of radiation exposure.

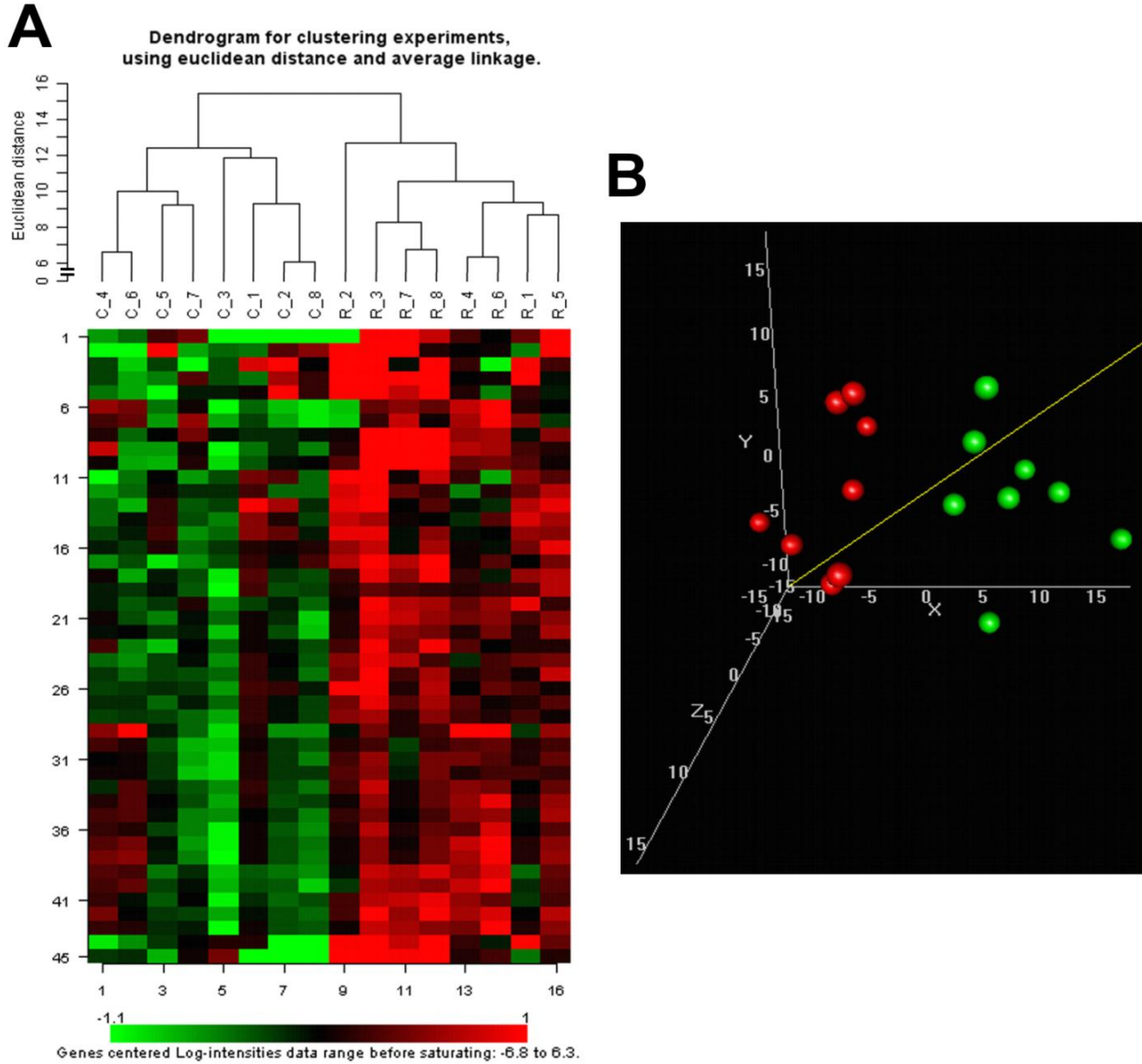


Fig. 1. miRNA signatures change significantly after irradiation. A) Hierarchical clustering. A heat map shows miRNA expression levels for all samples (columns) and miRNAs (rows). All patient control samples (labels starting with C) form a separate cluster from the samples obtained after radiation therapy (labels starting with R). B) Multidimensional scaling. Control samples (shown in green) and samples that were collected after total body irradiation (displayed in red) form two separate clusters.

^a Department of Radiation Oncology, Memorial Sloan-Kettering Cancer Center, New York, NY

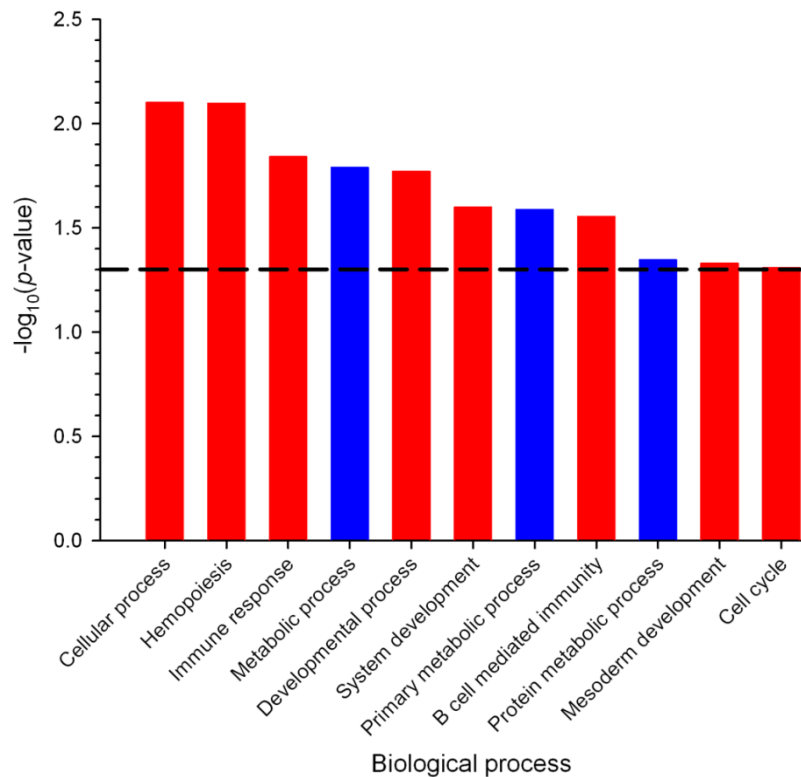


Fig. 2. miRNAs may regulate several biological processes after total body irradiation. Gene-ontology analysis of the predicted miRNA target genes revealed the biological processes in which the predicted target genes significantly responding to radiation are overrepresented (red columns) or underrepresented (blue columns). Processes above the horizontal dashed line exhibit statistically significant over- or underrepresentation at a p-value of < 0.05.

We estimated the effects of the radiation-induced miRNAs on cell processes by combining gene expression, software-assisted miRNA target analysis, and GO data analysis. A strength of our study is that we determined radiation-induced gene expression changes in addition to miRNA profiles. Consequently, we possess information on physiologically downregulated genes, and do not solely rely on bioinformatics-based predictions of miRNA targets. Overall, 38% of the downregulated genes were predicted targets of the upregulated miRNAs, using our context-score cutoff criterion. It should be noted that only downregulated, and not translationally repressed, mRNAs are included in this number as the detection of translationally repressed mRNAs requires different methods. Our GO analysis shows that miRNA target genes are involved in hemopoiesis, the immune response, B cell-mediated immunity, and other processes. Interestingly, miRNA control of genes involved in metabolic processes is decreased, which is most likely due to the underrepresentation of genes involved in metabolic processes among the differentially expressed genes (Fig. 2).

References

1. Shkumatava A, Stark A, Sive H, *et al.* Coherent but overlapping expression of microRNAs and their

targets during vertebrate development. *Genes Dev* 2009;23:466-481.
 2. Friedman RC, Farh KK, Burge CB, *et al.* Most mammalian mRNAs are conserved targets of microRNAs. *Genome Res* 2009;19:92-105.
 3. Croce CM. Causes and consequences of microRNA dysregulation in cancer. *Nat Rev Genet* 2009;10:704-714.
 4. Ferracin M, Veronese A, Negrini M. Micromarkers: miRNAs in cancer diagnosis and prognosis. *Expert Rev Mol Diagn* 2010;10:297-308.
 5. Taft RJ, Pang KC, Mercer TR, *et al.* Non-coding RNAs: regulators of disease. *J Pathol* 2010;220:126-139.
 6. Latronico MV, Condorelli G. MicroRNAs and cardiac pathology. *Nat Rev Cardiol* 2009;6:419-429.
 7. Nana-Sinkam SP, Hunter MG, Nuovo GJ, *et al.* Integrating the MicroRNome into the study of lung disease. *Am J Respir Crit Care Med* 2009;179:4-10.
 8. Kerr TA, Davidson NO. Therapeutic RNA manipulation in liver disease. *Hepatology* 2010;51:1055-1061.
 9. Hebert SS, De Strooper B. Alterations of the microRNA network cause neurodegenerative disease. *Trends Neurosci* 2009;32:199-206.

10. Simone NL, Soule BP, Ly D, *et al.* Ionizing radiation-induced oxidative stress alters miRNA expression. *PLoS One* 2009;4:e6377.
11. Shin S, Cha HJ, Lee EM, *et al.* Alteration of miRNA profiles by ionizing radiation in A549 human non-small cell lung cancer cells. *Int J Oncol* 2009;35:81-86.
12. Chaudhry MA. Real-time PCR analysis of micro-RNA expression in ionizing radiation-treated cells. *Cancer Biother Radiopharm* 2009;24:49-56.
13. Becker GJ, Bosma J, Hendee W. Radiation exposure from medical imaging procedures. *N Engl J Med* 2009; 361:2289-2290; author reply 2291-2282.
14. Hall EJ, Brenner DJ. Cancer risks from diagnostic radiology. *Br J Radiol* 2008;81:362-378.
15. Weinstock DM, Case C, Jr., Bader JL, *et al.* Radiologic and nuclear events: contingency planning for hematologists/oncologists. *Blood* 2008;111:5440-5445.
16. Waselenko JK, MacVittie TJ, Blakely WF, *et al.* Medical management of the acute radiation syndrome: recommendations of the Strategic National Stockpile Radiation Working Group. *Ann Intern Med* 2004;140:1037-1051.
17. Dainiak N. Hematologic consequences of exposure to ionizing radiation. *Exp Hematol* 2002;30:513-528. ■

Validation of the Micronucleus Assay as a Biodosimeter in the C57Bl Mouse Model

Brian Ponnaiya, Antonella Bertucci, Helen Turner and David J. Brenner

The micronucleus assay has been routinely used as a method to measure damage induced by ionizing radiation following in vivo exposure (1). This study was conducted to assess the suitability of using the assay as a biomarker for in vivo exposures under a range of doses and a range of sampling times post irradiation.

12 week old male C57Bl/6 mice were irradiated with total-body single fraction doses of 0, 1.75 Gy, 3.5 Gy, 5.25 Gy and 8.75 Gy with the ¹³⁷Cs gamma-ray irradiator located at the Center for Radiological Research. At 1, 2, 3, 5 and 7 days post-irradiation, ~200 ml were drawn from unanesthetized mice (2 mice/dose/time point) by submandibular bleeding and collected into heparinized capillary tubes. Blood from both mice were pooled and 20ml was overlaid on a ficoll column in a capillary tube. Tubes were centrifuged at 3700 rpm for 5 minutes to isolate the lymphocyte band and lymphocytes were suspended in 2ml of RPMI media containing 15% FBS and 2 % antibiotics. Cultures were stimulated with 5mg/ml PHA for 21 hours at which time cytochalasin B (3 mg/ml) was added to the cultures for an additional 30 hours. Cells were fixed and analysed for micronuclei as previously described (2). Data from 4 different experiments were pooled and frequencies were expressed as mean± SE.

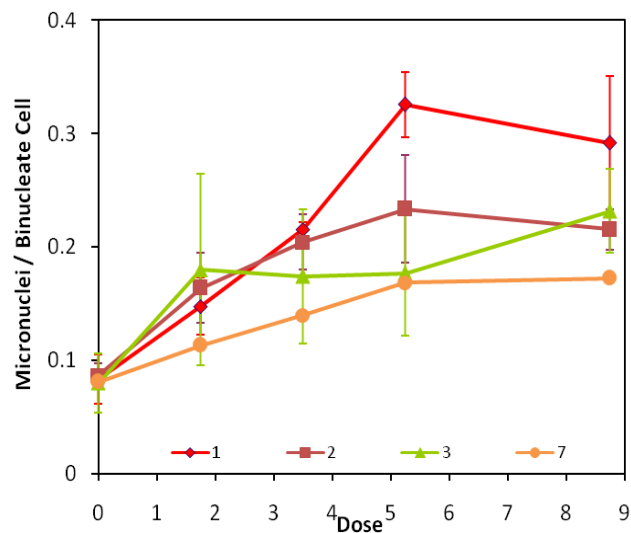


Figure 1. Frequencies of micronuclei in binucleate cells as a function of dose. n=4. Mean ± SE.

The frequencies of micronuclei observed per binucleate cell are presented in figure 1. There was no significant difference in levels of micronuclei in control samples over 7 days post irradiation.

At one day post irradiation, there was an increase in micronuclei in binucleate cells with increasing dose up to 5.25 Gy. With increasing time post irradiation, frequencies in the samples from irradiated mice decreased in a dose dependent manner but continued to remain higher than control levels for upto 7 days post irradiation.

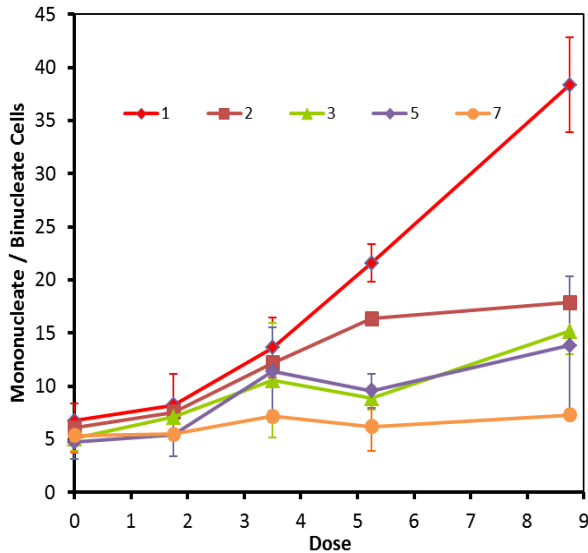


Figure 2. Ratio of mononucleate to binucleate cells as a function of dose. $n=4$, Mean \pm SE.

When the data were analyzed as the ratio of mononucleate to binucleate cells (figure 2) a clear dose response was observed at day 1 post irradiation. This would indicate that cells were not entering the cell cycle as a function of dose i.e. the higher the dose the less the number of cells cycling. With time post irradiation, more and more cells seemed to be cycling, such that by day 7 there were no difference between samples from control and irradiated mice.

Analysis of micronuclei in mononucleate cells is presented in figure 3. At day 1 there was no difference in micronuclei incidences in samples from control and irradiated mice. This was expected, given that cells have

to divide once to produce a micronucleus, therefore frequencies at day 1 are indicative of background levels.

Between days 2 and 3 there appeared to be a dose response up to 5.25 Gy, similar to that seen in micronuclei in binucleate cells at day 1. Yields at 5 and 7 days post irradiation had further increases at the highest dose. It

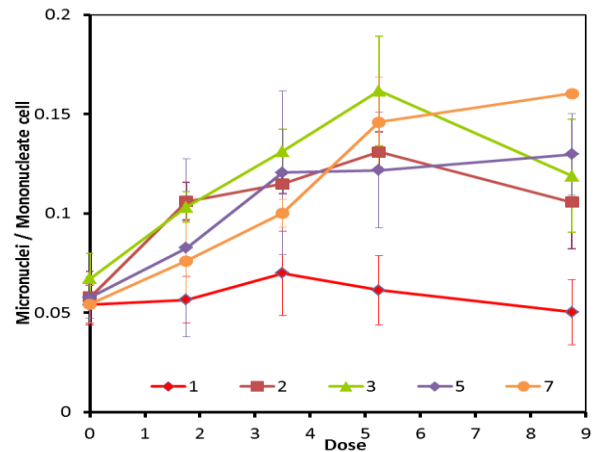


Figure 3. Frequencies of micronuclei in mononucleate cells as a function of dose. $n=4$, Mean \pm SE.

should be noted that with the exception of day 1, samples from irradiated mice demonstrated significantly different yields of micronuclei from controls between days 2 and 7.

In conclusion, using a combination of micronuclei per binucleated cell, micronuclei per mononucleated cell, and mononucleate per binucleate, it is feasible to generate a predictor of radiation dose to mice over the full studied dose and time range.

References

1. M. Fenech, The lymphocyte cytokinesis-block micronucleus cytome assay and its application in radiation biodosimetry. *Health Phys* 98, 234-243 (2010).
2. G. L. Erexson, A. D. Kligerman, M. F. Bryant, M. R. Sontag and E. C. Halperin, Induction of micronuclei by X-radiation in human, mouse and rat peripheral blood lymphocytes. *Mutat Res* 253, 193-198 (1991). ■



Members of Dr. Sally Amundson’s Laboratory (L-r): Dr. Shanaz Gandhi, Associate Research Scientist, Dr. Jarah Meador, Associate Research Scientist, Dr. Sunirmal Paul, Associate Research Scientist and Mr. Lihua Ming, Technician.

RARAF – Table of Contents

RARAF Professional Staff and Picture	117
Research using RARAF	117
Development of Facilities	118
Singletron Utilization and Operation	121
Training	125
Personnel	126
Recent Publications of Work Performed at RARAF	128

RARAF PROFESSIONAL STAFF



RARAF Staff (l-r): Alan Bigelow, Charles Geard, Sasha Lyulko, Andrew Harken, David Brenner, Yanping Xu, Guy Garty, Stephen Marino, Hamin Jeon and Gerhard Randers-Pehrson. Not shown: Antonella Bertucci, Brian Ponnaiya, Helen Turner and Gary Johnson.

David J. Brenner, Ph.D., D.Sc. – CRR Director, RARAF Director
Stephen A. Marino, M.S. – RARAF Manager
Gerhard Randers-Pehrson, Ph.D. – RARAF Associate Director, Chief Physicist
Charles R. Geard, Ph.D. – Senior Biologist
Guy Y. Garty, Ph.D. – Research Scientist
Alan Bigelow, Ph.D. – Associate Research Scientist
Brian Ponnaiya, Ph.D. – Associate Research Scientist
Helen Turner, Ph.D. – Associate Research Scientist
Antonella Bertucci, Ph.D. – Associate Research Scientist
Andrew D. Harken, Ph.D. – Post-Doctoral Research Scientist
Yanping Xu, Ph.D. – Post-Doctoral Research Scientist
Oleksandra Lyulko, – Pre-Doctoral Research Scientist

The Radiological Research Accelerator Facility

AN NIH-SUPPORTED RESOURCE CENTER – WWW.RARAF.ORG

Director: David J. Brenner, Ph.D., D.Sc.

Associate Director: Gerhard Randers-Pehrson, Ph.D.

Manager: Stephen A. Marino, M.S.

Research Using RARAF

The “bystander” effect is the response of cells that are not directly irradiated when in close contact with, or are even only in the presence of, irradiated cells. For the past several years, many of the biology studies, including those involving animals, have examined this effect. The emphasis of most of the present experiments is to determine the mechanism(s) by which the effect is transmitted, primarily direct gap junction communication through cell membrane contact. Both the Microbeam and the Track Segment Facilities continue to be utilized in various investigations of this phenomenon. The single-particle Microbeam Facility provides precise control of the number and location of particles so that irradiated and bystander cells may be distinguished, but is somewhat limited in the number of cells that can be irradiated. The Track Segment Facility provides broad beam irradiation that has a random pattern of charged particles but allows large numbers of cells to be irradiated quickly.

To investigate cell-to-cell communication in the bystander effect using the Track Segment Facility a special type of cell dish is used. These “strip” dishes consist of a stainless steel ring with thin Mylar foil glued to one side into which a second, slightly smaller dish is inserted. The Mylar foil glued to the inner dish has alternate strips of the Mylar removed. Cells are plated over the combined surface and are in contact. The Mylar on the inner dish is thick enough (38 μm) to stop the ^4He ions and the cells plated on that surface are not irradiated and are “bystander” cells.

Research into bystander effects in 3-D systems continued this past year. Cultured tissue samples were irradiated in a thin line with either helium ions or protons using the Track Segment Facility. A prototype fixture has been constructed and tested that would allow microbeam irradiation of the very thin ears of hairless mice. Another fixture has been tested that would enable the rapid irradiation of multiple *C. elegans* nematodes without anesthetization. The multiphoton laser system has been used to image zebrafish hatchlings in preparation for future microbeam irradiations by William Dynan at the Georgia Health Sciences University.

The multiphoton laser system is a tool that can be used independently of the charged particle microbeam to produce 3-D images of specimens or to irradiate them with the UV microspot. Several users, both internal and external, have begun to make use of this facility, particularly for 3-D imaging.

The experiments performed using the RARAF Singletron between January 1 and December 31, 2010 and the number of shifts each was run in this period are listed in Table I. Fractional shifts are assigned when experimental time is shared among several users (*e.g.*, track segment experiments) or when experiments run for more or less than an 8-hour shift. Use of the accelerator for experiments was 20% of the regularly scheduled time (40 hours per week), about 1/3 lower than last year. Twelve different experiments were run during this period. Five experiments were undertaken by members of the CRR, supported by grants from the National Institutes of Health (NIH) and the National Aeronautics and Space Administration (NASA). Seven experiments were performed by external users, supported by grants and awards from the Department of Defense (DoD), NASA, and the Department of Energy (DoE). Brief descriptions of these experiments follow.

Efforts to identify the cell-to-cell signaling transduction pathways involved in radiation-induced bystander responses were continued by Hongning Zhou and Tom Hei of the CRR (Exp. 110). In some experiments a fraction of the cells were irradiated either in the nucleus or the cytoplasm using the Microbeam Facility focused ^4He beam. Induced micronucleus formation in COX-2 wild type or heterozygote mouse embryo fibroblasts was significantly higher than in controls; however in COX-2 null mouse embryo fibroblasts this bystander response was dramatically reduced after either nuclear or cytoplasmic irradiation. Cytoplasmic irradiation induced mutagenesis in mitochondrial functional human skin fibroblasts, although the mutation induction was relatively lower than in the nuclear-irradiated cells. It induced, however, very little, if any, mutagenesis in directly irradiated cells without mitochondrial DNA. Furthermore, using real-time quantitative PCR they found that cytoplasmic irradiation with ^4He ions induced a transient increase in mitochondrial DNA content in human skin fibroblasts as a function of time post irradiation. One day post-irradiation, cells were stained with DiOC6, a cell-permeant, green fluorescent dye that is selective for the mitochondria of live cells. When compared to similarly-treated controls, irradiated cells showed a significant reduction in mitochondrial membrane potential, indicating a loss of function. These results indicate that mitochondria play a critical role in cytoplasmic

irradiation-induced genotoxicity and have implication for understanding the cellular response to DNA damage and low-dose radiation risk assessment.

Military personnel can be exposed to the radioactive alpha emitter and heavy metal depleted uranium (DU). Alexandra Miller of the Armed Forces Radiobiological Research Institute (AFFRI) continued studies using 125 keV/ μm ^4He ions from the Track Segment Facility to evaluate DU radiation-induced carcinogenesis using *in vitro* models and to test safe and efficacious medical countermeasures (Exp. 113). Human osteoblast cells (HOS) cells were irradiated with ^4He ions using the Track Segment Facility to evaluate the effect of the biological countermeasure phenylbutyrate (PB). The following endpoints were examined: survival, neoplastic transformation, chromosomal aberrations, and global DNA methylation status. The results demonstrated that 1) alpha particle exposure induced DNA hypomethylation; 2) PB can protect HOS cells from alpha radiation-induced neoplastic transformation and chromosomal damage.

A group led by Sally Amundson of the CRR concluded three experiments using cDNA microarray hybridization and other methods to investigate radiation-induced gene expression profiles in primary human fibroblast and epithelial cell lines. Shanaz Ghandhi and Lihua Ming used the Track Segment Facility for comparison of gene expression responses to direct and bystander irradiation (Exp. 133). Human lung fibroblast cells (IMR90) and human skin fibroblasts were plated on "strip" dishes for direct-contact bystander irradiations using a dose of 0.5 Gy of 125 keV/ μm ^4He ions. Cells were assayed for micro-nucleus formation and gene expression and western blot analysis was performed. A role for interleukin-33 in the signal transmission for the bystander effect was identified.

In the second experiment (Exp. 136), performed by Alexandre Mezentsev, artificial human tissue model Epi-200 (MatTek) was irradiated using the Track Segment Facility. The tissue is composed of ~20 layers of cells, which represent keratinocytes at different stages of differentiation. The goal of this project is to characterize the effects on tissue *ex vivo* of low and high doses of ionizing radiation. The tissues were irradiated with protons having an initial LET of ~10 keV/ μm or ^4He ions having an initial LET of ~73 keV/ μm , either over the entire tissue surface or in a narrow line (~25 μm) across the diameter using a thin, slit-shaped collimator. Two types of procedures were performed: isolation of total RNA and immunohistochemistry. The RNA provides quantification of gene expression by Microarray analysis and validation by quantitative real-time PCR. Microarray results are analyzed by computer using gene ontology procedures and network analysis, which normally has a graphical output representing the specific responses to the ionizing radiation. Tissue samples are also fixed in formalin, embedded in paraffin, and sectioned parallel to the line of irradiation for immunohistochemistry and counterstaining. This provides characterization of proteins of interest and describes their role in post-

irradiation events, such as transcriptional regulation, contribution to cell signaling mechanisms, and gap junction signaling.

In the third experiment, Sally Amundson used the Microbeam Facility to irradiate primary human lung fibroblasts either in the nucleus or the cytoplasm with 5.2 MeV ^4He ions. RNA was extracted at half-hour and four-hour post-exposure time points to perform global gene expression analysis in order to gain a better understanding of the cell signaling that arises from radiation damage to the cytoplasm and which damage response pathways require direct damage to DNA (Exp. 139). Results of the experiments have been unexpected; repeated irradiations have been performed and additional controls have been examined to confirm these results.

David Chen and Aroumougame Asaithamby from the University of Texas Southwestern Medical Center extended their work on DNA damage sensing and repair factors to the investigation of base-damage-repair dynamics in HT1080 human fibrosarcoma cells after microbeam irradiation (Exp. 141). The cells contain enhanced green fluorescent protein (EGFP) reporter attached to the base-repair protein 8-oxoguanine DNA glycosylase 1 (OGG1). As a preliminary step to microbeam irradiation, it was decided to verify that UV laser induction of OGG1 foci at UT Southwestern also could be observed at RARAF. The multiphoton microscope at RARAF was used in two modes: as an imaging device and as a UV microspot irradiator. For pre- and post-irradiation multiphoton microscopy imaging, 970 nm incident laser light, which acts as 485 nm during two-photon excitation, was used to excite EGFP. For UV microspot irradiation, the laser was tuned to 700 nm incident laser light, which acts as 350 nm at the microspot, to induce DNA damage in the cell nuclei. It was observed that when the laser energy delivered to a cell nucleus was excessive, the cell nucleus was virtually annihilated. When the delivered energy was reduced below the cell-killing threshold, OGG1 foci formation was observed along with an intact cell nucleus, verifying laser-induced UV OGG1 foci formation.

A study of the LET dependence of DNA fragmentation using the Track Segment Facility was undertaken by Dalong Pang of Georgetown University (Exp. 147). Viral plasmids in solution were made into a thin layer of known thickness by pipetting a small volume onto a standard track segment dish, placing a cover slide on the liquid, and forcing the liquid to the edges of the cover slip. The DNA was irradiated with doses from 1kGy to 8 kGy of 10 keV/ μm protons or 73 or 125 keV/ μm ^4He ions. The irradiated DNA samples were subsequently analyzed using the atomic force microscope at Georgetown University. The DNA fragment lengths were measured and grouped into various length intervals, and length-dose histograms were constructed. From the histograms, quantities such as the number of DSB per DNA and the spatial distribution of double-strand breaks (DSB) on a DNA molecule were derived. The LET dependence of these quantities was observed, indicating

the greater clustering capacity of high-LET radiations. Monte Carlo simulation of DNA fragment length distribution by the aforementioned radiations is underway and the results will be analyzed in comparison to the AFM measured data. Further validation and refinement of the model may be achieved through such comparisons. The biological significance of short DNA fragments in non-homologous end joining (NHEJ) generated by clustered DNA damage is being investigated using DNA binding, kinase activation, and rejoining assays. Proteins examined include Ku, DNA-PK, and DNA ligases.

A new wide-energy neutron spectrometer design, intended for use in the International Space Station to examine the neutron spectrum to which astronauts are exposed, was tested at RARAF by David Slaughter of Photogenics (Exp. 149). The spectrometer consists of a large plastic scintillator containing ${}^6\text{LiGd}(\text{BO}_3)_3\text{:Ce}$. Some of the neutrons lose all their energy in multiple collisions in the scintillator, producing an initial light pulse in the scintillator. The residual neutron is captured by ${}^6\text{Li}$, ${}^{10}\text{B}$, or natural Gd, which all have extremely large thermal neutron capture cross sections. The nucleus that has captured the neutron releases an energetic alpha particle or electron producing a second pulse in the detector, which indicates that the first pulse constituted the entire neutron energy. An advantage of this design is the direct measurement of the neutron spectrum. Most other spectroscopy systems require complicated deconvolution programs to determine the neutron spectrum. Spectrum measurements were made for neutron energies between 0.5 and 2.5 MeV as well as 5.9 and 14.0 MeV. The chamber was also irradiated with ~ 4.2 MeV protons to observe individual proton pulses.

A broad-beam charged particle facility has been developed at the LARN Laboratory at the University of Namur, Belgium. Stephané Lucas initiated an intercomparison of the LARN and RARAF irradiation facilities (Exp. 148). Three graduate students from the University of Namur assisted in performing the cell irradiations. Cell survival after irradiation of the cancer cell line A549 at RARAF with ${}^4\text{He}$ ions at dose rates similar to those used at LARN indicated a much greater cell killing than at the Belgian facility ($\alpha = 3.3$ vs. 2.4). Interestingly, they observed that irradiated EAhy926 endothelial cells, when co-cultured with un-irradiated A549, induced a significant mortality in the A549 cells, which was almost as high as observed after A549 cell irradiation. To better understand the interaction between the two cell types after irradiation, a gene expression analysis was performed using Taqman Low Density Arrays. Interestingly, p21 was not overexpressed by EAhy926 cells 24h after 1 Gy ${}^4\text{He}$ ion irradiation. The expression of GADD45A also did not change. This may suggest that p53 was not activated after EAhy926 cell irradiation or that the activation occurs earlier.

Measurements of cell and nucleus thicknesses were made for confluent and non-confluent A549 cells using the multiphoton microscope and staining with Hoechst 33342(nucleus), CellTracker Orange and CellMask Orange (cytoplasm and membrane).

David Cove, from the University of Leeds, UK and Ralph Quatrano from Washington University in St. Louis, where Dr. Cove was visiting, irradiated the moss *Physcomitrella patens* to produce mutant spores by charged particle irradiation using the Track Segment Facility (Exp. 150). He was assisted by Edward Tucker of Baruch College, CUNY, who actually performed the irradiations and had performed charged particle irradiations of the same moss at RARAF several years ago (Exp. 127). Ion beam irradiation is reported to induce DNA deletions up to about 10kb. Using arrays, the sequence deleted from the genome can be detected. The aim is to establish a procedure for the identification of genes, mutations in which lead to specific phenotypes. If this procedure could be made routine, it would open up a path to forward gene discovery, which is at present not available for this model system. Unfortunately, initial experiments to determine a survival curve for 10 keV/ μm protons suffered from contamination and erratic response.

An investigation into adaptive and bystander effects in the human colon cancer cell line HCT116 was initiated by David Boothman of the University of Texas Southwestern Medical Center (Exp. 151). Cells with either both genes or neither gene for p53 (p53^{+/+} or p53^{-/-}) were transfected with either insulin-like growth factor-1 (IGF-1) or clusterin (CLU), both tagged with green fluorescent protein (GFP), and irradiated with the charged particle microbeam and the Track Segment Facility. After irradiation, cells were examined for GFP foci to determine if there was a response to DNA damage by either of the tagged proteins. In these initial irradiations, an elevated GFP expression as a function of dose was not observed for the three cell types which had retained sufficient cells to justify imaging. Further work needs to be done to get these cell lines to attach to and grow on the microbeam and track segment dishes and in staining the cells sufficiently for microbeam irradiation.

Brian Ponnaiya and Howard Lieberman of the CRR, with the assistance of Shanaz Ghandhi, are studying the effect of Rad9 on radiation-induced changes in gene expression in human and mouse cells directly irradiated or as bystanders (Exp. 152). Human H1299 cells that have Rad9 knocked down and mouse ES cells that have a homozygous deletion of Rad9, along with wild type controls, are being irradiated on strip dishes using the Track Segment Facility. Optimal doses of ${}^4\text{He}$ ions in the range of 0.5 to 5 Gy are being determined by pilot studies. Cells will be collected at appropriate times after exposure up to 24 hours for gene expression analyses and micronucleus formation.

Table I. Experiments Run at RARAF January 1 - December 31, 2010

Exp No.	Experimenter	Institution	Exp. Type	Title of Experiment	Shifts Run
110	H. Zhou, T. K. Hei	CRR	Biol.	Identification of molecular signals of alpha particle-induced bystander mutagenesis	16.0
113	A. Miller	AFRRI	Biol.	Role of alpha particle radiation in depleted uranium-induced cellular effects	0.3
133	S. Ghandhi, S. Amundson	CRR	Biol.	Bystander effects in primary cells	4.0
136	A. Mezentsev S. Amundson,	CRR	Biol.	Bystander effects in 3D tissues	2.5
139	S. Amundson	CRR	Biol.	Signal transduction in cytoplasmic irradiation	3.5
141	A. Asaithamby D. Chen	Univ. of Texas Southwestern Medical Center	Biol.	Visualization of recruitment of DNA damage markers to the sites of DNA damage induced by microbeam irradiation	3.5
147	D. Pang	Georgetown Univ.	Biol.	LET dependence of DNA fragmentation by charged particles	8.5
148	S. Lucas	Univ. of Namur, Belgium	Biol.	Site comparison of two cell line irradiation with broad beam	3.0
149	D. Slaughter	Photogenics	Phys.	Characterizing a high-performance neutron spectrometer between 1-14 MeV using a LGB/PVT composite scintillator and PMT	3.5
150	D. Cove	Washington University	Biol.	Ion beam mutagenesis of the moss <i>Physcomitrella patens</i>	1.8
151	D. Boothman	Univ. of Texas Southwestern	Biol.	Role of ATM-IGF-1-sCLU in adaptive and bystander effects in human cancer cells.	1.8
152	B. Ponnaiya, H. Lieberman	CRR	Biol.	The role of Rad9 in mediating global gene expression in directly irradiated and bystander cells	0.8

Development of Facilities

Development continued or was initiated on a number of extensions of our facilities:

- Focused accelerator microbeams
- Focused x-ray microbeam
- Neutron microbeam
- Non-scattering particle detector
- Advanced imaging systems
- Targeting and manipulation of cells
- Small animal systems

Development of focused accelerator microbeams

The electrostatically focused microbeam has been operating reliably for the past year, consistently producing a beam spot 1-2 μm in diameter using a 500 nm thick silicon nitride exit window. This window has a larger area (1.5 mm x 1.5 mm), making it more useful for most irradiations than the thin (100 nm) window with dimensions of only 0.25 mm x 0.25 mm that is used when a sub-micron beam spot is desired.

Emphasis this year was on increased quality control and making the Microbeam a turn-key facility. Analog-to-digital converters were set up to monitor the control voltages to the six high voltage power supplies for the electrostatically focused charged particle microbeam, the output voltages and currents from those supplies, and the vacuum pressure at the upper electrostatic lens. This enables us to better diagnose any problems that might

occur with the lens rods. We now do a microbeam test run the evening before an irradiation. The next morning, after the accelerator has warmed up, the charged particle beam is found immediately and has a minimal beam spot diameter. This provides an earlier and trouble-free start for irradiations and consequently a greater throughput.

Because of damage to the quadrupole triplet rods in one of our compound lens systems in November 2009, 12 new ceramic quadrupole triplet rods were machined in our shop, a very painstaking and time-consuming process due to the precision required and the difficulty of machining ceramics. They were sent to the Institute of High Current Electronics in Russia in November for implantation of platinum ions to increase the surface resistivity, which reduces ion charge build-up on the insulating sections between the electrodes. The rods will return in early 2011. They will then be cleaned, the conductivities measured, the insulating sections carefully masked, and then sent out to have a gold layer 1 μm thick plated on the electrode sections of the rods to make them conducting. The rods will be tested in vacuum with high voltage using the new test fixture constructed last year. After testing, eight of the rods will be assembled into two quadrupole triplet lenses and the lenses mounted in an alignment tube for insertion into the microbeam beam line where the voltages on the lens elements will be adjusted to produce a beam spot with the smallest diameter.

The permanent magnet microbeam (PMM) uses a compound quadrupole triplet lens made from commercially available precision permanent magnets. Its design is similar to that for the lens system for the sub-micron microbeam, the major difference being that it uses magnetic rather than electrostatic lenses. It consistently has been able to produce a ^4He beam spot 5 μm in diameter and in early 2010 it was used for microbeam irradiations when the lenses for the electrostatic microbeam were being worked on. The quadrupole magnet strengths used to focus the beam have been adjusted to produce a focused 4.4 MeV proton beam, which will be used with the Point and Shoot system to develop the Fast and Shoot microfluidics system described below.

Focused x-ray microbeam

We have developed an x-ray microbeam to provide characteristic K_{α} x rays generated by proton-induced x-ray emission (PIXE) from Ti (4.5 keV). Charged particle beams can generate nearly monochromatic x rays because, unlike electrons, they have a very low bremsstrahlung yield.

A small x-ray source is produced by bombarding a Ti target with 1.8 MeV protons using a quadrupole quadruplet lens to focus the beam to $\sim 50 \times 120 \mu\text{m}$ on the target, reducing the requirements on the subsequent x-ray focusing system. The x rays used are emitted at 90° to the proton beam direction. The target is at an angle of 70° to the proton beam, reducing the apparent size of the beam spot in the vertical direction to $\sim 50 \times 50 \mu\text{m}$. A zone plate is used to focus the x-ray source to a beam spot 5 μm in diameter. The system is mounted on its own horizontal beam line on the 1st floor of RARAF and the x-ray beam is oriented vertically, so that the geometry of the microscope and stage is the same as for our charged particle microbeam systems. The diameter of the angle limiting aperture in front of the quadruplet lens has been increased, increasing the beam transmission by a factor of 4. By adjusting the lens voltages, the beam spot size was maintained.

New quadruplet rods have been machined in our shop, implanted with platinum ions, and the electrodes plated with gold. They have been tested to 10 kV using the lens rod test system and assembled into a new quadrupole quadruplet lens. This lens has an 8mm bore, significantly larger than the 2 mm bore on the existing quadruplet, which will allow much higher beam currents to be obtained greatly increasing the dose rate. The new lens has ground planes between each set of electrodes (5), providing better definition of the electric field than the previous lens, which only had ground planes at the ends and between the 2nd and 3rd elements (3).

Neutron microbeam

Neutrons produced by the $^7\text{Li}(p,n)^7\text{Be}$ reaction are emitted only in a forward conical volume when the proton energy is just above the reaction threshold (1.881 MeV). The half-angle of this cone is dependent on the proton

energy and increases with increasing energy. A focused proton microbeam 5 μm in diameter will be incident on a 1 μm thick lithium fluoride target. The backing material will be 20- μm thick Au, selected for its high density and thermal conductivity, which will stop the incident proton beam. Using a 1.886 MeV proton beam, thin samples in contact with the target backing will be exposed to a beam of neutrons 10-15 μm in diameter having energies from 10-50 keV. This will be the first neutron microbeam in the world.

The facility is being constructed on a horizontal beamline using a quadrupole quadruplet to focus the proton beam to $\sim 10 \mu\text{m}$ D. LiF targets have been obtained and construction is underway on the endstation and stage. The microscope, video camera and computer systems are being assembled and tested.

Non-scattering particle detector

Presently the RARAF microbeam endstation delivers a precise number of particles to thin samples by counting the particles traversing them using a gas proportional counter placed immediately above the cells. Because the ^4He ions have a very short range ($\leq 50 \mu\text{m}$), the medium over the cells must be removed to count the ions. To irradiate samples thicker than the range of the incident ions or to allow cell medium to remain in place during cell irradiations, a very thin particle detector is necessary between the beam exit window and the samples.

Development continued on an under-dish detector design that was initially investigated several years ago. An aluminum electrode was evaporated on one side of a thin silicon wafer and three parallel gold electrodes were evaporated on the opposite side, with only a small horizontal gap between the ends of the electrodes. The center gold electrode collects the charge in the diagonal region between it and the aluminum electrode on the opposite surface of the silicon. The other two gold electrodes are guards to reduce noise. Because the gap between the electrodes is much larger than the thickness of the wafer, the capacitance, and therefore the noise, is much lower than it would be if the electrodes overlapped. We have been unable to obtain wafers thinner than 10 μm . Efforts to thin down these wafers to $\sim 2 \mu\text{m}$ have been unsuccessful. The prototype detector produced a usable signal, but was too fragile for use, even with a 10 μm thickness, and quickly broke.

Other thin detector designs are being investigated. One design involves amorphous silicon deposited on the surface of a silicon nitride microbeam vacuum window. Another design is to implant nitrogen ions into a thin piece of silicon, etch the silicon from the opposite side leaving the silicon nitride layer formed by the stopped nitrogen ions and a 1-3 μm thick silicon layer on the implanted side. These designs are being developed in collaboration with the Mechanical Engineering Department of Columbia University and Michael Bardash at QEL, Inc.

Advanced imaging systems

New imaging techniques to view cells without using stain and to obtain three-dimensional images of unstained cells are of great importance for the microbeam irradiation facilities in order to avoid damage to the cells, to maintain physiological conditions, and to image thick samples, especially small animals, for targeting and observation.

Immersion-based Mirau interferometry (IMI) was developed at RARAF. An objective was constructed to function as an immersion lens using standard interferometric techniques by acquiring successive images at four positions with sub-wavelength separations using the vertical motion of the microbeam stage. It uses 540 nm (green) light for imaging and therefore does not induce UV damage in the cells. Interferometry is very sensitive to vibrations, even as small as a fraction of a wavelength. Although this system provides usable images in a vibration-free environment; on the electrostatic microbeam endstation small vertical motions due to vibrations in the building greatly reduce the image quality. Passive and active systems to reduce these vibrations were unsuccessful.

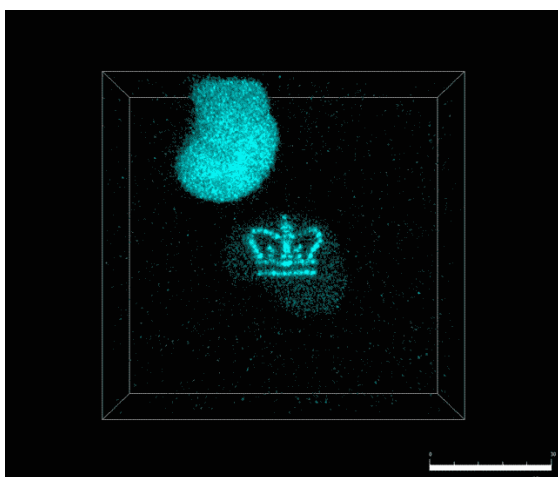


Fig. 1. Columbia crown logo formed in a single cell nucleus by laser UV microspot damage and visualized by fluorescent protein attached to single-strand DNA repair proteins.

In 2008, the feasibility of a new approach to overcome the vibration problem using Simultaneous Immersion Mirau Interferometry (SIMI) was demonstrated. Polarized light is split into equal components in the x and y planes, one of which undergoes a phase shift of 90° by use of $1/8$ wavelength ($\lambda/8$) waveplates. A polarization beam splitter is used to send the x and y components to form interferograms on a single camera. Since the images are taken simultaneously, there is no effect from the vibration. This system is also much faster than Immersion Mirau because only one image is necessary instead of four images at different distances, requiring 3 vertical

movements of the stage.

New optical elements are being fabricated to adapt the Immersion Mirau objective for Simultaneous Immersion Mirau Interferometry. The small, thin glass discs required (8 mm D, 0.2-0.3 mm thick) have been purchased and sent out to be coated, either as spot mirrors or partially reflective (10-85%) beam splitters. The discs will be assembled into 2- or 4-piece elements with $1/8\lambda$ waveplates between the glass discs. When fabrication is completed, these elements will be placed in the objective lens housing and tested on the microbeam facility.

A multi-photon microscope was developed for and integrated into the microscope of the single-particle Microbeam Facility in 2007 to detect and observe the short-term molecular kinetics of radiation response in living cells and to permit imaging in thick targets, such as tissue samples. Two photons delivered closely together in space and time can act as a single photon with half the wavelength (twice the energy). This method has the advantages that the longer wavelength of the light beam allows better penetration into the sample while still being able to excite the fluorophor at the focal volume, and less damage is produced in the portion of the sample not in the focal volume.

The multiphoton system can also be used as a laser “microspot” to induce UV damage in the focal volume of the laser spot, a capability that some RARAF users have requested. A 3-D image of single-strand DNA damage induced in a single cell nucleus by the UV laser spot and imaged using the multi-photon laser is shown in Figure 1 and in 3D on the home page of the RARAF web site (raraf.org). The Columbia crown logo is the result of the fluorescence of tagged single-strand DNA repair proteins at sites of damage caused by the microspot in a single cell nucleus and imaged by multiple laser scans of the cell at different depths, producing a 3D image. As mentioned above, the multiphoton laser was used to produce and visualize DNA base damage in HT1080 human fibrosarcoma cells for the Chen group.

Targeting and manipulation of cells

A new targeting system based on microfluidics is being developed to increase the throughput of the microbeam. In the Flow And Shoot (FAST) system, cells moving through a narrow capillary are imaged by a high-speed camera to track their trajectory. The charged particle beam is deflected using the Point and Shoot system to the position of the cell on the trajectory and the particle beam is enabled. The deflection coil currents will be changed continuously to follow the path of the cell until the requested number of particles is delivered. The system will be capable of tracking several cells at a time. In addition to increasing the speed of the irradiations, this system will be able to irradiate non-adherent cells, such as lymphocytes, that do not plate on surfaces and therefore do not have stable positions.

For preliminary testing of cell flow and targeting we have manufactured a PDMS microfluidic chip using soft lithography. The cross-section of the channel has a width of 200 μm and height of 20 μm , so that the cells, when targeted by the microbeam, flow in the immediate vicinity of the exit window. The flow rate is controlled by a syringe pump. The chip itself is vacuum sealed to the microbeam exit window by applying the house vacuum (~ 0.5 atm) to a 1mm square cross chamber surrounding the flow channel. This reversibly holds the PDMS chip in place and seals the bottom of the flow channel without permanently bonding or gluing the channel to the window. Therefore, the channel can easily be cleaned or replaced to prevent contamination of biological experiments. The top of the irradiation section of the microfluidic channel is designed to be 20 μm thick to let particles reach the detector above the channel. Further, we plan to integrate a nickel TEM grid above the channel to calibrate the beam size because the microfluidic channel does not permit traditional knife edge measurements. This chip has been used to test the microbeam cell tracking software.

Initial tests with fluorescent beads flowing through the channel and imaging at 25 frames/s using an image-intensified camera using resulted in errors in predicted bead position within 1 μm 90% of the time and within 2.5 μm 98% of the time. A fast camera has been ordered that will allow imaging at up to 1,000 frames/s. The increased imaging speed will make possible more accurate cell targeting and permit a higher flow rate, increasing throughput to as much as 100,000 cells/hr.

Another method for the irradiation of non-adherent cells is a novel cellular manipulation technique being adapted for the microbeam endstation at RARAF. We are developing an Optoelectronic Tweezer (OET) system, initially developed by our collaborators, the Ming Wu group at Berkeley National Laboratory. We have created a set of OET electrodes using the equipment provided in the clean room at Columbia University. As a preliminary test, we manufactured the devices on 1 mm thick glass slides. Future work will focus on reducing the thickness of the bottom substrate to allow charged particles to easily pass through.

The OET consists of two parallel-plate Indium Tin Oxide (ITO) electrodes. The top electrode is covered with a 1 μm thick layer of hydrogenated amorphous silicon (a-Si:H), a thin-film semiconductor that acts as a photoconductive layer. When light is focused on the surface of the a-Si:H, the conductivity of the layer increases by several orders of magnitude. By patterning a dynamic light image on the electrode, a reconfigurable virtual electrode is created. When the virtual electrode and its opposing plate electrode are biased with an AC voltage, a non-uniform AC field is created.

In the presence of a non-uniform electric field, a dielectric particle (e.g., cell) will feel a force caused by dielectric polarization (dielectrophoresis, DEP). The

conductivity of the fluid in the chamber must be carefully controlled as it will strongly affect the electric field in the fluid layer of the OET “sandwich”. If the resistance of the fluid layer is less than that of the a-Si:H, then the voltage drop will occur in the a-Si:H layer, and the DEP effect will be reduced in the liquid. The direction of the force is a function of the AC voltage frequency and the fluid conductivity. Below a certain frequency the cells are attracted by the force; at higher frequencies they are repelled.

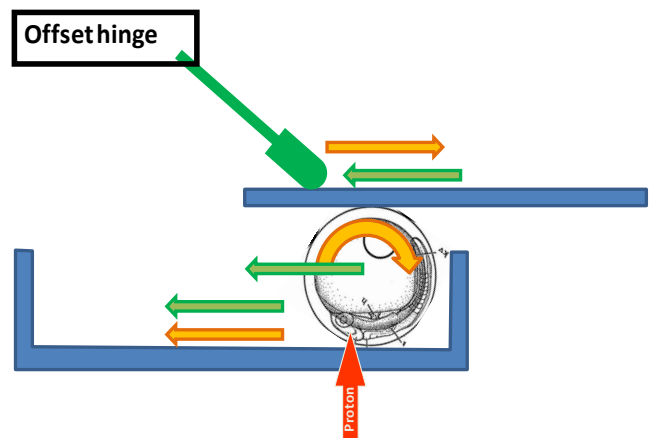


Fig. 2. Scheme of the fish embryo orientation system.

Initial tests have demonstrated the ability to manipulate fluorescent beads, moving them around with an image projected by a laser using the scanning mirror system constructed for multiphoton imaging. Future tests will be done using computer-generated images projected into the microscope.

Small animal systems

The advantages of *C. elegans* as a research tool are well-established, being a multi-cellular eukaryotic organism that is simple enough to be studied in great detail. From a practical perspective, it is small enough to be compatible with microbeam irradiation and a wide variety of mutants and transgenics are readily available as is a large community of *C. elegans* researchers.

In order to support high-throughput irradiations of *C. elegans* worms, we have developed, in collaboration with the Whitesides group at Harvard University, a microfluidic worm clamp for rapid immobilization of large numbers of live worms for morphological analysis and fluorescence imaging. The worm clamps manufactured for our use have four channels and a 10 μm thick polydimethylsiloxane (PDMS) bottom to allow charged particle penetration. We have begun testing these chips for anesthetic-free irradiation of *C. elegans* worms and have seen that the worms indeed remain immobilized. Using this clamp, irradiations can be performed at much higher throughputs than with anesthetized worms, which need to be manually handled individually.

In our initial irradiations of medaka embryos, each embryo was oriented so that the eyes of the embryo were positioned just above the microbeam focal point. The medaka eggs (~ 1 mm D) were rolled around manually using a cover slip to get the correct orientation and the stage was moved to position them over the beam. This was a laborious and time-consuming procedure, which greatly limited the number of specimens that could be irradiated.

Orientation of the fish embryos is being automated using a combination of an offset hinge-mounted probe and the microbeam stage. When the stage and hinge are moved in the same direction (Figure 2), the embryo is translated (green arrows). When the offset hinge and microbeam stage are moved in opposite directions, the embryo is rotated (orange arrows).

In continuing our collaboration with William Dynan (Georgia Health Sciences University, Exp.143), we are investigating the extension of our previous work in irradiating medaka embryos to the irradiation of zebrafish hatchlings. Dr. Dynan has been developing transgenic strains of zebrafish with DNA strand break repair proteins, such as 53BP1, tagged with yellow fluorescent protein (YFP). The novelty of attaching YFP to DNA repair protein is that it enables real-time imaging of the DNA repair process. Following charged particle irradiation, for instance, repair protein converges on DNA damage sites. Subsequent images of YFP reveal foci that indicate the location of DNA damage-and-repair sites. Dr. Dynan's goal is to observe and measure the dynamics of radiation-induced foci formation in single-cell nuclei within live zebrafish hatchlings.

The proposed experiments involve 72-hour post-fertilization transgenic tagged hatchlings, where organ formation is largely complete and the hatchlings are optically clear except for the eyes. At this stage, the hatchlings are about 200 μm thick and a few millimeters in length. During microbeam irradiations with protons, a hatchling will be anesthetized with Tricane. A thin layer of low-melting-point agarose will blanket the hatchling and hold it in place during primary imaging for targeting, irradiation, and follow-up imaging.

Since hatchlings differ significantly from the medaka embryos that we have worked with previously, initial work has involved 3D multiphoton imaging. Fixed hatchlings that were sent to RARAF were removed from their container by pipette and placed on a glass slide. Multiphoton z-stack images were acquired using a 10X objective. Each z-stack comprised 100 optical sections taken at 1- μm increments. During our preliminary multiphoton microscopy trials, three imaging modes were observed: a) YFP fluorescence, b) second harmonic generation (SHG) signal, and c) autofluorescence signal. These initial imaging results are encouraging in that they offer several approaches to identifying potential targets within a hatchling. With higher magnification we will be able to distinguish single cells, observe radiation-induced foci formation in irradiated cells, and also investigate

potential bystander effects in non-targeted cell nuclei.

Several of our users have requested that a mouse skin model be adapted for microbeam irradiation. The chosen model is the SKH-1 hairless mouse ear system. The hairless mouse is a very standard model and the hairless mouse ear is also well established, having first been used in 1980. The ear of the young adult hairless mouse is transparent and large, measuring approximately 13 mm in both length and width, and with an average thickness of 250 μm . Thus it is highly amenable to irradiation with our 5-MeV proton microbeam, which has a range of 350 μm .

We designed and constructed a dedicated mouse and mouse ear holder for microbeam irradiation. The mouse holder is designed to safely restrain the animals as well as support the use of anesthetics during microbeam exposure and is based on a system originally developed in 1980 by Elof Eriksson for microscopic observation of microcirculation in the hairless mouse ear.

The next step was the testing of our customized microbeam mouse/mouse ear holder. The mouse was immobilized using a low-dose cocktail of ketamine/xylazine. The anesthetized mouse was laid on its back on a customized conical area of the mouse holder, while its head was sustained by a customized support. The ear of the anesthetized mouse was then flattened onto the underside of a flat plate using gentle suction provided by a vacuum system incorporated in our holder. This configuration was chosen because in this position the mouse ear can be located underneath the open window of the ear holder, where it can be irradiated by the microbeam.

All tests were conducted in an environment controlled for temperature and humidity. The mouse was kept under observation for 48 hours post test to evaluate whether any sign of discomfort was induced by the anesthesia and handling/restraint procedures. Preliminary results of the tests showed that our microbeam mouse holder does not interfere with the mouse physiology, providing a useful platform for precise manipulation and targeting of in vivo structures using proton microbeams.

Singletron Utilization and Operation

Table II summarizes accelerator usage for the past year. The Singletron is started between 7 and 7:30 a.m. on most days from September through June and between 8 and 9 a.m. the rest of the year. The nominal accelerator availability is one 8-hour shift per weekday (~250 shifts per year); however the accelerator is frequently run well into the evening, often on weekends, and occasionally 24 hours a day for experiments or development. During one period this year the accelerator was run continuously for 10 days.

Accelerator use for radiobiology and associated dosimetry was about 2/3 of that for last year. About half of the use for all experiments was for microbeam irradiations and 40% for track segment irradiations.

Table II.
Accelerator Use, January - December 2010
Usage of Normally Scheduled Shifts

Radiobiology and associated dosimetry	18%
Radiological physics and chemistry	1.5%
On-line facility development and testing	46%
Safety system	2%
Accelerator-related repairs/maintenance	7%
Other repairs and maintenance	3%
Off-line facility development	30%

Approximately 45% of the experiment time was used for experiments proposed by external users, about 3 times the percentage for last year and about twice the number of shifts.

On-line facility development and testing was almost half the available time, about the same as the average for the past 5 years. This was primarily for development and testing of the electrostatically focused microbeam, the PMM, and the x-ray microbeam.

There were 18 shifts of Singletron maintenance and repair time this year due to routine maintenance of the ion source and replacement of the RF tubes used to excite the ion source plasma. This is the same as the average since the Singletron was installed 5 years ago and probably represents the minimum maintenance required. The Singletron charging system continues to be very stable and reliable.

Training

We again participated in the Research Experiences for Undergraduates (REU) project this past summer, in collaboration with the Columbia University Physics Department. Students attended lectures by members of different research groups at Nevis Laboratories, worked on research projects, and presented oral reports on their progress at the end of the 10-week program. Among other activities, the students received a seminar about RARAF and took a tour.

This year Margo Kinneberg of Vassar College, Poughkeepsie, NY participated in the program and worked with Sasha Lyulko on imaging and analyzing micronuclei in irradiated lymphocytes.

We are initiating our first RARAF Microbeam Training Course, to be held in the Spring of 2011. The training course will be designed to give interested physicists and biologists a thorough and hands-on introduction to microbeam technology. Potential

participants were notified by fliers as well as posted and verbal announcements at the Radiation Research Society meeting held in September and by e-mail, using an address list from the most recent Microbeam Workshop, held in 2009. Seventeen applications with CVs were received. The applicants were from the U.S., Europe, South America and the mid-East and had a wide range of education levels and experience, from undergraduate degree to post-doc to researcher. The applicants were about evenly split on gender and background: radiobiology or physics. Of these applicants, a class of 6 was selected. The students will receive lectures on microbeam physics and biology, view demonstrations of the procedures used to validate the microbeam size and position and the biological procedures used to prepare cells for irradiation, and will plate and irradiate cells with the microbeam themselves.

Dissemination

The content of our website is continually updated to reflect the current state of the research at RARAF. For regular users we offer useful information such as the current month's accelerator schedule, information on experiment scheduling, and our experiment scheduling form. For prospective new users there is a significant amount of information about the work done at RARAF and the capabilities of the facility, as well as forms and instructions for proposing new experiments. In the Dissemination section, we offer a list of papers detailing research performed at RARAF and published in peer-reviewed journals. Many of these papers and almost all recent papers are available in PDF format free from our web site. The web site also has information on the Slow and Fast Neutron and Charged Particle beams that are available for those interested. To further disseminate general information about microbeam technology, we are active participants in Wikipedia. We have created or significantly expanded encyclopedic entries for a number of topics such as microbeam, RARAF, and Mirau interferometry and have encouraged others in the microbeam community to participate in these efforts as well.

The 10th International Workshop: Microbeam Probes of Cellular Radiation Response will be hosted at Columbia University in March 2012 by RARAF personnel. This workshop provides a forum for the microbeam community to come together and discuss the present and future of microbeam research. The RARAF web site will be the central repository for information on this meeting.

Personnel

The Director of RARAF is Dr. David Brenner, the Director of the Center for Radiological Research (CRR). The accelerator facility is operated by Mr. Stephen Marino, the manager, and Dr. Gerhard Randers-Pehrson, the Associate Director of RARAF.

Dr. Charles Geard, the former Associate Director of the CRR, now spends most of his time at RARAF.

Dr. Brian Ponnaiya, an Associate Research Scientist, is the biology advisor for RARAF. He presently spends about half his time at the CRR

Dr. Alan Bigelow, an Associate Research Scientist, is continuing the development of the multiphoton microscopy system and the “microspot” irradiation facility as well as Optical Electronic Tweezers for manipulating cells.

Dr. Guy Garty, a Research Scientist, finished developing the permanent magnet microbeam (PMM) and is now developing the Flow and Shoot (FAST) system. He spends about half his time working on the National Institute of Allergy and Infectious Diseases (NIAID) project, for which he is the project manager.

Dr. Antonella Bertucci, a Postdoctoral Fellow, spends part of her time at RARAF working on small animal irradiation using the microbeam

Dr. Andrew Harken, a Postdoctoral Fellow, is responsible for the x-ray microbeam and the Point and Shoot targeting system. He is also working on the imaging of cells without stain using a highly sensitive EMCCD camera.

Dr. Yanping Xu, a Postdoctoral Fellow, has been working on the development of a neutron microbeam. He is also working on the NIAID project, developing an accelerator-generated neutron source with a spectrum similar to that at Hiroshima.

Sasha Lyulko, a graduate student in the Physics Department at Columbia University, is involved in developing the Simultaneous Immersion Mirau Interferometry (SIMI) system and also spent about half her time working on imaging on the NIAID project.

Dr. Stephane Lucas, a visiting professor, who arrived in September, 2009 on a sabbatical leave from the University of Namur, Belgium, stayed until May. Three students from the University of Namur visited RARAF and performed cell irradiations using the Track Segment Facility while he was here.

Dr. Alexandre Mezentsev, an Associate Research Scientist, irradiated cultured tissue systems using the Track Segment Facility and spent a portion of his time at RARAF. He left the CRR in August.

3. Hei, T.K., Zhou, H., Chai, Y., Ponnaiya, B., and Ivanov, V.N. Radiation Induced Non-targeted Response: Mechanism and Potential Clinical Implications. *Curr. Mol. Pharmacol.* 2010 Dec 14. [Epub ahead of print].
4. Hong, M., Xu, A., Zhou, H., Wu, L., Randers-Pehrson, G., Santella, R.M., Yu, Z. and Hei, T.K. Mechanism of genotoxicity induced by targeted cytoplasmic irradiation. *Br J Cancer.* **103**: 1263-1268 (2010) PMID: PMC2967061.
5. Ivanov, V.N., Zhou, H., Ghandhi, S.A., Karasic, T.B., Yaghoubian, B., Amundson, S.A. and Hei, T.K. Radiation-induced bystander signaling pathways in human fibroblasts: a role for interleukin-33 in the signal transmission. *Cell. Signal.* **22**: 1076-87 (2010) PMID: PMC2860693.
6. Kovalchuk, O., Zemp, F., Filkowski, J., Altamirano, A., Dickey, J.S., Jenkins-Baker, G., Marino, S.A., Brenner, D.J., Bonner, W.M. and Sedelnikova, O.A. MicroRNAome changes in bystander three-dimensional human tissue models suggest priming of apoptotic pathways. *Carcinogenesis* 31: 1882-1888 (2010) PMID: PMC2950932.
7. Lyulko, O.V., Randers-Pehrson, G. and Brenner, D.J. Immersion Mirau interferometry for label-free live cell imaging in an epi-illumination geometry. In: *Imaging, Manipulation, and Analysis of Biomolecules, Cells, and Tissues VIII*, Daniel L. Farkas, Dan V. Nicolau and Robert C. Leif, eds. *Proceedings of SPIE Vol. 7568*, SPIE, Bellingham, WA, 2010.
8. Schettino, G., Johnson, G.W., Marino, S.A. and Brenner, D.J. Development of a method for assessing non-targeted radiation damage in an artificial 3D human skin model. *Int. J. Radiat. Bio.* **86**: 593-601 (2010).
9. Xu, Y., Randers-Pehrson, G., Marino, S.A., Bigelow, A.W., Akselrod, M.S., Sykora, J.G. and Brenner, D.J. An accelerator-based neutron microbeam system for studies of radiation effects. *Radiat. Prot. Dosimetry.* 2010 Dec 3. [PubMed in process]. ■

RECENT PUBLICATIONS OF WORK PERFORMED AT RARAF

1. Ghandhi, S.A., Ming, L., Ivanov, V.N., Hei, T.K. and Amundson, S.A. Regulation of early signaling and gene expression in the alpha-particle and bystander response of IMR-90 human fibroblasts. *BMC Med. Genomics* **3**: 31 (2010) PMID: PMC2919438.
2. Ghandhi, S.A., Sinha, A., Markatou, M., and Amundson, S.A. Time-series clustering of gene expression in irradiated and bystander fibroblasts: an application of FBPA clustering *BMC Genomics* **12**: 2 (2011) PMID: PMC3022823.



Dr. Yanping Xu, Postdoctoral Research Scientist at RARAF.

Publications

1. **Bigelow AW, Randers-Pehrson G, Garty G, Geard CR, Xu Y, Harken AD, Johnson GW and Brenner DJ.** Ion, X-ray, UV and Neutron Microbeam Systems for Cell Irradiation. *AIP Conference Proceedings* **1336**: 349-53, 2011.
2. Bregues M, Paap B, Bittner M, **Amundson SA**, Seligmann B, Lenigk R, Korn R and Zenhausem F. Biodosimetry on small blood volume using gene expression assay. *Health Physics* **98(2)**: 179-85, 2010.
3. **Brenner DJ** and Hricak H. Radiation exposure from medical imaging: time to regulate? *JAMA*. **304**:208-9, 2010.
4. **Brenner DJ.** Medical imaging in the 21st century--getting the best bang for the rad. *New Engl J Med*. **362**:943-5, 2010.
5. **Brenner DJ.** Breast cancers: Prediction and prevention. *J Natl Cancer Inst*. **102**:444-5, 2010.
6. **Brenner, DJ.** Should we be concerned about the rapid increase in CT usage? *Rev Environ Health*. **25**:63-8, 2010.
7. **Brenner, DJ.** Slowing the increase in the population dose resulting from CT scans. *Radiat. Res*. **174**:809-15, 2010.
8. **Broustas CG**, Ross JS, Yang Q, Sheehan CE, Riggins R, Noone AM, Haddad BR, Seillier-Moiseiwitsch F, Kallakury BV, Haffty BG, Clarke R and Kasid UN. The proapoptotic molecule BLID interacts with Bcl-XL and its downregulation in breast cancer correlates with poor disease-free and overall survival. *Clin Cancer Res* **16(11)**:2939-48, 2010.
9. **Calaf GM**, Caba F, Farias J and Rothhammer F. Factors that influence the incidence of breast cancer in Arica, Chile (Review) *Oncology Letters* **1**: 583-588, 2010.
10. Camacho C, Mukherjee B, McEllin B, Ding LH, Hu B, Habib AA, Xie XJ, Nirodi CS, Saha D, Story MD, **Balajee AS**, Bachoo RM, Boothman DA and Burma S. Loss of p15/Ink4b accompanies tumorigenesis triggered by complex DNA double strand breaks. *Carcinogenesis* **31**: 1889-96, 2010.
11. **Chen C, Brenner DJ** and Brown RB. Identification of Urinary Biomarkers from X-Irradiated Mice Using NMR Spectroscopy. *Radiat Res* **175(5)**:622-30, 2011.
12. Chen Y, Zhang J, Wang H, **Garty G, Xu Y, Lyulko OV, Turner HC, Randers-Pehrson G**, Simaan N, Yao YL and **Brenner DJ.** Development of a robotically-based automated biodosimetry tool for high-throughput radiological triage. *Int. J. Biomech. Biomed. Robot.* **1**:115-125, 2010.
13. Coy SL, Krylov EV, Schneider BB, Covey TR, **Brenner DJ**, Tyburski JB, Patterson AD, Krausz KW, Fornace AJ and Nazarov EG. Detection of Radiation-Exposure Biomarkers by Differential Mobility Prefiltered Mass Spectrometry (DMS-MS). *Int J Mass Spectrom.* **291**:108-117, 2010.
14. Einstein AJ, **Elliston CD**, Arai AE, Chen MY, Pearson GD, Delapaz RL, Nickoloff E, Dutta A and **Brenner DJ.** Radiation dose from single-heartbeat coronary CT angiography performed with a 320-detector row volume scanner. *Radiology* **254**:698-706, 2010.
15. Farias JG, Puebla M, Acevedo A, Tapia PJ, Gutierrez E, Zepeda A, **Calaf G**, Juantok C and Reyes JG. Oxidative stress in rat testis and epididymis under intermittent hypobaric hypoxia: protective role of ascorbate supplementation. *J Androl* **31 (3)**: 314-321, 2010.
16. **Garty G**, Chen Y, Salerno A, **Turner H**, Zhang J, **Lyulko O, Bertucci A, Xu Y**, Wang H, Simaan N, Randers-Pehrson G, Yao YL, **Amundson SA** and **Brenner DJ.** The RABIT: a rapid automated biodosimetry tool for radiological triage. *Health Phys.* **98**:209-17, 2010.
17. **Ghandhi SA, Ming, L, Ivanov VN, Hei TK and Amundson SA.** Regulation of early signaling and gene expression in the alpha-particle and bystander response of IMR-90 human fibroblasts. *BMC Med Genomics* **3**:31, 2010.
18. **Ghandhi SA**, Sinha A, Markatou M and **Amundson SA.** Time-series clustering of gene expression in irradiated and bystander fibroblasts: an application of FBPA clustering. *BMC Genomics* **12**:2, 2011.
19. **Grabham P**, Hu B, **Sharma P** and **Geard C.** Effects of ionizing radiation on 3-Dimensional human vessel models: Differential effects according to radiation quality and cellular development. *Radiation Research* **175**: 21-28, 2010.
20. Han L, Hu Z, Liu Y, Wang X, **Hopkins KM, Lieberman HB** and Hang H. Mouse Rad1 deletion enhances susceptibility for skin tumor development. *Mol Cancer* **24, 9**:67, 2010.
21. **Hei TK, Zhou H, Chai Y, Ponnaiya B and Ivanov VN.** Radiation Induced Non-targeted Response: Mechanism and Potential Clinical Implications. *Curr Mol Pharmacol*, **4(2)**:96-105, 2010.
22. Hong, M, Xu A, **Zhou H**, Wu L, **Randers-Pehrson G** Santella RM Yu Z. and **Hei TK.** Mechanism of genotoxicity induced by targeted cytoplasmic irradiation. *Brit. J. Cancer* **103**: 1263-1268, 2010.
23. **Huang SX**, Jaurand MC, Kamp D W, Whysner J, and **Hei TK.** Role of mutagenicity in asbestos fiber

- induced carcinogenicity and other diseases. *J. Toxicol. Environ. Hlth.* **14**:1-67, 2011.
24. **Ivanov V**, Partridge, MA, **Huang SX**, and **Hei TK**. Suppression of the proinflammatory response of metastatic melanoma cells increases TRAIL induced apoptosis. *J. Cell Biochem.* **112**(2):463-75, 2011.
 25. **Ivanov VN**, **Ghandhi SA**, **Zhou H**, **Huang SX**, **Chai Y**, **Amundson SA** and **Hei TK**. Radiation response and regulation of apoptosis induced by a combination of TRAIL and CHX in cells lacking mitochondrial DNA: A role for NF- κ B-STAT3-directed gene expression, *Exp Cell Res* **1**;317(11):1548-66, 2011.
 26. **Ivanov VN**, **Zhou H**, **Ghandhi SA**, Karasic TB, Yaghoubian B, **Amundson SA** and **Hei TK**. Radiation-induced bystander signaling pathways in human fibroblasts: A role for interleukin-33 in the signal transmission. *Cell Signal*, **22**:1076-87, 2010.
 27. Karasic TB, **Hei TK** and **Ivanov VN**. Disruption of IGF-1R signaling increases TRAIL-induced apoptosis: A new potential therapy for the treatment of melanoma. *Exp Cell Res* **316**:1994-2007, 2010.
 28. Kovalchuk O, Zemp FJ, Filkowski J, Altamirano A, Dickey JS, Jenkins-Baker G, **Marino SA**, **Brenner DJ**, Bonner WM, Sedelnikova OA. MicroRNAome changes in bystander three-dimensional human tissue models suggest priming of apoptotic pathways. *Carcinogenesis* **31**:1882-8, 2010.
 29. **Leloup C**, **Hopkins KM**, Wang X, **Zhu A**, Wolgemuth DJ and **Lieberman HB**. Mouse Rad9b is essential for embryonic development and promotes resistance to DNA damage. *Dev Dyn* **239**(11):2837-50, 2010.
 30. **Meador JA**, Su Y, Ravanat JL and **Balajee AS**. DNA-PK deficient human glioblastoma cells are preferentially sensitized by Zebularine. *Carcinogenesis* **31**: 184-91, 2010.
 31. Murray NP, **Calaf GM**, Badinez L, Dueñas R, Badinez O, Orellana N, Reyes E and Fuentealba C. P504S expressing circulating prostate cells as a marker for prostate cancer. *Oncol Rep* **24** (3): 687-692, 2010.
 32. Partridge MA, **Chai Y** **Zhou H** and **Hei TK**. High throughput antibody based assays to identify and quantify radiation responsive protein biomarkers. *Int. J. Radiat. Biol.* **86**: 321-328, 2010.
 33. Roy D, Arason GA, Chowdhury B, Mitra A and Calaf GM. Profiling of cell cycle genes of breast cells exposed to etodolac. *Oncol* **23** (5): 1383-1391, 2010.
 34. Schettino G, **Johnson GW**, **Marino SA** and **Brenner DJ**. Development of a method for assessing non-targeted radiation damage in an artificial 3D human skin model. *Int J Radiat Biol.* **86**:593-601, 2010.
 35. **Shuryak I** and **Brenner DJ**. Effects of radiation quality on interactions between oxidative stress, protein and DNA damage in *Deinococcus* radiodurans. *Radiat Environ Biophys.* **49**:693-703,2010.
 36. **Shuryak I**, Sachs RK and **Brenner DJ**. Cancer risks after radiation exposure in middle age. *J Natl Cancer Inst.* **102**:1628-36, 2010.
 37. **Shuryak I**, Ullrich RL, Sachs RK, **Brenner DJ**. The balance between initiation and promotion in radiation-induced murine carcinogenesis. *Radiat Res.* **174**:357-66, 2010.
 38. Su Y, **Meador JA**, **Calaf G**, DeSantis P, **Zhao Y**, Bohr VA and **Balajee AS**. Human RecQL4 helicase plays critical roles in prostate carcinogenesis. *Cancer Res* **70**: 907-17, 2010.
 39. Su Y, **Meador JA**, **Geard CR** and **Balajee AS**. Analysis of ionizing radiation induced DNA damage and repair in human 3-dimensional skin model system. *Exp Dermatol* **19**: 16-22, 2010.
 40. Suit H, DeLaney T, Goldberg S, Paganetti H, Clasio B, Gerwick L, Niemierko A, **Hall E**, Hallman J and Trofimov A. Proton vs Carbon ion beams in the definitive radiation treatment of cancer patients. *Radiotherapy and Oncology* **95**: 3-22, 2010.
 41. **Wen G**, Hong M, **Calaf GM**, Roy D, Partridge MA, Li B and **Hei TK**. Phosphoproteomic profiling of arsenite-treated human small airway epithelial cells. *Oncol Rep* **23** (2): 405-412 2010.
 42. Zhou G, **Smilenov LB**, **Lieberman HB**, Ludwig T and **Hall EJ**. Radiosensitivity to high energy iron ions is influenced by heterozygosity for *Atm*, *Rad9* and *Brcal*. *Advances in Space Research* **46**: 681-86, 2010.



Members are setting up the monitor to watch the World Cup game at CRR 2010 picnic.



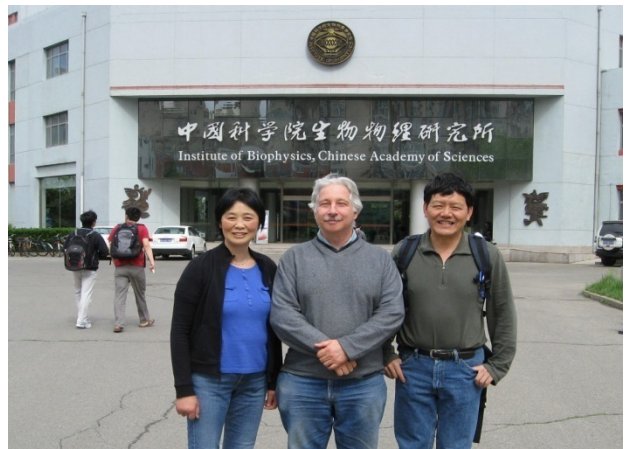
Dr. Howard Lieberman (back row second from the left) at the RSNA grant review panel meeting with other reviewers.



Dr. Tom Hei (front row second from the right) at the 5th NIRS International Open Laboratory Workshop in Chiba, Japan.



Dr. Sally Amundson (left) with Dr. Edouard Azzam (New Jersey Medical School Cancer Center) at the 2010 Annual Radiation Research Society Meeting, Maui, Hawaii.



(L-r): Drs. Aiping Zhu, Howard Lieberman and Haiying Hang (former member of Dr. Lieberman's laboratory) in front of the Chinese Academy of Sciences in Beijing, China.



Christmas lunch party of Drs. Tom Hei's and Howard Lieberman's laboratories.